UNIVERSITE DE LIMOGES

ECOLE DOCTORALE : Sciences et Ingeniérie pour l'Information

FACULTE des SCIENCES et TECHNIQUES de LIMOGES

Année : 2011 Thèse n° 84-2011

THESE

Pour l'obtention du

DOCTORAT DE L'UNIVERSITE DE LIMOGES

Discipline : Electronique des Hautes Fréquences et Optoélectronique

Spécialité : "Electronique des Hautes Fréquences, Photonique et Systèmes"

Présentée et soutenue publiquement par

José Manuel GONZÁLEZ

Composants innovants reconfigurables par voie optique pour des applications microondes

Date de soutenance: Jeudi 15 Décembre 2011

Thèse dirigée par Dominique BAILLARGEAT, Nicolas DELHOTE et Langis ROY

P. BLONDY	Professeur à l'Université de Limoges	**Président**
E. KERHERVE	Professeur à l'Université de Bordeaux	**Rapporteur**
E. RIUS	Professeur à l'Université de Bretagne Occidentale	**Rapporteur**
L. ROY	Professeur à Carleton University - Ottawa	**Examinateur**
D. BAILLARGEAT	Professeur à l'Université de Limoges	**Examinateur**
N. DELHOTE	Maître de Conférences à l'Université de Limoges	**Examinateur**
H. LEBLOND	Ingénieur à THALES ALENIA SPACE - Toulouse	**Invité**
S. McGARRY	Professeur associé à Carleton University - Ottawa	**Invité**
J. BOUCLÉ	Maître de Conférences à l'Université de Limoges	**Invité**

Acknowledgements

This thesis work has been carried out at *Xlim laboratory* in the MINACOM (MIcro et NAnotechnologies pour Composants Optoélectroniques et Micro-ondes).

I would like to show my gratitude to Professor **Dominique Cros**, Director of *Xlim* for welcoming me in his laboratory as well as to Professor **Valerie Mandrangeas**, who is the MINACOM department head, for permitting me to carry out my work at MINACOM.

I would like to thank Professor **Pierre Blondy** from the University of Limoges for accepting the position of president for the thesis jury.

Thanks Professor **Eric Kerhervé** from the University of Bordeaux and Professor **Eric Rius** from the University of Bretagne Occidentale for the interest they have shown in this work and accepting to review it.

I would like to thank Mr. **Hervé Leblond**, engineer at Thales Alenia Space, for accepting the invitation to this thesis defence as well as Professor **Johann Bouclé** from the University of Limoges for accepting the invitation and also for all his help with the *ZnO* material.

Thanks Professor **Steve McGarry** from Carleton University for accepting the invitation to this defence and because he has been very helpful these three years with many different projects I have carried out.

My supervisors, Mr. **Nicolas Delhote**, assistant professor of Limoges University, Professor **Dominique Baillargeat** from Limoges University and Professor **Langis Roy** from Carleton University for all their help and support during these difficult three years. Your encouragement and support have made the work easier and your technological knowledge has been vital for the work carried out. I am grateful for the supervision that all of you have provided.

I would also like to thank also Mrs. **Marie-Laure Guillat**, secretary of MINACOM department at Xlim and Mrs. **Blazenka Power**, administrator of DOE at Carleton University for their help with all the administrative issues and because their work simplifies the everyday life of the researchers and the Ph.D. students.

I cannot forget to thank my collegues at Xlim as **Fiffa, Marco, Lluis, Stefano, Hector, Khaled, Hussein, Mansoib, David and Ludovic** and every others that have shared their time during this three years but I might forget. I have to thank my collegues in Canada too such as **Nathan, Wenyao, Elizabeth, Hedy, Che, Garret, Greg, Atif, Arsalan, Bachir, Tosin** and others I might be forgetting.

Finally, I would like my friends and specially my family for all the support during my student life. They have always been close to me even though the physical distance is sometimes very great. Thanks then to my brother **Toño** and my sisters **Ruth and Maria** but also to my sister-in-law **Ruth** and my brothers-in-law **Ignacio and Antxoka**.

Mila esker denei zuen laguntzagatik.

José Manuel (Popi)

Contents

List of Figures

List of Tables

General introduction

Electronic devices have increased their complexity over the last few years, especially with the appearance of microwave devices operating at multiple bands and standards. In this context, the duplication of circuits carrying out the same functions at different frequencies results in an increase of the size of the developed circuit.

In order to avoid this problem, many researchers have shown lately the importance of tunable circuits, especially those involving passive structures such as filters and antennas which occupy most of the space in a telecommunication chain.

However, up until now, most of the research has focused on tunability methods such as the use of MEMS, varactors or other types of tunability requiring external electrical biasing. In this thesis, we will focus on developing tunable circuits based on optical control with both direct and indirect optical control methods.

Optical control offers great advantage compared to conventional tunability methods, as the light waves do not interact with the electromagnetic waves performing the circuit function. The responses of the circuits are then not affected by the control signals as is the case with methods requiring an electric field or a magnetic field to achieve tunability.

In order to analyze the advantages of optical tunability, the objective of **Chapter 1** will be to demonstrate that conventional tunability methods present some inconveniences compared to optical control. First of all, high frequency systems will be described to place the theme in its context. An overview of tunable microwave circuits will be given afterwards, including some examples of antennas, amplifiers, oscillators and filters. The third part of the first chapter will focus on tunability methods including varactor diodes, ferroelectric and ferromagnetic materials as well as Micro Electro Mechanical Systems (MEMS). Some characteristics of these tunability methods will be given, as well as their advantages or disadvantages. Finally, optical tunability will be presented, explaining why we consider this form of tunability to be attractive for future applications.

Once the work has been placed in its context and the importance of optical tunability established, **Chapter 2** will focus on new test structures for optically sensitive materials and on the materials themselves. The first part of the chapter will then be dedicated to explaining the material properties we are interested in. Then, two new test structures conceived to extract the material properties of optically sensitive materials at microwave frequencies will be presented. Finally, several photosensitive materials that could be exploited for our applications will be presented.

Chapter 3 will concentrate on direct optical control, explaining the main characteristics of this method as an introduction. The chapter will be divided into three main sections corresponding to the development of three main structures exploiting the direct optical control. The first section is a proof of concept of an LTCC photoconductive frequency tunable filter. The theoretical principle of this filter will be explained followed by simulations and its fabrication and measurements. In the last part, an optimization of this circuit will be presented. The second section presents a structure based on direct optical control, consisting of a tunable 3D dielectric resonator where a photoconductive material will be used to achieve tunability. Some theory about dielectric resonators will then be presented followed by the design and the simulations of our complete structure. The section will continue explaining some optimizations that have been carried out and will end by showing the measured results. The third section of this chapter presents a photorefractive frequency tunable filter employing a new polymer-based material. The section will begin with the explanation of the tunable capacitor used as the base line for the presented filter. The first simulated results, both circuit-based and electromagnetic-based, will be shown followed by the fabrication of the device and the measured results. Finally, improvements to the filter fabrication that yielded vastly superior results will also be presented.

After explaining direct optical control, **Chapter 4** focuses on indirect optical control. At the beginning of the chapter, indirect optical control will be presented showing some advantages of this method as well as some examples developed by other researchers. Then, a new structure using this method will be presented, a zero-bias optically controlled RF switch based on a standard CMOS technology.

The technology used in this process will be presented followed by the circuit design and layout. The measured results of the fabricated device will then be shown and the future prospects and conclusion will be given at the end.

This manuscript ends with the general conclusions and perspectives of this work. It is shown that some interest for future applications can be extracted from this thesis.

This thesis work has been carried out between *Xlim UMR 6172 laboratory* (joint lab between CNRS and University of Limoges) on one side, and the Department of Electronics of Carleton University on the other. This joint work has permitted to establish a joint collaboration between the two institutions taking advantage of the facilities and knowledge at both places to conduct the work in an optimum manner. The expertise in EM simulation tools and design from *Xlim laboratory* combined with the circuit modeling and fabrication of Carleton University leads to a complete understanding of the original structures developed during this work.

This thesis has been supported by the *France Canada Foundation for Research* to work on optically reconfigurable microwave components.

Chapter 1

Tunable Circuits and Methods Overview

Contents

The objective of the work presented in this report is to show the feasibility of new optically tunable radiofrequency (RF) circuits using organic polymer materials or any other forms of passive tunability methods.

The main idea of the work was to develop new polymer photosensitive materials, either photorefractive or photoconductive, and to use them on high frequency electronic devices. However, working through this topic, it has been seen that it might be difficult to achieve a good tunable circuit with a new material. So the approach has been to develop new tunability methods prioritizing the fact that the methods have to be passive and optically controllable.

Before explaining the work done during this Ph.D, an overview of the present day high frequency systems will be highlighted and we will continue later with an analysis of different tunability circuits and methods based on the bibliography reviewed.

The first part of this chapter will deal with high frequency systems, explaining some of their properties, their applications as well as their evolution. The second part will be about the different tunable circuits we can find currently and will point out the importance of these circuits as well as some of their possible applications. The third part will focus on the methods used at present for changing some of the properties of those circuits. Finally, we will dedicate the last section of this chapter to analyzing the importance of optical tunability, showing its advantages as well as its disadvantages and some examples done up until now.

1.1 Introduction to high frequency systems

1.1.1 Definition

It is generally admitted that the high frequency waves domain, or otherwise named microwaves, corresponds to a certain part of the electromagnetic waves spectrum, from submetric to millimeter waves, that is from frequency bands of 300 MHz to 300 GHz, or in wavelengths in vacuum from 1 m to 1 mm. This band is sometimes spread out to 100 MHz to 1000 GHz, that is, from 3 m to 0.3 mm. Commonly used designations for each frequency band are shown in Tab. 1.1.

The general consensus is that bands UHF, SHF and EHF bands constitute the high frequency domains, being SHF and EHF bands subdivided (IEEE 521 standard) (Table 1.2)

We could also establish commonality with other electronic domains, if the circuit conception and modeling concerns high frequencies. We only consider that microwave frequencies are involved when the propagation and radiating phenom-

Designation	Frequency band	Wavelength
ELF *(extremely low frequency)*	30 to 300 Hz	10 000 to 1000 km
VF *(voice frequency)*	300 to 3 000 Hz	1 000 to 100 km
VLF *(very low frequency)*	3 to 30 kHz	100 to 10 km
LF *(low frequency)*	30 to 300 kHz	10 to 1 km
MF *(medium frequency)*	0,3 to 3 MHz	1 000 to 100 m
HF *(high frequency)*	3 to 30 MHz	100 to 10 m
VHF *(very high frequency)*	30 to 300 MHz	10 to 1 m
UHF *(ultra high frequency)*	0,3 to 3 GHz	100 to 10 cm
SHF *(super high frequency)*	3 to 30 GHz	10 to 1 cm
EHF *(extremely high frequency)*	30 to 300 GHz	10 to 1 mm
	300 to 3 000 GHz	1 to 0,1 mm

Table 1.1: Common frequency bands

ena are taken into account, which normally is not the case. There is no fixed frontier between the domains but the importance of the electromagnetic phenomena is the criterion for deciding if we are in the microwave frequency domain or not.

1.1.2 General survey of the high frequency systems [1, 2]

The aim of this section is not to give a detailed historical and evolution of the hyperfrequencies, but to give some of the main technological advances. They are going to drive us to the latest technological solutions carried out for the conception of microwave circuits applied to telecommunications. It will therefore be easier to accomplish the new constraints related to size reduction, integrity density increase, and electrical and mechanical behaviors for example. The first historic application of electromagnetic waves is wired transmission, at the very beginning, during the

Designation	Frequency Range
L	1 to 2 GHz
S	2 to 4 GHz
C	4 to 8 GHz
X	8 to 12 GHz
K_u	12 to 18 GHz
K	18 to 27 GHz
K_a	27 to 40 GHz
V	40 to 75 GHz
W	75 to 100 GHz

Table 1.2: SHF and EHF bands

first half of the XIX century, telegraphic signals (digital signals coding a message) happened and later, vocal frequency modulated signals came. Currently, and actually even more and more, the electromagnetic waves, microwaves or not, are mostly used for the telecommunications.

After a slow progression over the centuries following the discoveries of electricity and magnetism, the history of electromagnetic waves (EM) has accelerated during the XIX century with some major milestones:

- Development of models describing the relations between electric and magnetic fields by Arago and especially by Ampère (1820).
- Highlight of the electromagnetic induction by Faraday (1864).
- Theory of electromagnetic waves and their speed calculation by Maxwell (1864).
- Highlight of electromagnetic waves propagation by Hertz (1885).

It is not until XX century that the history accelerates notably with the invention of the vacuum tube (Fleming - 1902), amplifier (De Forest - 1907) and the discovery of the crystal detector (1906). The technology since then evolved quickly to electromagnetic wave applications, both in commercial or military applications.

The 1920-1940 period saw then a raise of the frequency especially with the invention of the magnetron by Hull in 1920 and of the klystron by the Varian brothers in 1937. It was actually then when the high frequency domain was entered with the development of the propagation lines, antennas or passive circuits technologies for instance. The number of applications grew not only in telecommunications but also in radio and television broadcasting, although the material was still too bulky due to the conception of passive circuits. Even though it was known since 1903 (Hull - Germany) that the electromagnetic waves get reflected and diffracted with obstacles, it was only from 1934 that the fist nature scale experimentation of radars were introduced.

The World War II revealed how necessary the wireless transmissions and radar detection were for people's security. It provoked then a rapid development of **microwave technologies**, the consolidation of the circuit theory and antennas, and setting up of the industrial resources.

From 1940 to 1980, the technologies are mature, the design tools have developed and the industry masters the production of telecommunications systems and radar devices, although these products are still expensive and voluminous. For the base station telecommunications a grid of microwave relays was spread in France and Europe for the national communications. It is not until 1970s that the communications moved forward to the intercontinental links via satellites and that the **miniaturization technologies** are really considered.

It is the technological revolution that 1980-2000 years saw that will lead to an important reduction of the costs and to a certain democratization of microwaves: for example servitude radars for door opening, direct TV satellite reception, first generation of cell telephones, etc. During this period the computer resources improvement together with a **reduction of fabrication costs** permitted a development of powerful **conception tools** for microwave frequency devices, circuits and antennas. It results also in an **increase of the performance** and a **miniaturization** accompanied with a cost reduction.

In particular, the 1990s have seen an explosion of **mobile telecommunications**. The communications increasingly high data rates imposed since the beginning the choice of cellular networks and microwave frequency carriers. At UHF "high" band around 900 MHz at the beginning, on L band later around 1800 MHz and in S band (2500 MHz) now for the UMTS (*Universal Mobile Telecommunication System*). The need of miniaturization of mobile devices has been a potent factor for the **development of high frequency integrated circuits**.

Towards the end of the XXth century, the **MMIC** (*Monolithic Microwave Integrated Circuit*) becomes a really competitive product as it permits a new **costs reduction** allowing more **complexity**, and bringing a **performance increase**: it opens a track for the second and third generation cell telephones, to the use of optical based technologies, to active antennas, to local links (WLAN: *Wireless Local Area Network*, with different standards, Bluetooth, WiFi: *Wireless Fidelity*, ultra wideband...), to GPS (*Global Positioning System*) or to wireless tags (RFID: *Radio Frequency Identification Device*).

Over the last fifteen years, the telecommunications market has undergone a huge upheaval. The **cost reduction** has opened the access of radio technologies to the public. At present, wired technology is declining in popularity in favor of all wireless technology. This evolution can be found in telephone or television applications, domotics, the Internet or in data transfer. This phenomenon opens a way to new generations of mobile terminals multistandard and multiband.

The solution to design these new multistandard terminals is to duplicate the whole transmission chain with non tunable circuits (filters, antennas,...) creating a more voluminous device with a greater power consumption. In order to avoid the increase on volume and power consumption, one of the solutions proposed is to use tunable circuits. By using a tunable circuit, we avoid having multiple transmission chains, just trying to design the circuits to be able to operate on multiple standards. Up until now, the tunable circuits are used in one part of the reception chain (antenna, filter,...) and the other parts are designed to operate in a larger frequency band but tunability might be required for several devices in the same chain.

In modern wireless communication systems multi-band and multi-mode devices are taking more and more of the spotlight, becoming a major trend due to their ability to cover different communication standards with a single device. A new wireless paradigm called "cognitive radio" recently emerged as a hot research topic. This radio scans the available spectrum and change its network parameters (frequency, bandwidth, modulation) for maximum data transfer. Some essential components for the cognitive radio are tunable filters, tunable antennas and tunable high-efficiency power amplifiers.

1.1.3 Main application of high frequency systems nowadays and technological trends [3, 4]

Because of the occupation of the frequency spectrum, lots of applications are only conceivable working at higher frequencies, going from some GHz to a hundred GHz. The development of the technologies makes various utilizations possible. Some of these applications such as portable telephony (1800 MHz) or the satellite television direct reception (11 GHz) already require a mass production.

Other domains already cause or will shortly cause the development of a variety of systems. Some of those possibilities are listed here:

- In the **transport domain**, the systems being developed concern applications related to communications where there is a fixed tag and a mobile object: railway car management at 2.45 GHz [5], non-stop toll systems at 5.8 GHz [6] or radar types (anti-collision systems at 77GHz [7]) .

- **Military applications** use the highest frequencies, as high as 94 GHz [8], reserved for that.

- The **satellite communications** and their numerous applications (wireless telephony, multimedia television applications at 12 GHz, etc.) consist on data transfer using high frequency waves. We can quote here the American system GPS working at 1.5 GHz, its direct European competitor GALILEO working around 1.6 GHz as well as the Russian system GLONASS or the Chinese COMPASS [9].

- Finally the **telecommunications** that appeared several times in the domains already evoked consume resources at very high frequencies. It is in this context that rules defining protocols and the carrier frequency have appeared.

For example, in the United States, the standard 802.11 defines links at 1 Mbit/s at 2.4 GHz. the standard 802.11a defines links at a bit rate of 54 Mbit/s at a frequency of 5 GHz; the standard 802.11b (named WiFi) defines at a bit rate of 1, 5.5 or 11 Mbit/s at 2.4GHz. Similarly, for the last mile wireless frequencies of 24, 28 or 38 GHz are reserved [10]. In Europe, the frequencies for the last mile wireless are 3.5, 26 or 28 GHz [11, 12]. There exists also the " *Bluetooth*" protocol, a standard defining links between one master and seven slaves at 2.4 GHz with a bit rate of 1 Mbit/s for distances shorter than 4 m [13].

Since the beginning, the electronics got involved in a race to the high frequencies that has been addressed by the realization of several circuit at microwave frequencies, from around 2 GHz in the 1940s, to some hundreds of GHz nowadays. As we have just said, the evolution of the high frequency telecommunication is continuous and the principal objective remains to get the best performance improvement while reducing fabrication costs.

Integrated circuit complexity grows constantly, the electronics spread continually to new domains or applications and the use of wireless devices has increased drastically. This increased use has caused a need for more efficient devices with advanced functionality. Many of these devices must function over a range of frequencies and conditions which can be achieved using two different techniques. The device can be designed to function over a range of frequencies and conditions, or it can be designed to be tunable. Designing a circuit to operate over a range of frequencies usually comes at the cost of performance. However, if the circuit is made tunable, it can usually be designed to function with increased efficiency.

1.2 Tunable circuits

1.2.1 Introduction

In recent years, extensive research has been performed in electronically tunable microwave components for wireless front-end applications such as phase-shifters, antennas, oscillators and bandpass or bandstop filters. As the electromagnetic environment becomes more populated, frequency-agility and narrow operating bandwidths are becoming highly desirable for different components in RF front-ends. Tunable wideband microwave devices are essential in military applications and long-distance (satellite or troposcatter) communications [14–16]

One of the main applications of tunable circuits is the military according to [15]. Military applications require wide-band and tunable devices for electronic support measuring receivers. World War II and the invention of radar led to significant developments in filters at various laboratories in the U.S, for example at the Harvard Radio Research Laboratory (Cambridge, MA, USA), advances on tunable narrowband filters for searching receivers were made [17]. Electronically tunable circuits are used in scanning receivers as they give relatively fine frequency resolution, albeit at the expense of a relatively low probability of intercept [18]. They are also commonly used in microwave test equipment.

In military radar and tracking receiver systems, the electronic support measures (ESM) system serves to collect and classify information on all radar in the battlefield by amplitude, frequency and pulsewidth [19]. Therefore the receiver needs to cover wide frequency ranges. The electronic countermeasures (ECM) system, which is associated with the ESM system, can then take appropriate countermeasures such as jamming. The operation classifying the signals by frequency can be accomplished by employing tunable bandpass filters.

The recent trend in microwave systems is to enable adaptable and dynamically reconfigurable communication systems, such as software defined and cognitive radios where baseband processing is done using digital techniques [20].The spectrum of interest therefore is generally very wide however this makes the receiver susceptible to interferers that could saturate the system.

Frequency and polarization agility are necessary for many advanced communication systems. Frequency Hopping Spread Spectrum systems jump between many different frequencies at a high rate to provide immunity to jamming, narrow-band interferers , and multi-path fading. Software Defined Radio is a concept to realize the multimode wireless radio system which can exchange radio and protocol specification at different frequencies and polarizations to the various kinds of radios by software using digitalized systems and one hardware. Cognitive Radios, in which the frequency and data rate are automatically determined depending on the available spectrum at runtime, are currently being explored [21].

Also, the use of wireless devices has increased drastically over the last decade. This increased use has caused a need for more efficiency devices with increased functionality. The continuing demands for highly portable, more reliable, superior power efficient and above all, low cost wireless systems require that future wireless devices (such as cell phones and PDAs) must be compatible with different communication protocols and capable of operating over a wide frequency range. In addition, as wireless devices become more and more compact, the development of inexpensive and miniaturized tunable circuits with a high performance is crucial.

Wireless communication equipment used in cellular, wireless LAN, GPS, radar and other technologies, makes use of a number of tuned RF circuits. Tuned circuits play an important role in determining the overall signal quality, sensitivity, size and power consumption of mobile wireless devices and the base stations that serve them. Tuned circuits are designed to respond optimally when functioning at a specific frequency, power level or impedance. However, the mobility provided by wireless communications ensures that these conditions do not remain constant but vary considerably with location. Knowing that this variability is in store, the equipment designer often designs for nominal operating conditions and lives with sub-optimum performance when other conditions prevail. Or, the designer may make use of several components in a parallel configuration, switching between them as conditions change. In many cases, a better solution is the use of a single circuit that is not only tuned, but tunable. Tunable circuits can be adjusted, or re-tuned to function optimally as conditions change. Depending on the specific circuit where such tunability is used, the result may be savings in cost, reduction in size, improved battery life, better performance or increased manufacturability.

Each type of wireless network has a set of technical challenges that differ from the others. There are for example different cell phone standards where the frequency or other capabilities are different with each other. These standards differ also depending on the country of use. Despite this proliferation of standards and frequencies, it is highly desirable for a mobile device to roam seamlessly across geographic boundaries, accommodating different protocols and frequencies of use as required. It may also be desirable that it can be able to communicate in IEEE 802.11 standards, WAN and WLAN networks as well as with Bluetooth standard. At the same time, the consumer demands that all this added functionality do not come at the expense of size, cost or battery life. A number of such devices have appeared on the market in the form of tri-band or quad-band handhelds that incorporate multiple cellular modes as well as Bluetooth or WiFi functionality. This generally implies that the designer uses a number of circuits that are duplicated for each band, with the associated penalties of increased size, weight and cost. In contrast, a tunable circuit can perform the function of two or more parallel circuits with a simple change to one of the elements. Fig. 1.1 illustrates this situation for the case of duplexers in a tri-band system where a single tunable duplexer can replace three fixed duplexers.

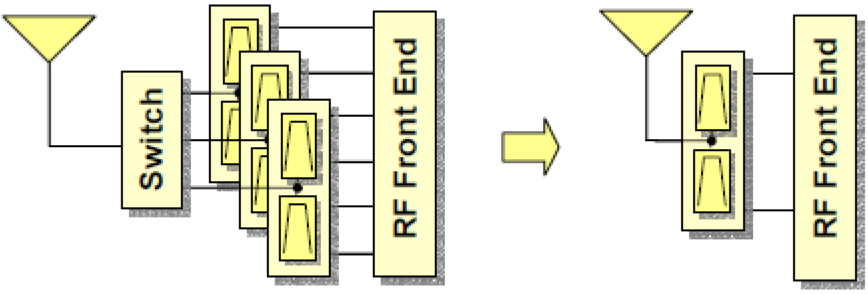

Figure 1.1: Tri-band system with three fixed duplexers and with a single tunable duplexer.

There are several devices on a receiver or a transmitter as can be seen in the example in Fig. 1.2 where a satellite front-end receiver is shown.

This reception chain is composed of an antenna followed by an image frequency filter and a low noise amplifier (LNA). The signal is later filtered again and amplified at RF frequencies. The received signal is then down converted using a mixer connected to a local oscillator (VCO or other) and filtered again by an IF filter. The last steps of the chain are an IF amplification and an analog/digital conversion. Most of these elements can be made tunable to operate in different frequency bands

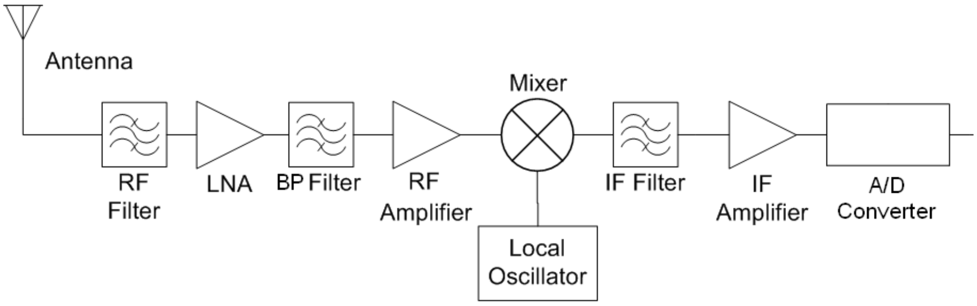

Figure 1.2: Satellite front-end receiver block diagram.

or standards.

Some examples of tunable elements are explained below.

1.2.2 Tunable antennas

Wireless systems use antennas to radiate power from the transmitter circuitry into the air or to receive signals from the air and direct them into the receiver. Antennas have impedances that affect how efficiently they can transfer or receive that power. The antenna's impedance is altered by the external environment surrounding it and therefore its power transfer efficiency is affected as the user moves. The effect can be quite drastic, changing the antenna's impedance several-fold. When tunability is employed in the antenna's matching circuitry, power transfer and resulting battery life or signal quality can be significantly increased.

Multi-mode communication applications have become popular and more demanding. The RF front end needs either a multiband or a wideband antenna to cover multi-standard operations. Apart from these, frequency agile systems must be able to receive signals over a large frequency range, and therefore, require again either wide-band or tunable antennas. A single reconfigurable antenna has the possibility of switching to all the required frequencies, thus eliminating the need for complicated wideband and multiband antenna solutions.

One class of tunable antennas takes advantage of PIN diodes to create multiple current paths and therefore resonant frequencies depending on the on or off diode state [22]. In order to configure multiple paths, tunable antennas using PIN diodes are typically layout-complicated and unable to present continuous frequency tunability.

RF MEMS [23] find many applications in tunable antennas as they demonstrate great tunning potential in terms of the low power consumption, better linearity and a large capacitance ratio. In spite of these superior features, the fabrication technology is relatively costly and the MEMS devices are therefore not as accessible as commercial tunning elements. Alternatively, loading varactor diodes to resonant antennas to demonstrate frequency [24] or polarization agility [25] has been widely employed.

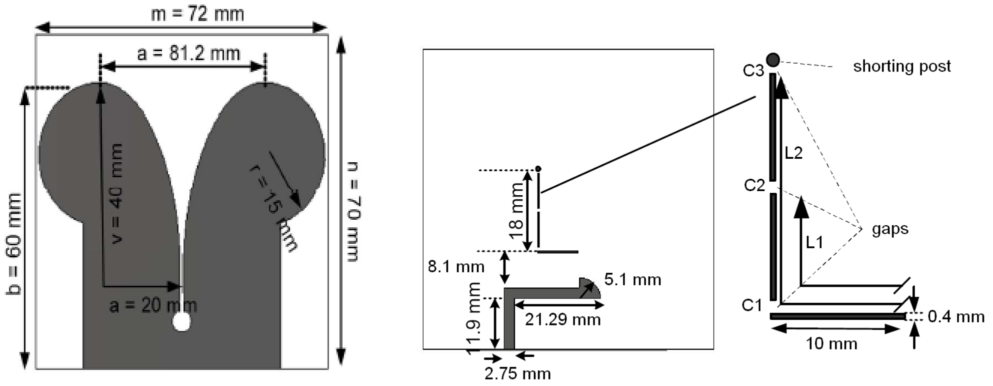

(a) Front view

(b) Rear view showing microstrip feed and resonator

Figure 1.3: Reconfigurable Vivaldi antenna [26]

In [26] a novel reconfigurable Vivaldi antenna with tunable stop bands is presented. A microstrip line resonator is coupled to the tapered slot, with three varactors used for tuning in the microstrip line. The antenna that Hamid *et al.* [26] propose has a band rejection that can be tuned at any specific frequency within the Vivaldi operating range, this is between 2 and 7 GHz. The proposed antenna used a microstrip resonator printed on the reverse side of the radiating element. The substrate used for this antenna has $\varepsilon_r = 2.2$ and height = 0.787 mm. Fig. 1.3 shows the reconfigurable Vivaldi antenna whereas the measured results where the tunability can be observed are shown in Fig. 1.4.

In [27] another frequency tunable antenna is presented base on ferrite materials. However, tunable antennas do not have to be only reconfigurable on frequency or polarizations, beam reconfigurable antennas are possible as it is shown in [28]. [29]

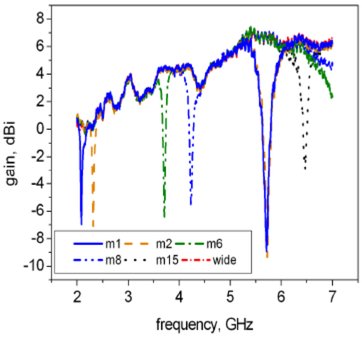

Figure 1.4: Measured results of the reconfigurable Vivaldi antenna [26].

and [30] show that this tunability could be used in antenna arrays for agile phase shifting as the schematics shown in Fig. 1.5.

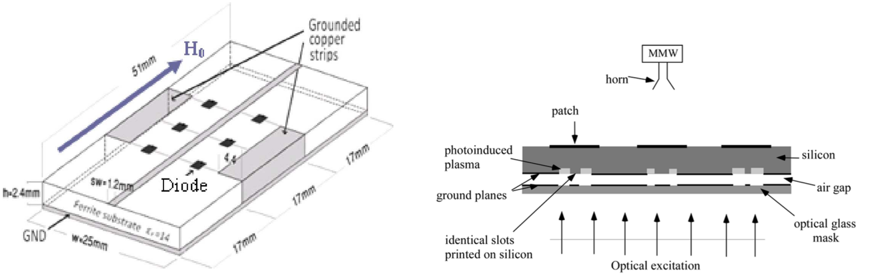

(a) Phased array antenna [29]. (b) Single layer reflectarray antenna [30].

Figure 1.5: Reconfigurable array antennas.

Finally, [31] shows a controlled wafer antenna where its surface can become reflector or absorber depending on the conditions applied to it as it can be seen in the results on Fig. 1.6.

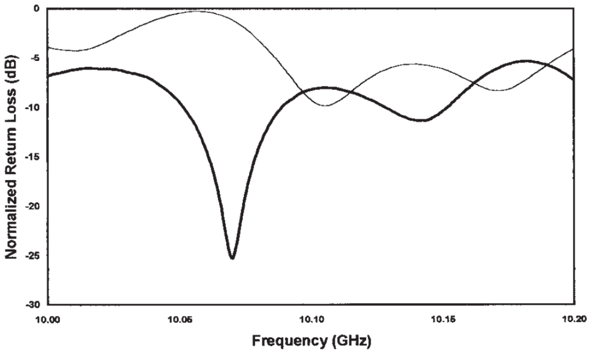

Figure 1.6: Measured results of the optically controlled absorber/reflector [31].

1.2.3 Tunable amplifiers

Frequency is not the only variable that may change as the user roams within a service area. In some wireless systems, the mobile device must adjust its output power downward as the user gets closer to the base station. This is done to assure that the base station receive the same power level from all users within its reach and the signal from the nearby user does not drown out the weaker signal from more distant users.

As an amplifier's power is adjusted away from its maximum output, there is also a resultant change in its impedance, a property that affects how efficiently power is transferred out of the amplifier. When the impedance is not properly matched, power is reflected backwards and wasted. Circuits called matching networks are designed specifically to improve the impedance related power transfer, but fixed matching networks can only provide optimum power transfer at one power level. Without concurrent adjustment of the matching circuitry, the efficiency of the amplifier decreases and battery power is wasted. A tunable matching circuit is able to adjust for the changing impedance of the amplifier and ensure maximum power transfer under all conditions, improving battery life. The use of an RF component called an isolator between the power amplifier and the antenna was common practice until recently. The isolator helped alleviate the mismatch situation between the power amplifier and the antenna, but its use has been largely discontinued due to the severe size constraints that exist for these products. The result is that the matching circuit in this part of the device has taken on even more importance [32, 33].

With the proliferation of wireless communication standards, reconfigurable microwave front-ends are becoming highly desirable. Particularly, it would be useful to have reconfigurable amplifiers that can be adjusted according to the application or to external conditions. Because the input and the output impedances of microwave transistors vary with the operating conditions, i.e., frequency, bias, bandwidth, temperature, etc., tunable matching networks are essential to having a single amplifier that can be reconfigured for these conditions. A few reconfigurable amplifiers based on RF-MEMS tunable devices have been proposed [34–36].

Certain types of wireless devices incorporate technologies like ultra-wideband (UWB) which transmits information using very low power, short impulses thinly spreading over a wide bandwidth. In order to receive signals within different frequency bands, a receiver front-end with a wideband low noise amplifier (LNA) is needed. Among the building blocks in the receiver front-ends, LNAs are added to amplify the signals from antennas without adding significant noise. A broadband LNA operated within 2-6 GHz is presented in [37] However, in order to increase the gain over the full bandwidth and to save power a tunable LNA could be designed, as the shunt-shunt feedback LNA presented in [38].

The interference and image rejection of collocated active radios in both frequency and space become a crucial issue especially for the multi-band and multi-mode applications. To address this problem, the CMOS LNA with image rejection filters [39, 40] and the differential phase rotator [41] have been proposed. However, these circuits have difficulty being applied to multi-band and multi-mode operation.

To overcome this problem, a SiGe HBT differential amplifier with frequency-tunable and multiple stopbands was presented in [42]. The circuit presented employs multiple LC-tank circuits, which are cascaded in a stacked form and connected between emitters of the differential transistor-pair to achieve multiple bandstop performance. In addition, each LC-tank circuit employs a varactor diode to achieve frequency-tunable performance. A schematic diagram of the frequency-tunable dual stopband differential amplifier is shown in Fig. 1.7(a) as well as simulated results in Fig. 1.7(b).

One of the main originalities of this work is not only that it is tunable, but also that the bandstop frequencies, (f_1 and f_2) can be tuned independently with the control V_{c1} or V_{c2} as shown in Fig. 1.8. They clearly demonstrate that the bandstop frequency can be tuned independently. f_1 varies from 0.5 to $0.8GHz$ for a fixed value of $f_2 = 1.1GHz$ while f_2 varies from 0.6 to $1.1GHz$ for a fixed value of $f_1 = 0.5GHz$.

Another way of achieving a tunable amplifier is to use transmission lines instead of the LC tanks mentioned above. There has been a demonstration of tunable millimeter-wave amplifier in 0.2 μm GaAs pseudomorphic-high-electron-mobility-

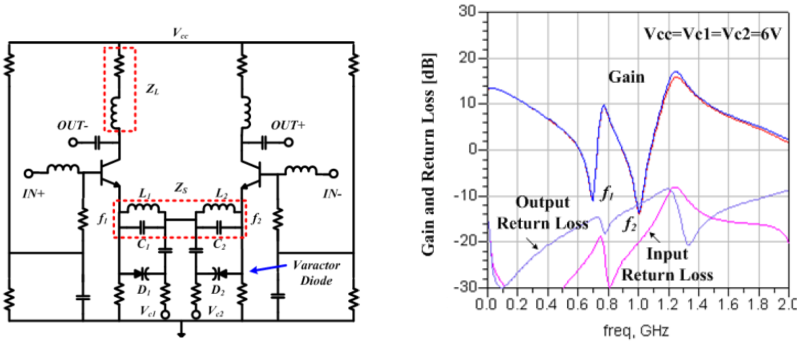

(a) Schematic (b) Simulated gain and return loss

Figure 1.7: Frequency-tunable dual-stopband differential amplifier [42].

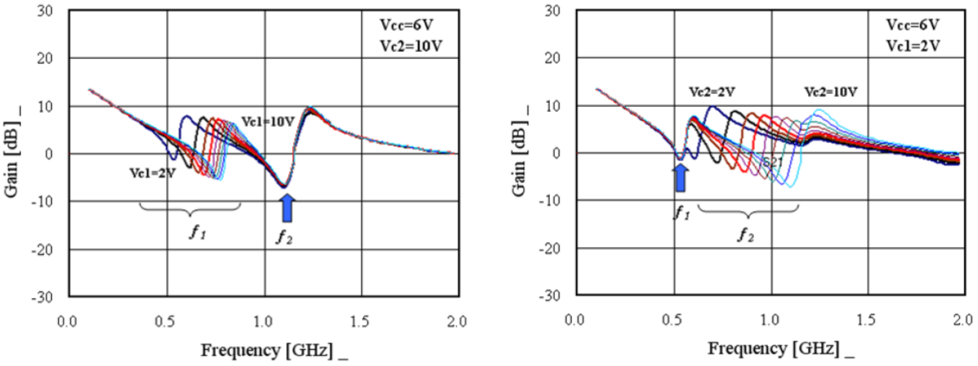

(a) Varied value of V_{c1} and fixed value of V_{c2} (b) Varied value of V_{c2} and fixed value of V_{c1}

Figure 1.8: Measured gain for the frequency-tunable dual-stopband differential amplifier [42]

transistor (pHEMT) process by manipulating the length of an open stub [43] as it can be seen on the schematic in Fig. 1.9.

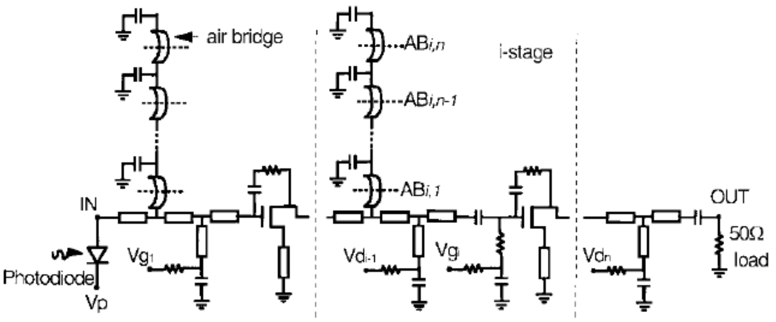

Figure 1.9: Schematic of the tunable pHEMT amplifier [43].

However, that tunable approach uses irreversible air-bridges, and does not provide balanced gain over different frequency bands. In another demonstration [44, 45], a tunable transmission line is shown to change the phase of the line by using a variable floating/ground metal between the signal line and the ground plane as in Fig. 1.10.

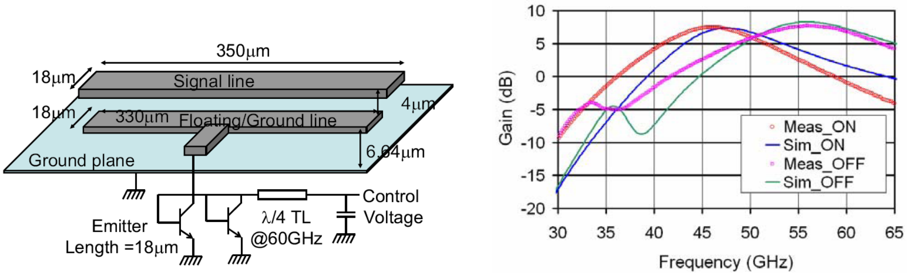

(a) Structure of the tunable line (b) Measured and simulated gain

Figure 1.10: $60GHz$ tunable amplifier [45]

1.2.4 Tunable oscillators

The multistandard mobile receiver is an integral part of a multifunctional architecture used to access present and future wireless data services such as Global System for Mobile (GSM) and Wideband Code Division Multiple Access (WCDMA). Recent trend in wireless industries indicates that the demand of multimode transceivers is evident, because of co-existence of second and third-generation cellular systems.

To add a multistandard feature to wireless receiver architecture, the voltage controlled oscillator (VCO) needs to be tunable. A significant amount of research has been carried out on the VCO; however, this component is still the most challenging component among RF designers. The main research challenges of the VCO design are low phase noise, low power consumption and on-chip implementation. Some research is being carried out now to make the frequency of use tunable.

The sudden increase of various kinds of wireless communication services results in the demand for the implementation of multi-band VCO because a tuning range of the VCO is one of the most critical elements for multi-standard frequency synthesizers. Therefore, the RF transceiver becomes more complex and consumes more power for wireless communication terminal. Many dual-band VCO-s have been developed for implementing dual-band transceivers providing various communication services to customers [46–48]. [49] is an example of a tunable VCO for multistandard mobile receiver working in three different bands (1.8 GHz, 3.6 GHz and 4.2 GHz) instead of the previous examples with just two bands.

Tunable oscillators are not only used in multiple-band systems. [50] presents a very simple tunable current-mode oscillator whereas [51] gives an example of a frequency-tunable power oscillator improved for high-efficiency. Some of the tunable oscillators nowadays have the oscillation condition and the oscillation frequency independently controllable [52].

In [53], Zamanillo *et al.* propose an optically controllable VCO whose electrical scheme is shown in Fig. 1.11.

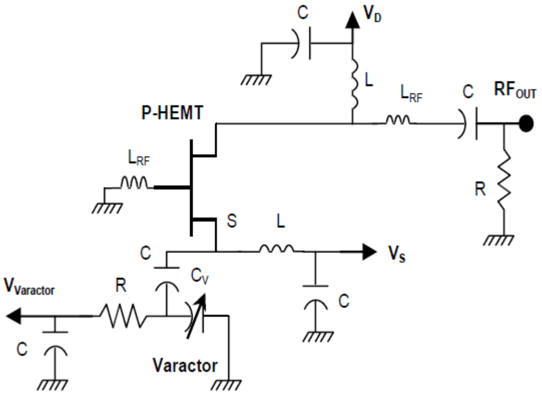

Figure 1.11: Electrical scheme of the optically tunable VCO [53].

In the presented VCO both the output power and the oscillation frequency are tunable depending on the optical power as show the graphs on Fig. 1.12

1.2.5 Tunable filters

Tunable passive filters are essential components of frequency-agile and adaptive multifunctional radio frequency circuits. The need for such circuits is being driven by the recent trend for communication systems to cover multiple frequency bands using a single set of front-end hardware. As wireless systems become more multifunctional, there will be an increased demand for reconfigurable filters that can be

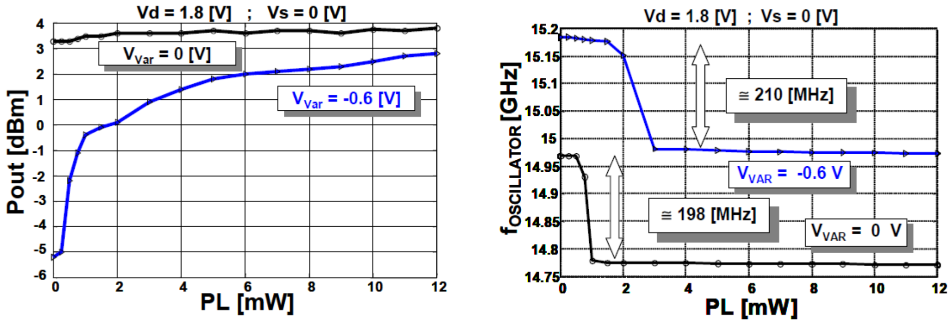

(a) VCO RF output power as a function of optical power (PL)

(b) VCO oscillation frequency tuning as a function of optical power (PL)

Figure 1.12: Measured results for the optically tunable VCO [53].

utilized for front-end pre-selection for next generation wireless systems [54].

A frequency reconfigurable filter is an alternative to a switchable filter bank [55, 56], employed in numerous communication systems for multiband operations. Indeed, by selecting different frequencies with an external electronic action, the reconfigurable filter provides a low-cost solution with a small size and low power consumption.

The current generation of wireless and satellite systems is designed with a specific function under restricted operating conditions such as a specific frequency band, channel bandwidth interference and traffic patterns. These systems lack the agility and adaptability to vary their operating conditions, which, in turn, limits their performance. While cell phones currently come with multiband capabilities, significant research effort is being directed toward implementing a similar functionality for future generations of wireless and satellite communication systems. These communication systems, however, require the use of microwave filters [57] with very high Q values requiring the development of novel tunable filter configurations. Park *et al.* have researched high Q filters, as high as $511 - 273$ over the frequency range and they show a tunable center frequency filter in the band $5.5-4.3GHz$ in [58]. A separately tunable center frequency or tunable bandwidth filter is presented in [59]. Fig. 1.13 shows the layout and the simulation results of a high Q narrow-band tunable filter with controllable bandwidth that was presented by Joshi *et al.* in [60]. They used low Q ($Q < 30$) varactors in the filter maintaining the (80%) of the quality factor of the original filter, achieving a Q higher than 400. The reverse bias is varied between $V_R = 28V$ to $V_R = 1V$ getting a bandwidth change of 34% at all the frequencies.

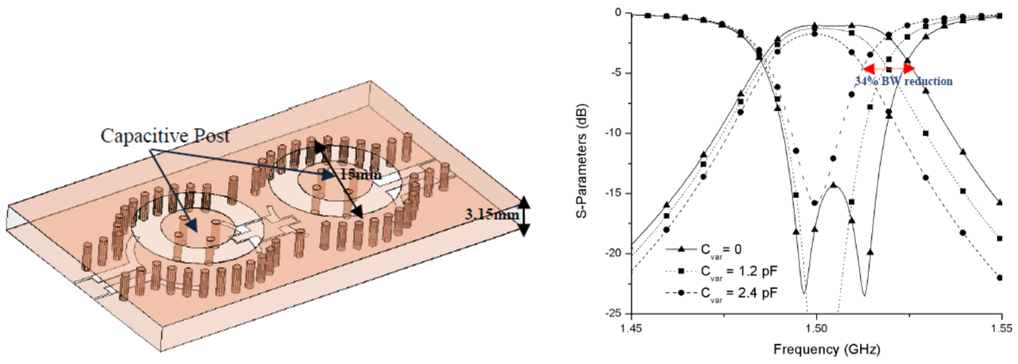

(a) Layout (b) Simulation results

Figure 1.13: High Q narrow-band filter with controllable bandwidth [60]

In [61], Fourn *et al.* present a tunable bandpass filter with control of the bandwidth and the central frequency separately using Dual Behavior Resonators (DBR). By simulations and experimental results they were capable of developing a second order millimeter bandpass filter with central frequency and relative bandwidth tunability of about 10 and 75% respectively at $30GHz$. Fig. 1.14 shows the simulated results for both the central frequency variations and the bandwidth tuning.

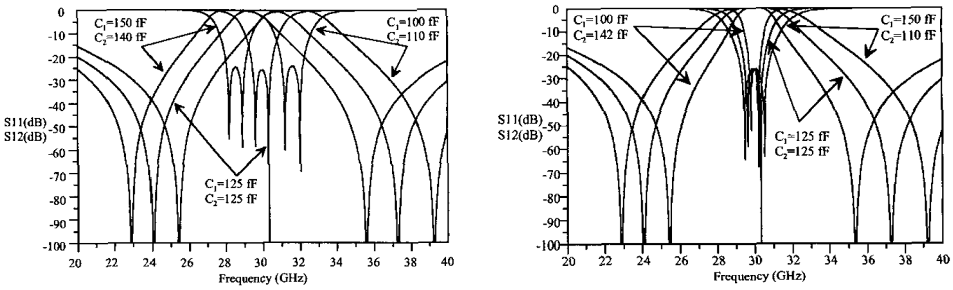

(a) Central frequency variations. (b) Bandwidth tuning

Figure 1.14: Simulated results of an ideal second-order DBR filter [61]

High Q tunable filters are often built using dielectric resonators, in order to get a low insertion loss filter. One of the major solutions is to use tunable dielectric resonators as presented in [62]. However, when tuning a dielectric resonator, there is a trade-off to be made between the tunability we want to achieve and the quality factor. In [63] this trade-off is clearly explained. It consists on a tunable dielectric resonator using MEMS (Fig. 1.15(a)) where depending on the distance between the tuning disk and the dielectric resonator itself the frequency shift increases while the quality factor decreases or viceversa as shown in Fig. 1.15(b).

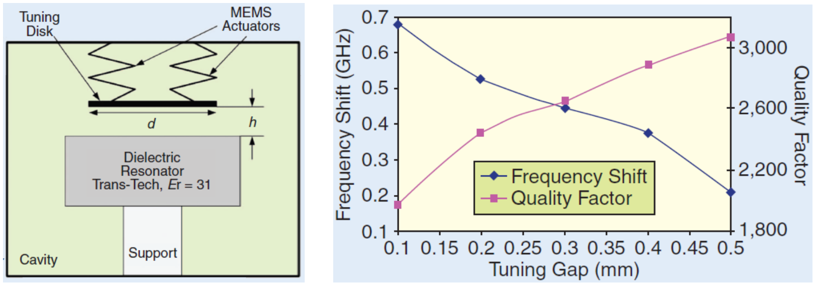

(a) Schematic of the tuning structure

(b) Frequency shift and Q as a function of the tuning gap

Figure 1.15: High Q tunable resonator with MEMS [63].

Most tunable filters used to-date are designed to be used at the front-end of a receiver and therefore must result in very low loss. However, under certain applications, when the interfering signals are strong enough, the tunable filter can be placed after a linear low-noise amplifier. In this case, it is important to build a small tunable filter. The filter must be completely reconfigurable, with control on both the center frequency and bandwidth for agile signal processing.

The ideal tunable filter must exhibit the following features: high loaded-Q value, wide tuning range, high tuning speed, good linearity, high power handling capability, small in size and mass and high reliability.

Sometimes, it is necessary to tune the circuit without disturbing the fields or degrading the quality. As an example of how to overcome this problem, [64] proposes to monitor the resonant frequency of each resonator of the filter independently by inducing higher order differential modes. [64] presents then a method for in-situ monitoring of the center frequency of a widely tunable evanescent-mode cavity filter using a differential mode generated by splitting the capacitive post in two. The frequency of the differential mode of each resonator is independently mapped to their common mode frequencies and this mapping is then used to automatically tune the filter from 1.4 to $3GHz$ without using the signal path through the filter. The measured insertion loss was $3.43dB$ and $3dB$ bandwidth as low as $10MHz$ (0.7% fractional bandwidth) at the low end and as high as $27.3MHz$ (0.9% fractional bandwidth) at the high end. Fig. 1.16 shows the result achieved for this filter.

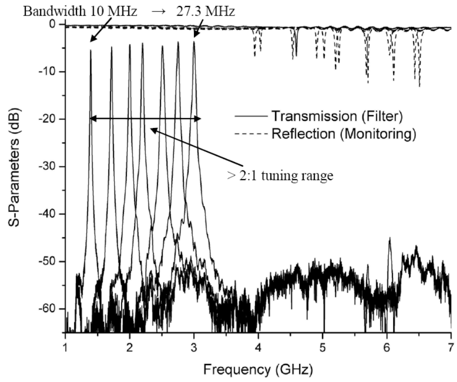

Figure 1.16: Measured filter tuning from 1.4 to $3GHz$ along with the high order differential modes used for tuning [64].

High-performance radio frequency (RF) tunable filters are needed in reconfigurable systems to facilitate efficient utilization of the available frequency spectrum. They are in demand front-end receivers for suppression of interfering signals and for relaxation of oscillator phase noise and dynamic range requirements. Although as already mentioned, tunable filters are also used to replace large filter banks in advanced systems concepts that self-adapt to environmental requirements. Tunable filters have been proposed for high power applications too. The advantages in this case are suppression of harmonics generated from the power amplifiers. In majority of these applications, the insertion loss of the tunable filter is a key design parameter. It directly impacts the noise figure for the front-end receiver applications while it directly impacts the transmitted power for high power applications.

A well-known problem for continuously tunable bandstop or bandpass filters is the variation of the bandwidth as the center frequency is tuned.Thus, one key challenge in the design of tunable filters then, is to maintain a constant relative bandwidth and a reasonable return loss performance over the tunning range. This is an important requirement for wireless and satellite applications and in the majority of other systems applications that require the use of tunable filters. In Fig. 1.17

can be observed both schematic and measured results of a tunable bandpass filters with BST (Barium Strontium Titanate) varactors biased between $0V$ and $40V$ that can be tuned from 6.2 to $7.5GHz$ of while maintaining a fractional bandwidth of approximately 13.8% as presented in [65].

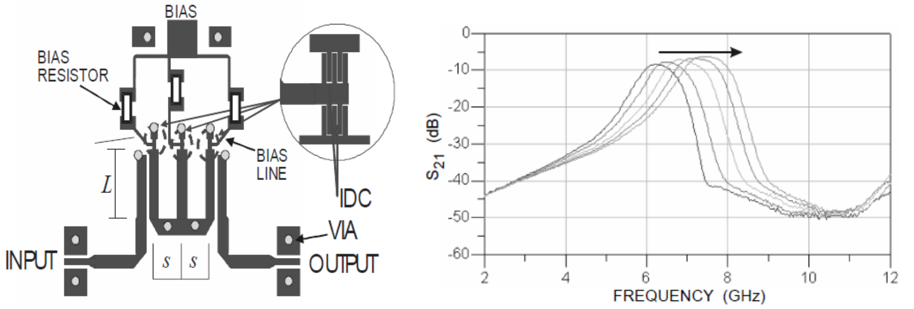

(a) Layout (IDC corresponds to the BST-based interdigitated capacitor)

(b) Measured transmission parameter (Bias from 0 to $40V$ in $10V$ steps)

Figure 1.17: Tunable bandpass filter with constant bandwidth [65]

In most filter structures, the variations of inter-resonator coupling and input/output coupling do not follow the variation in resonant frequency. This in turn causes the filter bandwidth to change and the return loss to degrade over the tuning range. The problem can be circumvented by having tuning elements that can tune the resonator center frequencies, the inter-resonator coupling and the input/output coupling. This however may increase the filter insertion loss and complicates the tunable filter design because of the large number of tuning elements needed.

Although different realizations of electronically tunable filters have been developed in past decades [66–68] most previous works have concentrated on tuning the resonator frequency either in a continuous or discrete fashion using semiconductor ferroelectric, or micro-electromechanical systems (MEMS) varactors. In [67], they present a 2-bit tunable band pass filter with quality factors below 100 and with only 4 different states for the filter while [68] presents a microstrip tunable filter with losses as high as $5dB$ requiring a biasing of $200V$. Such tunable filters exhibit high losses due to the loading effect caused by the varactor's impedance. Alternatively, the technique of integrating the active devices into the tunable filter design for loss compensation has been proposed and investigated [69].

In [69], Rauscher presents a $9.5-10.5GHz$ tunable notch filter with low insertion loss on the passband and with a rejection better that $-40dB$ on the notches. The varactors require a small bias ranging from 0.5 to $16V$. The measured passband insertion loss values, which include contributions from input and output connectors, range from $0.9dB$ at $6GHz$ to $1.6dB$ at $14GHz$. Measured results of this filter are shown in Fig. 1.18.

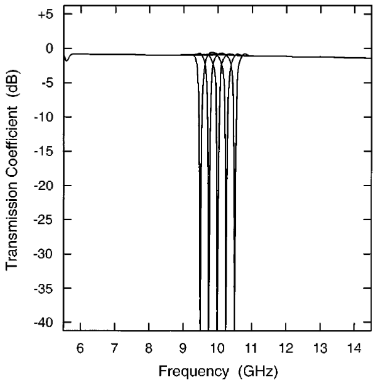

Figure 1.18: Measured response for the tunable notch filter [69].

There is an increasing interest in developing electronically tunable or reconfigurable filters for use in multi-band wireless communications and other applications [70, 71]. In [70] a novel electronically reconfigurable microwave bandpass filter based on a switched delay-line approach is presented. In contrast to conventional tunable filters, the approach enables the lossy and nonlinear switching elements to be used as part of the coupling elements rather than within the resonators. Therefore, the filter distinguishes itself through its ability to provide a wide tuning bandwidth with low passband loss and high linearity. The filter produced a maximum passband loss of 1.7 dB but the use of PIN diodes make the bias needed fairly high, $80mA$ current for the forward biasing. The work presented by [71] consists of an electronically tunable bandwidth filter based on BST capacitors. The authors present a filter that operates at the center frequency of around $1.8GHz$ and has the adjustable $3-dB$ bandwidth from $276MHz$ to $318MHz$. Hence, the tuning ratio of maximum to minimum bandwidth is 1.15 : 1 for a dc bias range from 0 to $35V$.

To this end, dual-mode microstrip resonator filters are attractive because each dual-mode resonator can be used as a doubly tuned resonant circuit and, therefore, the number of resonators required for a given degree of filter is reduced by half, resulting in a compact filter configuration [72–74]. [72–74] use this dual-mode resonance in a microstrip technology filter using a stepped-impedance ring resonator and a triangular patch resonator respectively.

As a precise example, [75] presents a new type four-pole dual-mode microstrip open-loop resonator filter with a quasi-elliptic function frequency response, which produce two finite-frequency transmission zeros on each side of the passband, leading to a symmetric and high selective filter response. The experimental four-pole tunable bandpass filter shows high selectivity on each side of the passband and more than $10dB$ return loss over a tuning range from 0.86 to 0.96GHz obtained with a variation on the bias from $10.6V$ to $34V$. Fig. 1.19 shows a photograph of the fabricated filter as well as the comparison between measured and simulated response made by Tang *et al.*

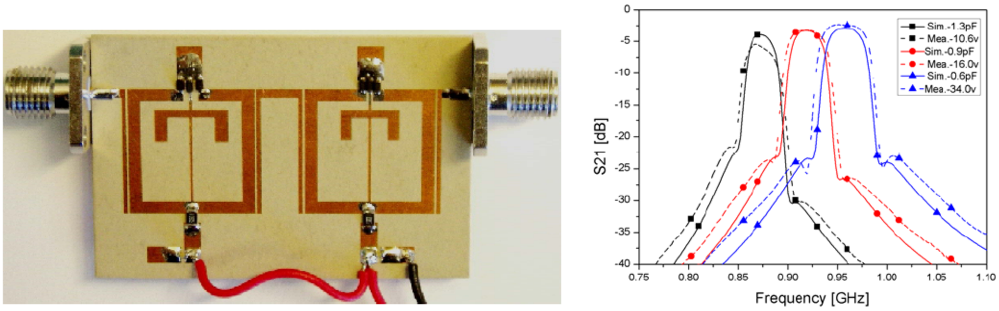

(a) Fabricated prototype

(b) Measured performance compared to simulated

Figure 1.19: Tunable microstrip quasi-elliptic function bandpass filter [75]

A new class of microwave reconfigurable filter based on switched delay lines (SDLs) approach is shown in [38]. A narrowband tunable filter with constant absolute bandwidth tuning based on the SDLs topology was shown in [76, 77].

It is known that one of the most common ways to tune a filter is the use of MEMS [78, 79] or varactor diodes [80, 81]. However, some structures such as filters based on split-ring resonator might be suitable for using with MEMS or varactors [82] but also for using a photosensitive material as Cadmium Sulfide [83]. Cadmium

Sulfide (CdS) is a highly photosensitive material that will be explained further in this report in section 2.3.1. Wu *et al.* used this material in [83] for developing a switchable microwave filter. They show that a bandpass filter working at $14GHz$ constructed by defining inter-coupled split ring resonators pattern on a microstrip line can be switch to an ordinary microstrip line with a switching ratio higher than 10 when the material is illuminated.

Other filters use ferromagnetic materials to be able to perform the tunability by applying a magnetic field as explained in [84]. Qiu *et al.* show a wideband bandpass filter with tunable center frequency of 5.90 to $17.80GHz$ and corresponding bandwidth of 1.27 to $2.08GHz$ is possible just applying two different nonuniform bias magnetic fields, centered at 2750 and $4150Oe$.

A complete overview of tunability methods will be given in section 1.3.

1.3 Tunability Methods

While there have been efforts to minimize the number of additional components used for dual-band/multiband applications to reduce the complexity, footprint and cost, researchers in industry and academia are also considering tunable RF/microwave components, which can address these challenges by designing electronically tunable subsystems. The components can therefore function optimally as conditions change. Depending on the specific circuit where such tunable components are used, the result may be a savings in cost, reduction in size, improvement in battery life, better performance, and/or increased functionality. These components can be designed using various technologies such as micro-electromechanical systems (MEMS), ferroelectric materials, solid-state varactor diodes, and ferrites or some others.

Some of these techniques will be explained in this section.

1.3.1 Varactor diodes

Among all the tunability techniques, electrical tuning of a capacitor is the simplest and most common choice for making tunable circuits. When the value of a capacitor in a circuit is changed, the impedance and phase relationships in the circuit are affected in predictable ways. Therefore, these parameters changes can be exploited to design RF/microwave components with greater functionality, higher performance, and reduced size and cost.

For mobile devices, small, low-cost and energy saving units are needed. This makes the concept of loading resonant planar structures by variable capacitances attractive, therefore varactor diodes are possible candidates for this kind of structures. The resonance of those structures must be solely defined by their electrical length to provide a significant tuning range. Unfortunately the quality factor Q of microstrip structures is limited to values largely below 200 at $8GHz$ and lower with an increase of the frequency [85] and a misuse of a varactor diode may increase the losses.

Varactor diodes have been used in tunable circuits as they are well-known devices that have been studied by many researchers over the years. Varactor or varicap diodes are semiconductor devices that are widely used in the electronics industry and in many applications where a voltage controlled variable capacitance is required. A voltage controlled capacitance is useful for tuning applications. A varactor diode is then a type of diode which has a variable capacitance that is a function of the voltage impressed on its terminals.

A varactor diode is a P-N junction diode in reverse bias and has a structure such that the capacitance and the series resistance of the diode varies with the reverse bias applied. Varactors are operated reverse-biased so no current flows, but since the thickness of the depletion zone varies with the applied bias voltage, the capacitance of the diode can be made to vary. The capacitance is controlled by the method of doping in the depletion layer. Typical values are from tens to hundreds of picofarads. The property of capacitance change is utilized to achieve a change in the frequency and/or the phase of an electrical circuit. A simple model of a packaged varactor diode is shown in Fig. 1.20:

In Fig. 1.20, $C_J(V)$ is the variable junction capacitance of the diode die and $R_S(V)$ is the variable series resistance of the diode die. C_P is the fixed parasitic capacitance arising from the installation of the die in a package. Contributors to the parasitic capacitance are the package material, geometry and the bonding wires

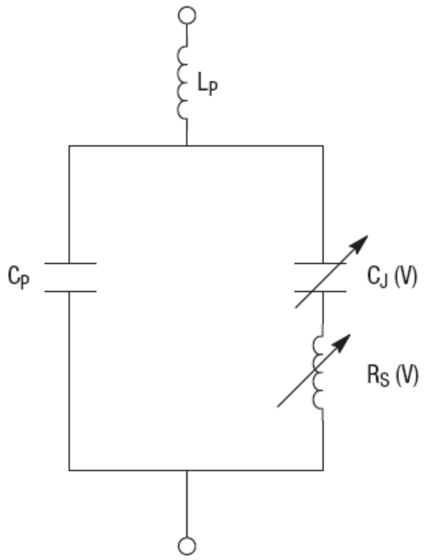

Figure 1.20: Model of a packaged varactor.

or ribbons. These factors also contribute to the parasitic inductance L_P. The contribution to the series resistance from the packaging is very small and may be ignored. Similarly, the inductance associated with the die itself is very small and may be ignored.

The key electrical parameters for a varactor diode are:

- Reverse breakdown voltage and reverse leakage current.
- Capacitance value and the capacitance-voltage change behavior.
- Quality factor (Q).

The reverse breakdown voltage and the reverse leakage current are typically measures of the intrinsic quality of the semiconductor diode. Their effect on the frequency or phase tuning behavior is only indirect and of secondary importance.

For the second main electrical parameter, the absolute capacitance of the varactor diode contributes to the total capacitance of the LC circuit in which it operates, and thus determines the frequency of operation. Additionally, the change of capacitance of a varactor diode with the change of applied reverse bias voltage is what governs the change of the frequency or the phase of the signal. Therefore, both parameters—the absolute capacitance value as well as the capacitance variation property—are extremely important for a user to understand. The capacitance and the capacitance change characteristic are both functions of the doping structure introduced within the semiconductor during the wafer fabrication process.

Finally, the quality factor is an important parameter for a varactor diode since it determines the frequency limit applicability for the diode.

Tunable bandstop filters with tunable center frequency, with a variation on the center frequency between $1.04GHz$ and $3.13GHz$ in the example in [86], bandstop filters with tunable center frequency and bandwidth individually as in [87] where either the center frequency can be tuned between 1.2 and $1.6GHz$ or the bandwidth is tuned from 70 to $140MHz$ at a fixed center frequency have been developed. The fabricated device from [86] is shown in Fig. 1.21.

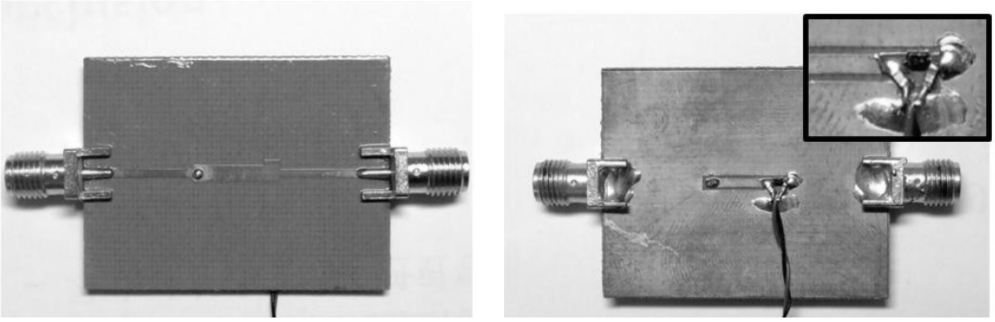
(a) Front view (b) Bottom view

Figure 1.21: Fabricated tunable bandstop filter based on varactor diodes [86]

Also, tunable bandpass filters [88] based on varactor diodes as well as other types of tunable circuits are available on the literature. In [88] a design with large tuning range from 800 to $1300MHz$ in combination with a small, tunable, relative $3-dB$-bandwidth from 5% to 15% and moderate insertion loss lower than $5dB$ is presented.

One inconvenience of the varactor diode is its high non-linearity, but for filtering applications at which we are interested, the main inconvenience is that none of the literature shows filters working above $4GHz$.

Most solid state varactor diodes are made with P-N junction diodes, but the depletion layer can also be made using a MOS-diode where the quality factor could extend to 100 in the best case [89] or a Schottky diode [90] with more moderate quality factors below 40.

1.3.2 Ferroelectric materials

Ferroelectric materials such as the Barium–Strontium–Titanate (BST) have recently become more attractive to the development of electronically tunable microwave circuits like tunable resonators, filters and phase shifters for frequency agile applications. In part, this is thanks to the development of low-cost fabrication processes for making ferroelectric thin films. Moreover, the power capability and fast tuning speed of this type of device are very appealing which somehow compensates for their high dielectric loss and low tunability. Nevertheless, these drawbacks are expected to be further improved by the optimization of the thin film fabrications and circuit designs.

Ferroelectric varactors are capable of out-performing solid-state varactors at microwave frequencies due to their very high dielectric constant, about 350 or even much higher depending on the material [91], comparing to SiO_2 and lower parasitic series resistance that leads to a higher Q-factor,, typically as high as a few tens but that can reach values up to 160 according to [92] . Unlike conventional varactors based on p-n junctions, Schottky diodes and MOS varactors, the characteristics of ferroelectric capacitors do not depend on substrate semiconductor characteristics such as doping density. In addition to silicon, once ferroelectric capacitors are optimized they can be integrated on a variety of substrates such as GaN, GaAs or silicon carbide. Ferroelectric capacitors made from $Ba_{1-x}Sr_xTiO_3$ (BST) are applied as varactors in tunable high-frequency circuit applications. An image of a fabricated device of these type is shown in Fig. 1.22.

Barium strontium titanate (BST), is being investigated with considerable interest as a dielectric material for tunable microwave device applications and has a relatively low loss tangent, lower than 0.05. By using these advantageous properties of BST, a number of advanced tunable capacitors have been successfully demonstrated and integrated into RF components such as tunable filters [71], tunable matching networks [94], voltage-controlled oscillators [95] and phase shifters [96].

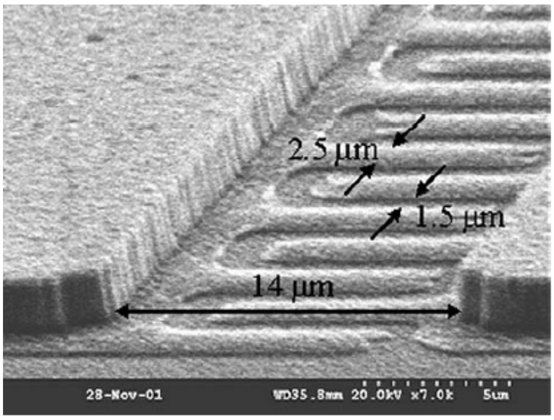

Figure 1.22: SEM photograph of a fabricated ferroelectric capacitor [93].

Varactors created from BST have no junction noise and have no preferred polarity compared to semiconductor varactor diodes. It is important to note that ferroelectric varactors are capable of much higher Q-factors, higher than 45 at $1GHz$ [97] than solid-state varactors that they are as low as 15 at $500MHz$ [98]. This is because the parasitic series resistance dominates the Q-factor at high frequency, and solid-state varactors, which have semiconductor material in the conduction path, have a higher series resistance than ferroelectric varactors with metallic (low resistance) electrodes [89]. Ferroelectric varactors offer high power-handling capability, fast tuning speeds, high tunability up to 50%, and low control voltages as low as $10V$ depending on the application.

Although ferroelectric materials can provide great changes depending on the electric field applied, they have some drawbacks for use as tunable dielectric materials too. The effect that ferroelectric materials utilize is heavily temperature dependent. Ferroelectric materials need to be crystalline in structure which makes them more expensive and difficult to use. There are also some limitation on the field strength of the microwave signals and where and how they can be used because of their electrical tunability.

1.3.3 Ferromagnetic materials

These materials are needed to accomplish functions such as phase tuning, attenuation, isolation, circulation and wideband antenna operation. The recent development of metamaterials, especially negative refractive index metamaterials (NIM) introduced new opportunities for multifunctional devices. Most NIM demonstrated are based on either periodic metallic resonators [99] or photonic crystals [100]. Dielectric resonators have also been studied to show the potential to provide both negative permeability and permittivity [101–103]. However, all these material types are limited by inherent narrow bandwidths and lack the ability to frequency tune essential properties. In order to obtain broadband negative refractive index, the periodicity and size of the elements like split ring resonators (SRR) must be altered. Ferroelectric materials have also been loaded into split rings to effectively enable frequency tunability by varying the bias voltage. However, the tunable bandwidth is still below 0.2 GHz mainly limited by the nature of split rings [104]. Another alternative approach is using magnetic materials instead of metallic resonators to generate negative permeability, which offer wideband and real-time frequency tunability by varying the magnetic bias field [105].

Even with the advances in passive integration technologies, inductors for VHF (30 MHz - 300 MHz) and UHF (300 MHz - 3 GHz) filters remain large components, inhibiting further miniaturization in various applications. The use of magnetic material is seen as an option to substantially decrease their size. Compared to alternative miniaturization approaches, like line-width reduction and efficient use of mutual inductance in multi-layer and multi-winding inductors, the use of ferrites is a unique option in ceramic based LTCC technology for example. While for the kHz and lower MHz frequency range high permeability ferrites are available [106], new cubic and hexagonal ferrites can reach gyromagnetic resonance frequencies well above 1 GHz and can be integrated into LTCC technology [107]. Fig. 1.23 shows the structure of a ferrite embedded on LTCC.

There is a strong need to address the long standing issues in ferrite phase shifter technology to allow the intrinsic advantages of this technology, such as low insertion loss and high power handling to be used to achieve new capabilities in modern military and commercial applications.

Phase shifters using ferrites have been proposed in [108] using to different types of ferrites, garnets and hexagonal ferrites.

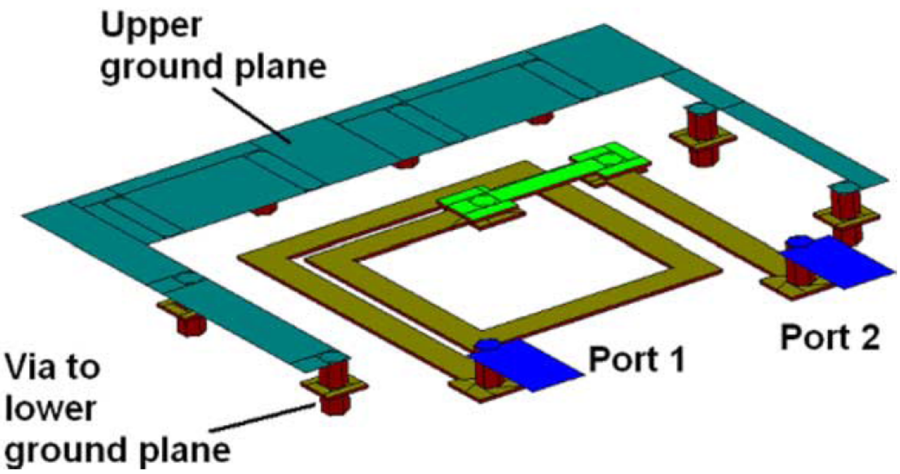

Figure 1.23: Structure of a ferrite embedded one layer coil with two windings [107].

Garnet ferrites, e.g. yttrium garnet (YIG), are widely utilized in high frequency devices because of their low dielectric and magnetic losses and moderate saturation magnetization values. Varying the externally applied magnetic field results in variation in the magnetic permeability and the phase velocity and insertion phase.

Unlike cubic garnet ferrites, hexagonal ferrites possess high magnetocrystalline anisotropy energy due to the hexagonal crystal structure. A number of different hexagonal ferrites have found applications in electronics, magnetic recording, permanent magnets, as well as high frequency devices. This material has previously been utilized to reduce bias field requirements in phase shifter [109] and circulator [110] devices operating in the millimeter-wave regime. Fig. 1.24 shows the measured results for the YIG phase shifter developed in [108].

An alternative approach to generating the necessary magnetic fields with drastically reduced power requirements involves utilizing the magnetoelectric (ME) effect to bias ferrite devices. The ME effect is defined by electric polarization induced by an applied magnetic field or, conversely, magnetic polarization induced by an applied electric field.

Magnetoelectric materials have great capability of energy conversion between magnetic field and electric field and can be used in many different domains, such as

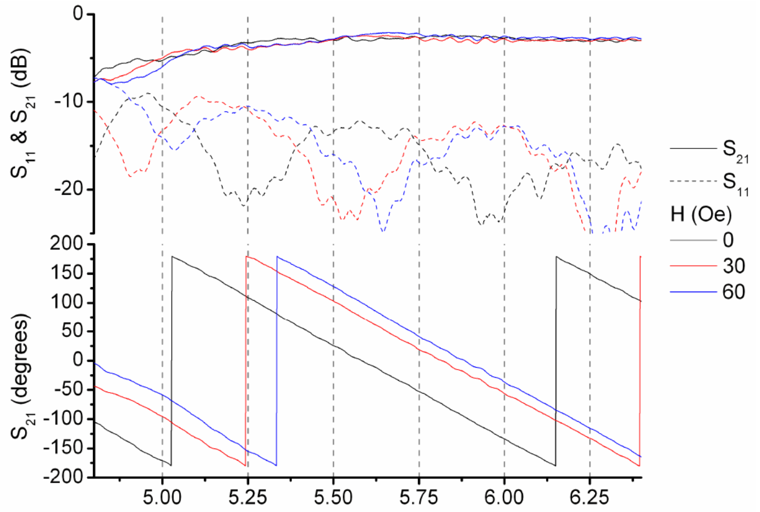

Figure 1.24: Measured results of the YIG phase shifter device for several values of applied magnetic field [108].

civil wireless communication systems, military phased array radar and microwave devices like filters, resonators, isolators, etc. Microwave devices based on laminated magnetoelectric materials have less consumption, wide-range frequency tuning by magnetic field higher than 75% and accurate electric tunability as low as 0.5% for an applied electric field of $E = 10kV/cm$ [111]. Thus, this dual tunability due to piezoelectric effect and ferromagnetic resonance (FMR) will have widely application prospects.

A specific type of magnetoelectric materials are the ferrite-ferroelectric (FF) heterostructures due to their response to elastic and electromagnetic force fields [112]. Such composites have permittivity, permeability and magnetoelectric susceptibility characteristics suitable for reciprocal and non-reciprocal signal processing devices. Ferrites are used in traditional microwave/millimeter-wave devices in which tunability is realized, through a variation of the bias magnetic field [113]. This ”magnetic” tuning could be achieved in a very wide frequency range, but is relatively slow and is associated with large power consumption. The circuit tunability is possible through magnetoelectric interaction in this type of materials as in the filters in [114, 115].

Fig. 1.25(a) shows a filter using laminated magnetoelectric layers (YIG/GGG/PZT - Yttrium Iron Garnet/Gadolinium Gallium Garnet/Zirconate

Titanate). Fig. 1.25(b) shows the predicted results of the filter. The observed frequency shift is quite low, nearly 60MHz for each 10Oe magnetic field increasing varying the frequency from 6.65 to about 6.8GHz without a huge change in the insertion loss.

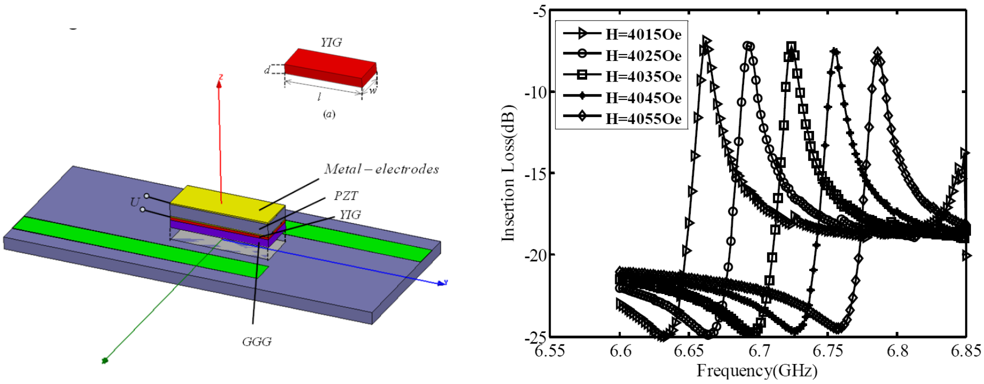

(a) Geometric structure

(b) Frequency shift predicted by applying a magnetic field

Figure 1.25: Magnetoelectric tunable filter [115]

These technologies, ferromagnetic and magnetoelectric, represent a new paradigm in high frequency ferrite device design with the specific goal of reducing size, weight, cost, and power consumption while maintaining the high power handling and low insertion loss properties intrinsic to ferrite-based devices. Such capabilities are particularly important in demanding present day applications, such as sensory systems of autonomous aerial, ground and underwater vehicles and are inadequately addressed by existing technologies.

1.3.4 Micro Electro Mechanical systems (MEMS)

MEMS encompasses several distinct types of devices including RF switches and relays, resonators, varactors and inductors. Interest in MEMS has grown dramatically in the last decade because of a wide range of applications. These include all type of wireless communications, radar, satellites, military radio, instrumentation and test equipment. Compared to conventional RF components, MEMS offer significant benefits, including lower power consumption, lower insertion loss, lower cost and smaller form factor. As a result, MEMS technology has become one of the most rapidly changing fields today.

MEMS technology is a combination of micromachining and IC technology. This technology allows the fabrication of mechanical structures with very small dimensions. MEMS devices employed in RF applications are termed as RF MEMS. MEMS technology is on the verge of revolutionizing RF applications. As semiconductor technology continues to progress towards smaller, lighter and super-integrated components and devices, the RF industry is reaping the benefits of micro-electro mechanical systems. MEMS RF technologies offer the advantages of low power consumption (near zero), low insertion loss (0.1 dB up to 40 GHz) and high isolation (>40 dB), as well as low volume and low mass [116]. Very high quality factor passive devices ($Q > 40$ for an inductor [117]), transmission line structures, and switches can be implemented using MEMS technology.

In addition to the potential offered by RF MEMS devices for integration and miniaturization, they also provide reconfigurability and tunability for multi-band and multi-standard operation.

As has been explained already, the MEMS technology has the potential of replacing many RF components such as switches, inductors, capacitors, phase shifter, surface acoustic wave (SAW) devices and ceramic filters used in today's mobile, communication and satellite systems. In many cases, such RF MEMS components would not only reduce substantially the size, weight, power consumption and component counts, but also promise superior performance in comparison with current technologies. In wireless and space applications complete RF systems, such as redundancy switch matrices, input multiplexers, and integrated front-end receivers, can be built with mass producibility and high reliability. Micromachining also enables new functionality and system capability that are not possible with current technologies.

Of the RF MEMS devices the most common ones are the **MEMS variable capacitors**, **MEMS tunable inductors** and **RF MEMS switches**.

1.3.4.1 MEMS variable capacitors

Varactor tuning techniques are widely employed in phase shifters, oscillators and tunable filters. MEMS technology has the potential of realizing variable capacitors with a performance that is superior to varactor diodes in areas such as non-linearity and losses. A MEMS parallel plate variable capacitor with an electrostatic actuator is considered the most convenient configuration due to simplicity of fabrication.

In Fig. 1.26 The structure of a curl-up-plate MEMS is shown as well as the measured tuning behavior of the varactor from work presented in [118].

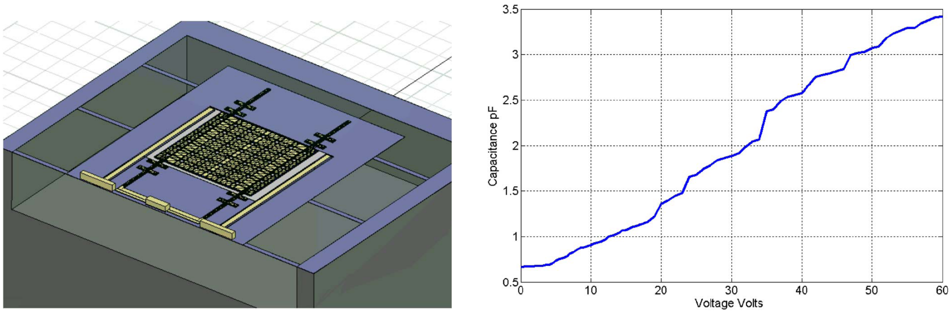

(a) Three-dimensional structure developed on HFSS

(b) Measured tuning behavior at 1 GHz over a DC bias voltage

Figure 1.26: Linear bilayer MEMS varactor [118]

In [119], Stefanini *et al.* show the design of a microwave tunable cavity. The results show a 10% frequency shift with only one MEMS capacitor keeping the unloaded quality factor higher than 500. Fig. 1.27 shows both an image of the structure as well as the simulated and measured results.

1.3.4.2 MEMS tunable inductors

High-Q inductors find widespread use in RF transceivers circuits. Examples include filters, matching networks of LNAs and tank circuits of VCOs. The availability of tunable inductors will make it possible to easily tune such circuits to circumvent the manufacturing tolerance limitations. MEMS tunable inductors can be also used to construct filters with tunable bandwidth and a tunable center frequency for frequency agile applications. The need for optimum tuning or impedance becomes

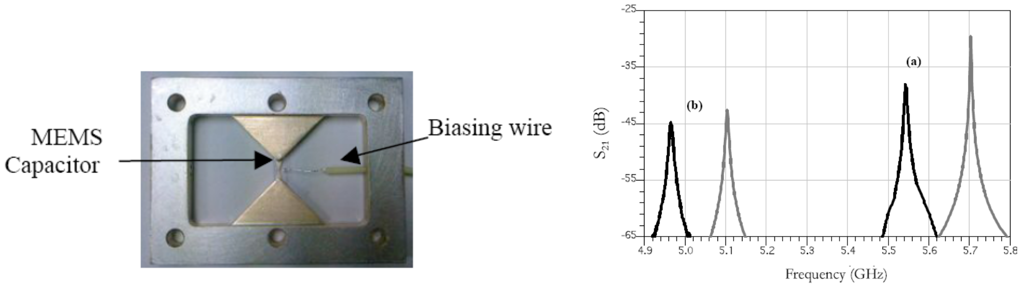

(a) Photograph of the structure.

(b) Measured (dark) and simulated (grey) results for the upstate (a) and the downstate (b)

Figure 1.27: Microwave tunable cavity [119]

more critical when optimum tuning or impedance matching in a broad frequency range is desired.

In Fig. 1.28 a SEM view of one of the tunable inductors developed by Rais-Zadeh *et al.* on [117] where the primary inductor and the secondary inductors can be connected or disconnected to achieve a tunability of 47% at 6GHz ranging from $1.1nH$ to $0.54nH$.

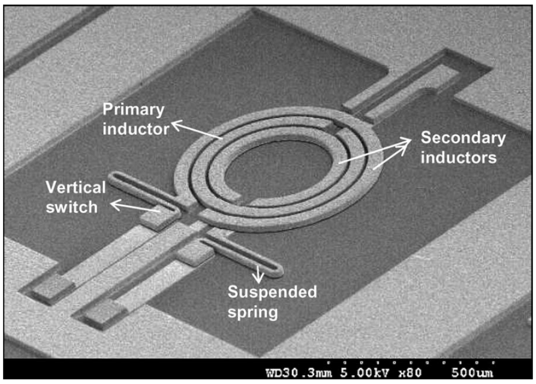

Figure 1.28: SEM view of a silver switched tunable inductor [117].

1.3.4.3 RF MEMS switch

The common microwave switches commonly employed in the microwave industry are mechanical-type switches (coaxial and waveguide) and semiconductor-type switches (PIN diode and FET). Mechanical coaxial and waveguide switches offer the benefits of low insertion loss, large off-state isolation, and high power handling capabilities. However, they are bulky, heavy and slow. On the other hand, semiconductor switches such as PIN diodes and FET provide much faster switching speed and are smaller in size and weight, but are inferior in insertion loss, dc power consumption, isolation and power handling capabilities than their mechanical counterparts. RF MEMS switches promise to combine the advantageous properties of both mechanical and semiconductor switches. They offer the high RF performance and low DC power consumption of mechanical switches but with the small size, weight and low cost features of semiconductor switches.

An RF MEMS switch is one of the basic building blocks in an RF communication system. Switches operating at frequencies of up to 40 GHz, with very low insertion loss and high isolation, have been successfully demonstrated [120], In addition, they consume very little energy, and exhibit very linear characteristics with extremely low signal distortion, making them ideally suited for modern radar and communication applications. Using RF MEMS switches, various RF circuits such as variable capacitors tunable filters, on-chip inductors, and phase shifters have been demonstrated with superior performance over conventional semiconductor devices.

In Fig. 1.29 a photograph of the RF MEMS switch demonstrated on [121] as well as its measured S-parameters.

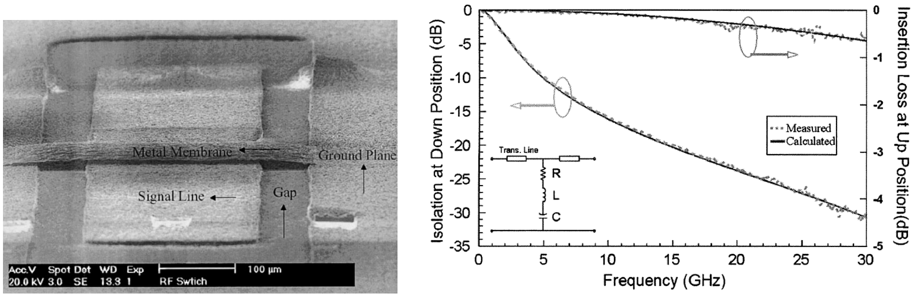

(a) Scanning electronic microscopy

(b) Measured S-parameters

Figure 1.29: RF MEMS switch [121]

Also, recent work in RF MEMS switches show a great switching time, lower than $50ns$ as it has been demonstrated in [122] by Verger *et al.*.

1.4 Optical tunability

All the methods explained in the previous section require a biasing or some sort of circuit that could degrade the response in the main behavior of the circuit. The use of optoelectronic techniques to control microwave circuits and systems continues to be an area of intense research and development. Besides the inherent speed advantages of this approach, the use of a laser to control multiple microwave circuits permits both a high degree of electrical isolation between the control signal and the microwave circuit and timing precision that can easily be in the picosecond regime. This is in addition to the inherent noise immunity of optical fibers.

The use of pin and varactor diodes has many disadvantages such as high loss, high power consumption, unacceptable SNR and distortion of the incident signals. RF MEMS provide a better solution in building tunable passives, which are necessary for multiband systems. MEMS are small, with low insertion loss, high Q and low power consumption, they introduce less signal distortion, but the tuning speeds are around the microsecond although some work at lower tuning times, about $50ns$ has been demonstrated lately [122]. Ferroelectric materials have fast tuning speeds and they are easily tuned by voltage only. The main disadvantage and the problem of ferroelectrics is high level dielectric losses.

As explained, the advantages of the **optically controlled** microwave devices include high isolation between the controlling optical beam and the microwave signal, no need for biasing lines, short response time, high power handling capacity, immunity to electromagnetic interference and low cost.

Optical tunability can be divided in two: **Indirect optical control** and **direct optical control**. The indirect control involves the use of photodiode or any other type of photosensitive device to convert the control optical signal into bias voltage which controls the working point of a microwave circuit nonlinear element, for instance a varactor or a switch device. An example extracted from [123] is shown in Fig. 1.30.

In the case of direct control, the optical signal is directly sent to the active regions of a microwave device thus changing its characteristics.

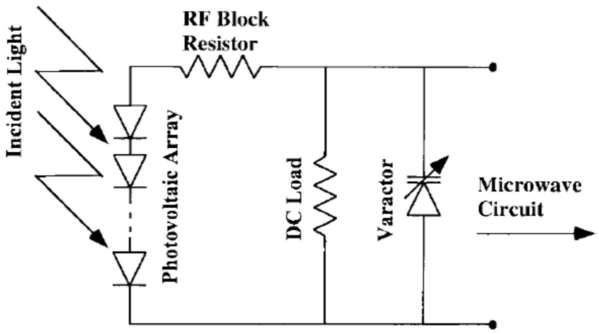

Figure 1.30: Schematic of an optically controlled circuit using indirect control [123].

When it comes to direct optical control there are two main effects that can be observed on a photosensitive materials, **photoconductivity** and **photorefractivity**.

Photoconductivity is the increase in the electrical conductivity of certain materials when they are exposed to light of sufficient energy. When light is absorbed by a material such as a semiconductor, the number of free electrons and electron holes changes and raises its electrical conductivity. To cause excitation, the light that strikes the semiconductor must have enough energy to raise electrons across the band gap, or to excite the impurities within the band gap. Certain semiconductors such as silicon, germanium or cadmium sulfide are strongly photoconductive or also the polymer polyvinylcarbazole in a lower level. Some examples of circuits exploiting the photoconductive effect using photoinduced plasma in silicon [124] or a silicon microring resonator [125] can be found in the literature. Fig. 1.31 shows the principle of the RF phase shifter as well as the measured results. In this example extracted from [125] the microring is tuned exploiting the thermal effect. Depending on the temperature, the delay on the microring will be different and the line will be shifted. Although they presented a thermal effect, this change could be optical too as silicon is photosensitive.

The photorefractive effect is a nonlinear optical effect seen in certain crystals and other materials that respond to light by altering their refractive index. The photorefractive effect is observed in materials which are both electrooptic and photoconducting. When a light pattern is incident on such a material, charges that

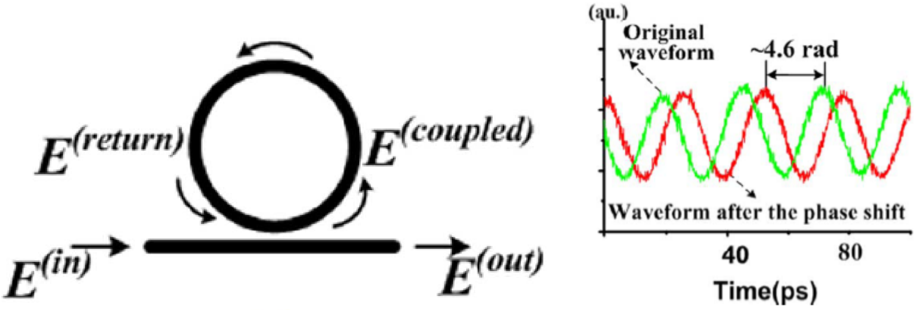

(a) Principle (b) Measured phase shift

Figure 1.31: Microring phase shifter [125]

are photogenerated in the illuminated regions, migrate and eventually get trapped at the dark regions of the sample. The resulting charge redistribution creates an internal electric field, the space charge field, which changes the refractive index via the electrooptic effect.

Over the last few years, optically reconfigurable circuits have been studied by many researchers. For instance, in [126] they present a basic idea of a tunable amplifier with a tuning range of $2.5 - 3.5GHz$ as well as reconfigurable antenna using silicon based technology.

Panagamuwa *et al.* have presented in [28] a more in depth study of a frequency and beam reconfigurable antenna using photoconducting switches. Fig. 1.32 shows the measured return loss of their antenna. From both switches on to both switches off, the resonant frequency shifts from $2.26GHz$ to $3.15GHz$. This is a shift of 39.4%. The $-10dB$ bandwidth is 9.5% for the on and 13.4% for the off states. In this work, no adverse effects due to fiber optic cables or the silicon wafers were observed.

Other passive optically controllable structures have been studied, such as the microstrip resonator presented in [127] where they achieved a tunability higher than 35% using open loop ring step impedance resonator although according to the authors further investigations need to be undertaken in this structure.

In [128], Draskovic *et al.* present a frequency switchable dual-band branch-line coupler. Fig. 1.33 shows the measured results for both states on and off, where the

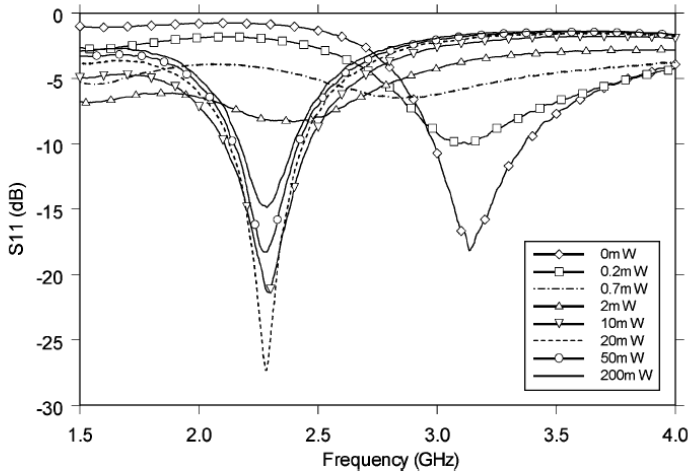

Figure 1.32: Measured change in return loss with increasing optical illumination for the frequency reconfigurable antenna [28].

optical power varies between $200mW$ and $0mW$. The frequency shifts of $230MHz$ and $160MHz$ are demonstrated in lower ($900MHz$) and upper ($1800MHz$) frequency bands respectively. The percentage frequency shift is 35% and 10% in lower and upper bands respectively.

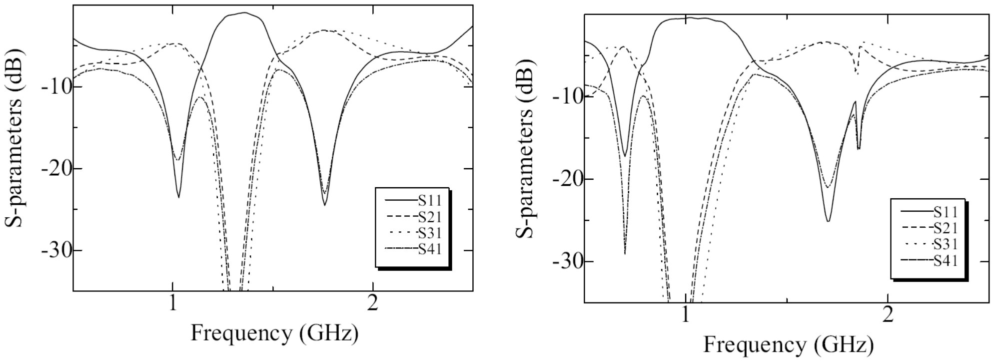

(a) Off state ($0mW$).

(b) On state ($200mW$).

Figure 1.33: Measured results of the frequency switchable coupler [128]

The indirect optical control as well as the photoconductive and photorefractive effects of the direct optical control will be explained in more detail in following chapters of this manuscript.

1.5 Conclusion

In this first chapter an introduction to high frequency systems has been given. Then a general overview of tunability circuits has been given followed by a review of the tunability methods.

The tunability methods require an external biasing that can potentially degrade the primary response of the designed circuit. Optical tunability shows great capabilities to avoid this problem as the optical waves do not interfere with the electromagnetic waves of the circuits themselves.

The main idea of this thesis is then to propose alternative solutions based on optical control to the common tunability methods such as ferroelectric materials, MEMS or variable capacitors as varactors. In this work we will focus on passive structures but the other circuits explained in this chapter could take advantage of the optical tunability applied to the circuits shown in this manuscript.

Optical tunability is a good candidate as an alternative solution to classical tunability in both the forms presented, indirect optical control and direct optical control.

Bibliography

[1] P. A. Carré, “Bréve histoire des télécommunications : du réseau simple au réseaux pluriels,” Oct. 1993. iii, 1, 3

[2] T. S. Saad and J. C. Wiltse, “50 years of the IEEE microwave theory and techniques society,” *IEEE Transactions on Microwave Theory and Techniques*, vol. 50, pp. 612–624, Mar. 2002. iii, 1, 3

[3] C. Saboureau, *Analyses électromagnétiques et méthodologies de conception associées, dédiées à l'optimisation de composants et modules millimétriques.* PhD thesis, University of Limoges, Sept. 2004. iii, 1, 7

[4] P. Chevalier, *Les hyperfréquences : Propriétés et Applications.* PhD thesis, University of Limoges, Sept. 2004. iii, 1, 7

[5] H. Inoue and T. Yuge, “Automatic car identification: Tests in the japanese national railways,” *32nd IEEE Vehicular Technology Conference*, pp. 463–468, 1982. 7

[6] K. Kwon, J. Choi, J. Choi, Y. Hwang, K. Lee, and J. Ko, “A 5.8 GHz integrated CMOS dedicated short range communication transceiver for the Korea/Japan electronic toll collection system,” *IEEE Transactions on Microwave Theory and Techniques*, vol. 58, pp. 2751–2763, Nov. 2010. 7

[7] K. Schmidt von Behren, D. Pienkowski, T. Mueller, M. Tempel, and G. Boeck, “77 GHz harmonic mixer with flip-chip Si-Schottky diode,” *14th International Conference on Microwaves, Radar and Wireless Communications MIKON*, vol. 3, pp. 743–746, 2002. 7

[8] W. Gerum, P. Malzahn, and K. Schneider, “94-GHz TWT for military radar applications,” *IEEE Transactions on Electron Devices*, vol. 48, pp. 72–73, Jan. 2001. 7

[9] G. Gibbons, “What race? what competition?,” *Inside GNSS*, Apr. 2009. 7

[10] D. Elad, A. P. S. Khanna, I. Armenta, J. Quibuyen, and R. Pumares, “Low cost ka band transceiver for digital radios,” *29th European Microwave Conference*, pp. 287–290, Oct. 1999. 8

[11] M. Milosavljevic, P. Kourtessis, and J. M. Senior, “Transparent wireless transmission over the ACCORDANCE optical/wireless segment,” *7th International Symposium on Communication Systems Networks and Digital Signal Processing (CSNDSP)*, pp. 138–142, July 2010. 8

[12] K. Nidaira, T. Shirouzu, M. Baba, and K. Inoue, “Wireless IP access system for broadband access services,” *IEEE International Conference on Communications*, pp. 3434–3438 Vol.6, 2004. 8

[13] H. Darabi, S. Khorram, E. Chien, M. Pan, S. Wu, S. Moloudi, J. C. Leete, J. J. Rael, M. Syed, R. Lee, P. Kilcoyne, B. Ibrahim, M. Rofougaran, and A. Rofougaran, “A fully integrated transceiver for bluetooth,” *23rd Annual Technical Digest Gallium Arsenide Integrated Circuit (GaAs IC) Symposium*, pp. 11–14, 2001. 8

[14] G. L. Matthaei, “Magnetically tunable Band-Stop filters,” *IEEE Transactions on Microwave Theory and Techniques*, vol. 13, pp. 203–212, Mar. 1965. 9

[15] I. C. Hunter, L. Billonet, B. Jarry, and P. Guillon, “Microwave filters-applications and technology,” *IEEE Transactions on Microwave Theory and Techniques*, vol. 50, pp. 794–805, Mar. 2002. 9

[16] J. D. Adam, L. E. Davis, G. F. Dionne, E. F. Schloemann, and S. N. Stitzer, “Ferrite devices and materials,” *IEEE Transactions on Microwave Theory and Techniques*, vol. 50, pp. 721–737, Mar. 2002. 9

[17] R. M. Fano and A. W. Lawson, *Microwave Transmission Circuits*, vol. 9 of *M.I.T. Rad. Lab.* New York: McGraw-Hill, 1948. 9

[18] S. T. Winnall and D. B. Hunter, “A fibre bragg grating based scanning receiver for electronic warfare applications,” *International Topical Meeting on Microwave Photonics*, pp. 211–214, 2002. 9

[19] J. Tsui, *Microwave receivers with electronic warfare applications.* Raleigh N.C.: Scitech Pub., 2005. 9

[20] W. H. W. Tuttlebee, “Software-defined radio: facets of a developing technology,” *IEEE Personal Communications*, vol. 6, pp. 38–44, Apr. 1999. 9

[21] J. Mitola and G. Q. Maguire, “Cognitive radio: making software radios more personal,” *IEEE Personal Communications*, vol. 6, pp. 13–18, Aug. 1999. 10

[22] A. F. Sheta and S. F. Mahmoud, “A widely tunable compact patch antenna,” *IEEE Antennas and Wireless Propagation Letters*, vol. 7, pp. 40–42, 2008. 12

[23] N. Kingsley, D. E. Anagnostou, M. Tentzeris, and J. Papapolymerou, “RF MEMS sequentially reconfigurable sierpinski antenna on a flexible organic substrate with novel DC-Biasing technique,” *Journal of Microelectromechanical Systems*, vol. 16, pp. 1185–1192, Oct. 2007. 13

[24] P. L. Chi, R. Waterhouse, and T. Itoh, “Compact and tunable Slot-Loop antenna,” *IEEE Transactions on Antennas and Propagation*, vol. 59, pp. 1394–1397, Apr. 2011. 13

[25] C. R. White and G. M. Rebeiz, “Single- and Dual-Polarized tunable Slot-Ring antennas,” *IEEE Transactions on Antennas and Propagation*, vol. 57, pp. 19–26, Jan. 2009. 13

[26] M. R. Hamid, P. Gardner, P. S. Hall, and F. Ghanem, “Reconfigurable vivaldi antenna,” *Microwave and Optical Technology Letters*, vol. 52, pp. 785–787, Apr. 2010. vii, 13, 14

[27] A. Shamim, J. R. Bray, N. Hojjat, and L. Roy, “Ferrite LTCC-Based antennas for tunable SoP applications,” *IEEE Transactions on Components, Packaging and Manufacturing Technology*, vol. 1, pp. 999–1006, July 2011. 13

[28] C. J. Panagamuwa, A. Chauraya, and J. C. Vardaxoglou, “Frequency and beam reconfigurable antenna using photoconducting switches,” *IEEE Transactions on Antennas and Propagation*, vol. 54, pp. 449–454, Feb. 2006. vii, 13, 43, 44

[29] S. I. M. Sheikh, A. A. P. Gibson, M. Basorrah, G. Alhulwah, K. Alanizi, M. Alfarsi, and J. Zafar, “Analog/Digital ferrite phase shifter for phased array antennas,” *IEEE Antennas and Wireless Propagation Letters*, vol. 9, pp. 319–321, 2010. 13, 14

[30] M. R. Chaharmir, J. Shaker, M. Cuhaci, and A. Sebak, “Novel Photonically-Controlled reflectarray antenna,” *IEEE Transactions on Antennas and Propagation*, vol. 54, pp. 1134–1141, Apr. 2006. 14

[31] V. Fusco and B. Nair, “Wafer-scale silicon optically controlled absorber/reflector surface,” *Microwave and Optical Technology Letters*, vol. 44, pp. 318–320, Feb. 2005. vii, 14, 97

[32] P. A. Dal Fabbro and M. Kayal, “RF power amplifier employing a frequency-tunable impedance matching network based on coupled inductors,” *Electronics Letters*, vol. 44, p. 1131, 2008. 15

[33] M. Liu, S. Wang, and F. Chen, “Design of RF amplifier with tunable active inductor,” *IEEE 8th International Conference on ASIC*, pp. 262–265, Oct. 2009. 15

[34] F. Domingue, A. B. Kouki, and R. R. Mansour, “Tunable microwave amplifier using a compact MEMS impedance matching network,” *European Microwave Integrated Circuits Conference, EuMIC.*, pp. 351–354, Sept. 2009. 15

[35] Q. Dongjiang, R. Molfino, S. M. Lardizabal, B. Pillans, P. M. Asbeck, and G. Jerinic, “An intelligently controlled RF power amplifier with a reconfigurable MEMS-varactor tuner,” *IEEE Transactions on Microwave Theory and Techniques*, vol. 53, pp. 1089–1095, Mar. 2005. 15

[36] A. Fukuda, H. Okazaki, and S. Narahashi, “A novel compact reconfigurable quad-band power amplifier employing RF-MEMS switches,” *36th European Microwave Conference*, pp. 344–347, Sept. 2006. 15

[37] L. Yang, S. Y. Kiat, A. Cabuk, M. Jianguo, A. D. Manh, and L. Zhenghao, “A novel CMOS low-noise amplifier design for 3.1- to 10.6-GHz ultra-wide-band

wireless receivers," *IEEE Transactions on Circuits and Systems I: Regular Papers*, vol. 53, pp. 1683–1692, Aug. 2006. 16

[38] R. M. Weng, W. Peng, and C. Y. Liu, "A 0.7 V tunable gain low noise amplifier for lower band DS-UWB applications," *IEEE International Conference on Ultra-Wideband, ICUWB*, pp. 530–533, Sept. 2009. 16, 26

[39] A. Raghavan, E. Gebara, M. Tentzeris, and J. Laskar, "An active interference canceller for multistandard collocated radio," *IEEE MTT-S International Microwave Symposium Digest*, pp. 723–726, June 2005. 16

[40] W. L. Chen, S. F. Chang, G. W. Huang, Y. S. Jean, and T. H. Yeh, "A Ku-Band Interference-Rejection CMOS Low-Noise amplifier using Current-Reused stacked Common-Gate topology," *IEEE Microwave and Wireless Components Letters*, vol. 17, pp. 718–720, Oct. 2007. 16

[41] T. K. Nguyen, N. J. Oh, C. Y. Cha, Y. H. Oh, G. J. Ihm, and S. G. Lee, "Image-rejection CMOS low-noise amplifier design optimization techniques," *IEEE Transactions on Microwave Theory and Techniques*, vol. 53, pp. 538–547, Feb. 2005. 16

[42] M. Shirata, T. Shinohara, M. Sato, and Y. Itoh, "An L-band SiGe HBT differential amplifier with frequency-tunable and multiple stopbands," *European Conference on Wireless Technology, EuWiT*, pp. 151–154, Oct. 2008. vii, 16, 17

[43] A. Miras and E. Legros, "High-gain frequency-tunable low-noise amplifiers for 38-42.5-GHz band applications," *IEEE Microwave and Guided Wave Letters*, vol. 7, pp. 305–307, Sept. 1997. vii, 17

[44] Y. H. Chun and J. S. Hong, "A novel tunable transmission line and its application to a phase shifter," *IEEE Microwave and Wireless Components Letters*, vol. 15, pp. 784–786, Nov. 2005. 18

[45] D. Dawn, S. Sarkar, P. Sen, S. Pinel, and J. Laskar, “60 GHz Silicon-Based tunable amplifier,” *38th European Microwave Conference, EuMC*, pp. 452–455, Oct. 2008. vii, 18

[46] J. Choi and C. Seo, “Broadband and low phase noise VCO using tunable metamaterial transmission line based on Varactor-Loaded Split-Ring resonator,” *Korea-Japan Microwave Conference, KJMW*, pp. 145–148, Nov. 2007. 19

[47] J. Y. Lee, S. H. Lee, H. C. Bae, and S. H. Kim, “A concurrent Dual-Band VCO with dual resonance in single resonator,” *Topical Meeting on Silicon Monolithic Integrated Circuits in RF Systems*, pp. 135–138, Jan. 2007. 19

[48] C. Jaewon and S. Chulhun, “Dual-band VCO using composite right/left-handed transmission line and tunable negative resistance based on pin diode,” *IEEE MTT-S International Microwave Symposium Digest*, pp. 241–244, June 2008. 19

[49] V. Vibhute, D. Fitrio, J. Singh, A. Zayegh, and A. Stojcevski, “A tunable VCO for multistandard mobile receiver,” *Second IEEE International Workshop on Electronic Design, Test and Applications, DELTA*, pp. 378–378, 2004. 19

[50] R. Sotner, J. Slezak, and T. Dostal, “Tunable oscillator using two CCTA-s and only grounded passive elements,” *9th International Conference on Environment and Electrical Engineering (EEEIC)*, pp. 447–450, 2010. 19

[51] S. W. Shin, G. W. Choi, H. J. Kim, S. H. Lee, S. H. Kim, and J. J. Choi, “Frequency-tunable high-efficiency power oscillator using GaN HEMT,” *IEEE MTT-S International Microwave Symposium Digest*, pp. 1000–1003, May 2010. 19

[52] B. Knobnob and M. Kumngern, “Electronically tunable quadrature oscillator with voltage and current outputs,” *International Conference on Electrical Engineering/Electronics Computer Telecommunications and Information Technology (ECTI-CON)*, pp. 28–31, May 2010. 19

[53] J. M. Zamanillo, J. Portilla, C. Navarro, and C. Perez-Vega, “Optical ports: next generation of MMIC control devices?,” *European Microwave Conference, EuMC*, pp. 1394–1398, 2005. vii, 19, 20

[54] R. Berezdivin, R. Breinig, and R. Topp, “Next-generation wireless communications concepts and technologies,” *IEEE Communications Magazine*, vol. 40, pp. 108–116, Mar. 2002. 20

[55] J. Liu, J. Liu, S. Li, S. He, Y. Liang, and H. Li, “Switchable low loss SAW filter bank with SAW notch filters,” *IEEE Ultrasonics Symposium, IUS*, pp. 1600–1602, Nov. 2008. 20

[56] S. Doberstein, “Switchable low-loss SAW filter banks with MEMS switches,” *IEEE Ultrasonics Symposium, IUS*, pp. 1294–1297, Oct. 2010. 20

[57] R. Cameron, R. Mansour, and C. M. Kudsia, *Microwave Filters for Communication Systems – Fundamentals, Design and Applications.* Hoboken N.J. Chichester: Wiley, 2007. 20

[58] S. J. Park, I. Reines, and G. Rebeiz, “High-Q RF-MEMS tunable evanescent-mode cavity filter,” *IEEE MTT-S International Microwave Symposium Digest*, pp. 1145–1148, June 2009. 20

[59] L. Kok-Yan and G. M. Rebeiz, “A miniature 8-16 GHz packaged tunable frequency and bandwidth RF MEMS filter,” *IEEE International Symposium on Radio-Frequency Integration Technology, RFIT*, pp. 249–252, Dec. 2009. 20

[60] H. Joshi, H. H. Sigmarsson, M. Sungwook, D. Peroulis, and W. J. Chappell, “High q narrow-band tunable filters with controllable bandwidth,” *IEEE MTT-S International Microwave Symposium Digest*, pp. 629–632, June 2009. vii, 20, 21

[61] E. Fourn, C. Quendo, E. Rius, A. Pothier, P. Blondy, C. Champeaux, J. C. Orlianges, A. Catherinot, G. Tanne, C. Person, and F. Huret, “Bandwidth

and central frequency control on tunable bandpass filter by using MEMS cantilevers," *IEEE MTT-S International Microwave Symposium Digest*, vol. 1, pp. 523–526, 2003. vii, 21

[62] R. Mansour, "High-Q tunable dielectric resonator filters," *IEEE Microwave Magazine*, vol. 10, pp. 84–98, Oct. 2009. 21

[63] W. D. Yan and R. R. Mansour, "Tunable dielectric resonator bandpass filter with embedded MEMS tuning elements," *IEEE Transactions on Microwave Theory and Techniques*, vol. 55, pp. 154–160, Jan. 2007. vii, 22

[64] H. H. Sigmarsson, A. Christianson, H. Joshi, S. M., D. Peroulis, and W. J. Chappell, "In-situ control of tunable evanescent-mode cavity filters using differential mode monitoring," *IEEE MTT-S International Microwave Symposium Digest*, pp. 633–636, June 2009. vii, 22, 23

[65] Z. F., W. M. Fathelbab, P. G. Lam, V. Haridasan, J. P. Maria, A. I. Kingon, and M. B. Steer, "A 6.2-7.5 GHz tunable bandpass filter with integrated barium strontium titanate (BST) interdigitated varactors utilizing silver/copper metallization," *IEEE Radio and Wireless Symposium, RWS*, pp. 638–641, Jan. 2009. vii, 24

[66] P. Wong and I. Hunter, "Electronically tunable filters," *IEEE Microwave Magazine*, vol. 10, pp. 46–54, Oct. 2009. 24

[67] A. Pothier, J. C. Orlianges, Z. Guizhen, C. Champeaux, A. Catherinot, D. Cros, P. Blondy, and J. Papapolymerou, "Low-loss 2-bit tunable bandpass filters using MEMS DC contact switches," *IEEE Transactions on Microwave Theory and Techniques*, vol. 53, pp. 354–360, Jan. 2005. 24

[68] J. Nath, D. Ghosh, J. P. Maria, A. I. Kingon, W. Fathelbab, P. D. Franzon, and M. B. Steer, "An electronically tunable microstrip bandpass filter using thin-film Barium-Strontium-Titanate (BST) varactors," *IEEE Transactions on Microwave Theory and Techniques*, vol. 53, pp. 2707–2712, Sept. 2005. 24

[69] C. Rauscher, “Varactor-tuned active notch filter with low passband noise and signal distortion,” *IEEE Transactions on Microwave Theory and Techniques*, vol. 49, pp. 1431–1437, Aug. 2001. vii, 24, 25

[70] W. W. Peng and I. C. Hunter, “A new class of Low-Loss High-Linearity electronically reconfigurable microwave filter,” *IEEE Transactions on Microwave Theory and Techniques*, vol. 56, pp. 1945–1953, Aug. 2008. 25

[71] C. Young-Hoon, H. Jia-Sheng, B. Peng, T. J. Jackson, and M. J. Lancaster, “BST-Varactor tunable Dual-Mode filter using variable Z_C transmission line,” *IEEE Microwave and Wireless Components Letters*, vol. 18, pp. 167–169, Mar. 2008. 25, 31

[72] M. Matsuo, H. Yabuki, and M. Makimoto, “Dual-mode stepped-impedance ring resonator for bandpass filter applications,” *IEEE Transactions on Microwave Theory and Techniques*, vol. 49, pp. 1235–1240, July 2001. 26

[73] J. S. Hong and S. Li, “Theory and experiment of Dual-Mode microstrip triangular patch resonators and filters,” *IEEE Transactions on Microwave Theory and Techniques*, vol. 52, pp. 1237–1243, Apr. 2004. 26

[74] J. S. Hong, H. Shaman, and Y. H. Chun, “Dual-Mode microstrip Open-Loop resonators and filters,” *IEEE Transactions on Microwave Theory and Techniques*, vol. 55, pp. 1764–1770, Aug. 2007. 26

[75] T. Wenxing and H. Jia-Sheng, “Tunable microstrip quasi-elliptic function bandpass filters,” *European Microwave Conference, EuMC*, pp. 767–770, Oct. 2009. vii, 26

[76] P. W. Wong and I. C. Hunter, “Parallel-coupled switched delay line (SDL) reconfigurable microwave filter,” *IEEE MTT-S International Microwave Symposium Digest*, pp. 513–516, June 2009. 26

[77] W. W. Peng and I. C. Hunter, “Electronically reconfigurable microwave bandpass filter,” *IEEE Transactions on Microwave Theory and Techniques*, vol. 57, pp. 3070–3079, Dec. 2009. 26

[78] S. Courreges, L. Yuan, Z. Zhiyong, C. Kwang, A. Hunt, and J. Papapolymerou, “A low loss X-Band Quasi-Elliptic ferroelectric tunable filter,” *IEEE Microwave and Wireless Components Letters*, vol. 19, pp. 203–205, Apr. 2009. 26

[79] D. Scarbrough, C. Goldsmith, J. Papapolymerou, and Y. L., “Miniature microwave RF MEMS tunable waveguide filter,” *European Microwave Conference, EuMC*, pp. 1860–1863, Oct. 2009. 26

[80] M. A. El-Tanani and G. M. Rebeiz, “A Two-Pole Two-Zero tunable filter with improved linearity,” *IEEE Transactions on Microwave Theory and Techniques*, vol. 57, pp. 830–839, Apr. 2009. 26

[81] C. Musoll-Anguiano, I. Llamas-Garro, Z. Brito-Brito, L. Pradell, and A. Corona-Chavez, “Fully adaptable band-stop filter using varactor diodes,” *Microwave and Optical Technology Letters*, vol. 52, pp. 554–558, Mar. 2010. 26

[82] A. Vèlez, F. Aznar, M. Durán-Sindreu, J. Bonache, and F. Martín, “Tunable coplanar waveguide band-stop and band-pass filters based on open split ring resonators and open complementary split ring resonators,” *IET Microwaves, Antennas & Propagation*, vol. 5, p. 277, 2011. 26

[83] J. Wu and I. Shih, “A novel switchable microwave filter constructed with Inter-Coupled Split-Ring resonators and photosensitive cadmium sulfide,” *International Symposium on Signals, Systems and Electronics, ISSSE*, pp. 435–438, July 2007. 26, 27

[84] Q. Gang, C. S. Tsai, B. S. T. Wang, and Z. Yun, “A YIG/GGG/GaAs-Based magnetically tunable wideband microwave Band-Pass filter using cascaded Band-Stop filters,” *IEEE Transactions on Magnetics*, vol. 44, pp. 3123–3126, Nov. 2008. 27

[85] A. Gopinath, “Maximum Q-Factor of microstrip resonators,” *IEEE Transactions on Microwave Theory and Techniques*, vol. 29, pp. 128–131, Feb. 1981. 28

[86] L. Sang-Yun, L. Won-Gyu, J. Won-Seok, and W. Y. Jong, “A tunable bandstop filter design using parallel coupled line resonator with varactor,” *Asia-Pacific Microwave Conference, APMC*, pp. 1–4, Dec. 2008. vii, 30

[87] A. C. Guyette, “Varactor-tuned bandstop filters with tunable center frequency and bandwidth,” *IEEE International Conference on Wireless Information Technology and Systems (ICWITS)*, pp. 1–4, Aug. 2010. 30

[88] C. Reck, R. Trommer, and L. P. Schmidt, “Bandpass filter with tunable bandwidth and center frequency based on varactor diodes,” *German Microwave Conference (GeMIC)*, pp. 1–4, Mar. 2011. 30

[89] P. Andreani and S. Mattisson, “On the use of MOS varactors in RF VCOs,” *IEEE Journal of Solid-State Circuits*, vol. 35, pp. 905–910, June 2000. 31, 32

[90] J. Grajal, V. Krozer, E. Gonzalez, F. Maldonado, and J. Gismero, “Modeling and design aspects of millimeter-wave and submillimeter-wave schottky diode varactor frequency multipliers,” *IEEE Transactions on Microwave Theory and Techniques*, vol. 48, pp. 700–711, Apr. 2000. 31

[91] B. Ouagague, H. B. El-Shaarawy, S. Pacchini, S. Payan, A. Rousseau, M. Maglione, and R. Plana, “BST tunability study at DC and microwave frequencies by using IDC and MIM capacitors,” *Asia-Pacific Microwave Conference Proceedings (APMC)*, pp. 1837–1840, Dec. 2010. 31

[92] T. S. Kalkur, A. Jamil, and N. Cramer, “Characteristics of voltage controlled oscillators implemented with tunable ferroelectric high-k capacitors,” *15th IEEE International Symposium on the Applications of Ferroelectrics, ISAF*, pp. 364–367, July 2006. 31

[93] Y. Yong-Kyu, K. Dongsu, M. G. Allen, J. S. Kenney, and A. T. Hunt, “A reduced intermodulation distortion tunable ferroelectric capacitor-architecture

and demonstration," *IEEE Transactions on Microwave Theory and Techniques*, vol. 51, pp. 2568–2576, Dec. 2003. vii, 32

[94] A. Tombak, "A Ferroelectric-Capacitor-Based tunable matching network for Quad-Band cellular power amplifiers," *IEEE Transactions on Microwave Theory and Techniques*, vol. 55, pp. 370–375, Feb. 2007. 31

[95] A. Jamil, T. Kalkur, and N. Cramer, "Tunable ferroelectric Capacitor-Based Voltage-Controlled oscillator," *IEEE Transactions on Ultrasonics, Ferroelectrics and Frequency Control*, vol. 54, pp. 222–226, Feb. 2007. 31

[96] E. G. Erker, A. S. Nagra, Y. L., P. Periaswamy, T. R. Taylor, J. Speck, and R. A. York, "Monolithic Ka-band phase shifter using voltage tunable $BaSrTiO_3$ parallel plate capacitors," *IEEE Microwave and Guided Wave Letters*, vol. 10, pp. 10–12, Jan. 2000. 31

[97] A. Mahmud, T. Kalkur, A. Jamil, and N. Cramer, "A 1-GHz active phase shifter with a ferroelectric varactor," *IEEE Microwave and Wireless Components Letters*, vol. 16, pp. 261–263, May 2006. 32

[98] H. S. Kim, Y. S. Sohn, and S. Y. Choi, "Fabrication and characteristics of varactor diode for UHF TV tuner operated within ultra-low tuning voltage," *Electronics Letters*, vol. 43, p. 423, 2007. 32

[99] M. C. Gwinner, E. Koroknay, L. Fu, P. Patoka, W. Kandulski, M. Giersig, and H. Giessen, "Periodic large-area metallic split-ring resonator metamaterial fabrication based on shadow nanosphere lithography," *European Conference on Lasers and Electro-Optics and the European Quantum Electronics Conference. CLEO Europe - EQEC*, pp. 1–1, June 2009. 33

[100] I. K. Hwang, G. H. Kim, and Y. H. Lee, "Optimization of coupling between photonic crystal resonator and curved microfiber," *IEEE Journal of Quantum Electronics*, vol. 42, pp. 131–136, Feb. 2006. 33

[101] J. Wang, Z. Xu, Z. Yu, X. Wei, Y. Yang, J. Wang, and S. Qu, "Experimental realization of all-dielectric composite cubes/rods left-handed metamaterial," *Journal of Applied Physics*, vol. 109, p. 084918, 2011. 33

[102] T. Ueda, A. Lai, and T. Itoh, "Demonstration of negative refraction in a cut-off Parallel-Plate waveguide loaded with 2-D square lattice of dielectric resonators," *IEEE Transactions on Microwave Theory and Techniques*, vol. 55, pp. 1280–1287, June 2007. 33

[103] J. S. Derov, B. Turchinetz, E. E. Crisman, A. J. Drehman, and R. Wing, "Negative index metamaterial for selective angular separation of microwaves by polarization," *IEEE Antennas and Propagation Society International Symposium*, pp. 3753–3756 Vol.4, 2004. 33

[104] T. H. Hand and S. A. Cummer, "Frequency tunable electromagnetic metamaterial using ferroelectric loaded split rings," *Journal of Applied Physics*, vol. 103, p. 066105, 2008. 33

[105] P. V. Parimi, P. Peyton, J. M. Kunze, C. Vittoria, and V. G. Harris, "Novel microwave devices using tunable negative index metamaterials and ferrites," *IEEE International Workshop on Antenna Technology, iWAT*, pp. 1–4, Mar. 2009. 33

[106] K. Chan-Young, K. Hee-Jun, and K. Jong-Ryoul, "An integrated LTCC inductor," *IEEE Transactions on Magnetics*, vol. 41, pp. 3556–3558, Oct. 2005. 33

[107] M. Matterskammerer, U. Mackens, K. Reimann, R. Pietig, D. Hennings, B. Schreinemacher, R. Mauczok, S. Gruhlke, and C. Martiny, "Material properties and RF applications of high k and ferrite LTCC ceramics," *Microelectronics and Reliability*, vol. 46, pp. 134–143, Jan. 2006. vii, 33, 34

[108] A. L. Geiler, J. Wang, I. Viswanathan, S. D. Yoon, J. S. Gao, Y. Chen, C. Vittoria, and V. G. Harris, "Miniature, tunable, and power efficient ferrite

phase shifter devices," *Proceedings of the IEEE 2009 National Aerospace & Electronics Conference (NAECON)*, pp. 281–287, July 2009. vii, 33, 34, 35

[109] X. Zuo, P. Shi, S. A. Oliver, and C. Vittoria, "Single crystal hexaferrite phase shifter at ka band," *Journal of Applied Physics*, vol. 91, p. 7622, 2002. 34

[110] P. Shi, H. How, X. Zuo, S. A. Oliver, N. E. McGruer, and C. Vittoria, "Application of single-crystal scandium substituted barium hexaferrite for monolithic millimeter-wavelength circulators," *IEEE Transactions on Magnetics*, vol. 37, pp. 3941–3946, Nov. 2001. 34

[111] Y. K. Fetisov and G. Srinivasan, "Electric field tuning characteristics of a ferrite-piezoelectric microwave resonator," *Applied Physics Letters*, vol. 88, p. 143503, 2006. 35

[112] G. Srinivasan, E. Rasmussen, J. Gallegos, R. Srinivasan, Y. Bokhan, and V. Laletin, "Magnetoelectric bilayer and multilayer structures of magnetostrictive and piezoelectric oxides," *Physical Review B*, vol. 64, Nov. 2001. 35

[113] A. Okamoto, "The invention of ferrites and their contribution to the miniaturization of radios," *IEEE GLOBECOM Workshops*, pp. 1–6, Nov. 2009. 35

[114] G. Srinivasan, A. S. Tatarenko, and M. I. Bichurin, "Electrically tunable microwave filters based on ferromagnetic resonance in ferrite-ferroelectric bilayers," *Electronics Letters*, vol. 41, p. 596, 2005. 35

[115] H. M. Zhou, Z. L. Xia, and J. H. Deng, "The research of Dual-Tunable magnetoelectric microwave filters: Numerical simulation of the magnetoelectric microwave filters based on theoretical model of electric tuning ferromagnetic resonance," *Third International Conference on Communications and Mobile Computing (CMC)*, pp. 258–261, Apr. 2011. vii, 35, 36

[116] J. Wellman and A. Garcia, "High power (>1W) application RF MEMS lifetime performance evaluation," *NASA Electronics Parts and Packaging Program (NEPP)*, 2008. 37

[117] M. Rais-Zadeh, P. A. Kohl, and F. Ayazi, "MEMS switched tunable inductors," *Journal of Microelectromechanical Systems*, vol. 17, pp. 78–84, Feb. 2008. vii, 37, 39

[118] M. Bakri-Kassem and R. R. Mansour, "Linear bilayer ALD coated MEMS varactor with high tuning capacitance ratio," *Journal of Microelectromechanical Systems*, vol. 18, pp. 147–153, Feb. 2009. vii, 38

[119] R. Stefanini, M. Chatras, A. Pothier, J. C. Orlianges, and P. Blondy, "High q tunable cavity using dielectric less RF-MEMS varactors," *European Microwave Conference*, pp. 1444–1447, Oct. 2009. vii, 38, 39

[120] J. B. Muldavin and G. M. Rebeiz, "High-isolation CPW MEMS shunt switches," *IEEE Transactions on Microwave Theory and Techniques*, vol. 48, pp. 1045–1052, June 2000. 40

[121] C. Hung-Pin, Q. Jiangyuan, B. A. Cetiner, F. De Flaviis, M. Bachman, and G. P. Li, "RF MEMS switches fabricated on microwave-laminate printed circuit boards," *IEEE Electron Device Letters*, vol. 24, pp. 227–229, Apr. 2003. vii, 40

[122] A. Verger, A. Pothier, C. Guines, A. Crunteanu, P. Blondy, J. C. Orlianges, J. Dhennin, F. Courtade, and O. Vendier, "Sub-hundred nanosecond reconfiguration capabilities of nanogap RF MEMS switched capacitor," *IEEE MTT-S International Microwave Symposium Digest (MTT)*, pp. 1–1, May 2010. 40, 41

[123] A. S. Nafra, O. Jerphagnon, P. Chavarkar, M. VanBlaricum, and R. A. York, "Indirect optical control of microwave circuits using monolithic optically variable capacitors," *IEEE Transactions on Microwave Theory and Techniques*, vol. 47, pp. 1365–1372, July 1999. vii, 41, 42

[124] B. Boyer, J. Haidar, A. Vilcot, and M. Bouthinon, "Tunable microwave load based on biased photoinduced plasma in silicon," *IEEE Transactions on Microwave Theory and Techniques*, vol. 45, pp. 1362–1367, Aug. 1997. 42

[125] C. Qingjiang, L. Qiang, Z. Ziyang, Q. Min, Y. Tong, and S. Yikai, "A tunable broadband photonic RF phase shifter based on a silicon microring resonator," *IEEE Photonics Technology Letters*, vol. 21, pp. 60–62, Jan. 2009. vii, 42, 43

[126] D. Draskovic, C. Christodoulou, and D. Budimir, "Optically reconfigurable RF circuits," *Proceedings of the Fourth European Conference on Antennas and Propagation (EuCAP)*, pp. 1–3, Apr. 2010. 43

[127] D. Budimir, L. Athukorala, and G. Zouganelis, "Optically switchable microstrip resonators for RF/Microwave multifunctional systems," *Internation Topical Meeting on Microwave photonics*, pp. 267–270, Sept. 2008. 43

[128] D. Draskovic, C. Panagamuwa, D. Budimir, and J. C. Vardaxoglou, "Frequency switchable dual-band branch-line couplers," *European Microwave Conference EuMC*, pp. 133–136, Oct. 2009. vii, 43, 44

Chapter 2

New test structures and materials

Contents

In the first half of this chapter, several structures for measuring the relative permittivity (ε_r) and the loss tangent ($tan\delta$) of optically tunable materials at microwave frequencies will be explained. The second half will focus on the photosensitive materials studied with these new structures and the properties of the materials characterized with them.

However, it is important to be familiar with some major properties of the materials in order to have a better understanding of the structures developed and the materials tested.

2.1 Material properties

Two main properties of a material will be explained here, the **relative permittivity** (ε_r) and the **conductivity** (σ). These two properties are really close related but they will be treated as individual parameters in this explanation as this will allow us to make a clear difference between photorefractive and photoconductive materials.

2.1.1 Relative permittivity

In electromagnetism, absolute permittivity (ε) is the measure of the resistance that is encountered when forming an electric field in a medium. In other words, permittivity is a measure of how an electric field affects, and is affected by, a dielectric medium.

The permittivity of a medium describes how much electric field or flux is generated per unit charge. Less electric flux exists in a medium with a high permittivity per unit charge due to polarization effects [1].

Permittivity relates to a material's ability to transmit an electric field as defined earlier. The reduction of the electric field inside a material is accomplished by the displacement of charges that align with the electric field. This effect is known as electric polarization.

The relative permittivity of a material under given conditions reflects the extent to which it concentrates electrostatic lines of flux. Technically, it is the ratio of the amount of electrical energy stored in a material by an applied voltage, relative to that stored in a vacuum. The linear permittivity (ε) of a homogeneous or isotropic material is usually given relative to that of free space, as a relative permittivity ε_r as in eq. 2.1 and it is measured in Farads per meter (F/m).

$$\varepsilon = \varepsilon_r \varepsilon_0 = (1 + \chi)\varepsilon_0. \tag{2.1}$$

where ε_r is the relative permittivity of the material and χ is the electric susceptibility, both dimensionless characteristics.

ε_0 is the permittivity of the vacuum or free space permittivity and it is defined as follows:

$$\varepsilon_0 \triangleq \frac{1}{c_0^2\mu_0}\frac{F}{m} = 8.85418... \times 10^{-12}\frac{F}{m}. \tag{2.2}$$

where c_o is the speed of the light in free space and μ_0 is the vacuum permeability.

Permittivity is directly related to electric susceptibility, which is a measure of how easily a dielectric polarizes in response to an electric field. If we assume the medium to be linear the susceptibility (χ) is defined as the constant of proportionality relating an electric field $\vec{E}$ to the induced dielectric polarization density $\vec{P}$ as in eq. 2.3 [1].

$$\vec{P} = \varepsilon_0\chi\vec{E}. \tag{2.3}$$

The susceptibility of a medium is related to the relative permittivity by eq. 2.4.

$$\chi = \varepsilon_r - 1. \tag{2.4}$$

So in the case of vacuum $\chi = 0$.

The electric displacement ($\vec{D}$) is also related to the polarization density ($\vec{P}$). When a homogeneous isotropic material has an electric field $\vec{E}$ applied to it, the electric flux $\vec{D}$ is given by eq. 2.5.

$$\vec{D} = \varepsilon_0\vec{E} + \vec{P}. \tag{2.5}$$

The susceptibility of a material is also defined by eq. 2.6 as it is shown in [2].

$$\chi = \frac{N\alpha}{\varepsilon_0}. \tag{2.6}$$

where α is the average electronic polarization of the material in $F \cdot m^2$ and N is the number of particles per unit volume in $atoms/m^3$.

Materials can be classified according not only to their permittivity but also to their conductivity, σ. Dielectric materials are associated with lossless or low-loss materials, where the condition in 2.7 is satisfied.

$$\frac{\sigma}{\omega\varepsilon_r\varepsilon_0} \ll 1. \tag{2.7}$$

A perfect dielectric is a material that has no conductivity, thus exhibiting only a displacement current. In this materials the relative permittivity is a real number. However, most materials have a conductivity, even if it is low, this implies that the material is not longer considered as a lossless material and the relative permittivity is a complex number so the loss tangent ($\tan\delta$) and the conductivity need to be taken into account.

The loss tangent is a parameter of a dielectric material that quantifies its inherent dissipation of electromagnetic energy. The loss tangent is defined as the ratio of the lossy reaction to the electric field E in the curl equation to the lossless reaction. The loss tangent is given by eq. 2.8:

$$\tan\delta = \frac{\omega\varepsilon_r'' + \sigma}{\omega\varepsilon_r'}. \tag{2.8}$$

Strictly speaking, photorefractivity refers to a material's change in refractive index n when subjected to light or an electric field. Given the square-root relationship between refractive index and dielectric constant, **in this thesis** all materials whose relative permittiivity (dielectric constant) change with light will be called **photorefractive** materials.

2.1.2 Conductivity

Electrical conductivity (σ) measures a material's ability to conduct an electric current and its unit is Siemens per meter (S/m). The conductivity is the reciprocal quantity to the electric resistivity (ρ) which is a measure of how strongly a material opposes the flow of electric current.

$$\sigma = \frac{1}{\rho}. \tag{2.9}$$

The complex permittivity of a material is expressed as follows:

$$\varepsilon = \varepsilon' - \jmath\varepsilon'' = \varepsilon_0(\varepsilon'_r - \jmath\varepsilon''_r). \tag{2.10}$$

Eq. 2.10 normally refers to materials known as general media.

As previously explained in 2.1.1, the real part of the relative permittivity (ε'_r) is related to the electric susceptibility of the material while the imaginary part (ε''_r) accounts for the loss in the medium, normally referred to as the loss tangent ($\tan\delta$).

As it has been mentioned already, materials can be classified according to their conductivity. We have shown the condition to be a lossless or low-loss materials in 2.7. For a material be considered as a good conductor the material has to meet the condition in 2.11.

$$\frac{\sigma}{\omega\varepsilon_r\varepsilon_0} \gg 1. \tag{2.11}$$

Materials that do not fall in either limit of 2.7 or 2.11 are considered the general media.

For a conductive material, eq. 2.10 is converted to eq. 2.12 as the imaginary part of the permittivity is related to the conductivity.

$$\varepsilon = \varepsilon_0\Big(\varepsilon_r - \jmath\varepsilon''_r - \jmath\frac{\sigma}{\omega\varepsilon_0}\Big). \tag{2.12}$$

When a material is illuminated by a light source and its loss tangent changes, we usually assume that this change is due to a change in its conductivity, this effect is called **photoconductivity**.

2.2 Test structures

For extracting the properties of a material, a test structure is needed. Multiple test structures have been developed by the researchers over the years, but many of them extract the parameters at very low frequencies [3] which is not suitable for the microwave structures in this thesis as the electric permittivity depends on frequency as it can be seen in eq. 2.13

$$\varepsilon_r(\omega) = \frac{\varepsilon(\omega)}{\varepsilon_0}. \tag{2.13}$$

Nevertheless, a huge effort has been made over the last few years for characterizing microwave materials at high frequencies [4] and it can be considered now as a well established field although lots of challenges are still encountered. Especially for our materials, needing the material to be characterized under illumination make techniques like the use of slow wave propagation lines at high frequencies presented in [4] not suitable.

A significant amount of literature can be found about different techniques such as reflection, transmission, resonator or the resonant-perturbation method, for measuring microwave properties of a material in books [5] or review papers published discussing specific techniques and their advantages and disadvantages [6] [7].

In this section we are going to explain two basic test structures and the method employed to characterize photosensitive materials at microwave frequencies.

2.2.1 Coplanar lines

Some of the materials considered for this work are photoconductive materials and we are interested only on their conductivity. In order to extract these properties, a very simple test structure has been developed to extract the conductivity in an easy way.

The structure consists of a coplanar line (CPW), and a coplanar line with a gap in the center conductor, both with a back ground plane as in Fig. 2.1.

Previous research about illuminating coplanar lines has been done. In [8] a whole theoretical analysis is done for a coplanar waveguide that has been illuminated. In the presented work, they focus on analyzing the effects of illuminating the coplanar waveguide when a plasma region is included between the center conductor and the ground. In our case we are mostly interested to the change of the line response rather than in a theoretical analysis and modelling.

The work presented in [9] is closer to our structure as a silicon finite-ground coplanar waveguide and lumped component modelling is presented. The paper

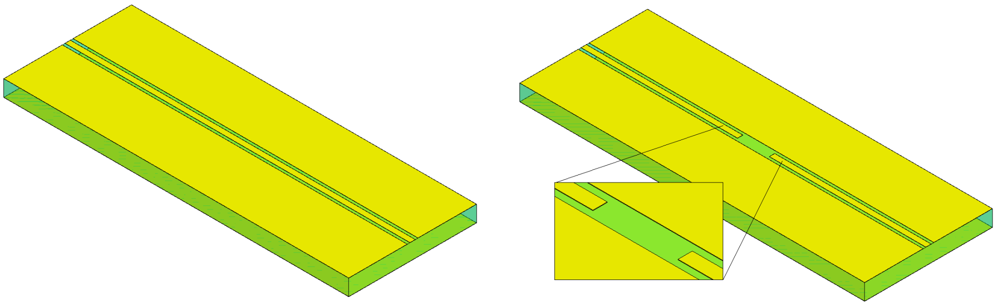

(a) Coplanar line without gap. (b) Coplanar line with gap.

Figure 2.1: Coplanar lines (CPW) structures on HFSS

shows how the conductivity of the substrate increases in the presence of illumination and they present a model explaining that change together with some measurements. Again, the work is more about the theory behind the coplanar lines which is not what we were interested in doing.

The main characteristic of our work is its simplicity. We wanted to create a simple structure allowing the extraction of the conductivity of a material quite easily.

The structure consists on a 50Ω coplanar line working from 1 to $10GHz$ optimized using Ansoft HFSS. In the Fig. 2.2 the structure is shown where the main characteristics can be checked.

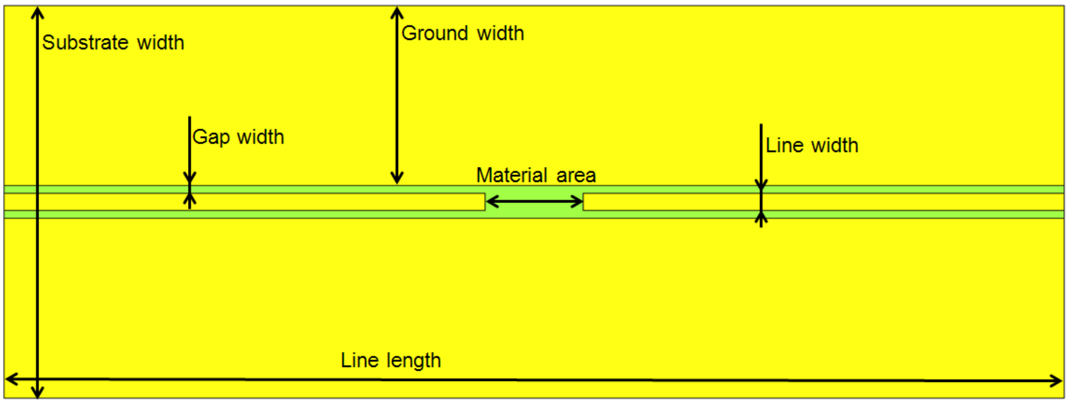

Figure 2.2: Sizes of the coplanar line with gap.

A simulation of the coplanar line has thus been done followed by the simulation of the coplanar line with the gap in the center conductor and the results are shown in Fig. 2.3.

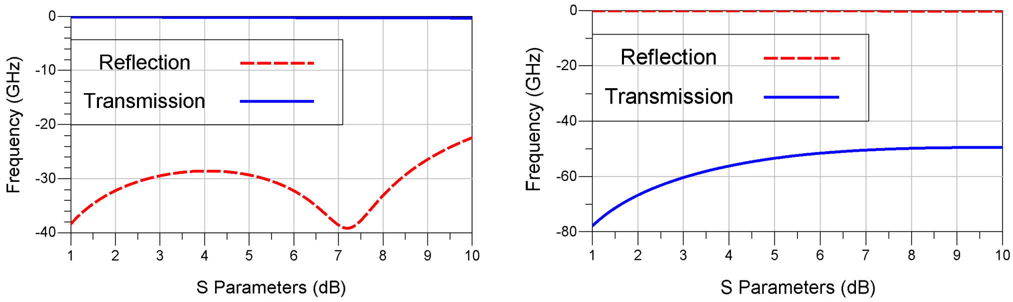

(a) S parameters of the coplanar line without gap.

(b) S parameters of the coplanar line with a gap on the center conductor.

Figure 2.3: Simulation results of the coplanar lines without a material deposited.

These are basic coplanar lines so the results are as expected. For the coplanar line without the gap, the transmission is close to $0dB$ while the reflection coefficient is below $-20dB$ over the whole band as shown in Fig. 2.3(a). In the case of the coplanar line with a gap in the center conductor the results are just the opposite. The reflection is close to $0dB$ while there is no transmission at all this value staying below $-40dB$.

These lines were fabricated on a $635\mu m$ alumina substrates. A metal lift-off photolithography process was used for the fabrication of the coplanar lines. First of all a dark field mask for the structure is made, then $2\mu m$ of silver are deposited using an evaporation technique. Finally, a development step removes the material where needed. A microscope photograph of one of the fabricated devices is shown in Fig. 2.4.

Due to fabrication issues such as tolerances and uncertainties of the machines, there is a slight difference between the designed lines and the fabricated ones. Those different values are shown in table 2.1 but they are not very important and acceptable for our characterization method as the designed values and the fabricated values are very close to each other.

The proposed method consists of measuring the S parameters of both lines, the one with the gap and the one without the gap and modelling it on HFSS taking into account the exact size of the structure. The material is then deposited on top

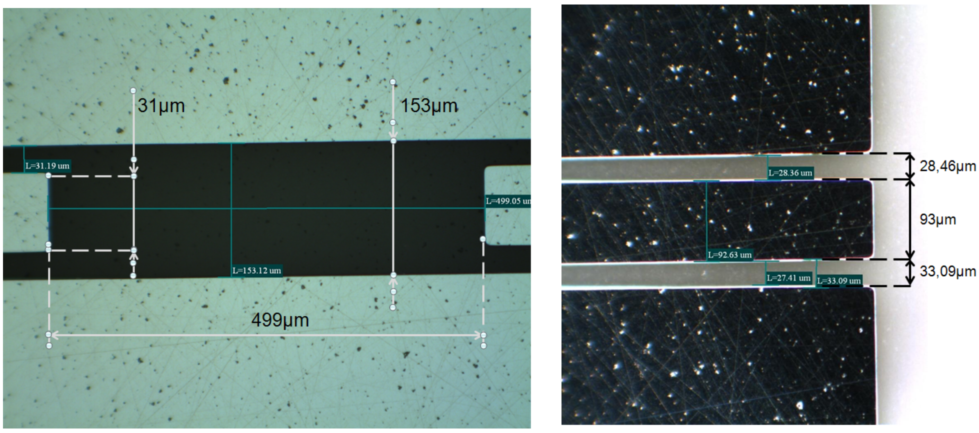

(a) Detail of the gap (b) Detail of the input port.

Figure 2.4: Photographs of the fabricated coplanar line.

Parameter	**Designed value**	**Fabricated value**
Substrate width	$2mm$	$2mm$
Line length	$5.4mm$	$5.4mm$
Line width	$84\mu m$	$93\mu m$
Gap width	$42\mu m$	$31\mu m$
Ground width	$916\mu m$	$923\mu m$
Material area	$500\mu m$	$499\mu m$

Table 2.1: Extracted values for the material under dark condition

of the line without the gap on the center conductor and also in the gap left for the material on the other line as it can be seen on Fig. 2.5.

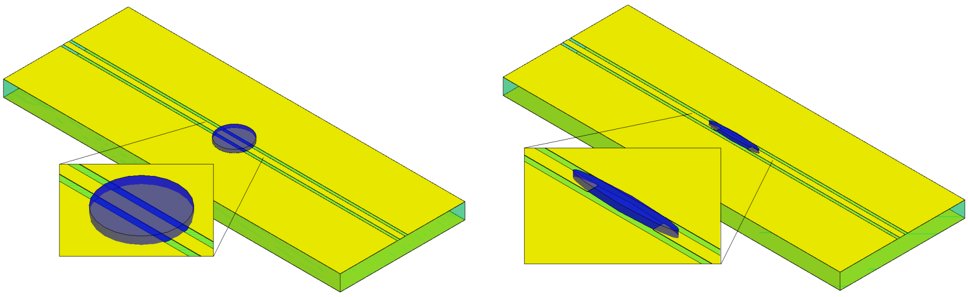

(a) Coplanar line without gap and the material deposited. (b) Coplanar line with the gap and the material deposited.

Figure 2.5: HFSS 3D structures of the coplanar lines.

By simulation, and knowing roughly the properties of the material deposited, we simulate the structure by just varying the conductivity of the material until the simulated and the measured results match.

The main idea is that the transmitted and reflected waves will change gradually depending on the conductivity.

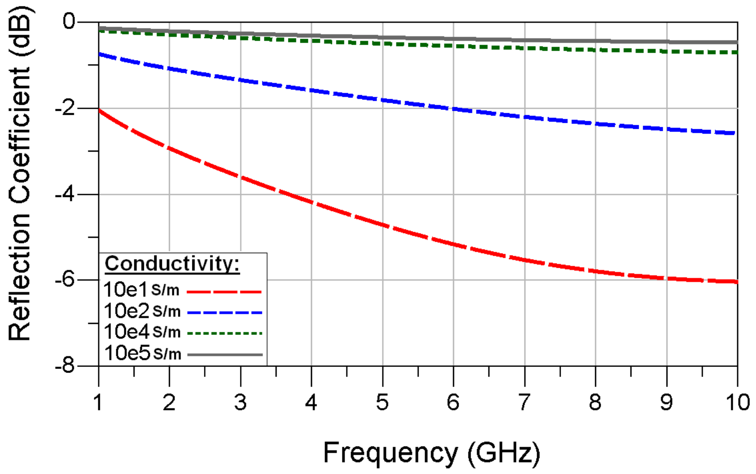

(a) Reflection coefficient (S_{11}).

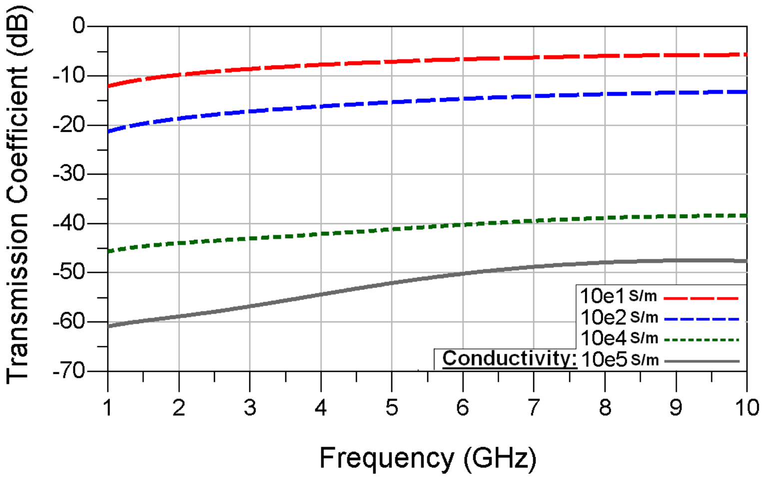

(b) Transmission coefficient (S_{21}).

Figure 2.6: Simulation of a coplanar line with a conductive material deposited on top.

The effect of placing a conductive material in the middle of the line is known from the electromagnetic theory. If a conductive material is placed in the middle of the line, the line will be shorted and no transmission will occur between the input and the output ports of the coplanar line. Depending on how conductive is the material, the transmission level will be higher or lower as it can be observed in Fig. 2.6.

Fig. 2.6(a) shows the simulated reflection coefficient of the coplanar line and how as the material becomes more conductive the reflection coefficient is higher. This is a result of having a better quality connection between the center conductor and the grounds and indicates that an electromagnetic wave will be blocked from the input port to the output port more easily if the material deposited on the line is more and more conductive as it can be conclude from Fig. 2.6(b).

Similar simulations have been done for the line with a gap in the conductor and the results match the electromagnetic theory as it can be seen in Fig. 2.7.

As expected, and contrary to the line without the gap, in this case the transmission is better as the conductivity of the material increases (Fig. 2.7(b)). It can be seen as creating continuity of the line with that material. In the same way, the reflection is better while the material conductivity increases as most of the energy will be transmitted to the output port (Fig. 2.7(a)).

The aim of this method is to measure photoconductive materials, that is, to be able to extract the conductivity of the material in the dark but also when a light source shines on them.

2.2.2 Interdigitated capacitor

The explanation of this structure will be divided in two subsections. First of all the design and fabrication of the interdigitated capacitor and it will be followed by the characterization method developed.

This work has been carried out with T. Morolari, a Master's student from Carleton University.

2.2.2.1 Design and fabrication

During his research, T, Morolari designed a structure based on the reflection characterization method. The main objective of his work was to develop a structure capable of characterizing an optically tunable or photosensitive material. After some

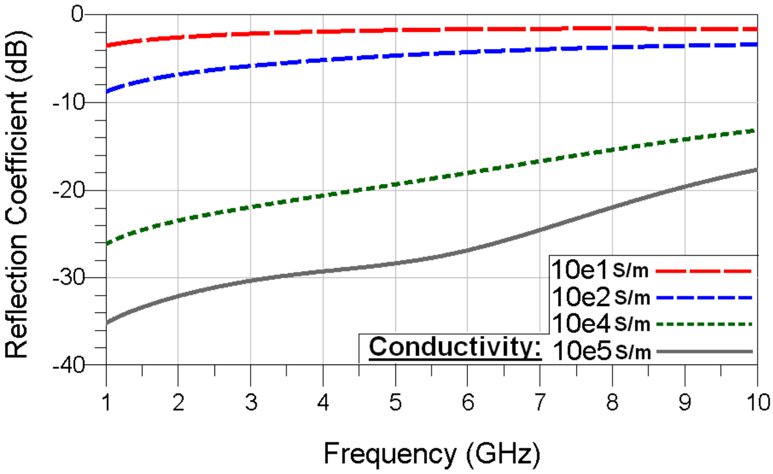

(a) Reflection coefficient (S_{11}).

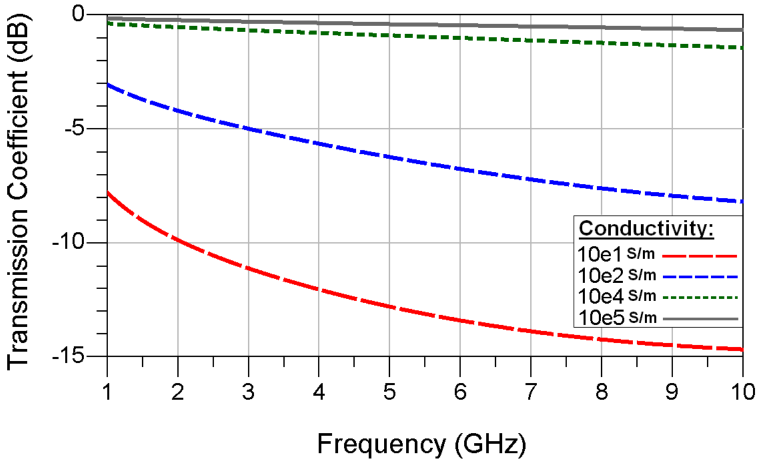

(b) Transmission coefficient (S_{21}).

Figure 2.7: Simulation of a coplanar line with a gap and a conductive material deposited on top.

research, he decided that the best idea was to fabricate a one port interdigitated capacitor (IDC) as the one shown in Fig.2.8:

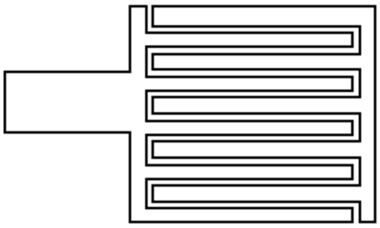

Figure 2.8: Basic idea of a one port interdigitated capacitor.

This type of capacitor is really useful for the type of characterization needed to be done. First, the material properties can be extracted fairly easily from the measured impedance of the capacitor and, second, the capacitor itself could be used directly as a tuning element in a microwave circuit or antenna as its properties have been already determined. This is called an ”in-situ” material characterization.

Interdigitated structures are well-know for characterization of materials or even for characterizing biological cells as for the interdigitated LC resonator in [10] or the capacitor in [11] but these two structures use the transmission method rather than the reflection characterization method.

The reflection characterization method consists of directing an electromagnetic wave to the material under test and extracting the parameters of interest from the reflection coefficient defined at the reference plane. In the case of this interdigitated capacitor, the material under test (MUT) will be deposited on the top of the fingers of the capacitor in order to maximize the effect of the material in the structure. Fig. 2.9 shows the structure developed on the commercial software Ansoft HFSS (High Frequency Structure Simulator). The capacitor is at the end of a standard CPW 50Ω line.

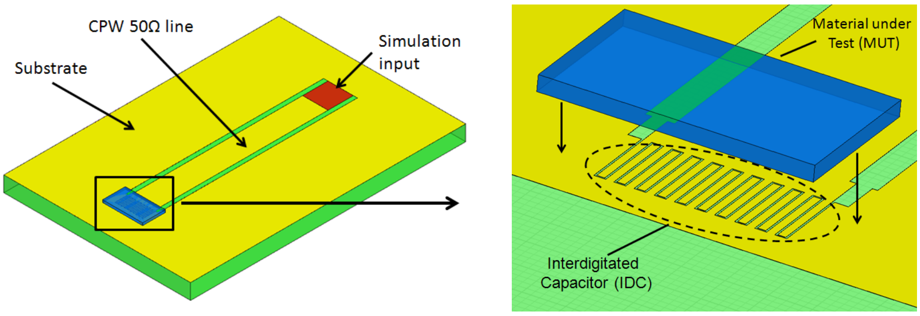

(a) Whole structure (b) Detail of the interdigitated fingers

Figure 2.9: Design of the interdigitated structure on HFSS

In Fig. 2.9(b), is shown a close view of the fingers of the capacitor with the layers separated. On top of the substrate aluminum is deposited to create the interdigitated capacitor. The material to be tested (MUT) would be deposited on top of the fingers. The substrate used for this interdigitated capacitor is a $1.22mm$ height Corning 7059 substrate with the characteristics shown in table 2.2.

Property	**Value**
Electric permittivity (ε_r)	5.84 @ $1MHz/20°C$
Loss tangent ($\tan\delta$)	0.001 @ $1MHz/20°C$

Table 2.2: Properties of Corning 7059 substrate

The capacitor itself is made of Aluminum with a thickness of $3\mu m$. The main properties of the metal are in table 2.3.

Property	**Value**
Electric permeability (μ_r)	1.000021
Conductivity (σ)	$3.5 \times 10^7 S/m$

Table 2.3: Properties of Aluminum

A photograph of one of the fabricated samples is shown in Fig.2.10. Each disk has four different interdigitated capacitors.

Figure 2.10: Fabricated sample with four interdigitated capacitors.

This test structure was already started by T. Morolari so the goal was to developed a suitable characterization method with the designed capacitor. The capacitor size was defined by T. Morolari during his Master's research [12] for working in the range from 1 to $10GHz$. In Fig. 2.11 the simulation results of the structure developed by T. Morolari are shown:

The results in Fig. 2.11(c) show that the behavior of the structure is that of a capacitor. The change from the bottom half part of the Smith Chart to the top half at $2.9GHz$ agrees with the change of phase from $-180°$ to $-180°$ on Fig. 2.11(b). Finally, in Fig. 2.11(a) we see that the insertion losses increase a little bit as the

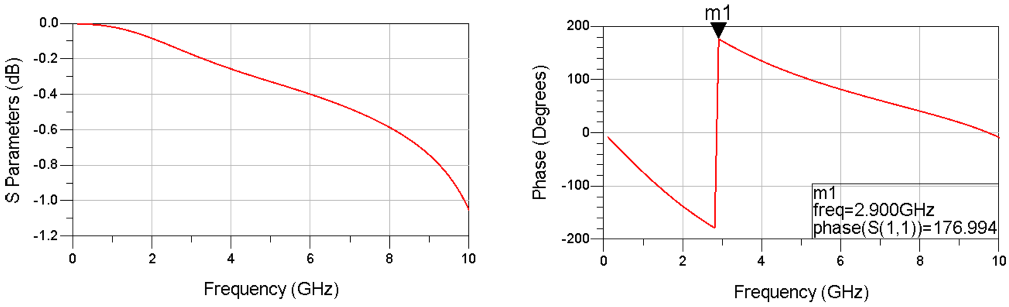

(a) Magnitude of the S_{11} parameter. (b) Phase of the S_{11} parameter.

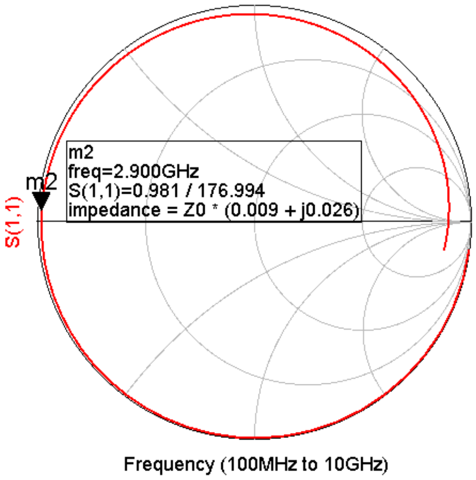

(c) S_{11} parameter on the Smith chart.

Figure 2.11: Simulated results of the first designed interdigitated capacitor.

frequency increases.

Although there was a whole process for defining the optimal size of this interdigitated capacitor [12], due to fabrication tools limits, the fabricated device's dimensions do not correspond with the dimensions of the design.

These disagreements between the designed capacitor and the fabricated one will cause some changes on the device response, especially in the resonant frequency of the capacitor that will disappear. This fact will also imply that the simulations will need to be redone in order to be in accord with the actual fabricated device. The greatest change is the feed line length which was increased from $2mm$ to $13.2mm$ in order to move the resonant part of the structure further away from the edges of the glass slide.

Fig. 2.12 shows the final dimensions of the fingers and the gaps of the integrated capacitor after measuring them under the microscope.

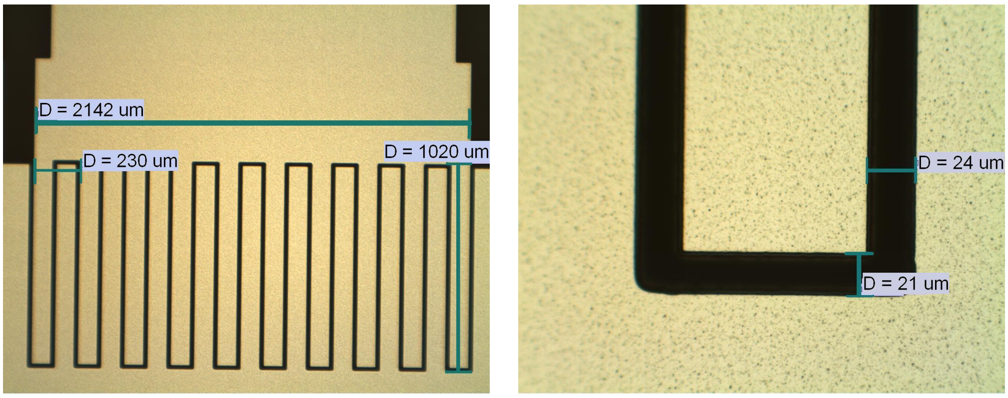

(a) Width and length of the fingers (b) Width of the gaps

Figure 2.12: Dimensions of the fabricated interdigitated capacitor

The optimal situation would have been to measure this samples with a GSG (ground-signal-ground) probe station, however, this was not possible with the resources we had at Carleton University, so a 50Ω SMA connector was mounted on the edge of the disk using silver epoxy. The inclusion of a connector will make the performances of the capacitor not to be the same especially when working at higher frequencies. A transition from a coaxial line to a coplanar line is introduced and this will cause losses to increase. The calibration of the measuring tool will be done at the connector so this transition will be included in the results and may cause some resonances to appear.

A photograph of the disk with the SMA connector and some material already deposited is shown in Fig. 2.13

2.2.2.2 Characterization method

Once the interdigitated structure is designed and fabricated, it is important to spend some time defining the characterization method that will be utilized.

The first idea is to use a reflection characterization method and that is why a one port interdigitated capacitor has been fabricated. Using the measured S_{11} parameters, we want to be able to extract the properties of the material, both the

Figure 2.13: Photograph of the fabricated sample with the SMA connectors mounted and materials deposited.

relative permittivity (ε_r) and the loss tangent ($\tan\delta$). The proposed method is to measure the interdigitated capacitor without any materials and with materials and then, using the simulation software, to extract the wanted parameters matching the measured results with the post-simulation results.

Fig. 2.14 shows the block diagram for the characterization method developed and explained in the following paragraphs.

Based on this block diagram, we can divide the method in four main parts:

1. Measuring the S parameters of the circuit: these will be the results that will need to be matched. The S parameters measured on the VNA will be extracted in this part.

2. Creating and simulating a lumped component equivalent circuit, circuit model: creating a lumped component circuit will permit a better understanding of the circuit and it will permit dividing the structure into several subsections (connector, feed line, interdigitated capacitor - IDC). The most critical part of this section of the method is extracting a lumped component model for the connector that can be used in the last part of the method. This part will provide a lumped component model for the connector, the feed line and the IDC separately.

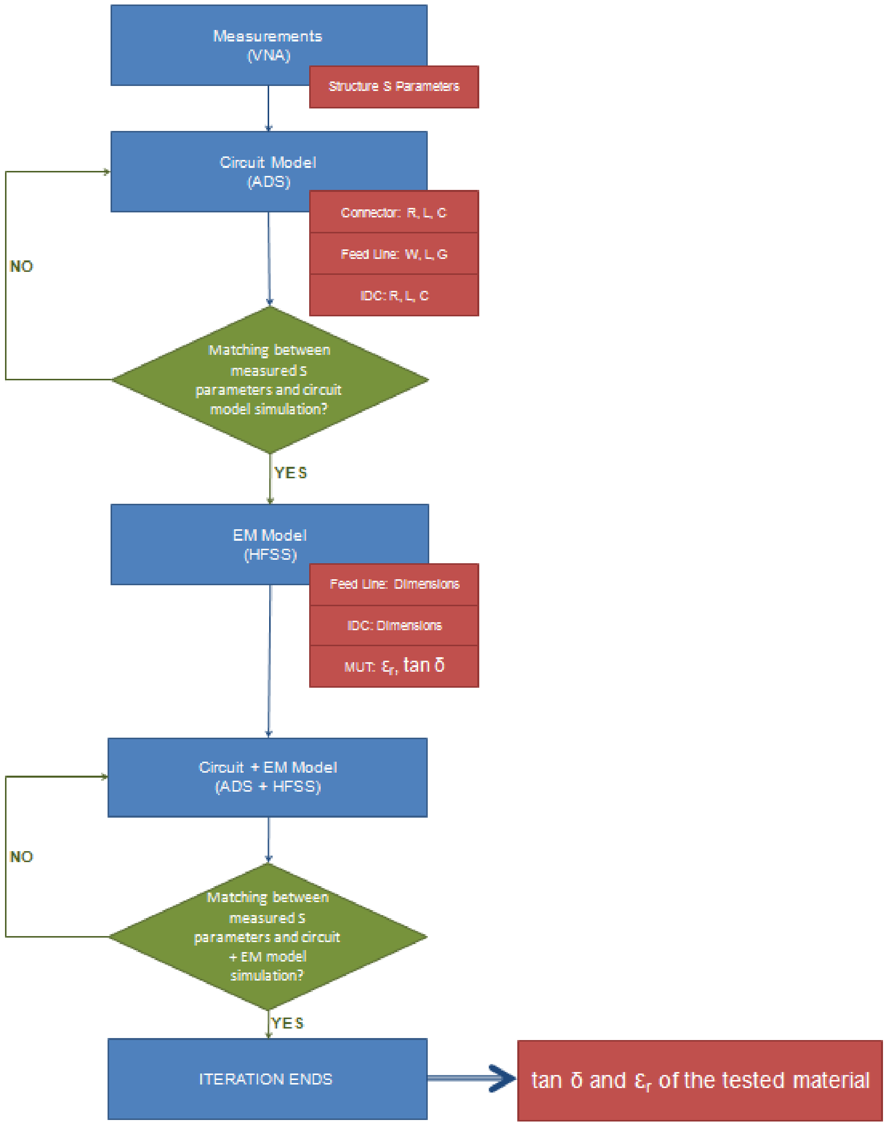

Figure 2.14: Block diagram of the characterization method for the interdigitated capacitor.

3. Creating and simulating a 3D structure of the feed line and the interdigitated capacitor to simulate on a EM (ElectroMagnetic) software: this is the software from which we will extract the structure or the properties of the material depending on the iteration and taking into account the fabricated dimensions of the device.

4. Comparing the measured results with the simulated results of the combination

of the connector lumped components model and the EM simulation response of the feed line and interdigitated capacitor: due to fabrication issues, the connector could not be described accurately in a 3D software because the manufacturing imperfections could not be taken into account.

For modeling the lumped components circuits the software used is ADS (Advanced Design System) of Agilent Technologies while for the 3D structure EM simulation HFSS from Ansoft has been chosen. As we can observe in the block diagram in 2.14, there are two loops. The first one is to match the measured results with the circuit model, which allows extracting the values of the lumped components. In the last part of the method, the simulated results from the EM software are combined with the lumped component model of the connector and they are simulated together. These results are compared with the measured results and the second loop stops when these two results match.

This structure has been developed to work with new photosensitive materials so it has to permit the extraction of the parameters of the materials under dark condition as well as under illumination. We have three different scenarios to work with and to apply the previous method:

1. Work with the plain disk: first of all we are going to measure the S parameters of the plain interdigitated capacitor without any material deposited on the fingers. After that we are going to develop a lumped components model that matches the measured results. This model will be divided in three different parts: connector, feed line and capacitor. Finally we are going to design the feed line and the capacitor itself in HFSS. From this first iteration, we are going to extract the model of the connector that will be taken into account later and the exact dimensions of the feed line and the interdigitated capacitor. All these parameters will not change in the next two iterations. The material will just be added on top of the structure.

2. Work with the disk with the material deposited under dark condition: the first step is to measure the S parameters of the sample that will be later matched.

We continue with the development of the lumped components model. However, in this case we will only try to find the part corresponding to the capacitor as the part corresponding to the connector and the feed line will remain the same as in the case of the plain disk. Finally, we will use the HFSS structure developed before but the material on top of the fingers will be simulated and the properties extracted by matching the measured results just varying the loss tangent and the relative permittivity. The comparison with the measured results will be done again with the simulation results of the circuit model of the connector combined with the EM simulations of the feed line and the IDC developed on HFSS.

3. Work with the disk with the material deposited under illumination: this part is very similar to the one under dark condition. The only change is that depending on the difference on the measured results, we will know if the difference is related to the loss tangent or to the permittivity.

This method has been validated but some problems due to connector and uncertainties with the materials have come up. The connector was mounted on the glass substrate but the silver epoxy, the air gaps and the exact connections could not be measured accurate enough to create a valid HFSS model.

This structure is focused on extracting the relative permittivity and the loss tangent of any material spread on top of the capacitor. Because of that, it is therefore more suited to the characterization of photorefractive materials.

This method has thus been tested with two different photorefractive materials, Silicon nano-particles in a polymer and Cadmium Sulphide (CdS) in a polymer matrix as it will be explained more in detail in section 2.3. More information about these photosensitive materials will be given in sections 2.3.2 and 2.3.1.

2.2.3 Experimental setup

The setup used for measuring the S parameters of the capacitor and the coplanar lines consisted on using an *Agilent 8720ES* Vector Network Analyzer (VNA) connected to the interdigitated capacitor with the material under test (MUT) on it and illuminated with a broadband light lamp. The network analyzer was calibrated using *SOLT* (Short-Open-Load-Through) calibration method using the commercial calibration kit *850525 Economy*. Fig. 2.15 shows a photograph of the setup utilized.

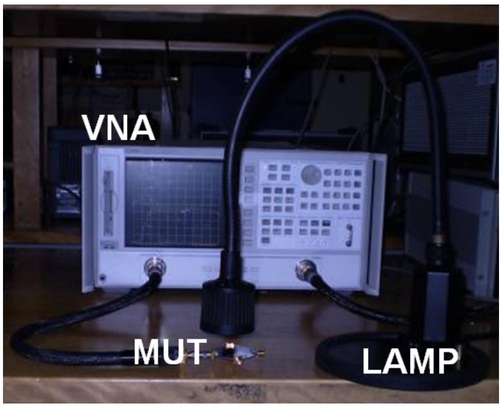

Figure 2.15: Measurement setup for the interdigitated capacitor.

This setup was used for the characterizations described in the next section 2.3.

The next section will focus on the materials and will investigate their characteristics.

2.3 New materials

Four different potential materials have been characterized using different methods in order to use them in new tunable microwave structures. This work focuses more on characterizing the material at microwave frequencies rather than in the creation of the materials themselves.

However, this section will try to explain the basic properties of the materials as well as their fabrication process.

The first material that will be described in this section is a material based on Cadmium Sulfide (CdS), a photorefractive material. Then, a material based on nano-crystalline Silicon ($nc-Si$) also called Silicon nano-particles and another based on Zinc Oxide (ZnO) will be explained, both of them photoconductive materials. A more developed material will be explained later on, that is thermoconductive: Vanadium Dioxide (VO_2). Even if it is not a photosensitive material, it was considered for study because depending on the results heating the material with a light source could be considered.

2.3.1 Cadmium Sulfide (CdS)

2.3.1.1 Theory

The first studied material is a photorefractive material. Actually, this material will take advantage of the photoconductivity of its particles to produce a change on the complex permittivity of the material. A new optically tunable dielectric material is thus proposed. This material can be seen as a composite consisting of photoconductive spheres dispersed in an insulating polymer. Changing the conductivity of the spheres therefore changes the effective permittivity of the material. Changes in temperature will also have an effect on the photoconductivity of the spheres, however photoconductivity is not overly sensitive to temperature.

The particles used are from cadmium sulfide (CdS) as it has been previously used at Carleton University and both N. Jess [13] and T. Morolari [12] have showed promising capabilities of the CdS. The particles of CdS used are approximately spherical and have an average diameter of $1\mu m$.

The properties of bulk CdS extracted from [14] are as follows:

- Electron mobility: $\mu_e = 160cm^2/Vs$
- Hole mobility: $\mu_h = 15cm^2/Vs$
- Low frequency or static relative permittivity: $\varepsilon_r(0) = 8.5$
- Relative permittivity in the optical range: $\varepsilon_r(\infty) = 5.26$
- Minority carrier life time: τ is $22.3\mu s$ to $57.4\mu s$
- Bandgap is $2.4eV$

As enumerated in the list above, the bandgap is $2.4eV$, which means that wavelengths shorter than $520nm$ will be absorbed and create a single electron-hole pair as it can be deduced from 2.14.

$$E(eV) = hv = \frac{hc_0}{\lambda} = \frac{(4.13566733 \times 10^{-15} eVs)(299792458 m/s)}{\lambda} \approx \frac{1240 eVnm}{\lambda nm}. \tag{2.14}$$

where h is the Planck constant and c_0 is the speed of light.

The characterized materials were prepared by Prof. Steven McGarry at Carleton University. Four different films were made: polymer; polymer and dopant; polymer, CdS and dopant; and polymer and CdS. These four different samples were measured as it permitted the validation of the characterization apparatus and to test if a type of sample worked better than the others.

First, the dopant ($20mg$ if $CuCl_2$) was mixed with the polymer and solvent ($4g$; 20% 3571 dielectric polymer from DuPont). Next, the CdS was added to the mixture and this latter was left for some time, over 100 hours, to allow the copper to diffuse into the CdS. The volume fill fraction of the CdS was 72.2%. Each of the four different samples were deposited using a screen printing process onto glass cover slips. The samples were cured on a hotplate at 140°C for at least 30 minutes. The polymer-CdS samples are shown in Fig. 2.16.

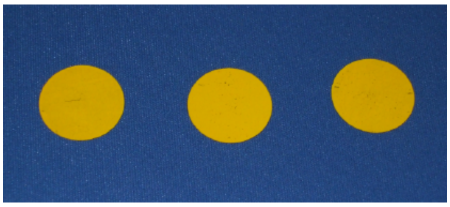

Figure 2.16: Glass cover slips with polymer-CdS deposited film [13].

The thickness of the samples were measured using a Dektak profilemeter. Measuring the polymer and the polymer-dopant samples proved difficult due to the fact they were thinner than expected, about $1.5 - 2\mu m$. The samples with CdS were measured to have a thickness of $9 - 11\mu m$. These looked to have a rough surface and some visible gaps, which means the thickness measurements are suspect for these samples as well.

For characterizing these samples some assumptions were made. These assumptions are:

- The material is uniformly illuminated.
- The minority carrier lifetime is not affected by strong illumination.
- All spheres dispersed in the material get illuminated equally or the charge diffuses to them all equally.

The apparatus used for the characterization is the open single post dielectric resonator (OSiPDR) developed by N. Jess during his Master's thesis [13] that can be seen in Fig. 2.17.

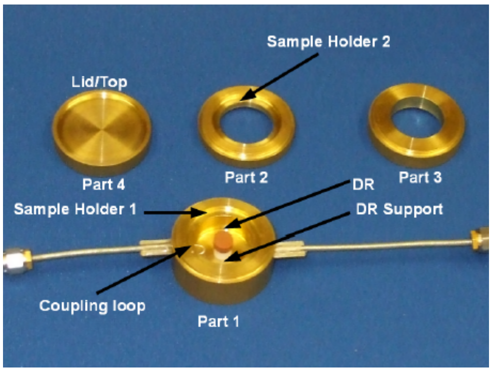

Figure 2.17: Fabricated pieces of the open single post dielectric resonator [13].

The structure is just a dielectric resonator inside a metallic cavity. This resonator mode $TE_{01\delta}$ is excited with coupling loops. On top of the resonator is placed the material under test in a cylindrical disc form and it can be illuminated from the top as the cavity is open. Fig. 2.18 shows a cross section of the OSiPDR showing where the materials for characterization should be placed.

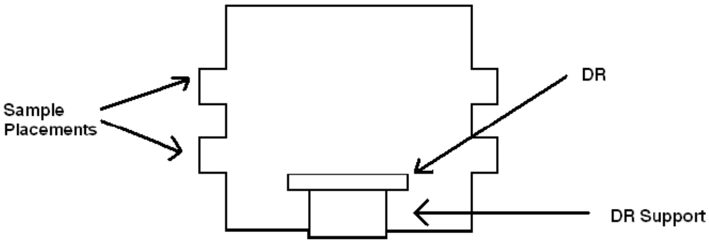

Figure 2.18: Cross section of the OSiPDR (All components are cylindrical) [13].

The material was characterized in the dark and under light conditions. The light source used was an Oriel quartz tungsten lamp (bulb 6333). The optical power applied to the OSiPDR was $0.22W$ and was measured with a coherent 1D100 thermopile sensor connected to a Coherent Lasermate 1D power meter.

The average values extracted at a frequency of $8GHz$ are in the table 2.4. From all the samples studied, the values of the undoped CdS are presented here as this samples show the best characteristics.

Property	**Value (Dark)**	**Value (Light)**
Electric permittivity (ε_r)	4	4.6
Loss tangent ($\tan\delta$)	0.05	0.12

Table 2.4: Extracted values for the material under dark and light condition for the CdS at $8GHz$

This mix of CdS and polymer shows then great capabilities for the use in optically tunable microwave devices. However, an improvement on the losses should be made, and with the study carried on by N. Jess [13] this seems totally possible for further study.

With the theoretical analysis carried out during his Master's thesis, N. Jess proved that with a lower concentration of CdS particles in the polymer matrix, the same change on the real part of the permittivity would be achieved with an important decrease on the imaginary part which is close relation with the losses of the material.

Based on this consideration CdS and polymer mixture has been deposited on top of this interdigitated capacitor which is the most appropriated structure for material characterization.

On the material side, as it has been already mentioned, a lower volume fill fraction of the CdS particles would most likely provide greater change on the relative permittivity while lowering the loss tangent, which would result in a better material for microwave applications. Indeed, this has been achieved with a different formulation of the material that was described in Section 2.3.1.2. This improved material is employed in Section 3.3.

2.3.1.2 Experimental results

We will present here an experimental result of the method explained in section 2.2.2.2 for the interdigitated capacitor.

a)Measurements: As stated in the description of the method, the first part consists on working with the plain disk, that is, the interdigitated capacitor without material and measure its S_{11} parameters. At the same time, the first part of the work for the cases with the material (both under dark and illuminated condition), is also to measure the S_{11} parameters and has been done. These three initial measurements allow us to compare the results of all the three cases at once in Fig. 2.19.

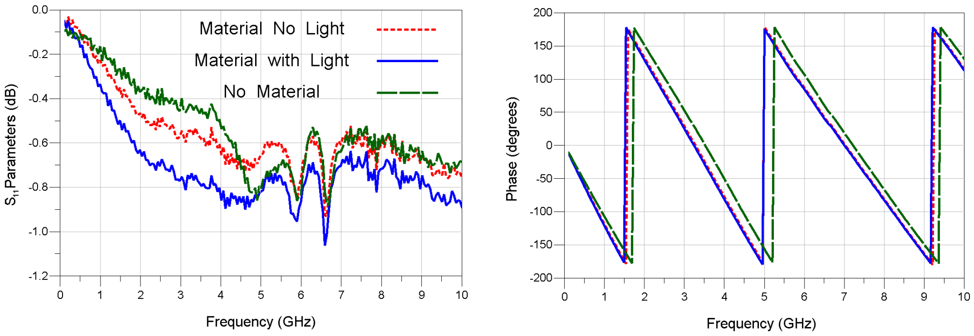

(a) Magnitude of S_{11} in dB. (b) Phase of S_{11} in degrees.

Figure 2.19: Measured results of the interdigitated capacitor

The measured results on Fig. 2.19(a) show that there is a small change between the results of the capacitor without the material deposited and the capacitor with light. There is also an increase of the losses when the CdS-polymer mix is deposited. We assume from this result that the material is a little bit lossy and that those losses increase when the material is illuminated. This means that the loss tangent ($\tan\delta$) is not zero for the material under dark condition and that its value will be higher when the material is illuminated.

When we look at the phase, Fig. 2.19(b), we observe that there is a change when the material is deposited on the capacitor but it stays the same when that material is under dark condition or illuminated. From here, we can conclude that once the material is deposited, the relative permittivity will remain the same when the material is illuminated or when it is not.

The results up to $5GHz$ show an expected result of a capacitor. However, at frequencies over $5GHz$, due to uncertainties with the mounted SMA connector where the transition between the connector mounted for measuring purposes and the coplanar lines is really abrupt making some unexpected resonances appear. These resonances make it impossible to characterize our materials over $5GHz$.

All these results will be broadly studied in the next section and the behavior of the capacitor will be explained giving specific values of capacitance and its changes.

b)Lumped elements model: Following the method described in section 2.2.2.2, the next step is to model the plain interdigitated capacitor using lumped components. When developing this model, we observed that the influence of the connector was quite important and that a model for the connector was necessary. At the same time, in order to decompose the structure as much as possible, the feed line was simulated as a separate part. In Fig. 2.20 we can see the three different parts of the lumped components model.

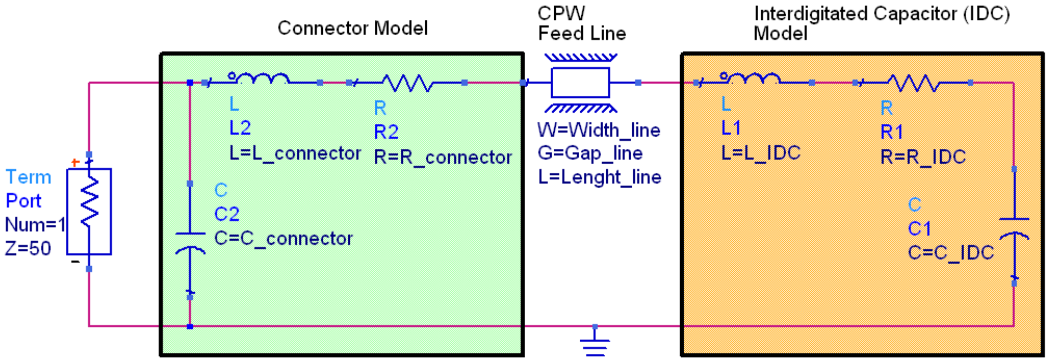

Figure 2.20: Lumped components model of the interdigitated capacitor.

The global model has been optimized so the simulation matches closest with the measured results. The values for the model are in Table 2.5

The lumped component model simulation results are compared to the measured results in Fig. 2.21.

It is observed that the results compared in Fig. 2.21 match well up to $5GHz$ but those results differ at frequencies higher than that. This is due to the SMA

Section	**Parameter**	**Value** (Blank IDC)
Connector	R_connector	0.12Ω
	L_connector	$0.8nH$
	C_connector	$0.3pF$
Feed Line	Width_line	$1.9mm$
	Gap_line	$0.39mm$
	Length_line	$13.2mm$
Intedigitated Capacitor	R_IDC	1.7Ω
	L_IDC	$1.2nH$
	C_IDC	$1pF$

Table 2.5: Values of the lumped components model for the blank interdigitated capacitor.

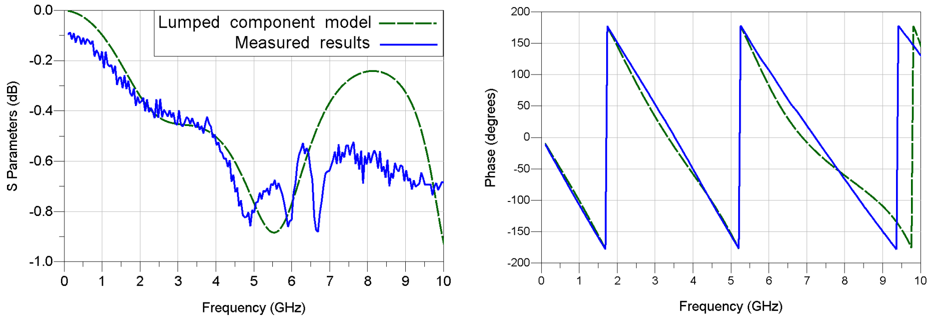

(a) Magnitude of S_{11} in dB.

(b) Phase of S_{11} in degrees.

Figure 2.21: Comparison of the S_{11} parameters of the blank capacitor up to $10GHz$

connector. The lumped component model of the connector works fine up to $5GHz$ but at higher frequencies the model would be much more complicated. The aim of this work is to have a quick estimate of the properties of the material so modeling the connector more accurately was not a priority. From now on all the results will be presented up to $5GHz$ at this will validate our characterization structure and method.

c)EM model: Once the lumped component model has been developed, and in order to extract in a later iteration of the method the values of the material properties, the design of the interdigitated capacitor has been drawn and simulated on HFSS. The 3D structure designed has been shown already in Fig. 2.9(a) but in this case the material on top of the fingers of the capacitor has not been simulated as we are working with the blank capacitor for now. To be as close as possible to the fabricated device, we have taken the measurements done under the microscope to size the structure.

In the 3D structure simulated on Ansoft HFSS, only the feed line and the interdigitated capacitor have been designed. It would have been a good idea to draw the connector in Ansoft HFSS in order to simulate the whole structure electromagnetically. However, this was not possible because all the uncertainties related to the connector. The connector was mounted on the edge of the glass using silver epoxy and it was not possible to take into account the volume of silver epoxy, where the connections were exactly made or the air gaps that there were to develop an accurate and reliable structure on Ansoft HFSS. This implies that the results from HFSS need to be combined with the lumped component model of the connector.

The S parameters of the feed line and the interdigitated capacitor retrieved from Ansoft HFSS are then associated to the connector circuit model with ADS. The global result is then compared to the measured S parameters.

Fig. 2.22 shows the ADS circuit that permits the association of the connector lumped elements model and the capacitor Ansoft HFSS model. Note that the values of the connector remain the same, as the connector has not changed and the HFSS model will replace only the feed line and the lumped component model of the interdigitated capacitor.

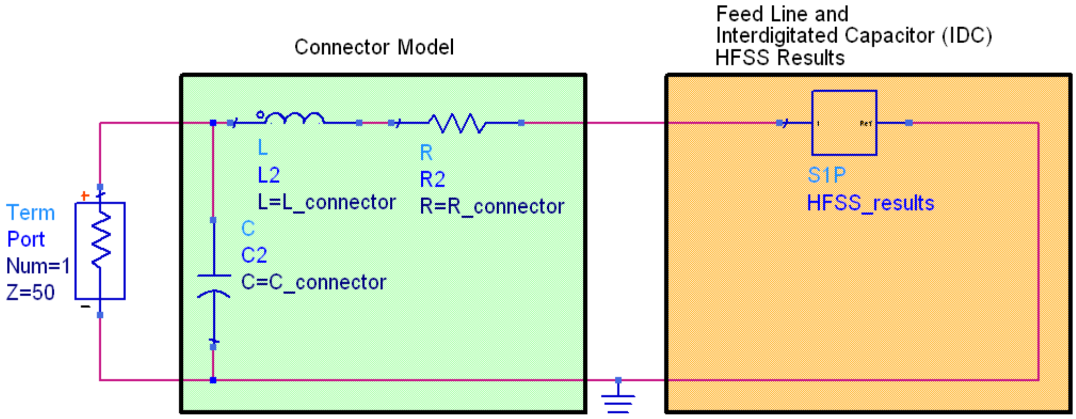

Figure 2.22: Lumped components model for the connector and EM simulations of the feed line and IDC.

A comparison of the three obtained results: lumped component model, Ansoft HFSS model and measured results is shown in Fig. 2.23.

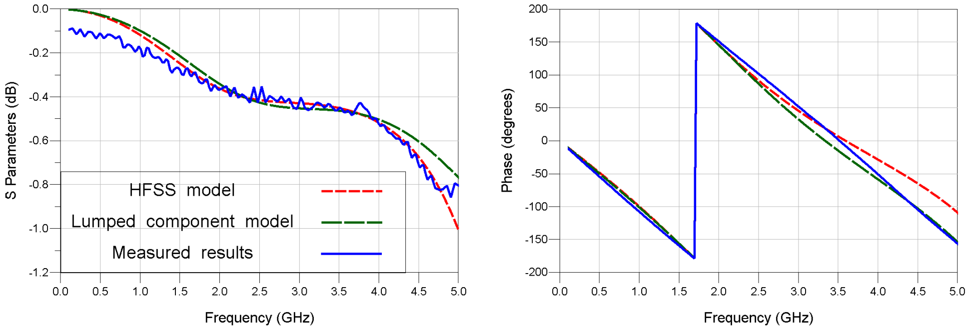

(a) Magnitude of S_{11} in dB.

(b) Phase of S_{11} in degrees.

Figure 2.23: Comparison of the S_{11} parameters of the blank capacitor up to $5GHz$

Although there is a slight difference between the three results, we consider that both the lumped component model and the 3D structure are well enough defined to get an estimation of the material properties on the following steps of the method.

d)Material characterization: For this step, simulation are performed with Ansoft HFSS using different values for the material permittivity and loss tangent. The S parameters retrieved from each simulation are then associated to the lumped element model of the connector on ADS and the whole model is compared to the measured S parameters.

The values of the relative permittivity and the loss tangent are then swept in a way that the simulation matches the measured results. The values founded are shown in table 2.6.

Property	**Value**
Electric permittivity (ε_r)	4
Loss tangent ($\tan\delta$)	0.04

Table 2.6: Extracted values for the material under dark condition

The ADS full lumped component circuit (connector, feed line and interdigitated capacitor) is also tuned to match the measured S parameters. As expected, only the values of R, L and C parameters of the capacitor show some changes as compared to the values retrieved from the blank capacitor. More particularly, the associated resistance changes from 1.7 to 1.8Ω proving that the material without illumination is indeed lossy. These values can be seen in table 2.7.

Section	**Parameter**	**Value** (Blank IDC)	**Value** (Dark material)
Connector	R_connector	0.12Ω	0.12Ω
	L_connector	$0.8nH$	$0.8nH$
	C_connector	$0.3pF$	$0.3pF$
Feed Line	Width_line	$1.9mm$	$1.9mm$
	Gap_line	$0.39mm$	$0.39mm$
	Length_line	$13.2mm$	$13.2mm$
Intedigitated Capacitor	R_IDC	1.7Ω	1.8Ω
	L_IDC	$1.2nH$	$1.1nH$
	C_IDC	$1pF$	$1.3pF$

Table 2.7: Values of the lumped components model for the interdigitated capacitor with the material deposited under dark condition.

The simulated results of the lumped components model and the HFSS model compared to the measured results are shown in 2.24.

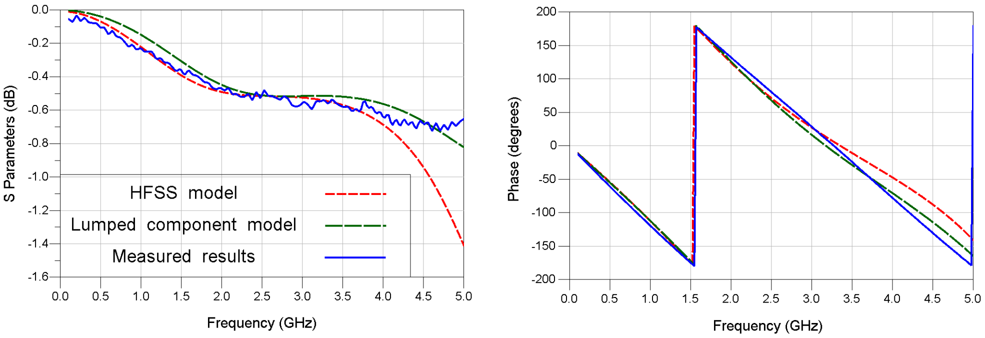

(a) Magnitude of S_{11} in dB.

(b) Phase of S_{11} in degrees.

Figure 2.24: Comparison of the S_{11} parameters of the capacitor with material deposited under dark condition

Comparing the three curves, a slight difference appear again at the higher frequencies due to the effect of the connector as has been mentioned already. However, the values presented in table 2.6 are considered correct as the matching between the results is good enough.

The last part of the method is to extract the material properties of the illuminated material from the 3D structure simulation. Following the same method, the calculated values on Ansoft HFSS for the material under illumination after matching of the simulations and the measured S parameters are shown in table 2.8.

Property	**Value (Dark)**	**Value (Light)**
Electric permittivity (ε_r)	4	4
Loss tangent ($\tan\delta$)	0.04	0.11

Table 2.8: Extracted values for the material under dark and light condition

As in the previous iteration, the ADS lumped component model used is the same. The connector and the feed line model are kept the same when the structure is under the effect of an optical source.

The values for the lumped component model of the interdigitated capacitor with the material deposited on top of it and illuminated are shown in table 2.9.

Section	**Parameter**	**Value** (Blank IDC)	**Value** (Dark material)	**Value** (Light material)
Connector	R_connector	0.12Ω	0.12Ω	0.12Ω
	L_connector	$0.8nH$	$0.8nH$	$0.8nH$
	C_connector	$0.3pF$	$0.3pF$	$0.3pF$
Feed Line	Width_line	$1.9mm$	$1.9mm$	$1.9mm$
	Gap_line	$0.39mm$	$0.39mm$	$0.39mm$
	Length_line	$13.2mm$	$13.2mm$	$13.2mm$
Intedigitated Capacitor	R_IDC	1.7Ω	1.8Ω	2.9Ω
	L_IDC	$1.2nH$	$1.1nH$	$1.1nH$
	C_IDC	$1pF$	$1.3pF$	$1.3pF$

Table 2.9: Values of the lumped components model for the interdigitated capacitor with the material deposited under illumination.

Once again, the lumped component model agrees with the extracted properties of the material. The only value that changes between the circuit model with the material under dark condition and the one under illumination is the resistor associated to the interdigitated capacitor, corresponding to an increase in the loss tangent.

A comparison of the measured, lumped component model simulation and the 3D structure simulation results is available in Fig. 2.25

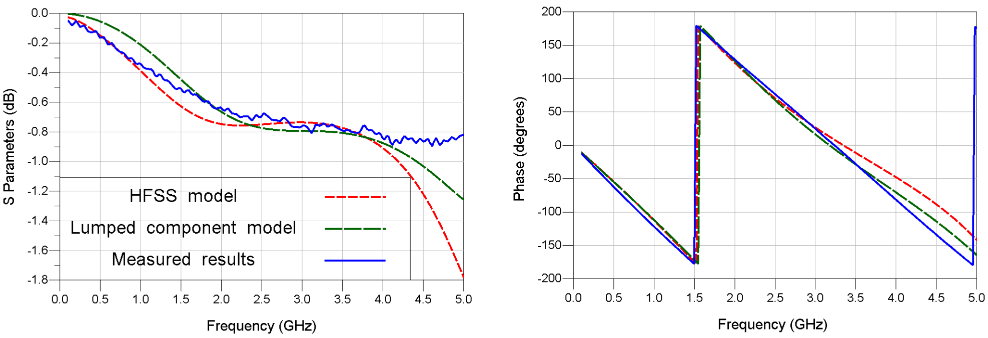

(a) Magnitude of S_{11} in dB. (b) Phase of S_{11} in degrees.

Figure 2.25: Comparison of the S_{11} parameters of the capacitor with material deposited under dark condition

As in the previous results, only a slight difference is observed between the simulated and the measured results at the higher frequencies so the calculated material properties values are considered correct.

We can see that our model shows no changes of the permittivity when the material is illuminated or not. The loss tangent however goes from 0.04 to 0.11 when the material goes from the dark to the lighted state. We can note that we are close to the values of table 2.4, validating the characterization technique with an interdigitated capacitor.

However, due to fabrication difficulties, material deposition uncertainties and the inclusion of the connector, the characterization is not optimal. That is most likely why the change on the relative permittivity was not observed with our interdigitated capacitor. The fabricated device did not show the resonance of the interdigitated capacitor making the structure less sensitive to a change on the real part of the permittivity of the material.

The deposition method is not accurate enough to allow knowledge of the exact surface of deposition or its thickness making impossible an accurate characterization of the materials. Anyways, this method gives a good estimation of the material properties at microwave frequencies which is a first step to consider if such photorefractive materials are interesting for further study.

For a future use of this structure it would be desirable to be able to isolate the effects of the SMA connector by using a GSG probe station so a study of a wider band could be carried out and the effects observed would be related only with the test structure itself.

In the material side, as it has been already mentioned, a lower volume fill fraction of the CdS particles would most likely provide the same change on the relative permittivity while lowering the loss tangent which would result in a better material for microwave applications.

2.3.2 Nano-crystalline Silicon ($nc - Si$)

Silicon (Si) is well known in the electronics industry as it is the principal component of most semiconductor devices, most importantly integrated circuits or microchips. Silicon is widely used in semiconductors because it remains in its semiconductor state at higher temperatures and because its native oxide is easily grown in a furnace and forms a good semiconductor/dielectric interface.

Silicon has an indirect bandgap of $1.1eV$ corresponding to an infrared wavelength of $1.1\mu m$, which creates a problem with silicon: being sensitive to light, which is normally an unwanted property for electronic designers. However, this property can be exploited to create photosensitive materials.

It is known that the dielectric material properties of silicon can be changed by means of an appropriate optical source. Incident optical energy with the appropriate wavelength and intensity can be made to induce a plasma in the semiconductor material. A large amount of work has been carried out exciting silicon plasma regions [15]. A microstrip filter was developed by Murata *et Al.* [16] containing a silicon light-induced plasma region as it can be seen in Fig. 2.27.

The results of this paper indicate that the center frequency of pass band is shifted from $5.49GHz$ to $6.25GHz$.On the other hand, the insertion loss increases from $2.45dB$ to $4.70dB$ when illuminated by light. This results are shown in Fig. 2.27(b).

The biggest problem when using these plasma regions is that the insertion losses increase by light illumination. The filter proposed in [16] has the benefit that the deterioration of the insertion loss can be suppressed by setting the plasma region

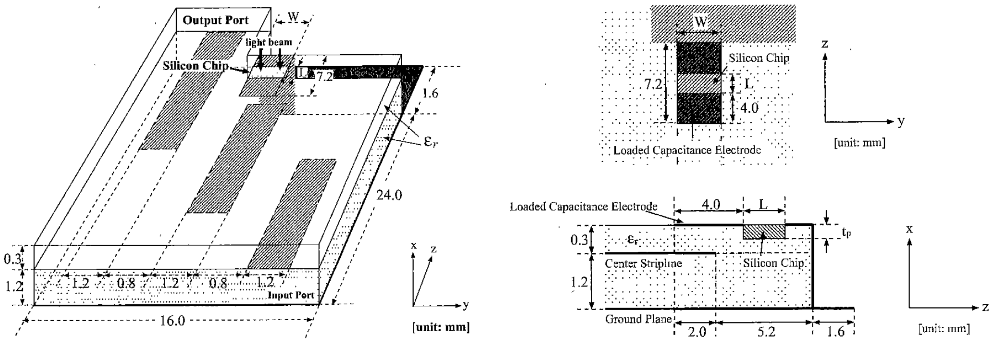

(a) Whole structure.

(b) Close view of the loaded capacitance.

Figure 2.26: Microstrip filter with a loaded capacitance containing a light-induced plasma region [16]

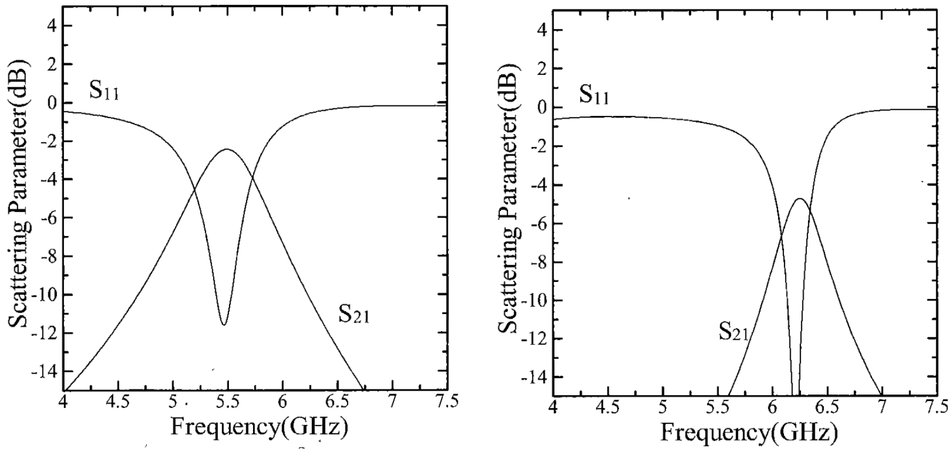

(a) OFF State.

(b) ON State.

Figure 2.27: Simulated S parameters [16]

apart from the area where the electromagnetic fields concentrate reducing the losses from $3.7dB$ to $1.69dB$ by reducing the length of the light-induced plasma region from $L = 0.8mm$ to $L = 0.4mm$ but always maintaining the frequency shift. The simulation results of this improvement are shown in Fig. 2.28.

The silicon material, and more precisely its electromagnetic transmission and reflection properties, can be made to vary from low loss on transmission to high loss on transmission. Using this effect, [17] demonstrate a wafer-scale all-silicon array that can be made to absorb or reflect an incident polarized signal. The antenna consists on a printed dipole array whose load terminals are matched to the input impedance

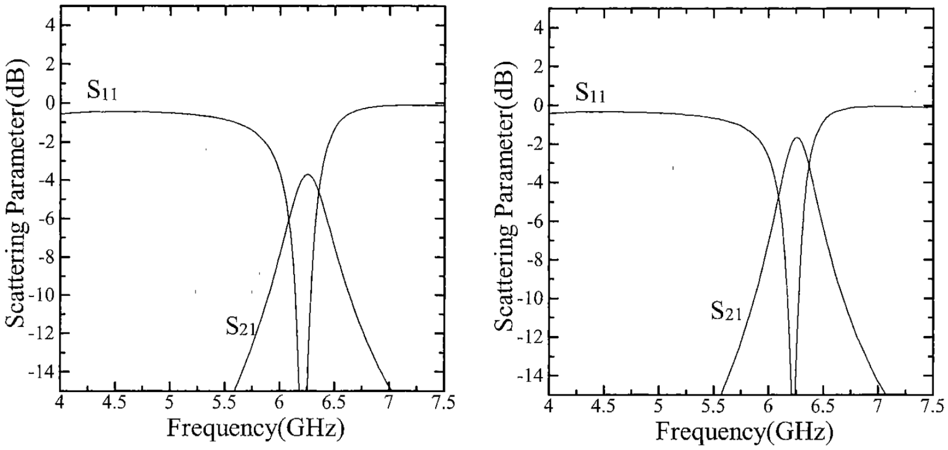

(a) Length of the plasma region $L = 0.8mm$ (b) Length of the plasma region $L = 0.4mm$.

Figure 2.28: Simulated S parameters for the improved filter [16]

of the dipole and a sheet of unprocessed high-resistivity silicon as a superstrate with respect to the dipole array. Optically induced plasma in this superstrate changes its transmission/reflection properties to such an extent that the overall assembly can be made to perform the function of a spatial microwave absorber or reflector. In the light on state, the superstrate reflects incident electromagnetic energy, while in the dark, the superstrate is considerably more transparent and the electromagnetic energy transmitted through it is absorbed by the matched dipole array.

The interest of our work was not on using a plasma state of the silicon but on using silicon nano-particles in a polymer material to create a photoconductive material. Contrary to bulk silicon, silicon nano-particles exhibit behaviour of direct bandgap materials. This makes it very sensitive to light with good rejection ratio. The bandgap, electron and hole mobility in nano-crystalline silicon can be varied by varying the nano-particle sizes. Recent research has shown that reducing the size of a silicon crystal to a few tens of atoms ($\sim 1nm$) effectively creates a "direct" wide-bandgap material [18] [19]. Light couples to the particles efficiently to produce electron-hole pairs. Contrary to bulk silicon, the electron hole pairs do not appreciably recombine via non-radiative processes, allowing charge separation and collection.

In order to exploit the properties of the silicon nano-particles, these particles were in a first iteration mixed with 3571 dielectric polymer from DuPont. The silicon nano-particles were mixed with the polymer by combining them and stirring it with a glass stir stick. After that, they were spread by hand and applied onto the glass coverslips. The measurements of this first iteration did not show any measurable changes with the light.

In a second iteration the polymer was replaced with an epoxy but again no measurable changes were appreciated. Finally, and knowing that the bandgap can be modified changing the particle sizes, these two host materials were tried with micro-particles instead of nano-particles and no significant changes were seen again.

The lack of good results is most likely due to extremely low minority carrier lifetimes. From the literature, this material is expected to be a good photoconductive material and that is why it was analyzed. Further studied need to be carried out doping the particles or putting the particles through some types of excitation such as firing or annealing.

2.3.3 Zinc Oxide (ZnO)

2.3.3.1 Theory

The third material considered for this work is also a photoconductive material. Zinc Oxide (ZnO) is a piezoelectric, optoelectronic and n-type semiconductor. Main properties of this inorganic compound are good transparency, high electron mobility, wide bandgap or strong room- temperature luminescence among others. ZnO has also the advantage that it is nontoxic and stable under normal environmental conditions as well as having a low growth temperature and higher radiation hardness, which are suitable for fabrication of long-lifetime devices.

Zinc oxide films can be deposited by different methods such as evaporation, pyrolysis, chemical vapor deposition (CVD), sputtering, laser ablation technique, spin-coating, etc.

ZnO-based materials have attracted much attention due to its wide bandgap of $3.37eV at 300K$ and also to its large exciton binding energy of $\sim 60meV$. Zinc oxide has potential application for transparent thin film transistors, surface acoustic wave

(SAW) devices, light emitting devices, lasing diodes and especially photoconductive sensors [20], photoconductive switches [21] and ultraviolet (UV) detectors [22]. Work presented by Liu *et al.* on [22] shows a good example of an ultraviolet photoconductive detector based on ZnO thin film. The main problem using this semiconductor is its photoresponse time typically equal or above $0.1\mu s$. However, in this first step of the research we are interested mainly in the state change rather than in parameters as the speed so the zinc oxide is potentially a good candidate as its state change seem to be very important. As an example, Fig. 2.29 shows the results of the UV detector from [22].

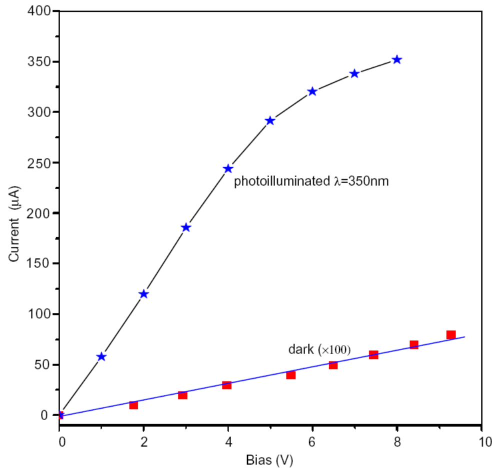

Figure 2.29: $I-V$ curve of a UV photodetector for dark current and photocurrent ($350nm 1\mu W$ light illumination) [22].

ZnO is normally used doped with other materials such as gallium (Ga) [23], magnesium (Mg) [24] or aluminum (Al) [25]. Nevertheless, even if the bandgap can be augmented with the doping, we used a non-doped ZnO in this work at this early stage.

The aim was to deposit the material in the coplanar lines explained in section 2.2.1 and among all the deposition methods available for this material, the one used was the chemical spray pyrolysis (CSP). This task was carried out by Dr. Johann Bouclé who is an associate professor at the University of Limoges.

Spray pyrolysis method is well-known for its simplicity and possibility to produce cheap large area films. The source compound used for this setup was zinc acetate.

ZnO films were deposited onto heated substrates by spraying zinc acetate diluted in methanol. The resulting solution was sprayed onto heated substrates held at a constant temperature of $400°C$. Nitrogen (N) was used as the carrier gas.

All deposition parameters have an important influence on the physical properties of the films. However, the substrate temperature is the most important one. The schematic arrangement of spray pyrolysis set-up is shown in Fig. 2.30

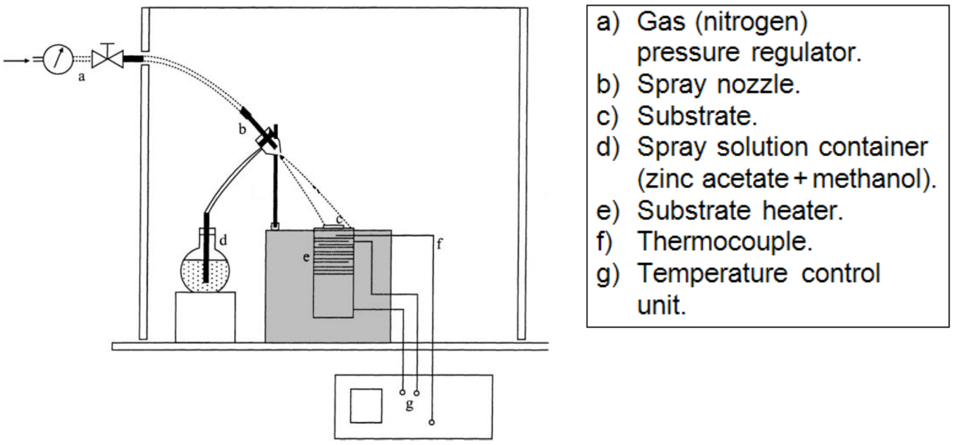

a) Gas (nitrogen) pressure regulator.
b) Spray nozzle.
c) Substrate.
d) Spray solution container (zinc acetate + methanol).
e) Substrate heater.
f) Thermocouple.
g) Temperature control unit.

(a) Schematic arrangement (b) Parts of the schematic.

Figure 2.30: Spray pyrolysis method setup [26]

The solution made with the zinc acetate and the methanol is in the spray solution container (d) and with the help of the gas, nitrogen in this case, it will be sprayed via the spray nozzle (b) on top of the heated substrate (c). The substrate is heated with the substrate heater (e) and its temperature is measured with the thermocouple (f) and controlled using the temperature control unit (g). When the solution is in contact with the air, a chemical reaction happens and the ZnO appears. This method of deposition offers the best properties but it is normally used for large surfaces.

For our coplanar lines test structures a small surface needed to be covered with the ZnO material so in order to solve this problem, the lines were covered with a brass mask with a $1mm$ hole for depositing the material. This could be done in the simple lines but it is not accurate enough for the CPW lines with a gap in the center conductor.

However, for these latter lines, the material was deposited by drop casting using a micro-syringe. The solution was deposited using the micro-syringe right in the spot where the material need to be deposited and the substrate was heated afterwards in order to decompose the precursor reagents making the ZnO appear. This drop casting with a micro-syringe method is more accurate in terms of surface covered but the properties of the zinc oxide in this case are not as good. Also the heating makes the solution spread a little bit.

For both deposition methods the particles sizes were between 20 and $50nm$ and the thickness of the material deposited is $1\mu m$.

A four point probe resistivity measurement was used at the *Xlim laboratory* at low frequency and showed that the ZnO which can be deposited by this method has a conductivity of $\sigma = 0.36 \times 10^{-3} S/m$ in the dark and this conductivity increases to $\sigma = 2.2 \times 10^{-2} S/m$ when the material is illuminated. The material was illuminated using a UV hand lamp.

That change and especially those values are too low for our applications. Short tests were run however to see if the coplanar lines structures are sensitive enough for detecting the change in conductivity between the dark/illuminated states of the material.

2.3.3.2 Experimental results

The structure used for characterizing the ZnO material is the one explained in section 2.2.1 whose 3D view can be observerd in Fig. 2.31.

Fig. 2.32 shows the reflection and the transmission coefficient of the measured simple coplanar line compared to the line with the material on top. These images show a slight change on both coefficients which would imply a very low conductivity.

The measurements with the material on top of the structures did not show any change under the influence of the light due to the slow change on conductivity expected so the results named “material line” correspond to both the illuminated and dark states as the results happened to be the same under the influence of the broadband light applied.

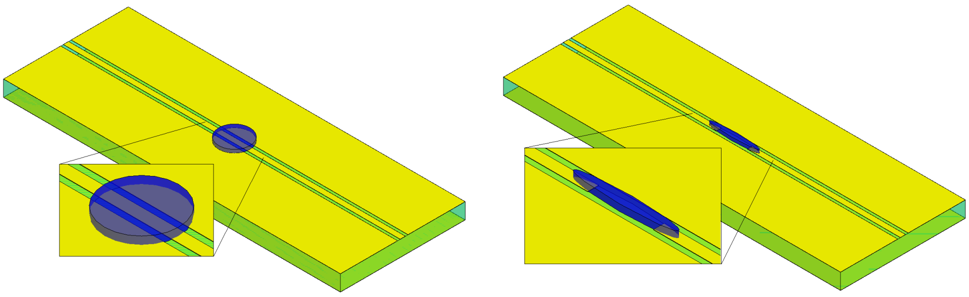

(a) Coplanar line without gap and the material deposited.

(b) Coplanar line with the gap and the material deposited.

Figure 2.31: HFSS 3D structures of the coplanar lines.

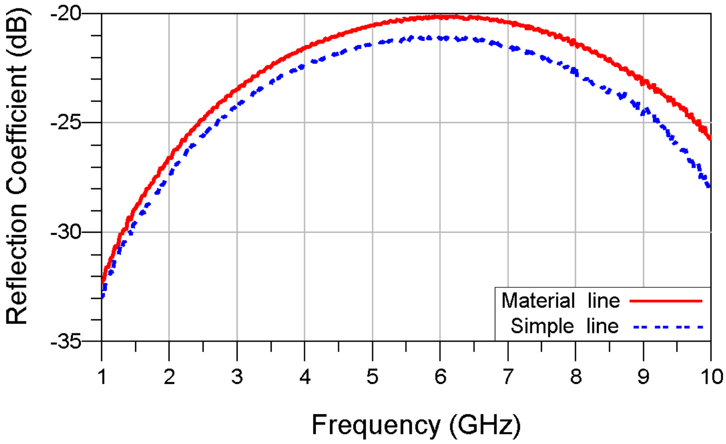

(a) Reflection coefficient (S_{11}).

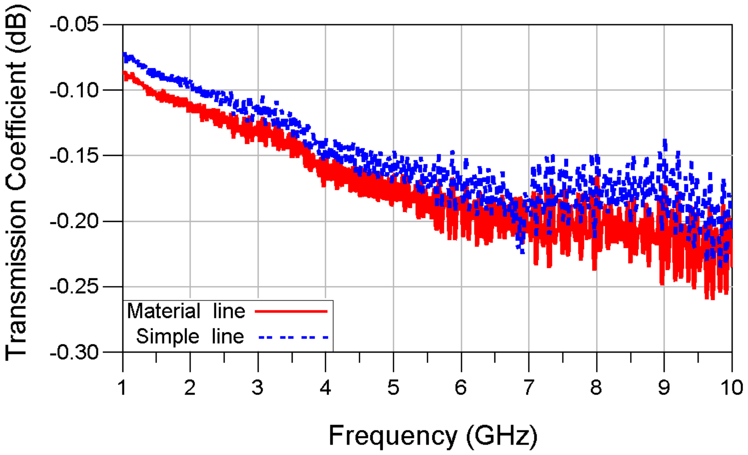

(b) Transmission coefficient (S_{21}).

Figure 2.32: Measured results of the simple coplanar line.

We observe that due to the low conductivity of the ZnO the difference of the S parameters between the line with the material and the one without it is really weak but it is in accord with the simulations and the transmission decreases when a material with a very low conductivity is deposited on the line. Same thing happens when we compare the coplanar line with a gap in the center conductor in absence of material and with the material deposited as in Fig. 2.33.

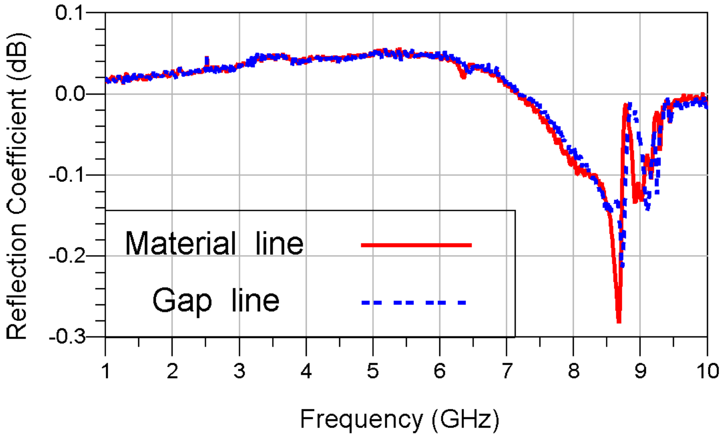

(a) Reflection coefficient (S_{11}).

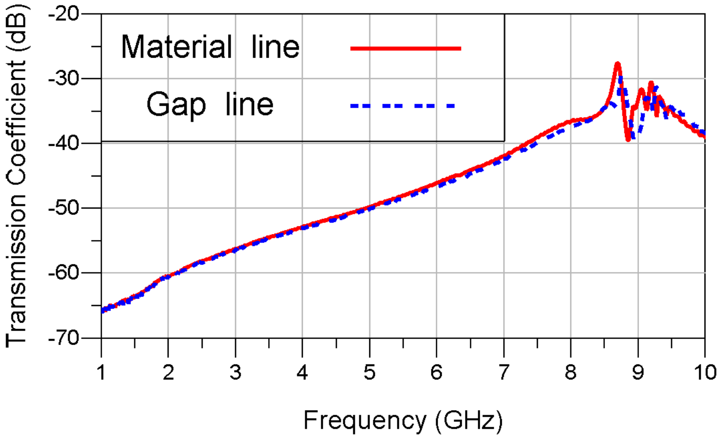

(b) Transmission coefficient (S_{21}).

Figure 2.33: Measured results of the coplanar line with a gap in the center conductor.

Almost no difference can be observed in these results as the conductivity of the material is so low, however a slight increase on the transmission parameter is present in Fig. 2.33(b) which agrees with the simulations that have been made before.

Unfortunately, the illumination did not cause any change in the response of the coplanar lines. Several reasons can explain this situation: first of all, the conductivity is too low in any case, and it is widely known that for most materials the conductivity decreases as the frequency increases so the structures developed cannot measure a conductivity that small.

The second reason is related to the light used for exciting the material. As it has been explained, the ZnO reacts under UV light so a light source with power at $385nm$ would be needed. We have used a broadband light which means that our current light source cannot generate any charge carriers, and therefore conductivity change, because it has not enough optical power at that wavelength.

As a conclusion of this coplanar lines structure, it has been seen that an estimation of the conductivity would be possible as the lines are sensitive enough and show a change in their response when the material is deposited as well as when it is illuminated. Nevertheless, as the material we tested in this structure had such a low conductivity and no change under optical illumination, we did not do the whole characterization process.

We conclude for the ZnO that it seems a possible material to use in microwave tunable circuits from the information read in the literature but further study need to be done with the appropriate light sources working at UV wavelengths.

2.3.4 Vanadium Dioxide (VO_2)

The last material explored was also a material where a change on the conductivity was expected. Despite the fact the aim of this thesis is to develop an optically tunable device, this material is sensitive to the temperature or “thermosensitive”. A good result with this material would open a research direction of heating the material with a light source, matching perfectly with the topic of study.

Vanadium Dioxide (VO_2) presents the particularity of transiting between an isolating state to a metallic one. This transition is accompanied by an important modification of its electrical and optical properties. The electric resistivity of the VO_2 decreases some orders of magnitude which means that the conductivity increases the same amount and also the reflectivity increases especially in the infrared domain.

There are several methods for the deposition of the vanadium dioxide, the one used at *SPCTS (Science de Procédés Céramiques et de Traitements de surface)* by Prof. Corinne Champeaux is laser ablation. This technique permits obtaining great quality films presenting very interesting electric properties, with very big changes on the resistivity between the semiconductor and the metallic states [27, 28]. This type of technique allows the deposition over big surfaces ($\sim 10cm$ of diameter) and permits also creating multilayer films.

Laser ablation is the process of removing material from a solid surface by irradiating it with a laser beam. It is a process based on the interaction between radiation and material. At low laser flux, the material is heated by the absorbed laser energy and evaporates or sublimates. At high laser flux, the material is typically converted to a plasma. Usually, laser ablation refers to removing material with a pulsed laser, but it is possible to ablate material with a continuous wave laser beam if the laser intensity is high enough.

The technique used in this work for deposition is Pulsed Laser Deposition (PLD), a type of laser ablation that presents several advantages compared to other deposition techniques especially for thin films fabrication.

The principle of this technique consists on focusing a laser beam over a target of the material that has to be deposited and to place a heated substrate in front of the laser impact as in Fig. 2.34. With the beam contact, the target will be evaporated creating a material cloud that will be settled on the face-to-face substrate.

The high instantaneous power from the laser creates a mixed plasma that is ejected perpendicularly to the target, which is face to face with the substrate. The ejected material is collected on the substrate creating a thin film. The whole system is in a vacuum chamber in order to avoid deposition contamination. The heating of the substrate is made with an halogen lamp and the temperature is kept between 500 and $700°C$.

The VO_2 material has only been deposited on sapphire because the properties of this substrate, more precisely its crystalline orientation, are optimal for accommodating the material. The thickness of the material is below $500nm$ and typically

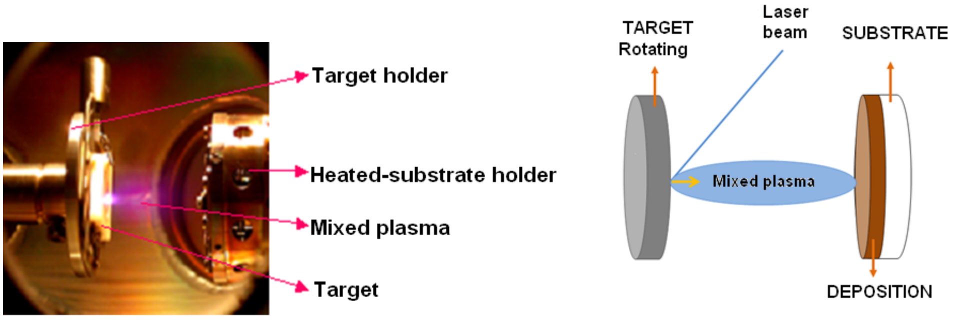

(a) General diagram. (b) Mixed plasma creation.

Figure 2.34: Laser ablation technique [29].

at about 250nm [30].

Some characterizations of this material has been carried out at *Xlim* at low frequency, normally at DC [30]. We are mostly interested in the conductivity but the measurements done, most of the time give information about resistivity, which is just the inverse of the conductivity as in eq. 2.15.

$$\rho = \frac{1}{\sigma}. \tag{2.15}$$

A lot of different optimizations were made with these thin films of VO_2 and the best resistivity they could get was $\rho = 1.09 \times 10^{-2}\Omega \cdot m$ at ambient temperature, $20°C$ and of $\rho = 2.17 \times 10^{-6}\Omega \cdot m$ at $90°C$ [30]. This values correspond to a conductivity of $\sigma = 9.17 \times 10^{1} S/m$ and $\sigma = 4.61 \times 10^{5} S/m$ respectively.

These results are really promising and a tunable filter can be developed if these results could be exploited. Fig. 2.35 shows the resistance change with the temperature for one of the samples studied in [30].

As it has been seen, this material has potential for creating a tunable microwave device. However, lots of unknown parameters need still to be studied. First of all, the conductivity/resistivity measurements only have been done on DC and it is known that the materials behave differently at microwave frequencies so we can already suppose that this material will not perform as well in a microwave device [31].

Nevertheless, this is not the main problem with the VO_2, the thickness control

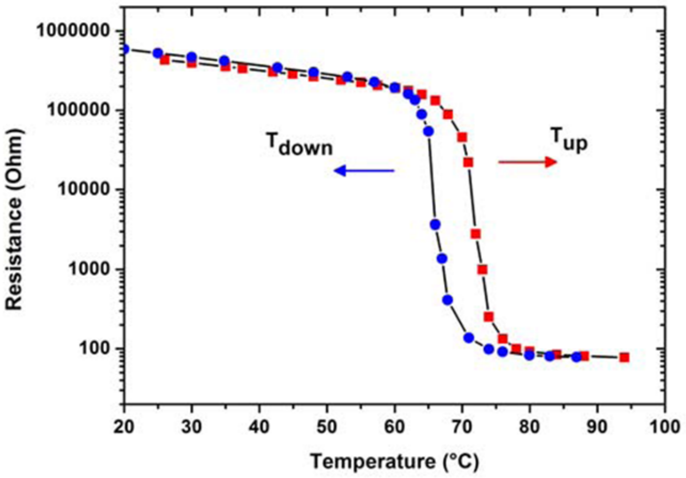

Figure 2.35: Resistivity *vs* temperature for a VO_2 film [30].

will be crucial for developing a good quality microwave device. Having such a thin material deposited, not even a few skin depths, a big part of the electromagnetic waves will pass through and the devices will not behave properly. This will be tedious for simulations as well because of the mixing of really thin films and bigger structures. This will be explained in more depth in Chapter 3.

Anyways, with further study of the properties and with a better mastering of the deposition to create thicker films, this material shows really good performances for developing thermosensitive and even photosensitive microwave devices.

2.4 Conclusion

This chapter has focused on several new materials that could be used for optically tunable circuits. In order to know if a material is suitable for photosensitive microwave applications, the materials need to be characterized prior to their use.

The first part of the chapter explained the properties of a material we are interested in. The second part of the chapter was dedicated to the explanation of the test structures for characterizing materials at microwave frequencies. The final part of the chapter was about the materials themselves and some experimental results.

The test structures presented showed that they would work fine for characterizing the materials at microwave frequencies and for extracting the properties we are interested on as far as the conductivity of the tested photoconductive material remains higher than $10^1 S/m$.

The materials discussed in the last part of the chapter seem to be useful for their application in optically sensitive microwave devices. In particular, the CdS-polymer material displayed a 13% change of relative permittivity with optical illumination. However, this was accompanied by an increase in loss tangent from 0.05 to 0.12.

In fact, all of the materials presented need a lot of improvement, but they still show some potential interest for microwave devices. In the case of VO_2, this material exhibits a very significant change of DC conductivity through temperature change (which could be induced optically) and therefore VO_2 appears as a good candidate for microwave devices and will be investigated further in section 3.2 in next chapter 3.

Bibliography

[1] D. Pozar, *Microwave engineering.* Hoboken NJ: J. Wiley, 3rd ed., 2005. 64, 65

[2] K. Kao, *Dielectric phenomena in solids : with emphasis on physical concepts of electronic processes.* Amsterdam: Elsevier Academic Press, 2004. 65

[3] B. Boehme, M. Roellig, and K. J. Wolter, "Material characterization of organic packaging materials to increase the accuracy of FEM based stress analysis," *2nd Electronics System-Integration Technology Conference ESTC.* 67

[4] A. L. Franc, E. Pistono, and P. Ferrari, "Conception optimisée de lignes à ondes lentes pour la mesure de couches diélectriques minces de la RF au millimétrique," *17ièmes Journées Nationales Micro-ondes*, May 2011. 68

[5] L. Chen, *Microwave electronics measurement and materials characterization.* Chichester Hoboken, NJ: J. Wiley, 2004. 68

[6] J. Krupka, "Frequency domain complex permittivity measurements at microwave frequencies," *Measurement Science and Technology*, vol. 17, pp. R55–R70, June 2006. 68

[7] J. Sheen, "Comparisons of microwave dielectric property measurements by transmission/reflection techniques and resonance techniques," *Measurement Science and Technology*, vol. 20, p. 042001, Apr. 2009. 68

[8] W. Platte and B. Sauerer, "Optically CW-induced losses in semiconductor coplanar waveguides," *IEEE Transactions on Microwave Theory and Techniques*, vol. 37, pp. 139–149, Jan. 1989. 68

[9] S. J. Spiegel and A. Madjar, "Impact of light illumination and passivation layer on silicon finite-ground coplanar-waveguide transmission-line properties," *IEEE Transactions on Microwave Theory and Techniques*, vol. 48, pp. 1673–1679, Oct. 2000. 68

[10] C. Dalmay, A. Pothier, P. Blondy, F. Lalloue, and M. O. Jauberteau, "Label free biosensors for human cell characterization using radio and microwave frequencies," *IEEE MTT-S International Microwave Symposium Digest*, pp. 911–914, June 2008. 75

[11] C. Dalmay, A. Pothier, P. Blondy, M. Cheray, F. Lalloue, and M. O. Jauberteau, "RF biosensor based on microwave filter for biological cell characterisation," *European Microwave Conference EuMC*, pp. 041–044, Oct. 2009. 75

[12] T. Morolari, *Characterization of Optically Sensitive Polymer and Application to Microwave Antenna*. PhD thesis, Carleton University, Ottawa, 2009. 76, 77, 84

[13] N. Jess, *Development and Characterization of an Optically Tunable Dielectric Material*. PhD thesis, Carleton University, Ottawa, Canada, Sept. 2010. viii, 84, 85, 86, 87

[14] O. Madelung, *Semiconductors : data handbook*. Berlin: Springer, 3rd ed., 2004. 84

[15] A. M. Yurek, M. G. Li, C. D. Striffler, and C. H. Lee, "Modulation of millimeter-waves using diode laser illumination of a silicon waveguide," *International Journal of Infrared and Millimeter Waves*, vol. 5, pp. 1381–1388, Oct. 1984. 96

[16] M. Murata, T. Kitamura, and M. Geshiro, "Microstrip filters with a loaded capacitance containing a Light-Induced plasma region," *IEEJ Transactions on Electronics, Information and Systems*, vol. 123, pp. 397–400, 2003. viii, 96, 97, 98

[17] V. Fusco and B. Nair, "Wafer-scale silicon optically controlled absorber/reflector surface," *Microwave and Optical Technology Letters*, vol. 44, pp. 318–320, Feb. 2005. vii, 14, 97

[18] G. Allan, C. Delerue, and M. Lannoo, “Nature of luminescent surface states of semiconductor nanocrystallites,” *Physical Review Letters*, vol. 76, pp. 2961–2964, Apr. 1996. 98

[19] M. Nayfeh, N. Rigakis, and Z. Yamani, “Photoexcitation of Si-Si surface states in nanocrystallites,” *Physical Review B*, vol. 56, pp. 2079–2084, July 1997. 98

[20] S. Chang, S. Chang, Y. Chiou, C. Lu, T. Lin, Y. Lin, C. Kuo, and H. Chang, “ZnO photoconductive sensors epitaxially grown on sapphire substrates,” *Sensors and Actuators A: Physical*, vol. 140, pp. 60–64, Oct. 2007. 100

[21] B. Yuan, X. J. Zheng, Y. Q. Chen, B. Yang, and T. Zhang, “High photosensitivity and low dark current of photoconductive semiconductor switch based on ZnO single nanobelt,” *Solid-State Electronics*, vol. 55, pp. 49–53, Jan. 2011. 100

[22] K. Liu, J. Ma, J. Zhang, Y. Lu, D. Jiang, B. Li, D. Zhao, Z. Zhang, B. Yao, and D. Shen, “Ultraviolet photoconductive detector with high visible rejection and fast photoresponse based on ZnO thin film,” *Solid-State Electronics*, vol. 51, pp. 757–761, May 2007. viii, 100

[23] J. Sun, F. J. Liu, H. Q. Huang, J. W. Zhao, Z. F. Hu, X. Q. Zhang, and Y. S. Wang, “Fast response ultraviolet photoconductive detectors based on ga-doped ZnO films grown by radio-frequency magnetron sputtering,” *Applied Surface Science*, vol. 257, pp. 921–924, Nov. 2010. 100

[24] D. Y. Jiang, J. Y. Zhang, K. W. Liu, Y. M. Zhao, C. X. Cong, Y. M. Lu, B. Yao, Z. Z. Zhang, and D. Z. Shen, “A high-speed photoconductive UV detector based on an $Mg_{0.4}Zn_{0.6}O$ thin film,” *Semiconductor Science and Technology*, vol. 22, pp. 687–690, July 2007. 100

[25] Z. Xu, H. Deng, J. Xie, Y. Li, and X. Zu, “Ultraviolet photoconductive detector based on al doped ZnO films prepared by sol gel method,” *Applied Surface Science*, vol. 253, pp. 476–479, Nov. 2006. 100

[26] B. Joseph, “A study on the chemical spray deposition of zinc oxide thin films and their structural and electrical properties,” *Materials Chemistry and Physics*, vol. 58, pp. 71–77, Feb. 1999. viii, 101

[27] F. Dumas-Bouchiat, C. Champeaux, A. Catherinot, A. Crunteanu, and P. Blondy, “RF-microwave switches based on reversible semiconductor-metal transition of vo_2 thin films synthesized by pulsed-laser deposition,” *Applied Physics Letters*, vol. 91, p. 223505, 2007. 106

[28] M. Maaza, “Direct production of thermochromic VO_2 thin film coatings by pulsed laser ablation,” *Optical Materials*, vol. 15, pp. 41–45, Sept. 2000. 106

[29] R. Eason, *Pulsed laser depostion of thin films : applications-led growth of functional materials.* Hoboken NJ: J. Wiley, 2006. viii, 107

[30] M. C. Georgescu, *Elaboration de matériaux innovants appliqués à la conception de dispositifs hyperfréquences.* PhD thesis, University of Limoges, Limoges, Oct. 2010. viii, 107, 108

[31] D. Bouyge, A. Crunteanu, O. Massagué, J. C. Orlianges, C. Champeaux, A. Catherinot, A. Velez, J. Bonache, F. Martin, and P. Blondy, “Applications of vanadium dioxide (VO_2)-loaded electrically small resonators in the design of tunable filters,” *European Microwave Conference (EuMC)*, pp. 822–825, Sept. 2010. 107

Chapter 3

Direct Optical Control

Contents

As has been mentioned in Chapter 1 optical control is divided in two main categories: direct optical control and indirect optical control. In this chapter the work done with direct optical control will be presented.

In **direct optical control**, the optical signal is directly fed to the active regions of a microwave device thus changing its characteristics. In direct optical control there is then no conversion of the optical excitation in another type of signal: the optical tunability happens directly where the optical source is applied.

Three different applications exploiting direct optical control will be explained in this chapter. The first part will explain the concept of tunable microwave filter that can take advantage of photoconductive materials to change its response between two different states. Following this agile filter, a concept of a tunable 3D resonator will be given depending on the conductivity of a photosensitive material as well. Finally a tunable filter which changes its response based on a photorefractive material will be given.

3.1 LTCC photoconductive tunable filter

In order to exploit the photoconductivity of some of the materials explained in section 2.3, a tunable low temperature co-fired ceramic (LTCC) filter has been designed.

LTCC technology can be defined as a way to produce multilayer circuits with the help of single tapes, which are used to apply conductive, dielectric or resistive pastes on. LTCC devices are made by processing a number of layers independently and assembling them into a device as a final step. This methodology results in savings in terms of cost, time and it reduces the circuit dimensions because of the access to quasi 3D topologies. Another advantage of the LTCC technology is that as layers are processed independently, every single layer can be inspected and, in the case of inaccuracy or damage, replaced before firing preventing, in this way, the need of manufacturing a whole new circuit.

Low temperature co-fired ceramic (LTCC) devices are monolithic, ceramic microelectronic devices. In this context “co-fired ceramic” means that the ceramic support structure and any conductive, resistive, and dielectric materials are fired in a kiln at the same time, and “Low temperature” means that the sintering, temperature is less than $1000°C$. Because of the low firing temperature of about $850°C$ it is possible to use low resistivity materials such as copper, silver and gold [1]. LTCC devices include capacitors, inductors, resistors, transformers, and hybrid circuits. The LTCC process can also be used to make packages for ICs. This differs from semiconductor device fabrication where layers are processed serially; each new layer being fabricated on top of previous layers.

The integration for multiple components is not only made horizontally but also vertically opening the way to conceptions in three dimensions. This three dimensional conception is determinant on circuit miniaturization and permits a lot of flexibility on filter conception using multiple layers. All the components are placed in a compact way with the best possible interconnection. The future of LTCC is thus especially its use in SiP (System in Package) and in SoP (System on Package) devices.

This section will focus on two filters developed at *Xlim Laboratory* working at two different frequencies. The aim of this work was to check if these filters could be combined in only one filter and depending on the light applied, make it work at $8.8GHz$ when the filter is in its OFF state or light off, and at $6.2GHz$ when the filter is ON or illuminated. Although the filter was already designed when this Ph. D. started, a whole study to know if it could be used with a photoconductive material has been carried out and some improvements have been done for the light routing.

This section will then be divided in several parts. First of all, the theoretical principle of the resonator will be given, followed by some simulation to extract the properties of the material that would be needed. After that, a section will be devoted to the fabrication and measurement of initial prototypes. We will continue explaining an optimization for light routing as well as the measurements of these improved prototypes. The final part will focus on the future prospects of this filter and a conclusion about this idea.

3.1.1 Theoretical principle of a capacitively loaded resonator

Any resonator can be simplified as a lumped equivalent circuit by using inductors and capacitors, i.e. LC elements. For an LTCC resonator such as the one shown in Fig. 3.1, this equivalence is easily achieved by considering the via posts as inductors and the top plates as capacitors.

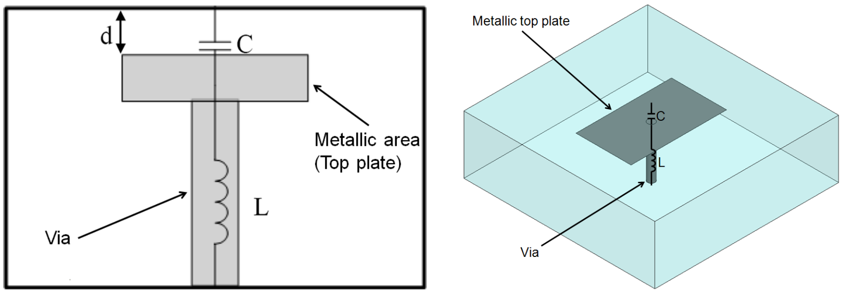

(a) Front view. (b) Top view.

Figure 3.1: Simplified resonator as a circuit.

The resonator used for this filter it is based in the resonator used by L. Rigeaudeau in [2]. As shown in Fig. 3.1, the resonator consists of a via and a top plate inside a cavity.

The resonance frequency is calculated with the classic formula:

$$f_r = \frac{1}{2\pi\sqrt{LC}}. \tag{3.1}$$

In [3], Ferrand *et al.* show the dependence of the operating frequency with the distance between the resonator and the height of the cavity where it is placed. That dependence exists also with the surface area of the resonator.

It is easily understood that the frequency depends on L and C values, and that these factors are directly linked to the via and plate dimensions of the LTCC resonator.

In order to explain the correspondence of the frequency with the resonator's geometry, it is only necessary to consider the characteristic equation of a capacitor:

$$C = \frac{\varepsilon \cdot A}{d}. \tag{3.2}$$

where d represents the distance from the sheet to the upper ground plane and A represents its surface.

The reconfigurability of this filter is then based on the principle of the LTCC resonator used in [3]. For this purpose, the possibility of changing the total surface area of the equivalent capacitor is accomplished with two additional metallized "wings" that can eventually be connected or disconnected in order to increase or decrease the resonator's operating frequency as shown in Fig. 3.2.

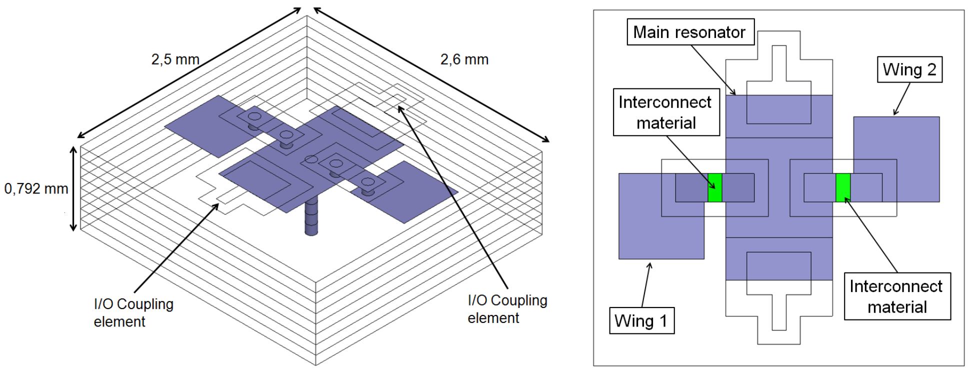

(a) 3D View.

(b) Top view.

Figure 3.2: LTCC filter with metallized "wings" added to the central resonator.

For the connection between the main resonator and the lateral "wings", some extra vias are used to reach the top layer of the structure. To facilitate circuit development, the wings are placed on the top of the modules as these metallizations, in the future, will be made of a photoconductive material instead of the metal employed for these first simulations. The size of the interconnect between the main resonator and the wings is very small, only $0.2mm$ by $0.1mm$, which might make the accurate material deposition difficult.

For simplicity and to understand the tunability, we can define the LTCC filter with the equivalent circuit presented in Fig. 3.3 where L makes the function of the via, C_res1 and C_res2 the function of the top plate of the main resonator and C_wing1 and C_wing2 would correspond to the lateral wings. Obviously, in the disconnected case, the capacitors associated with the wings would not exist.

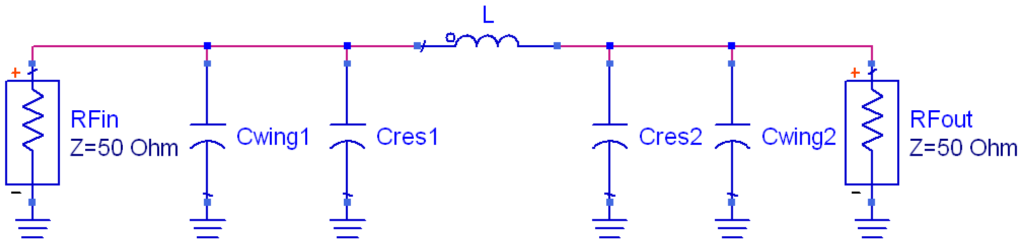

Figure 3.3: Equivalent circuit of the LTCC filter.

The tunability is achieved by increasing the total surface of the top plate. The surface of a plate of a capacitor is directly proportional to its capacitance value as stated in eq. 3.2. The capacitance is at the same time inversely proportional to the square of the resonant frequency as it has been shown in eq. 3.1. An increase in the total size of the capacitor surface with the connection of the additional wings will then produce a decrease in the resonant frequency of the filter. In Fig. 3.3 we have defined this connection as adding a capacitor in parallel.

In this study we wish to demonstrate a frequency tunable filter based on optical control. For this objective, we have used a filter already developed by L. Rigeaudeau in [2] where we have added the optical reconfigurability. The filter used would change frequency from $f_1 = 8.8GHz$ in its OFF operating state ($Z_{photoconductive\ material} = \infty$, light switched off, non conductive interconnect material) to a frequency $f_2 = 6.2GHz$ in its ON state ($Z_{photoconductive\ material} = 0$, light switched on, conductive interconnect material).

The wings have been designed to produce a Δf of $2.5GHz$ with the use of two square metallizations of $0.6mm$ per side. All metallized surfaces are $5\mu m$ thick. If a smaller Δf is desired, the total surface needs to be smaller too, so a reduction of the wings' size would result.

For instance, the Δf is calculated as $\Delta f = f_{r_1} - f_{r_2}$. From eq. 3.1 and eq. 3.2 we can calculate de change in frequency with the equation 3.3.

$$\Delta f = \frac{1}{2\pi\sqrt{L\frac{\varepsilon A_1}{d}}} - \frac{1}{2\pi\sqrt{L\frac{\varepsilon(A_1+A_2)}{d}}} = \cdots = f_{r_1}\left(1 - \frac{\sqrt{A_1}}{\sqrt{A_1+A_2}}\right). \tag{3.3}$$

Where A_1 correspond to the area of the resonator plate and A_2 corresponds to the area of the wings. From eq. 3.3 we see that a bigger area of the wings will result in a bigger shift in frequency.

3.1.2 Simulations

In this analysis section we wish to evaluate the required properties of the material that will form the connections between the wings and the main resonator.

To obtain these properties the simulations have been done in two stages. First, a perfect connection or disconnection between the main resonator and the wings is considered. For the perfect connection, we have use a perfect metal between the main resonator and the wings whereas in the disconnected case, no material was placed in the space for the interconnect. Afterwards, the electrical conductivity of the material linking the main resonator and the wings is changed from a very high value to a minimal value to determine which ranges of electrical conductivity are suitable for this application.

The initial optimization of this filter is done for operation at the higher frequency ($8.8GHz$) and its reconfigurability is based solely on the achievement of the lower operating frequency ($6.2GHz$) and not on other factors such as the external quality factor that affects the bandpass response.

In Fig. 3.4 the predicted change of $2.5GHz$ is observed. However, it is appreciated that operation at the $6.2GHz$ center frequency leads to insertion losses that are somewhat high for an LTCC filter, around $2.2dB$. These losses appear as a result of making the $8.8GHz$ filter response the priority but further filter optimization would be possible to moderate the $6.18GHz$ filter losses.

However the high losses on the transmission parameter of the ON state are due to the reduction of the bandpass of the filter related with the external quality factor. It would be enough to change the external quality factor increasing the band pass

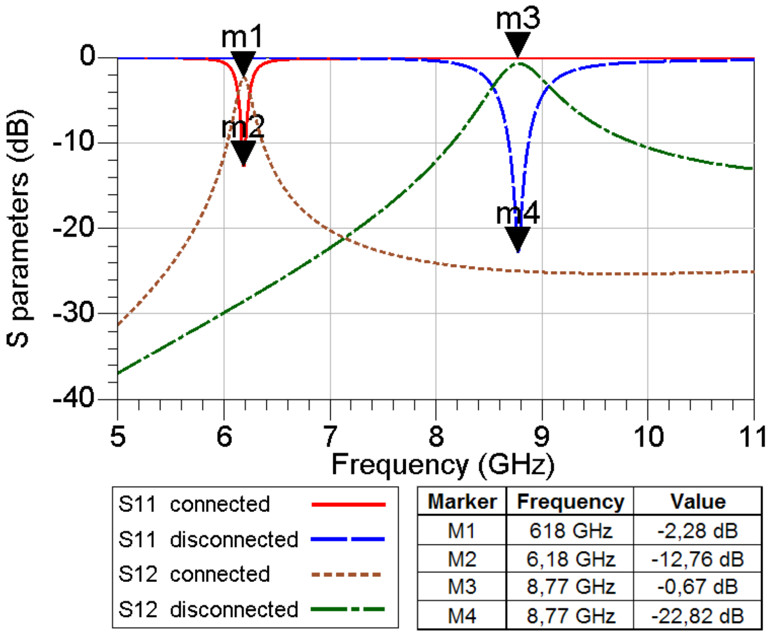

Marker	Frequency	Value
M1	618 GHz	-2,28 dB
M2	6,18 GHz	-12,76 dB
M3	8,77 GHz	-0,67 dB
M4	8,77 GHz	-22,82 dB

Figure 3.4: Simulation of the LTCC filter with ideal connections.

for obtaining a better transmission. The unloaded quality factor for the OFF state is $Q_0 = 177$ obtained from simulations and it is only reduced to $Q_0 = 167$ on the ON state so we can consider that this losses are effectively due to the external quality factor, related with the couplings.

As already explained, these first simulations are for the case of a perfect connection or disconnection. However, it cannot be expected from the study made in chapter 2 that the photoconductive materials will work as ideal switches but rather that they will have a low enough conductivity when the resonator and the wings are disconnected, and a relatively high conductivity when the connection is needed.

Several simulations have been done with materials of different electrical conductivities linking the resonator and the wings. These simulations allow the determination of the material's required conductivity ranges for proper operation of the tunable filter.

Fig. 3.5 corresponds to the simulation in which the material's conductivity increases by a factor of 10 for each curve, from a very low conductivity of $\sigma = 1 \times 10^{-7} S/m$ to a conductivity of $\sigma = 1 \times 10^{-2} S/m$.

From this simulation it has been extracted that an interconnect conductivity

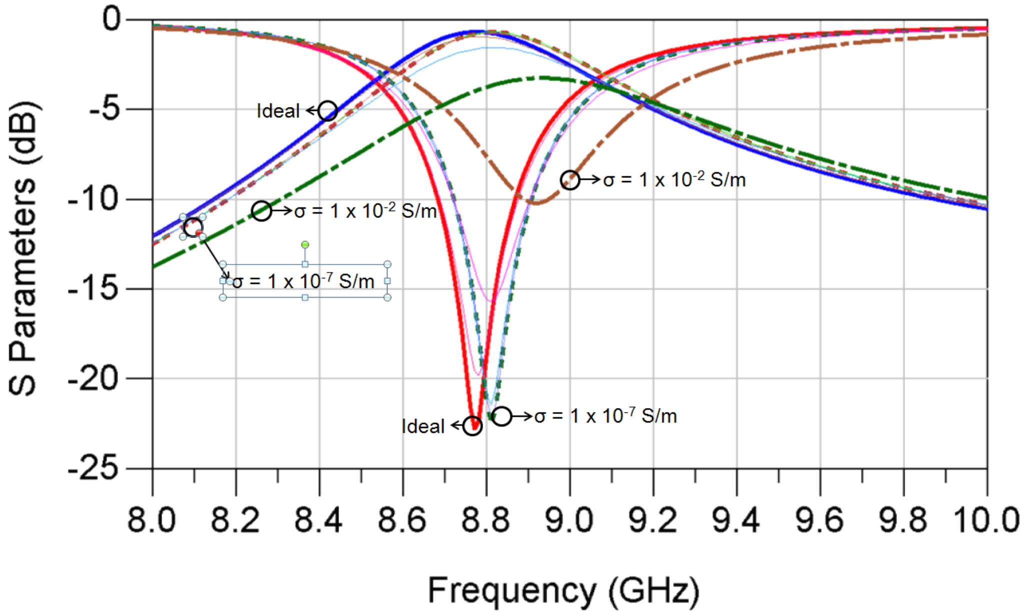

Figure 3.5: Simulation of the LTCC filter when the “interconnection” between the main resonator and the wings is accomplished with a material of finite (but low) conductivity.

lower than $\sigma_{max} = 10^{-3} S/m$ is needed for the filter to work correctly in the OFF state ($Z = \infty$), that is, at the higher frequency ($f_1 = 8.8GHz$).

Indeed, when the material conductivity remains lower than $\sigma_{max} = 10^{-3} S/m$, the filter insertion losses are less than $1.56dB$ and the central frequency is $f_0 = 8.81GHz$, compared to the ideas case where the losses where $0.04dB$ at $f_0 = 8.77GHz$ which is acceptable for this filter. With this electrical conductivity, the unloaded quality factor has been simulated and it is only $Q_0 = 37$, much lower than the unloaded quality factor obtained for the case with no connection of $Q_0 = 177$.

The same type of simulation has been done to extract the minimum conductivity of the interconnect for proper operation of the filter in its ON state ($Z = 0$, $f_2 = 6.2GHz$). In this case, as shown in Fig. 3.6, the material's conductivity has been decreased by a factor of 10 per curve, starting from a conductivity of $\sigma = 1 \times 10^{+7} S/m$ and dropping to $\sigma = 1 \times 10^{+4} S/m$.

Now it is seen that the required conductivity for proper filtering at f_2 in the ON state is at least $\sigma_{min} = 10^{+5} S/m$. Keeping the conductivity higher than this

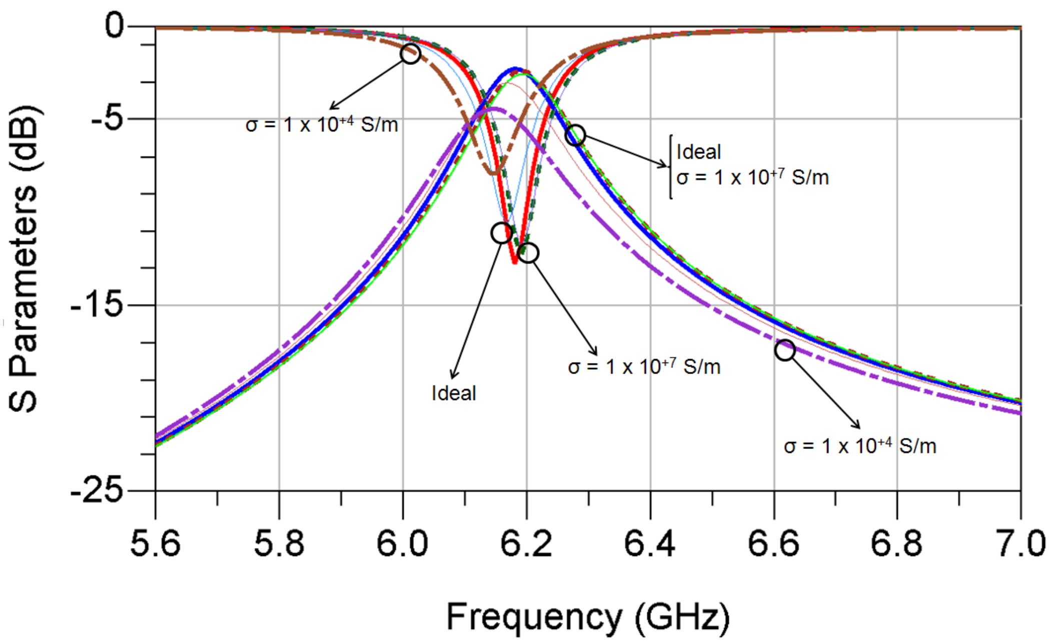

Figure 3.6: Simulation of the LTCC filter when the“interconnection” between the main resonator and the wings is accomplished with a material of finite (but high) conductivity.

value, the insertion losses for this conductivity value are at $3.04dB$ which is not much higher than the insertion losses of $2.28dB$ of the ideal case. The frequency only shifts $10MHz$ from the central frequency of $f_0 = 6.18GHz$ obtained with the ideal simulation to $f_0 = 6.17GHz$ obtained with this finite conductivity of $\sigma_{min} = 10^{+5}S/m$. As for the unloaded quality factor, it is reduced from the $Q_0 = 167$ obtained for the ideal disconnection to $Q_0 = 70$ obtained for this finite conductivity. This value continues to decrease as the electrical conductivity decreases.

Although the insertion losses become more important in both states with non perfectly conductive or non-conductive materials, the filter function is still acceptable for a proof-of concept on the use of these new photoconductive materials. As it has been mentioned before, this filter was issued from [2] so the filter design was fixed. We add the adjustable part to this previous filter so it is not possible to change the external coupling or other characteristics of the filter so the optimization is limited by these fixed characteristics.

We conclude from this study that the photoconductive material is required to have a conductivity lower than $\sigma_{max} = 10^{-3} S/m$ when it is not under the influence of an optical source, and a conductivity higher than $\sigma_{min} = 10^{+5} S/m$ when it is illuminated.

3.1.3 Fabrication and measurements

The preliminary filter circuit has been manufactured by VTT Electronics, as a module having eight $99\mu m$ thick layers of Ferro A6S whose relative permittivity is $\varepsilon_r = 5.9$ and its loss tangent is $tan\delta = 1.3 \times 10^{-3}$. The conductor used is silver ($\sigma = 4.7 \times 10^{+7} S/m$) and the circuit's total size is $3.648 \times 3.504\ mm$.

In order to show the basic principle of this tunable device, the filter with perfect connections between the main resonator and the wings, and the filter without any such connection have been created separately and a photograph of them can be seen in Fig. 3.7.

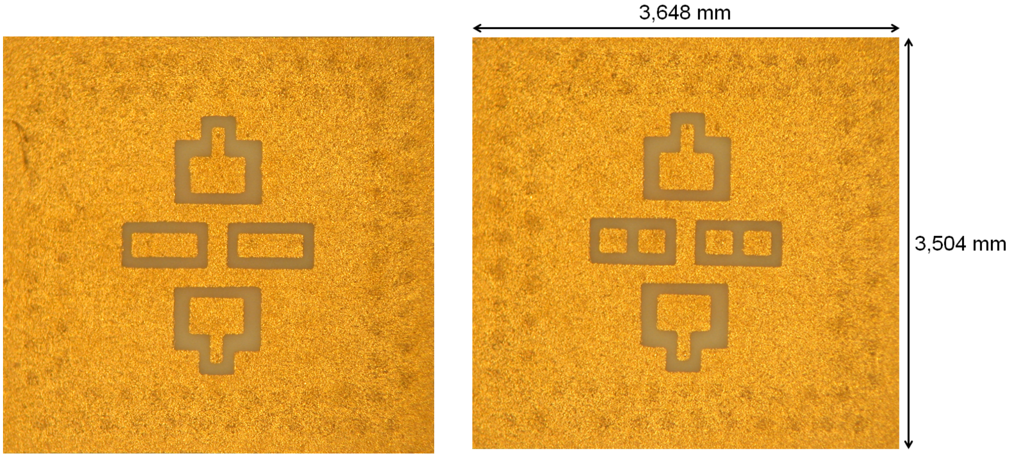

(a) Perfect connection between the main resonator and the wings: ON state.

(b) No connection between the main resonator and the wings: OFF state.

Figure 3.7: Photograph of the manufactured LTCC filters.

Fig. 3.8 shows the measurements of both independent circuits superposed in the same figure.

Comparing the measured results in Fig. 3.8 with the simulated results in Fig. 3.4 we can see that the results are not too far from each other.

For the filter without connection between the main resonator and the wings or

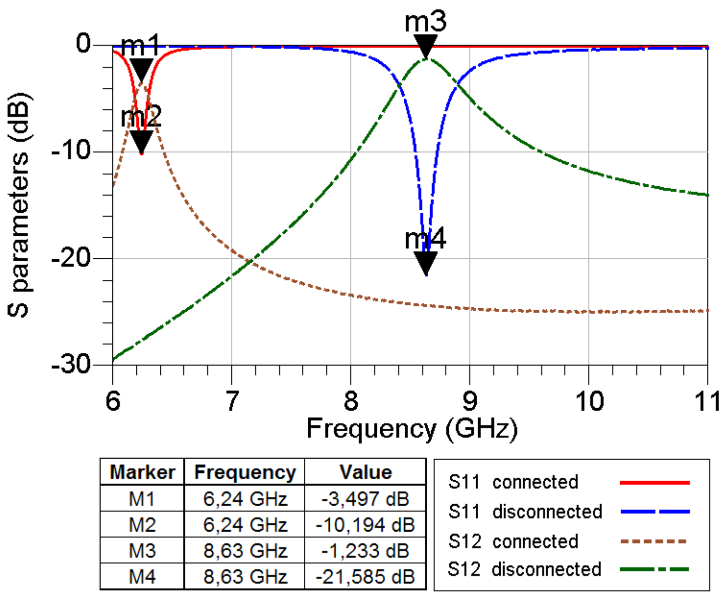

Marker	Frequency	Value
M1	6,24 GHz	-3,497 dB
M2	6,24 GHz	-10,194 dB
M3	8,63 GHz	-1,233 dB
M4	8,63 GHz	-21,585 dB

Figure 3.8: Measured results of the fabricated LTCC filters.

OFF state filter, it can be observed that the measured and the simulated results match very closely but there is a slight change of center frequency of $\Delta f \approx 170MHz$ decreasing from $8.8GHz$ obtained at the simulation stage to $8.63GHz$ in measurement. We observe also that the insertion losses increase from $0.7dB$ simulated to $1.2dB$ measured.

For the ON state filter, main resonator and wings connected, we observe a very small difference too. In this case, the center frequency deviation is only $\Delta f \approx 30MHz$, increasing from $6.2GHz$ simulated to $6.23GHz$ measured. On the other hand, the insertion losses become more important, amounting to $3.5dB$ instead of the $2.3dB$ simulated. A frequency shift of $2.39GHz$ has therefore been observed between the two states

All these differences between the simulation results and the measurements can be attributed to the fabrication tolerances introduced by this choice of technology. According to [4] these tolerances are:

- Line width of $200\mu m$: $\pm 5\mu m$.
- Gap between to lines of $75\mu m$: $\pm 1\mu m$ to $9\mu m$.
- Narrowing of X-Y layers after firing: $15\% \pm 2\%$.

- Narrowing of Z layer after firing: $35\% \pm 5\%$.

The observed differences obtained from this comparison are negligible and therefore the analysis and design method are believed to be validated. The next stage in the development of the optically tunable LTCC filter will be the use of a photoconductive material to connect the main resonator with the wings and to route the light to the places where the material is placed.

The optical study has not been carried out as the material could not be deposited in the filters at the time. However, when the filter was analyzed for including the reconfigurability, it was seen that some optimizations were possible even without the results of the optical control of the first fabricated run. With the optimizations proposed in the next section, a better response is expected when the material is ready to be deposited.

3.1.4 Optimizations of the circuit

From the results of the previous sections it has been demonstrated that a reconfigurable LTCC filter can be realized under the specific geometric and material conditions described. The next step, however, is particularly complicated given that the total interconnection space is on the order of $0.1 \times 0.2mm$, restricting significantly the area to connect the main resonator with the wings.

Taking into account the reduced dimensions of the circuit, and especially of the interconnections, it is virtually impossible to imagine the implementation of the required switching action using conventional electronic components such as PIN diode, MEMS or varactor diodes with typical values of around $1mm$ by $1mm$ or even down to the range of $20\mu m$ for the MEMS. These elements cannot be integrated easily: on the one hand, we have the problem of finding the necessary space within the minimal size of the component, and on the other, the need for a bias circuit of some type in close proximity that will perturb the electromagnetic behaviour of the whole system.

The goal is therefore the inclusion of materials within the LTCC filter structure that can change from a conductive state to a non-conductive state. In the first version of the circuit, the material had to be deposited on top of the circuit and then be illuminated from outside as shown in the schema in Fig. 3.9. This type of illumination could result on a lack of conductivity in the bottom part of the material, the part in contact with the circuit itself. Also the light would not be routed and therefore more complex circuits would not be possible.

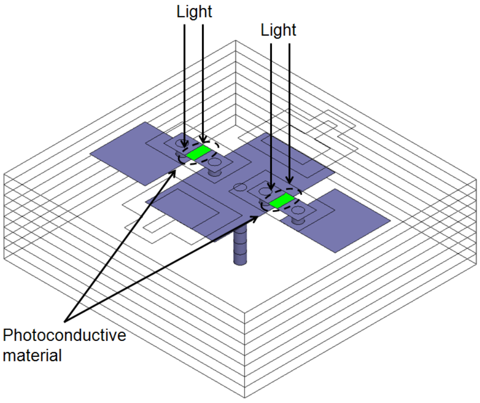

Figure 3.9: Schema of illumination idea for the basic circuit.

In order to avoid this problem, in the next run of circuits fabricated two main improvements have been made. The first one, is to take the wings further away from the main resonator having this way more space for the material to be deposited. The distance between the main resonator and the wings has been increased from $0.15mm$ of the previously presented circuit to $1.15mm$ in this new optimized version. The size of the interconnect would be the same and the access to the wings would be done using a metal strip. The material could go over the metal without changing the behaviour of the filter as it is shown in Fig. 3.10(a).Also, for depositing the material, a hole would be made in the interconnect in a way that the material could go in between the main resonator and the wings, and not only on top. Fig. 3.10(b) shows the top view of this new interconnection with the sizes of it but without the material going over the metal surfaces and the hole for the optical fibre can be observed between the two interconnection metals.

The final improvement is the inclusion of a cavity under the interconnection, in order to introduce an optical fiber, or to illuminate using a VCSEL. This improvement would provide the possibility of illuminating the interconnections separately

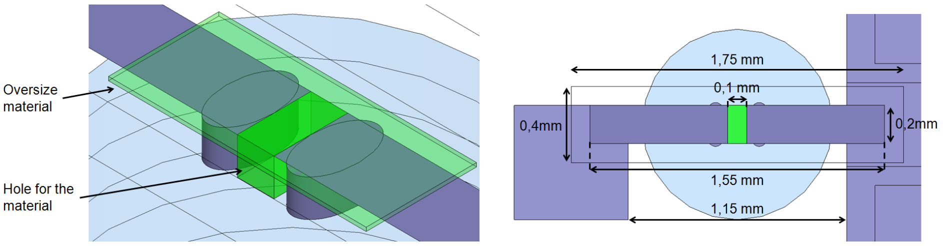

(a) Detailed view of the interconnectio with the material going over the space reserved for it.

(b) Top view of the new bigger interconnection.

Figure 3.10: Detailed views of the bigger interconnection of the optimized filter.

permitting in this way more flexibility and the filter to work in more different states. Fig. 3.11 show the Ansoft HFSS 3D structure for this new run.

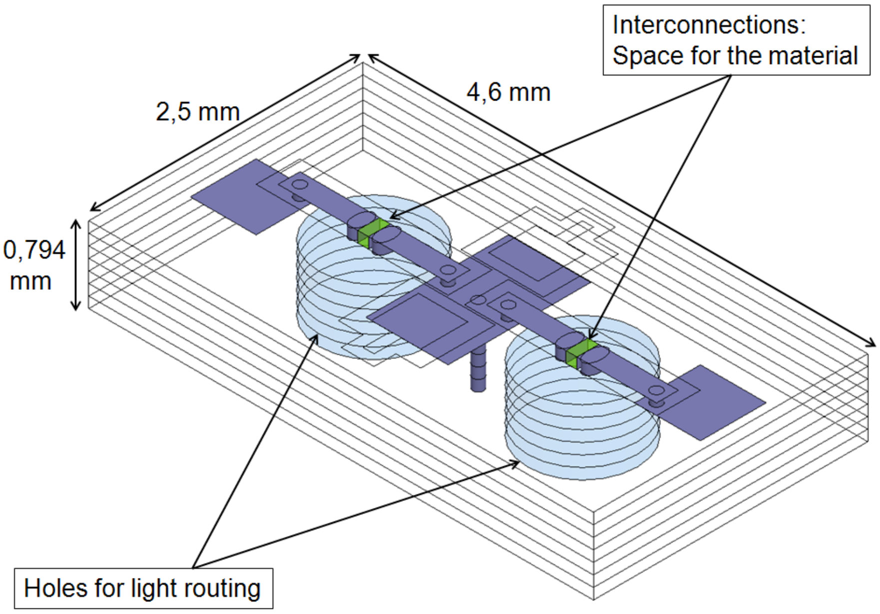

Figure 3.11: Design of the optimized LTCC filter.

The overall response of this new filter is slightly different from the previous one. An increase on the size of the overall circuit, especially the increase on the metal connecting the wings to the main resonator results in a decrease of the frequency. The simulated results of this new structure are shown in Fig. 3.12.

If we compare the simulated results in Fig. 3.4 corresponding to the previous version of the filter with the results of the new version showed in Fig. 3.12, it is

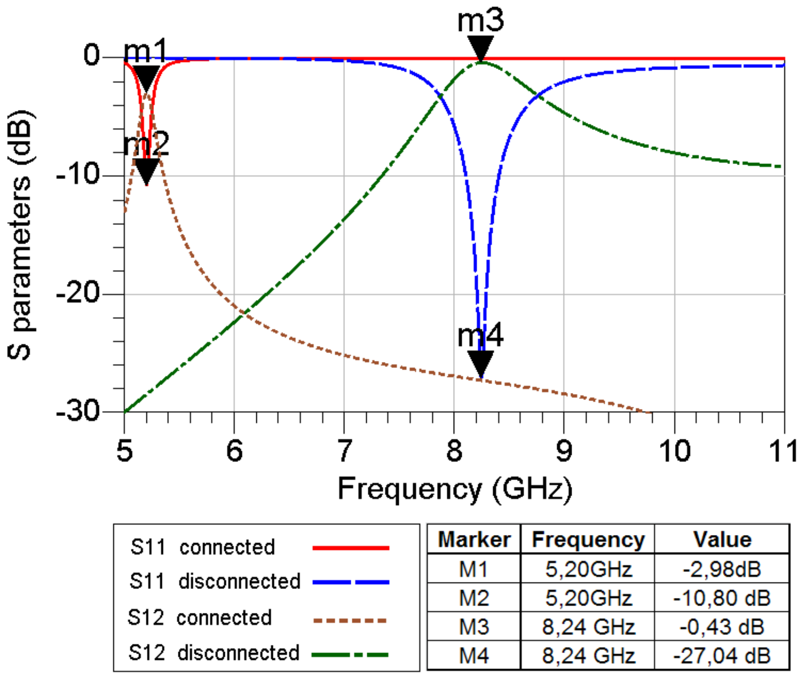

Marker	Frequency	Value
M1	5,20GHz	-2,98dB
M2	5,20GHz	-10,80 dB
M3	8,24 GHz	-0,43 dB
M4	8,24 GHz	-27,04 dB

Figure 3.12: Simulation results of the optimized LTCC filter.

obvious that the working frequency of the filter has been reduced. For the OFF state,the filter frequency is $8.24GHz$ while it was $8.8GHz$ for the first design. When it comes to the connected state, as it is in this state where the effect of the size increasing is maximized, the ON state frequency is $5.2GHz$ ($6.4GHz$ for the first design).

Three types of these filters have been fabricated following the same procedures as for the previous circuits. In order to have an estimate of the response of this new version of the filter, the ideal cases where the connection is made with silver and another without any connection have been fabricated. Finally, a circuit with a gap for the material has been fabricated too in order to deposit the materials. The measured results of the two ideal cases are shown in Fig. 3.13.

We observe again a slight difference between the simulated results and the measured results probably due to the fabrication tolerances. For the ON state filter, the frequency drops from $5.20GHz$ in simulation to $5.14GHz$ measured whereas in the OFF state the frequency drops to $7.98GHz$ in measurements from the $8.24GHz$ simulated.

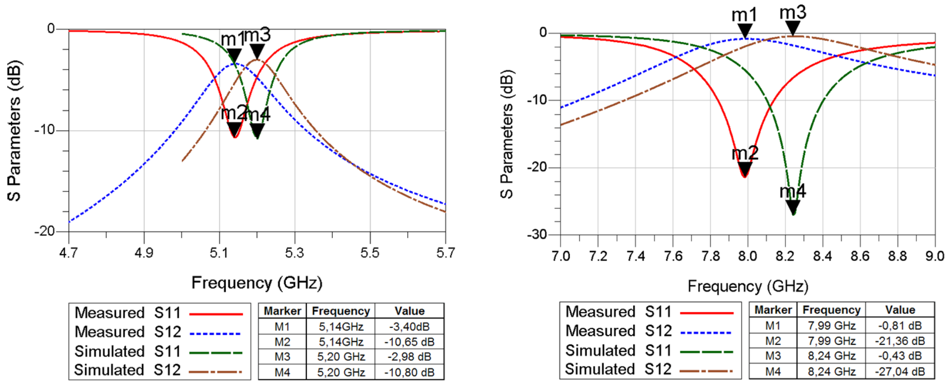

Marker	Frequency	Value
M1	5,14GHz	-3,40dB
M2	5,14GHz	-10,65 dB
M3	5,20 GHz	-2,98 dB
M4	5,20 GHz	-10,80 dB

Marker	Frequency	Value
M1	7,99 GHz	-0,81 dB
M2	7,99 GHz	-21,36 dB
M3	8,24 GHz	-0,43 dB
M4	8,24 GHz	-27,04 dB

(a) Perfect connection between the main resonator and the wings: ON state.

(b) No connection between the main resonator and the wings: OFF state.

Figure 3.13: Measured results of the optimized LTCC filter.

In terms of losses, there is an increase from simulation too. For the ON state, that increase goes from the $2.98dB$ simulated to $3.40dB$ in measurements. For the OFF state the measured losses are $0.81dB$ ($0.43dB$ simulated).

A $2.85GHz$ frequency shift between the ON and OFF state for this optimized filter is thus achieved.

An optimization of the filter has been achieved then with the possibility of routing the light and allowing some more space for the material to be deposited.

3.1.4.1 Future prospects

The future prospects of this filter are especially the deposition of a photoconductive material to do the interconnections. The material considered for this filter, and from the results obtained in the previous chapter is the vanadium dioxide first because of its electrical conductivity change really promising. However, the deposition of this material in the ceramics used for the LTCC might be difficult and some studies are being carried on at this time.

The second material considered is the zinc oxide, as it is supposed to be photoconductive. We have seen that the conductivity is too low for the moment and that the change in conductivity is not enough for this application. Nevertheless, in case of an improvement of the material properties, this material would be considered for this kind of tunable filter.

With the new version of the filter, where the light could be routed through the structure, the flexibility of this kind of filter has been improved greatly. With the routing, different connections can be illuminated at different times creating not only two states but several ones. If the filters are designed with different sizes, a filter with x wings will provide 2^x different states, for example a filter with two different wings will provide 4 different states while with three wings the possibilities double providing 8 states.

For instance, in order to show this idea, a filter working in the $2GHz$ to $4GHz$ band based on the same LTCC resonator has been designed and simulated. The size of the wings are $1.5mm$ and $1.8mm$ so four different states can be achieved with this filter as Fig. 3.14 depicts.

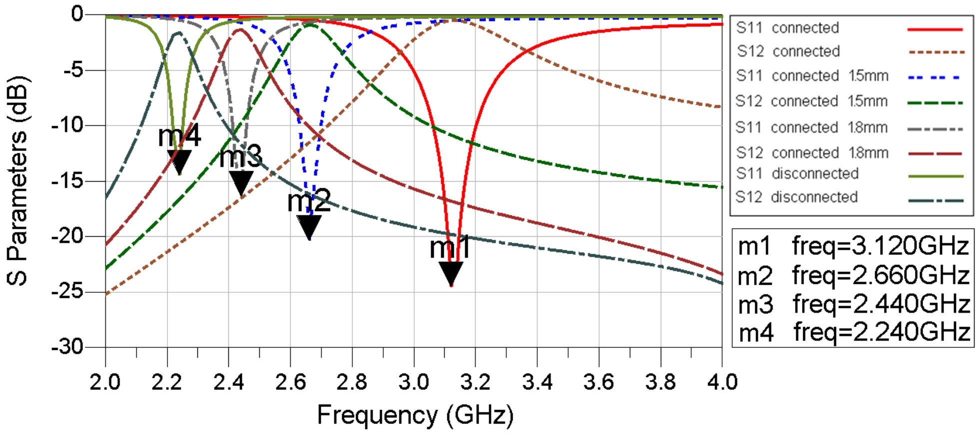

Figure 3.14: Simulation results of the 4 state LTCC filter.

It is clearly seen that the filter is working at $3.12GHz$ when both wings are connected and its frequency shifts down gradually working at $2.66GHz$ when the $1.5mm$ wing is connected, at $2.44GHz$ when the $1.8mm$ wing is connected and finally at at $2.24GHz$ when both wings are connected achieving a total frequency shift of $900MHz$.

3.1.5 Conclusion

In this section, we studied the proof of concept of a tunable LTCC filter. The filter employs a resonator inside an LTCC cavity whose total surface can be changed by connecting or disconnecting supplementary metallic wings, changing the center frequency from $8.8GHz$ to $6.2GHz$ in the first version of the circuit and from $8.24GHz$ to $5.20GHz$ in the optimized version.

A first version and an optimized version of the filter have been validated in simulations as well as experimentally. Prototypes have been measured for both versions in the ON and OFF states, corresponding to a perfect connection between the main resonator and the wings and to a perfect disconnection between the two, respectively.

The intent is to implement the resonator-wing interconnects with optically sensitive materials, photoconductive materials more precisely. The conductivity ranges of the polymer material required for proper operation of the tunable filter have been determined to be $\sigma < 10^{-3}S/m = \sigma_{max}$ and $\sigma > 10^{+5}S/m = \sigma_{min}$.

Finally the future prospects of this type of filter have been presented with an improvement in the space designated to the material and with the possibility of routing the light resulting in more flexibility in the agility of the filter.

Some parts of this work have been presented in two national conferences, URSI 2009 in Spain and 2010 CCECE in Canada (see Appendix B).

3.2 Tunable 3D dielectric resonator

In this section a tunable dielectric resonator will be presented. This resonator will take advantage of the thermoconductive material presented in the previous chapter, the vanadium dioxide (VO_2). Optimal results of this temperature dependent resonator could open a new frontier towards optically tunable components, as the temperature change could be achieved with the use of an optical source.

This section will be divided in six main parts. First of all basics about resonators will be given in the theory part and it will be followed with the simulations of the resonators. After that, the section will continue with the explanation of the experience plan optimization method used for the correct placement of the photoconductive material followed with the fabricated devices and their measurements. Finally the future prospects of this resonator will be given and a conclusion part will finish this section.

3.2.1 Resonator theory

A dielectric resonator is an electronic component that exhibits resonance for a narrow range of frequencies, generally in the microwave band.

The use of dielectric resonators for the creation of filters has been widely studied over the years as dielectric resonators present a great unloaded quality factor, largely over 10000 at high frequencies around $5GHz$ depending on the dielectric constant of the material used [5]. The combination of these high quality factor resonators results in narrow band filters.

The most common form of resonators and the one used for this work, is the cylindrical resonator, a puck-shaped resonator placed in the middle of a metallic cavity using a support. The use of this support placing the dielectric resonator further away from the metallic wall of the cavity avoids the metallic losses associated with it and permits the use of the $TE_{01\delta}$ mode that has been widely use in filters especially in wireless base stations [6].

One of the main advantages of this type of resonator, and especially working with this mode, is that it can be excited with a lot of different techniques as it can be seen in Fig. 3.15 from [7]

Although lots of techniques are possible for exciting this dielectric resonator, for example, exciting the electric field using a dipole or the use of a waveguide, the most usually used method is the excitation of the magnetic field by a loop.

The most used materials for 3D dielectric resonators are ceramics due to their high permittivity and the low dielectric losses. These really low losses will produce the high quality factors expected in this kind of resonators, the lower the losses, the higher the quality factor. The fact of using a high permittivity material results on a minimization of the structure as is resonance frequency is inversely proportional to the material's permittivity as in eq. 3.4 from [7].

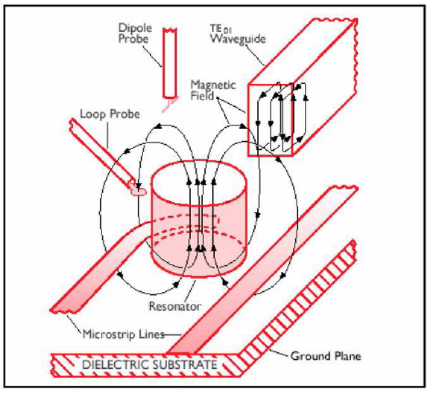

Figure 3.15: Excitation techniques for a dielectric resonator working in its $TE_{01\delta}$ mode [7].

$$f = \frac{34}{a\sqrt{\varepsilon_r}}\left(\frac{a}{h} + 3.45\right). \tag{3.4}$$

where a and h are the radius and the height of the resonator in mm an ε_r the relative permittivity, unitless. The frequency calculated will be in GHz.

The interest of using dielectric resonators is then the reduction of the dimension of the structure always keeping a fairly high quality factor.

The systems using a dielectric resonator are composed by four basic elements:

- Dielectric resonator: The type of dielectric resonator as well as the material that is going to be used together with the resonant mode will be chosen according to the constraints imposed by the application in terms of quality factor, resonant frequency and frequency isolation.

- Metallic cavity: The size of the metallic cavity will be chosen also depending on the wanted quality factor and the frequency isolation. A bigger distance between the metallic walls of the cavity gives a higher quality factor, so one might think that this distance should be maximized. However, a bigger cavity will lower fundamental mode resonance frequencies creating more and more higher order modes that will interfere with the resonance frequency of the resonator so a trade-off between these two parameters is needed in order to have a high enough quality factor with a good frequency isolation.

- Support: The aim of this part of the system is to place the resonator further away from the bottom of the cavity avoiding in this way an increase of the metallic losses which leads to a decrease on the quality factor. The support is normally made of a material whose permittivity is really close to the relative permittivity of the air, $\varepsilon_r = 1$, and whose losses are as low as possible.

- Excitation system: The excitation system is the way the resonant mode will be excited, depending on the mode chosen the excitation mode will be different as not all the modes can be excited with all the excitation systems so a suitable excitation type needs to be chosen depending on the mode that is wanted.

All these parts are used for any structure where a dielectric resonator is involved. However, the aim of our work is to develop a tunable dielectric resonator using a material where the conductivity changes under certain conditions. The way this happens, we can consider it as altering the resonators main mode with the introduction of a conductive material in its middle.

If we introduce a conductive material in the middle of the structure, as the conductive materials modify the electromagnetic waves distribution, the material will perturb the resonant mode and it will produce a change in the frequency as well as in the unloaded quality factor. Depending on the position and on the size and the conductivity of the material, the frequency shift will be greater or the quality factor will change a lot. Examples of this changes will be shown in next section.

3.2.2 Design and simulations

The dielectric resonator will be fabricated on alumina from the CTTC (Centre de Transfert de Technologies Ceramiques) using the stereolithography process.

The properties of the alumina used at CTTC and called from now on CTTC alumina are:

- Relative permittivity: $\varepsilon_r = 9.8$.

- Loss tangent: $tan\delta = 5 \times 10^{-5}$.

Although the stereolithography fabrication process permits the fabrication of very complex dielectric resonators, in order to simplify the first use of a conductive material in the dielectric resonator, we are going to use a cylindrical resonator or a puck size resonator as it can be excited easily.

In this work we want to work with a frequency higher than $10GHz$. We are going to use a commonly used resonator where the radius of the resonator is equal to the height of the resonator.

$$R_{RD} = h_{RD}. \tag{3.5}$$

From eq. 3.4, the resonant frequency of the fundamental mode, $TE_{01\delta}$, of a cylindrical dielectric resonator can be calculated. If we isolate the radius of the resonator in that equation for the condition we chose in eq. 3.5 we obtain the following equation:

$$R_{RD} = \frac{34}{f\sqrt{\varepsilon_r}}\left(\frac{a}{a} + 3.45\right) = \frac{34 \cdot 4.45}{f\sqrt{\varepsilon_r}} = \frac{151.3}{f\sqrt{\varepsilon_r}}. \tag{3.6}$$

Wanting to work in a frequency higher than $10GHz$, we solved eq. 3.6 for the arbitrarily chosen value of $13GHz$ obtaining a necessary radius of $3.7mm$ but we rounded the radius to $4mm$ for the simulations and fabrication. In the theoretical formula the $4mm$ radius and $4mm$ height resonator will provide a resonant frequency for the fundamental mode of $f_{TE_{01\delta}} = 12.08GHz$. This formula is just an estimation and an electromagnetic solver will be needed to obtain an accurate value of the resonant frequency.

For reducing the simulation time, as we are going to be interested to the dielectric resonator frequency, the size of the simulated cavity will be $h_{cavity} = 2 \times h_{RD} = 8mm$ and $R_{cavity} = 2 \times R_{RD} = 8mm$ as it is not too big compared to the dielectric resonator itself.

We need enough frequency isolation between the resonant modes of the dielectric resonator and those of the cavity. In order to verify the frequency isolation, we are going to calculate the theoretical resonant frequencies of this cavity. The first mode excited in a cavity depend on the relation between the diameter of the cavity with its height. From Fig. 3.16, if we take the value of the relationship $(D/h)^2$, we can find the modes that are excited.

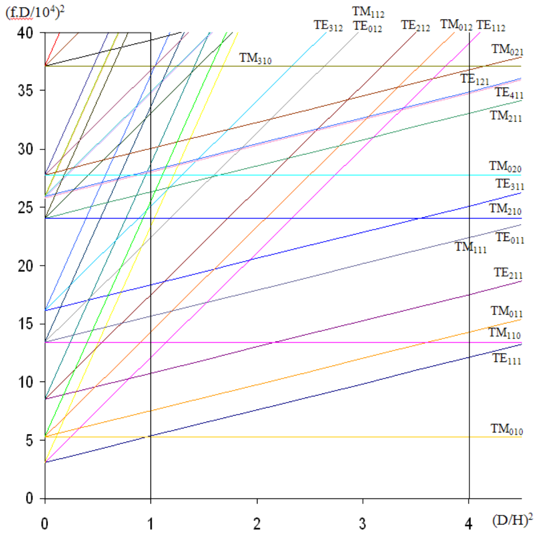

Figure 3.16: Resonant modes of a cylindrical resonant cavity.

For our work the relationship $((D/h)^2 = 4)$, so the first excited mode is the mode TM_{010} followed by the mode TE_{111}. For calculating the resonant frequency, we are going to make a difference between the TE and the TM modes. The TE_{mnp} mode is calculated with eq. 3.7

$$f_{c_{mnp}} = \frac{c}{\sqrt{\mu_r \cdot \varepsilon_r}} \sqrt{\left(\frac{x'_{mn}}{2\pi R_{RD}}\right)^2 + \left(\frac{p}{2h_{RD}}\right)^2}. \tag{3.7}$$

where

c: speed of light.

μ_r: relative permeability.

ε_r: relative permittivity.

x'_{mn}: Zeros of Bessel $J'_{mn}(x)$ function.

For the $TMmnp$ mode the expression for calculating the resonant frequency is given by eq. 3.8

$$f_{c_{mnp}} = \frac{c}{\sqrt{\mu_r \cdot \varepsilon_r}} \sqrt{\left(\frac{x_{mn}}{2\pi R_{RD}}\right)^2 + \left(\frac{p}{2h_{RD}}\right)^2}. \tag{3.8}$$

where

c: speed of light.

μ_r: relative permeability.

ε_r: relative permittivity.

x_{mn}: Zeros of Bessel $J_{mn}(x)$ function.

The first eight resonant frequencies of the cavity chosen for the simulation are in table 3.1.

Mode	**Resonant frequency**
TM_{010}	$14.35\,GHz$
TE_{111}	$21.73\,GHz$
TM_{110}	$22.87\,GHz$
TM_{011}	$23.61\,GHz$
TE_{211}	$26.15\,GHz$
TM_{111} and TE_{011}	$29.57\,GHz$
TM_{210}	$30.65\,GHz$
TE_{311}	$31.31\,GHz$

Table 3.1: Calculated resonant frequencies for the simulation cavity.

The resonant modes of the single cavity are then at frequencies higher than $14.35GHz$. However, the inclusion of the dielectric resonator and the support will modify these modes. Modes due to the dielectric resonator (and support) will have then to be considered.

In this simulation step, we will not take into account the support as this will be made on Rohacell whose permittivity is very close to the one of the air ($\varepsilon_r = 1.067$) and the loss is extremely low ($tan\delta = 0.004$). This will facilitate the simulation of the whole structure.

The last element of the system is the excitation technique. All the simulations are in eigenmodes, so the excitation system is not critical right now. However, we know that the excitation system that will be used are coupling loops introduced from the sides of the cavity so we are going to chose the modes to work with taking this information into account.

Up until now, all the extracted resonant frequencies have been extracted using theoretical formulas which are not very accurate and which do not allow us to introduce changes in the resonator. The next step then is to verify the theoretically extracted values through the use of an electromagnetic software.

The electromagnetic solver used is the software developed at *Xlim laboratory* by Dr. Michel Aubourg called EMXD. It is software based on the finite elements method and whose reliability has been largely proved over the last few years.

The first simulation carried out is just the cavity in eigenmodes. This simple structure can be seen in Fig. 3.17. This simulation will provide us the resonant frequencies as previously calculated. For this first simulation we will not care about the quality factor as we only want to know at which frequencies we will find resonant frequencies corresponding to the cavity.

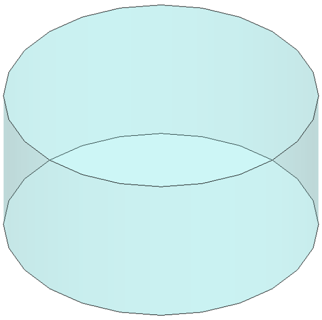

Figure 3.17: Design of the simulated cylindrical resonant cavity.

The resonant frequencies from the simulation software are compared to the theoretically calculated values in table 3.2

The differences between most of the modes are negligible as it can be seen in the comparison on table 3.2. These results validate the electromagnetic solver.

Also, the use of the electromagnetic solver permits us to plot the electric or the

Mode	**Resonant frequency** (Theoretical)	**Resonant frequency** (Simulated)
TM_{010}	$14.35\,GHz$	$14.3579\,GHz$
TE_{111}	$21.73\,GHz$	$21.7234\,GHz$
TM_{110}	$22.87\,GHz$	$22.8781\,GHz$
TM_{011}	$23.61\,GHz$	$23.6058\,GHz$
TE_{211}	$26.15\,GHz$	$26.1451\,GHz$
TM_{111} and TE_{011}	$29.57\,GHz$	$29.5714\,GHz$
TM_{210}	$30.65\,GHz$	$30.6649\,GHz$
TE_{311}	$31.31\,GHz$	$31.3077\,GHz$

Table 3.2: Calculated and simulated resonant frequencies for the simulation cavity.

magnetic field of each mode which will allow us to decide whether the coupling loops will be suitable or not for exciting the chosen modes. In Fig. 3.18 the fundamental mode TM_{010} of the cavity is shown.

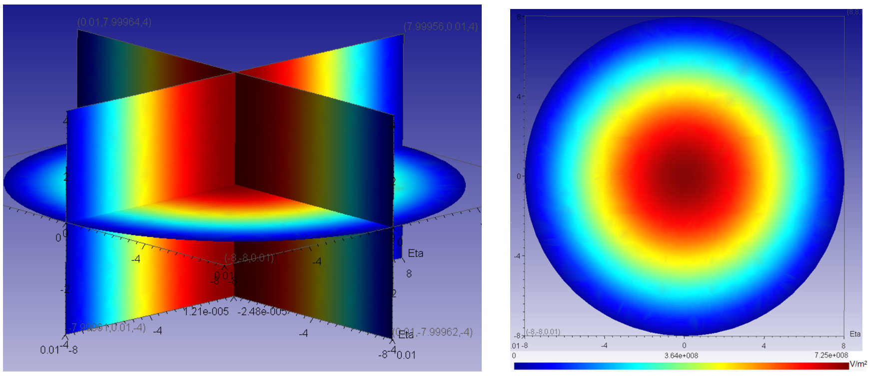

(a) 3D view. (b) Top view.

Figure 3.18: Fundamental mode TM_{010} of the simulation cavity.

Once the cavity has been simulated, the next step is to simulate the dielectric resonator within the cavity. In order to simulate the dielectric resonator, the resonator (yellow) will be placed in the middle of the cavity (blue) as shown in Fig. 3.19 and the whole structure will be simulated in eigenmodes.

As the whole structure composed by the resonator and the cavity is simulated together, resonant frequencies corresponding to the cavity and those of the dielectric resonator will be obtained from the simulation. Analyzing the electric or magnetic field in the structure we can determine which mode is resonating as well as if it

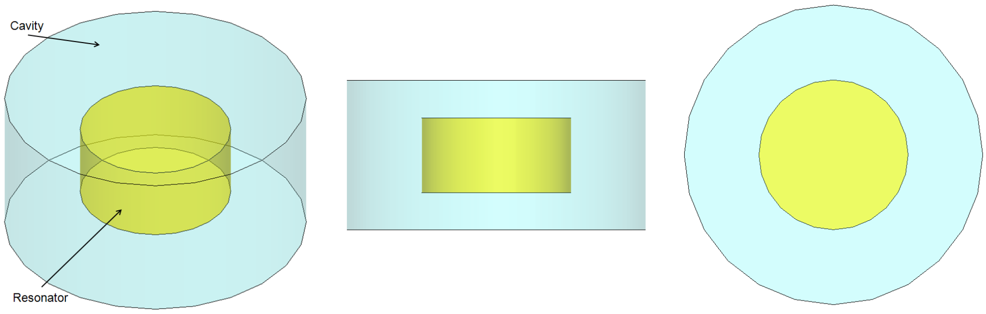

(a) 3D view. (b) Front view. (c) Top view.

Figure 3.19: Design of the simulated dielectric resonator and the metallic cavity.

corresponds to the dielectric resonator or to the metallic cavity. We have simulated the structure between $13GHz$ and $24GHz$ and the resonances founded are shown in table 3.3.

Mode	**Resonant frequency**	**Structure**
TE_{011}	$13.372\,GHz$	Resonator
TM_{011}	$13.673\,GHz$	Resonator
TM_{012}	$15.141\,GHz$	Resonator
TM_{121}	$18.414\,GHz$	Resonator
TE_{211}	$19.041\,GHz$	Resonator
TM_{021}	$19.309\,GHz$	Resonator
TE_{211}	$19.883\,GHz$	Cavity
TE_{012}	$20.901\,GHz$	Resonator
TM_{010}	$21.299\,GHz$	Cavity
TM_{111}	$21.636\,GHz$	Resonator
TE_{311}	$23.235\,GHz$	Resonator
TE_{221}	$23.843\,GHz$	Resonator
TM_{020}	$23.857\,GHz$	Resonator

Table 3.3: Simulated resonant frequencies for the dielectric resonator inside the metallic cavity.

It can be seen from the table 3.3 that the two cavity modes excited will not affect any of the resonant modes of the dielectric resonator as there is a frequency difference of at least $300MHz$. The frequency separation between two consecutive modes is at least $250MHz$ for all the frequencies below $23GHz$.

The next step of this study is to place the photoconductive material inside the resonator. After a study on the quality factor and the frequency shift it has been seen that only five modes of all the modes presented before show exploitable results. That is why from now on we are going to present only the results for the following modes:

- Mode TE_{011} at 13.372GHz.
- Mode TM_{011} at 13.673GHz.
- Mode TM_{121} at 18.414GHz.
- Mode TE_{012} at 20.901GHz.
- Mode TM_{111} at 21.636GHz

The photoconductive material considered for this work is the vanadium dioxide (VO_2) described in the previous chapter. This material's structure needs to be crystalline in order to have the photoconductive properties. The expertise at *SPCTS laboratory* is to deposit the VO_2 on a sapphire substrate. As our resonator is made of alumina, we are going to use a sapphire substrate covered in both sides with a VO_2 layer and then this VO_2 covered substrate will be placed inside our resonator.

The inclusion of a sapphire sheet will imply a little change in the resonant frequencies as the properties of the sapphire differ a little bit from those of the alumina. The losses of the sapphire are considered so small that for simulation we will consider its loss tangent as $tan\delta = 10^{-5}$ while the relative permittivity will be $\varepsilon_r = 10$. The thickness of the sapphire sheet is 250μm.The simulated structure is shown in Fig. 3.20.

The structure is basically the same as the previous one but in this case a sapphire sheet is introduced in the middle of the resonator. The simulated resonant frequencies of the resonant mode of interest are shown in table 3.4 with a comparison with the previously obtained results.

The shift in frequency with the inclusion of the sapphire is very small but it is better to account for that change. The final step is then to include the conductive

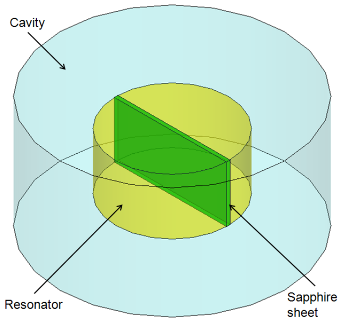

Figure 3.20: Design of the simulated dielectric resonator and the metallic cavity with the sapphire inside the resonator.

Mode	**Resonant frequency** (without sapphire)	**Resonant frequency** (with sapphire)
TE_{011}	$13.372\,GHz$	$13.372\,GHz$
TM_{011}	$13.673\,GHz$	$13.633\,GHz$
TM_{121}	$18.414\,GHz$	$18.355\,GHz$
TE_{012}	$20.901\,GHz$	$20.838\,GHz$
TM_{111}	$21.636\,GHz$	$21.553\,GHz$

Table 3.4: Compared results for the simulated resonant frequencies for the dielectric resonator inside the metallic cavity with and without the sapphire sheet.

material. For the next simulation, the sapphire sheet will be replaced with a sapphire sheet covered on both side by a conductive material as shown in Fig. 3.21. The conductive material later on will be a VO_2 layer of $250nm$.

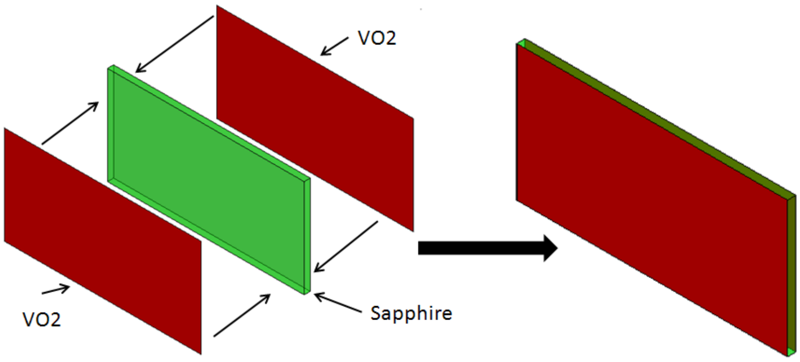

Figure 3.21: Sapphire covered with vanadium dioxide.

In the first simulation, to see how the fields are affected with the inclusion of a conductive material, we have done the simulation defining the VO_2 as a perfect conductor. The frequencies considering the material a perfect conductor are shown in table 3.5.

Mode	**Resonant frequency** (insulator)	**Resonant frequency** (perfect conductor)	**Frequency shift**
TE_{011}	$13.372\,GHz$	$13.634\,GHz$	$262\,MHz$
TM_{011}	$13.633\,GHz$	$13.736\,GHz$	$103\,MHz$
TM_{121}	$18.355\,GHz$	$18.641\,GHz$	$286\,MHz$
TE_{012}	$20.838\,GHz$	$21.091\,GHz$	$253\,MHz$
TM_{111}	$21.553\,GHz$	$21.640\,GHz$	$87\,MHz$

Table 3.5: Simulated resonant frequencies for the whole structure with a perfect conductor or an insulator.

As it has been explained before, the frequency shift can be seen as a perturbation on the resonant mode of the resonator. For explaining this concept we are going to take the example of one of the studied modes, the mode TE_{011} more precisely. The electric field are shown in Fig. 3.22.

As it can be seen in the different images from Fig. 3.22, the resonant mode is a TE_{011}. However, if we compare the mode in Fig. 3.22(a) and 3.22(b) with the mode in Fig. 3.22(c) and 3.22(d) a slight difference can be appreciated. In the cutting plane where the sapphire is placed, there is almost no electric field in the case of a perfect conductor as the electromagnetic waves cannot go through metallic walls. A low intensity electric field is in the sapphire, between the two conductor material sheets. This alteration in the resonant mode electromagnetic distribution will change the resonant frequency as well as the quality factor. A similar effect has been observed in the rest of the modes, which is normal as the shift in frequency has been demonstrated.

The final step is then to define a material where the conductivity changes. As we have stated, the material considered is the vanadium dioxide presented before. The conductivities extracted under continuous voltage were about $\sigma = 9 \times 10^{1} S/m$ at ambient temperature, $20°C$ and $\sigma = 5 \times 10^{5} S/m$ at $90°C$ as it was mentioned in the previous chapter. For the next simulations we have used then conductivities of $\sigma = 1 \times 10^{+1} S/m$ for the off state and $\sigma = 1 \times 10^{+5} S/m$ in order to take some

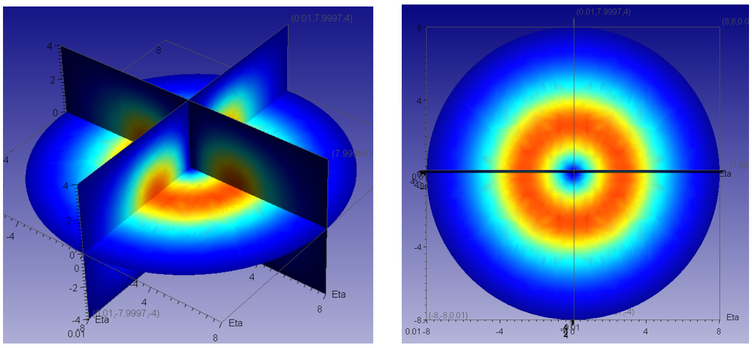

(a) 3D view of the case with an insulator as material.

(b) Top view of the case with an insulator as material.

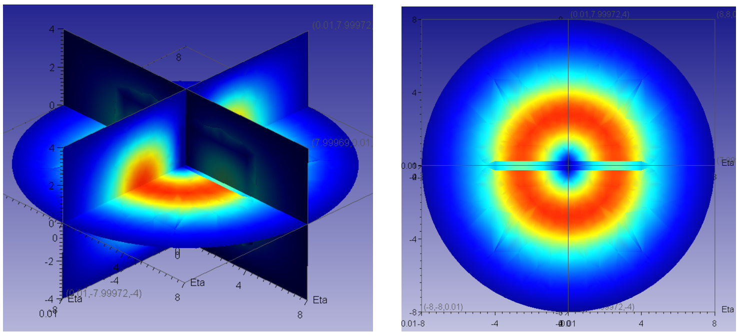

(c) 3D view of the case with a perfect conductor as material.

(d) Top view of the case with a perfect conductor as material.

Figure 3.22: Electric field in the resonator for the mode TE_{011}.

margins when we will use this material at high frequencies. We decided to add two other simulations with $\sigma = 1 \times 10^{+2} S/m$ and $\sigma = 1 \times 10^{+4} S/m$. We are going to present then these different results. First of all we are going to imagine a change between $\sigma = 1 \times 10^{+1} S/m$ and $\sigma = 1 \times 10^{+5} S/m$ with the frequency shift of that change and we will follow those results with the less optimistic case, the change between $\sigma = 1 \times 10^{+2} S/m$ and $\sigma = 1 \times 10^{+4} S/m$.

In all these cases, the VO_2 covered sapphire keep the same configuration depicted in Fig. 3.20.

Table 3.6 shows the results for the bigger change in conductivity and table 3.7 shows the results for the change between $\sigma = 1 \times 10^{+2} S/m$ and $\sigma = 1 \times 10^{+4} S/m$.

As it can be observed in tables 3.6 and 3.7, modes with a high quality factor correspond to a small frequency shift and inversely modes with a bigger frequency shift are modes where the quality factor is quite low.

Mode	$\sigma = 1 \times 10^{+1} S/m$		$\sigma = 1 \times 10^{+5} S/m$		Δf
	$f_0(GHz)$	Q_0	$f_0(GHz)$	Q_0	(MHz)
TE_{011}	13.372	214	13.620	538	248
TM_{011}	13.650	1543	13.712	512	62
TM_{121}	18.364	214	18.623	581	259
TE_{012}	20.871	343	21.077	1003	206
TM_{111}	21.602	1507	21.634	3272	32

Table 3.6: Simulated results for conductivities $\sigma = 1 \times 10^{+1} S/m$ and $\sigma = 1 \times 10^{+5} S/m$.

Mode	$\sigma = 1 \times 10^{+2} S/m$		$\sigma = 1 \times 10^{+4} S/m$		Δf
	$f_0(GHz)$	Q_0	$f_0(GHz)$	Q_0	(MHz)
TE_{011}	13.435	116	13.593	219	158
TM_{011}	13.652	673	13.688	376	36
TM_{121}	18.421	158	18.589	247	168
TE_{012}	20.930	213	21.056	431	126
TM_{111}	21.610	962	21.629	1852	19

Table 3.7: Simulated results for conductivities $\sigma = 1 \times 10^{+2} S/m$ and $\sigma = 1 \times 10^{+4} S/m$.

Trying to get a higher quality factor with bigger frequency shifts, some optimizations have been carried out in this structure. These optimizations are shown in section 3.2.3.

3.2.3 Optimization

The frequency shift and the change in quality factor depend on the placement of the vanadium dioxide in the structure. If we place the conductive material in a place where the electric field is maximum, the frequency shift will be great to the detriment of the quality factor. If we place the material where the electric field is low, the quality factor will stay high but the frequency shift will be extremely low. A trade-off is then needed to get a high enough frequency shift with a good enough quality factor.

To improve this trade-off, two different optimizations have been done. First of all, different configurations of the VO_2 have been simulated and the results analyzed. The second optimization method was based in the response surface methodology and the work has been carried out with Khaled Khoder, a Ph. D. student from *Xlim laboratory*.

3.2.3.1 Different configurations

For this first optimization, nine different configurations of the VO_2 have been studied, placing one, two or three sheets of $250\mu m$ sapphire substrate covered with the $250nm$ of conductive material on both sides placed in the middle of the resonator.

Only configurations number 2 and number 3 will be presented in this chapter as they will be considered for fabrication (Configuration 1 is the previous configuration). The rest of the configuration structures as well as the simulation results are shown in Appendix A.

Configuration 2

Configuration 2 consist on only one $2mm$ high material sheet placed right on the middle of the resonator as shown in Fig. 3.23.

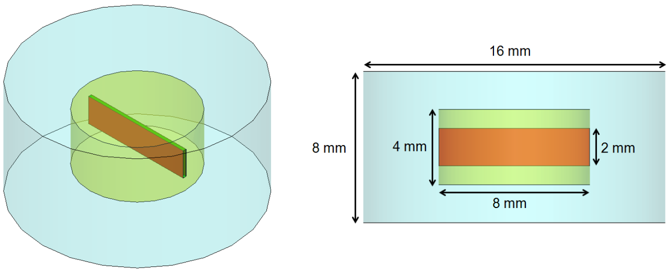

(a) 3D view.

(b) Top view.

Figure 3.23: Design of the configuration 2 for the optimization.

The simulation results for the change between $\sigma = 1 \times 10^{+1} S/m$ and $\sigma = 1 \times 10^{+5} S/m$ are in table 3.8 and for the change between $\sigma = 1 \times 10^{+2} S/m$ and $\sigma = 1 \times 10^{+4} S/m$ in table 3.9 later.

This structure shows modes where a low frequency shift of about $15MHz$ is observed with simulated quality factors over 1800. Other modes where low quality factors around 200 have been simulated with frequency shifts over $100MHz$. As this structure has that double feature (high Q/low Δf and low Q/high Δf) depending on the resonant mode, a fabrication will be considered for further study

Mode	$\sigma = 1 \times 10^{+1} S/m$		$\sigma = 1 \times 10^{+5} S/m$		Δf
	$f_0(GHz)$	Q_0	$f_0(GHz)$	Q_0	(MHz)
TE_{011}	13.383	329	13.558	620	174
TM_{011}	13.671	2861	13.697	1307	27
TM_{121}	18.401	464	18.579	708	178
TE_{012}	20.904	1196	20.820	146	84
TM_{111}	21.640	2891	21.653	1897	13

Table 3.8: Simulated results for conductivities $\sigma = 1 \times 10^{+1} S/m$ and $\sigma = 1 \times 10^{+5} S/m$ for configuration 2.

Mode	$\sigma = 1 \times 10^{+2} S/m$		$\sigma = 1 \times 10^{+4} S/m$		Δf
	$f_0(GHz)$	Q_0	$f_0(GHz)$	Q_0	(MHz)
TE_{011}	13.424	176	13.535	275	111
TM_{011}	13.672	1721	13.688	931	16
TM_{121}	18.436	248	18.552	327	116
TE_{012}	20.920	630	20.988	153	68
TM_{111}	21.644	2147	21.656	1805	12

Table 3.9: Simulated results for conductivities $\sigma = 1 \times 10^{+2} S/m$ and $\sigma = 1 \times 10^{+4} S/m$ for configuration 2.

with measurements.

Configuration 3

Configuration 3 is a sheet of $1mm$ in height on the top section of the resonator and placed along the whole diameter as shown in Fig. 3.24.

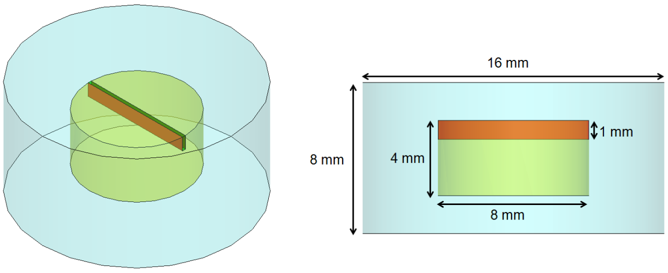

(a) 3D view. (b) Top view.

Figure 3.24: Design of the configuration 3 for the optimization.

The simulation results obtained for the VO_2 conductivity change between $\sigma = 1 \times 10^{+1} S/m$ and $\sigma = 1 \times 10^{+5} S/m$ are in table 3.10 and for the change between

$\sigma = 1 \times 10^{+2} S/m$ and $\sigma = 1 \times 10^{+4} S/m$ in table 3.11 later.

Mode	$\sigma = 1 \times 10^{+1} S/m$		$\sigma = 1 \times 10^{+5} S/m$		Δf
	$f_0(GHz)$	Q_0	$f_0(GHz)$	Q_0	(MHz)
TE_{011}	13.383	1011	13.452	1080	69
TM_{011}	13.683	4524	13.702	945	19
TM_{121}	18.424	1650	18.488	1274	64
TE_{012}	20.899	861	20.985	1907	86
TM_{111}	21.641	3168	21.652	5024	12

Table 3.10: Simulated results for conductivities $\sigma = 1 \times 10^{+1} S/m$ and $\sigma = 1 \times 10^{+5} S/m$ for configuration 3.

Mode	$\sigma = 1 \times 10^{+2} S/m$		$\sigma = 1 \times 10^{+4} S/m$		Δf
	$f_0(GHz)$	Q_0	$f_0(GHz)$	Q_0	(MHz)
TE_{011}	13.396	505	13.440	569	44
TM_{011}	13.684	3071	13.693	1133	9
TM_{121}	18.433	822	18.474	727	41
TE_{012}	20.922	515	20.975	923	53
TM_{111}	21.642	1952	21.650	2813	8

Table 3.11: Simulated results for conductivities $\sigma = 1 \times 10^{+2} S/m$ and $\sigma = 1 \times 10^{+4} S/m$ for configuration 3.

Configuration 3 shows a slight frequency shift for most of the modes. However, a frequency shift of about $50MHz$ with fairly high quality factors above 500 can be achieved for modes TE_{011}, TM_{121} and TE_{012}.

The fabrication of these two structures as well as the previously presented structure with the material along the whole structure have been considered and the measured results will be presented in section 3.2.4

3.2.3.2 Response surface methodology

In order to optimize in a more automated way the placement of conductive material in the resonator, a response surface methodology has been used.

The design of experiments for the study of response surface methodology appeared in the second half of the XX century in 1951 [8]. They have been developed in different scientific domains such as biology, chemistry, human sciences and agronomy [9–11].

The objective of this methodology is, more than organizing in a hierarchy the effect of different factors, to describe as precisely as possible the behavior of the response as a function of the factors. The goal of this type of study is then the establishment of a model of the studied phenomenon based on the experimentation [12]. This design of experiments permit to determine which values of the input factors of a device need to be adjusted for obtaining one or more desired responses; they use polynomial models for the calculation.

The number of tests of a design of experiments for the study of response surface methodology grows rapidly depending on the number of input factors. A response surface methodology will be then an efficient and economic strategy if we limit the number of involved factors.

That is why the design of experiments for the study of response surface methodology need a first step of screening the factor, except if the parameters that need to be optimized are known beforehand.

The construction of a design of experiment for the study of the response surface methodology need the knowing of the input factor that are influential on the response we want to optimize.

We have had two attempts to have an optimal result of our resonator with a conductive material.

In the first attempt, we have considered two different rectangles, representing two sapphire substrates covered with vanadium dioxide on both sides that could move around the structure. The result of the response surface methodology will provide us the values of height and width of those two rectangles as well as their position in the resonator. Fig. 3.25 shows the front view of the resonator with the two rectangles as well as the inputs used.

The inputs of the schematic are:

- X_1: Corresponds to the position of the first sheet in the ordinate axis. It can vary between 0 and $8mm$.
- Y_1: Corresponds to the position of the first sheet in the abscissa axis. It can

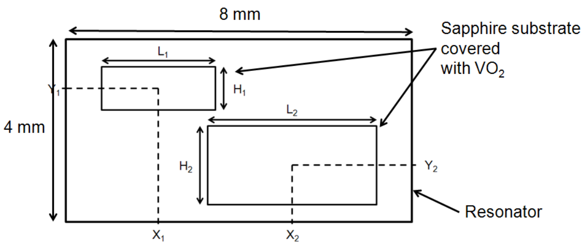

Figure 3.25: Schematic of the initial attempt of the response surface methodology (cut plane).

vary between 0 and $4mm$.

- L_1: Corresponds to the length of the first sheet. It can vary between 0 and $8mm$.
- H_1: Corresponds to the height of the first sheet. It can vary between 0 and $2mm$.
- X_2: Corresponds to the position of the second sheet in the ordinate axis. It can vary between 0 and $8mm$.
- Y_2: Corresponds to the position of the second sheet in the abscissa axis. It can vary between 0 and $4mm$.
- L_2: Corresponds to the length of the second sheet. It can vary between 0 and $8mm$.
- H_2: Corresponds to the height of the second sheet. It can vary between 0 and $2mm$.

With all these inputs, K. Khoder made the design of experiments that will be needed. Considering the input parameters 90 simulations have to be done for the plan in order to make the method determine what is the optimized values for the parameters.

The simulations were carried out for the conductivities studied before: $\sigma = 1 \times 10^{+1} S/m$, $\sigma = 1 \times 10^{+2} S/m$, $\sigma = 1 \times 10^{+4} S/m$ and $\sigma = 1 \times 10^{+5} S/m$. It was decided that the output of the method would be the quality factor of each mode and instead of using the resonant frequency, it would be the frequency shift between different conductivities (Δf).

These outputs should be given for each of the five modes of interest so over 2000 simulations are needed to have the possibility of using this method. Because of the symmetries of the test, the amount of simulations could be reduced to 625 which is still a very high number.

The goal with the use of this method was to find a configuration where a frequency shift greater than $50MHz$ could be found with fairly high quality factors, over 500 but attempting to values over 800 if possible.

This attempt being too ambitious, we limited then the design to only one sheet of sapphire covered with VO_2. Also, in order to reduce the number of simulations to be done, the symmetries of the resonator were exploited and the sheet can only be placed in a quarter of the structure as shown in Fig. 3.26. The schematic shows also the name of the inputs for this selected attempt.

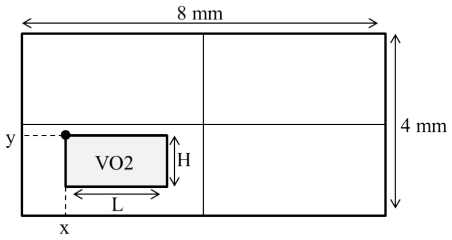

Figure 3.26: Schematic of the selected attempt of the response surface methodology.

The input factors in this attempt are:

- X: Corresponds to the position of sheet in the ordinate axis. It can vary between 0 and $3.5mm$.
- Y: Corresponds to the position of sheet in the abscissa axis. It can vary between 0.5 and $2mm$.
- L: Corresponds to the length of the sheet. It can vary between 0.5 and $4mm$.
- H: Corresponds to the height of the sheet. It can vary between 0.5 and $2mm$.

In order to make sure that the sheet will be placed in the wanted part of the structure, two other constraints were defined for the model:

- $L + X \leq 4$.
- $Y - H \geq 0$

For this selected attempt, only the mode $TE_{01\delta}$ with $\delta = 1$ will be studied as it is the fundamental mode of the resonator and only the conductivities of $\sigma = 1 \times 10^{+2} S/m$ and $\sigma = 1 \times 10^{+4} S/m$ will be studied.

The outputs of the model that will be optimized later are:

- Q_{0_2}: The quality factor of the resonator with a material whose conductivity is $\sigma = 1 \times 10^{+2} S/m$.
- Q_{0_4}: The quality factor of the resonator with a material whose conductivity is $\sigma = 1 \times 10^{+4} S/m$.
- $\Delta f_{2\to 4}$: The frequency shift between the two studied cases.

The response surface methodology needs with these defined parameters to get the results from 21 tests which implies less simulations than the initial attempt.

Once the results of the test have been calculated three different goals have been defined for our structure:

- $Q_{0_2} \geq 800$.
- $Q_{0_4} \geq 800$.
- $\Delta f_{2\to 4} \geq 50 MHz$.

Using an optimization method based on a polynomial model, K. Khoder provided us the best solution the method found for our structure. The values of the solution are in table 3.12.

The design corresponding to this values is in Fig. 3.27.

Input	**Value**
X	$0mm$
Y	$2mm$
L	$2.5mm$
H	$1.5mm$

Table 3.12: Input results for the selected attempt of the response surface methodology.

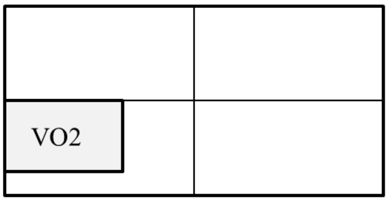

Figure 3.27: Schematic of the resulting structure from the response surface methodology.

Response	$\Delta f_{2\to4}(MHz)$	Q_{0_2}	Q_{0_4}	$f_{0_2}(GHz)$	$f_{0_4}(GHz)$
Model	55	707	9772	13.367	13.319
EM Simulation	47	500	532		
Diference (%)	14.5	29	94		

Table 3.13: Output results for the selected attempt of the response surface methodology $\sigma = 1 \times 10^{+2} S/m$ and $\sigma = 1 \times 10^{+4} S/m$.

The results found through this method both from the model and from the electromagnetic simulations are shown in table 3.13 as well as the difference between them.

It is observed that the difference between the values found by the polynomial mode are quite far from the electromagnetic simulation results. However, a frequency shift of $50MHz$ for quality factors about 500 are found for the smaller change in conductivity. These results are the best results we can achieve currently, however a better solution is expected in the future.

The method presented here has therefore, for such resonator, to be seen as a trend provider which will give one optimal solution for the placement of the sapphire substrate within the resonator. The model evaluated Δf provided by the method is reasonably close to the simulated one. The unloaded Q_0 provided by the model is indeed too optimistic but definitely indicates that "high" Q_0 values could be reached and the the Q_0 does not decrease between the $\sigma = 1 \times 10^{+4} S/m$ and the $\sigma = 1 \times 10^{+2} S/m$ cases.

This information is valuable enough to take it into account and can therefore help the designer to refine its structure dimensions with some retrosimulations.

The simulations of this best solution found by the optimization method have been simulated for the greater change in conductivity, the change between $\sigma = 1 \times 10^{+1} S/m$ and $\sigma = 1 \times 10^{+5} S/m$ and the simulation results are presented in table 3.14.

Response	$\Delta f_{1\to5}(MHz)$	Q_{0_1}	Q_{0_5}	$f_{0_1}(GHz)$	$f_{0_5}(GHz)$
EM Simulation	42	1566	1584	13.363	13.322

Table 3.14: Output results for the selected attempt of the response surface methodology for $\sigma = 1 \times 10^{+1} S/m$ and $\sigma = 1 \times 10^{+5} S/m$.

The results for this greater change in conductivity show a much better response with quality factors of 1500 keeping a frequency shift close to $50MHz$.

The selected attempt of this response surface method exploited the symmetries of the resonator. Trying to make the frequency shift bigger than the one obtained with the model, it has been tried to double the sheet, of the same size exploiting these symmetries.

The sheet has been doubled along the vertical central axis (Fig. 3.28(a)), along the horizontal axis (Fig. 3.28(b)) and finally along the central point (Fig. 3.28(c)).

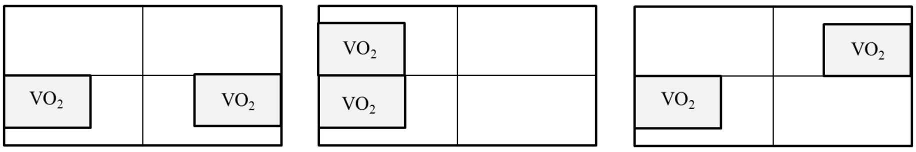

(a) Symmetry along vertical axis.
(b) Symmetry along horizontal axis.
(c) Symmetry with the center of the structure.

Figure 3.28: Schematic of the front view of the resonator with double sheets.

These new structures have been simulated with the electromagnetic software and the obtained results are shown in table 3.15 for the greater change in conductivity,

$\sigma = 1 \times 10^{+1} S/m$ and $\sigma = 1 \times 10^{+5} S/m$.

Symmetry	$\Delta f_{1\rightarrow 5}(MHz)$	Q_{0_1}	Q_{0_5}	$f_{0_1}(GHz)$	$f_{0_5}(GHz)$
Vertical	83	834	835	13.359	13.275
Horizontal	68	815	1271	13.360	13.292
Center	78	830	971	13.359	13.281

Table 3.15: Output results for the selected attempt of the response surface methodology for $\sigma = 1 \times 10^{+1} S/m$ and $\sigma = 1 \times 10^{+5} S/m$.

As it can be observed from the results, doubling the area with sapphire and the conductive material, the quality factors have decreased compared to the previous simulation. However, a little increase on the frequency shift is observed for all the tested structures.

A clear tradeoff between Δf and Q_0 is therefore drawn here.

As a conclusion for the response surface methodology is that there is a direct relationship between the quality factor and the frequency shift. An increase on the performances on one of these parameters is made in detriment of the other so a trade-off is needed between them.

The method itself could be a good help for the designer even if many simulations are required making it useful for structures with a low number of input parameters (4 or 5) and output parameters (1 or 2).

3.2.4 Fabrication and measured results

As it has been explained, not all the studied devices have been fabricated and measured. Only the initial case with a sheet of sapphire covering the whole structure and the configurations 2 and 3 presented in section 3.2.3.

The fabrication of the resonator has been made at the CTTC (Centre de Transfert de Technologies Ceramiques) using a process called stereolithography.

Stereolithography process, showed in Fig. 3.29, is a fast prototyping technique which allows the fabrication of accurate three dimensional structures which cannot be made by standard shaping means such as pressing or moulding. The processing is based on a layer-by-layer polymer stereolithography.

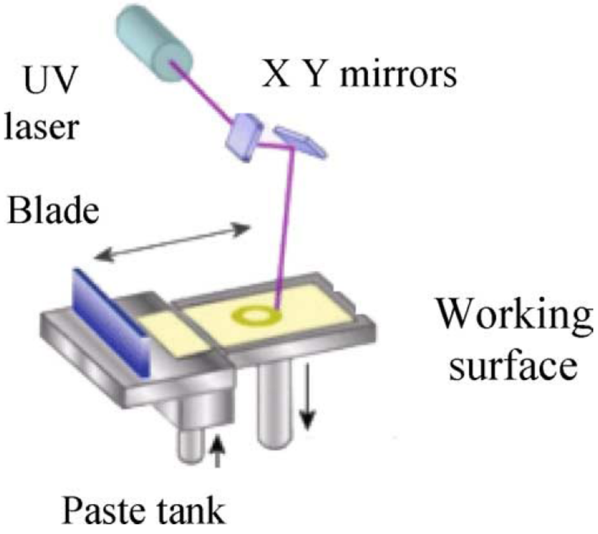

Figure 3.29: Principle of stereolithography 3D process [13].

A paste compound with ceramic powder, binders, monomers and photosensitive resin is deposited on the working surface (Fig. 3.29 by a blade which gives an accurate layer thickness. Then, and Argon ionized UV laser, having a $100\mu m$ spot size, draws on the layer the pattern corresponding to a slice of the 3D structure by polymerizing the paste. The process is repeated for each slice until the whole structure is completed. After that, the monomer surplus is eliminated and the obtained piece is debinded and sintered. The ceramic material used for this fabrication is alumina (Al_2O_3).

The fabrication of the basic resonator has been made by defining to half of the structure so a $250\mu m$ sapphire substrate covered by VO_2 on both sides could be placed between the two half-parts. For the configurations 2 and 3, the shape of the fabricated resonator is the one of the whole dielectric resonator but with a slot for the substrate with the conductive material.

The cavity used in simulations is not the same as the one used in simulation. A cavity with a diameter of $30mm$ and a height of $30mm$ already available at *Xlim laboratory* has been used. To make sure that the resonances of the cavity will not interfere with the resonant modes of the resonator, the resonant frequencies of the cavity have been calculated using the equations 3.7 and 3.8 for the TE and the TM modes respectively. The calculated frequencies are shown in table 3.16.

Mode	Resonant frequency
TM_{010}	$7.655\,GHz$
TE_{111}	$7.704\,GHz$
TM_{011}	$9.143\,GHz$
TE_{211}	$10.932\,GHz$
TE_{112}	$11.590\,GHz$
TM_{110}	$12.197\,GHz$
TM_{012}	$12.593\,GHz$
TM_{111} and TE_{011}	$13.182\,GHz$
TE_{212}	$13.947\,GHz$
TE_{311}	$14.277\,GHz$
TM_{112} and TE_{012}	$15.772\,GHz$

Table 3.16: Calculated resonant frequencies for the measurements cavity.

According to simulations, the fundamental mode of the resonator, $TE_{01\delta}$ would be at $13.3GHz$ so the resonant modes of the cavity will not affect the resonance.

For exciting the modes coupling loops will be used as they couple well the fundamental mode of the resonator. The VO_2 changes its conductivity with a change in the temperature so the material needs to heated. In order to do that, the whole structure is heated using a resistance. The metallic cavity is placed on top of the resistance and when a voltage is applied to the resistance, this is heated and the whole structure increases its temperature. The measured temperature(from ambient to $90°C$) has been measured on top of the cavity.

As we are mainly interested in optical control, the idea in the future is to heat the VO_2 using an optical source not a resistance as we have done in these measurements. Having the VO_2 in precise places, would allow us to route the light with high enough intensity to make the material change its state from insulator to conductor.

To place the resonator in the middle of the cavity, a Rohacell disc has been used as this have very low loss tangent ($tan\delta = 0.004$) and its relative permittivity is close to that of the air ($\varepsilon_r = 1.067$).

The measurement setup is shown in Fig. 3.30.

The three different structures presented before in simulations (basic configuration, configuration 2 and configuration 3) have been measured but although the study was made for five different modes, the measurement setup only allowed to

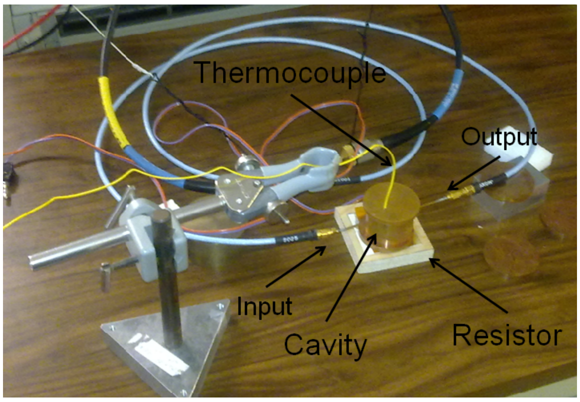

Figure 3.30: Measurement setup used for the dielectric resonator.

excite the fundamental mode so the measured results of this mode will be presented.

On the first step, the cavity without support and resonator as well as the cavity with the support was measured to check if the support could handle the high temperatures as well as to see the variations introduced by a change on the temperature. The measured results of the cavity with the support are shown in table 3.17

Voltage (V)	**Temperature** ($°C$)	$f_0(GHz)$	Q_0
0	20	13.1165	2807
31	37	13.1095	2842
41	45	13.1070	3156
50	75	13.0981	4001

Table 3.17: Measured resonant frequencies for the cavity with the support.

A small change in the resonant frequency is observed with the increase in the temperature while the quality factor becomes higher due to the better conductivity of the copper ($\sigma = 5.96\times^{+7}$ at 20°C and $\sigma = 7.24\times^{+7}$ at 80°C [14]) of the metallic cavity at higher temperatures. This changes will be taken into account in the analysis of the results for the three structures.

3.2.4.1 Basic configuration

The first measured results presented here are the results corresponding to the first studied structure where the sapphire occupies the whole section of the resonator.

The first made measurements correspond to the structure with no sapphire and VO_2 in order to analyze the behavior of the resonator under the temperature. The space reserved for the sapphire will be in this first simulation replaced with a substrate of alumina of the same physical characteristics. Fig. 3.31 shows the measured results in a chart view to plot how the quality factor increases with the temperature while the resonant frequency decreases. The temperature will be achieved with approximately the same voltage as in the previous measurements.

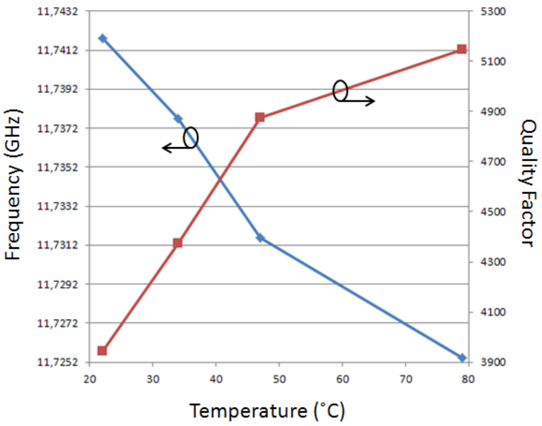

Figure 3.31: Chart of the measured results for the basic configuration without sapphire and VO_2.

From 22°C to 79°C, the change in frequency with the increase in temperature is $16 MHz$ and the increase of the quality factor is of 1200 due to the better conductivity of the copper as explained before. The resonant frequency of this structure loses about $3 MHz$ for a +10°C variation on the temperature.

Resonant frequencies and quality factors of the structure when the conductive material is placed in the middle of the resonator are shown in Fig. 3.32.

The results show that not very big change on the resonant frequency appears with the change of the temperature. The greatest change happens at 61°C where the quality factor starts decreasing. A huge drop of the quality factor is then observed when the temperature gets to 72°C. We clearly see here the modification of the VO_2 conductivity. The thickness of the VO_2 on the sapphire for this structure is only $250 nm$.

Considering that from 61°C to 72°C the overall structure frequency not taking

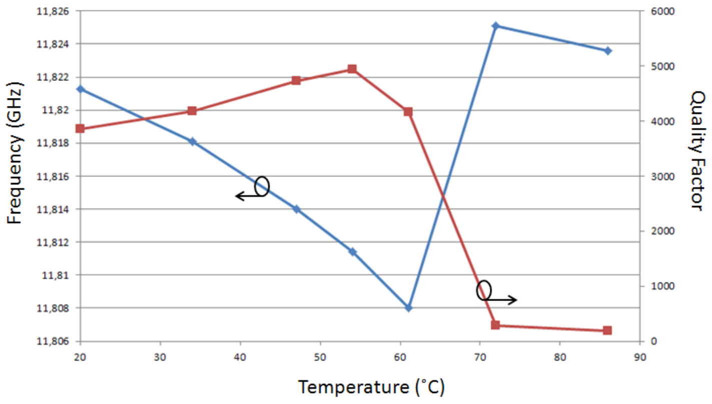

Figure 3.32: Chart of the measured results for the basic configuration with sapphire and VO_2.

into account the VO_2 effect loses about $3MHz$, we can consider that the VO_2 gives a $+20MHz$ shift when heated from $61°C$ to $72°C$. The quality factor is however severely decreased from more than 4000 to 286. The simulation results showed that the VO_2 would provide a quality factor of $Q_0 = 538$ for a conductivity of $\sigma = 1 \times 10^{+5}$ and a $Q_0 = 219$ for a conductivity of $\sigma = 1 \times 10^{+4}$.

Theoretically and referring to the tables 3.6 and 3.7, the VO_2 metal state seems to show a conductivity close and a bit above $\sigma = 1 \times 10^{+4} S/m$ at $11.8GHz$. The $20MHz$ shift observed experimentally is however much lower than the expected variation of at least $150MHz$. Nevertheless, the expected effect when the VO_2 sheet changes its state is observed.

If we consider that the VO_2 layer presents no conductivity at ambient temperature, the simulated unloaded Q showed by the resonator within its cavity is 3930 (3853 experimentally) simulated with a conductivity of the copper of $\sigma = 4.9 \times 10^{+7} S/m$, slightly lower value than the theoretical conductivity of $\sigma = 5.96 \times 10^{+7}$. Considering the experimental results, it would be accurate enough to consider that, without heating, the VO_2 could be considered as a lossless dielectric sheet. When we heat it, the $250nm$ thick VO_2 layer showed a behavior of a metal layer with a $\sigma = 1 \times 10^{+4} S/m$ conductivity.

3.2.4.2 Configuration 2

The same type of study has been carried out for the configuration 2 presented in section 3.2.3 corresponding to one of the optimizations done.

The measured results without conductive materials are shown in Fig. 3.33.

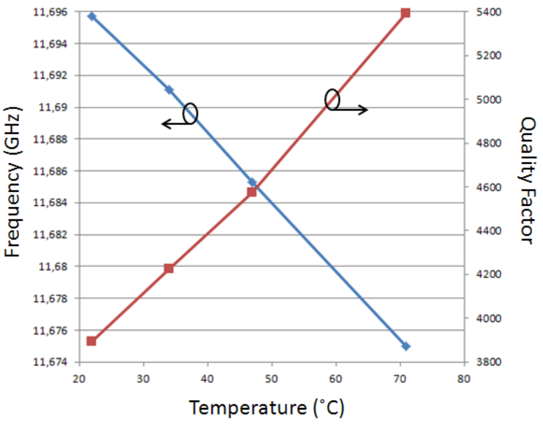

Figure 3.33: Chart of the measured results for configuration 2 without sapphire and VO_2.

Again the change in frequency is around $22MHz$ from $71°C$ to $61°C$ with an increase of the quality factor assumed to be caused by the better conductivity of the metal of the cavity. A graphical view of the results is shown in Fig. 3.33. The structure (dielectric resonator + cavity + support) resonant frequency loses around $4MHz$ for a $+10°C$ temperature increase.

The results of the same structure but with the $VO2$ placed in the structure are shown in Fig. 3.34.

In these results we observed that up until the temperature of $61°C$ the frequency is $4MHz$ less every $10°C$ rise as seen previously. The quality factor also increases as expected.

From $61°C$ to $72°C$ we see a degradation step, with the quality factor going from 4910 to 344 (620 when $\sigma = 1 \times 10^{+5} S/m$ and 275 when $\sigma = 1 \times 10^{+4} S/m$ obtained in simulation). Considering that, without the VO_2 sheet the resonator frequency will lose $4MHz$, we can conclude that the VO_2 sheet heated from $61°C$ to $72°C$ provides a $+14MHz$ frequency shift.

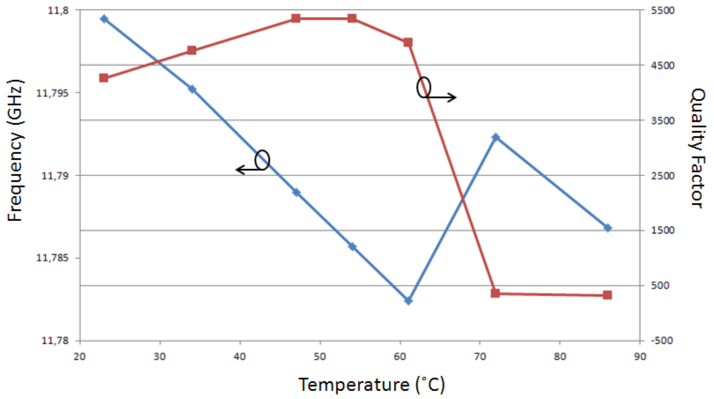

Figure 3.34: Chart of the measured results for configuration 2 with sapphire and VO_2.

Tables 3.8 and 3.9 again show that, on the metallic state, the VO_2 layer shows a conductivity close to $\sigma = 1 \times 10^{+4} S/m$. Again, the frequency shift is less than expected. However, compared to the basic configuration, the quality factor is better with a 344 measured value (286 for basic configuration) and the frequency shift is lower with a Δf of $14MHz$ ($\Delta f = +25MHz$ in the basic configuration).

The trend theoretically expected, i.e. "higher" Δf associated with lower Q is verified here. Finally, when the temperature continues to increase, there is no change in the frequency due to the VO_2, only the change that we obtained without it while the quality factor decreases. We can consider this process the stabilisation step, to continue heating after this point is not useful as it only results in a degradation of the quality factor without changing the frequency.

3.2.4.3 Configuration 3

The last configuration measured is the configuration number 3 and the same process has been followed. The structure without conductive material has been measured and the results are presented in Fig. 3.35.

As in the previous configurations there is a slight frequency shift with a bigger change on the quality factor.

The measured results with the material in place are shown in Fig. 3.36.

The results of configuration 3 show a behaviour close to that of the configuration

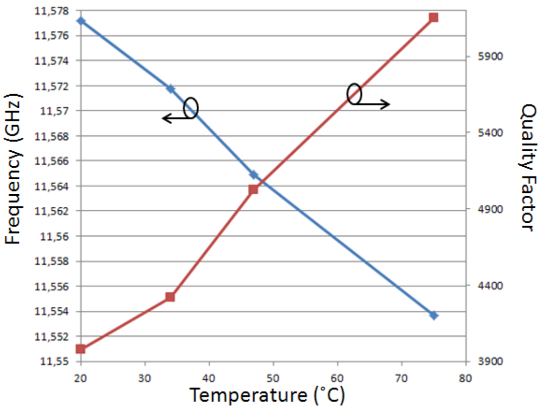

Figure 3.35: Chart of the measured results for configuration 3 without sapphire and VO_2.

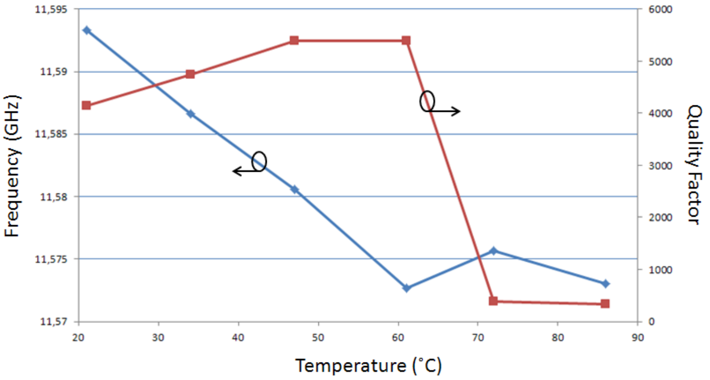

Figure 3.36: Chart of the measured results for configuration 3 with sapphire and VO_2.

2. At the beginning, up until a temperature of $61°C$ the frequency drops about $4MHz$ every $10°C$ while the quality factor increases due to the better conductivity of the metal at higher temperature. However, when the temperature increases, the degradation and the stabilisation happen at the same time as the quality factor drops to 400 with a frequency shift due to the VO_2 layer of about $7MHz$ taking into account the $-4MHz$ shift due to the heating of the overall structure from $61°C$ to $72°C$.

As seen with the configurations 1 and 2, a better quality factor of 394 (286 and 344 for configurations 1 and 2 respectively) when the VO_2 turns into its metal state is expected with a lower frequency shift of only $+7MHz$ ($+25MHz$ and $+14MHz$

for configurations 1 and 2 respectively).

3.2.4.4 Discussion

After the measurements have been done, a post-simulation has been tried to get the values of the conductivity of the VO_2 at low temperature as well as at high temperature. However, from the measured results, where the quality factors are higher than the quality factors in simulations, it has been considered that the VO_2 was lossless at its cold state and that the conductivity when heated has been estimated to be around $\sigma = 1 \times 10^{+4} S/m$.

The results were not optimal due to the large number of variables that were not measurable and could then not be included in the simulation, such as air gaps between the sapphire sheet covered with the conductive material and the resonator itself.

Also, it was not possible to resimulate the structure exactly as it was and to extract the exact values of the conductivity because the thickness of VO_2 was only $250nm$. This thickness is too low compared to the skin depth of the VO_2.

The skin depth is defined as the depth below the surface of a conductor at which the current density has fallen to $1/e$ of the current density in the surface of it. It is normally calculated with the formula in eq. 3.9.

Working at a frequency of $13GHz$ the skin depth for the VO_2 if we consider a conductivity of $\sigma = 1 \times 10^{+4} S/m$ the skin depth is about $\delta = 44\mu m$ and it gets decreased to $\sigma = 14\mu m$ if the conductivity considered is $\sigma = 1 \times 10^{+5} S/m$. The thickness used right now is then too low for the application. A thickness of at least $14\mu m$ would be needed and a thickness equal to some skin depths would be desirable. The conductivity of a material having a skin depth of about $250nm$ would be at least $\sigma = 3 \times 10^{+8} S/m$.

$$\delta = \sqrt{\frac{2\rho}{\omega\mu}} = \sqrt{\frac{2}{2\pi f \mu_0 \mu_r \sigma}} \approx 503\sqrt{\frac{1}{\mu_r f \sigma}}. \tag{3.9}$$

where

ρ: Electrical resistivity in $\Omega \cdot m$.

ω: Angular frequency in rad/s.

μ: Absolute magnetic permeability in N/A^2.

f: Frequency in Hz.

μ_r: Relative magnetic permeability.

μ_0: Magnetic constant $\mu_0 = 4\pi \times 10^{-7} N/A^2$.

σ: Electrical conductivity in S/m.

The skin depth of the VO_2 is quite big. In the future, if the conductivity of the VO_2 could be improved, the skin depth would decrease enormously with the increase of the conductivity of each order of magnitude. For instance, the skin depth of a material with a conductivity of $\sigma = 1 \times 10^{+6} S/m$ is only $\delta = 4\mu m$ and for a conductivity of $\sigma = 1 \times 10^{+7} S/m$ decreases to $\delta = 1.4\mu m$ closer to the thickness of VO_2 that can be deposited right now.

The electromagnetic software used for simulation use finite element methods and it does not allow meshing such small thickness in a structure that is some orders of magnitude bigger.

Table 3.18 shows a summary of the measured results. The frequency shift as well as the quality factor at ambient temperature (Q_{cold}) and at 72°C (Q_{hot}) are shown in this table.

Configuration	Δf **(MHz)**	Q_{cold}	Q_{hot}
1	+25	3853	286
2	+14	4258	344
3	+7	4152	394

Table 3.18: Summary of the measured results for the three configurations.

Fig. 3.37 presents in a graphical way the tradeoff that is needed between the quality factor and the frequency shift. The three different configurations follow this tradeoff as expected and we can conclude from the curves presented that the crossing between the quality factor and the frequency shift would be the best tradeoff. We estimate this tradeoff to be for a frequency shift of $\Delta f = 17MHz$ a quality factor higher than $Q_0 = 330$.

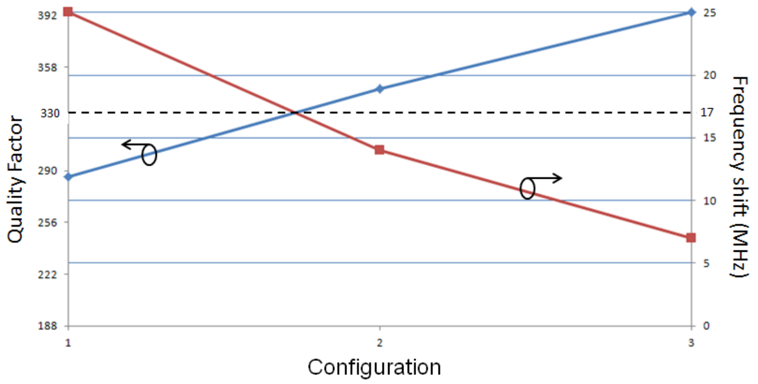

Figure 3.37: Tradeoff between quality factor and frequency shift.

3.2.5 Conclusion

A tunable dielectric resonator has been presented with a thermoconductive material as the tunability method. The theoretical study followed by the electromagnetic simulations have been shown for the fundamental mode working at $13GHz$ as well as for the most interesting modes.

The optimization of the structure have been presented too, both based on theoretical study as well as the response surface methodology. Finally the measured results of the structure have been presented.

In all the states of the study have been observed that a tradeoff between the quality factor and the frequency shift as the increase in the frequency shift would imply a decrease in the quality factor and inversely. The frequency shift observed in measurements means that the VO_2 changes to its metallic state but a strong degradation of the quality factor happens.

The best tradeoff that can be achieved according to the measured results would be a $\Delta f = 17MHz$ and $Q_0 = 330$. The structures measured shows a minimal frequency shift of $\Delta f = 7MHz$ for a maximum quality factor of $Q_0 = 394$ and on the other end a maximum frequency shift of $\Delta f = 25MHz$ for a minimum quality factor of $Q_0 = 286$.

From the measured results, we can simplify the behavior of the VO_2 and consider that at ambient temperature, it is not conductive at microwave frequencies and that it passes to its metallic state with a conductivity of $\sigma = 1 \times 10^{+4} S/m$ at $11.8GHz$.

Once the VO_2 has change to its metallic state, it is useless to continue heating as there would not have an effect on the frequency, only a degradation of the quality factor.

The skin depth of the VO_2 at $13GHz$ is about $\delta = 4\mu m$ if we consider a conductivity of $\sigma = 1 \times 10^{+4} S/m$ so thicker deposition would be needed in order to have a better performance of the filter as some skin depths for the thickness of the material would be desirable.

The VO_2 is a thermoconductive material, so it changes its conductivity with the temperature. However, as we are mostly interested in optical control, the idea is to heat the vanadium dioxide with an optical source of high enough intensity directly to the material.

This behavior of the vanadium dioxide in the 3D resonator could be used for security applications. A filter could be developed that under certain conditions, high temperature more specifically, behaves as an attenuator. Such a structure would need a high sensitivity that would be achieved with this structure where the unloaded quality factor varies from some thousands to about 300.

We have to thank for their help in this work to Prof. Corinne Champeaux for the deposition of the VO_2 on the sapphire substrate. We would like to thank to K. Khoder and Prof. Annie Bessaudou for their help for using the optimization method.

3.3 Photorefractive CdS tunable filter

A new photorefractive material based on cadmium sulfide (CdS) loaded polymer has been presented in Chapter 2. The formulation that exhibited the more significant change of relative permittivity under optical illumination will be employed here.

In this section we are going to present a tunable filter that uses reconfigurable capacitors built with this photorefractive material.

To begin, a new CdS-polymer MIM capacitor will be presented followed by the explanation of the tunable microwave filter. Afterwards the two fabrication runs and measured results will be described.

3.3.1 New CdS-polymer MIM capacitor

The previously presented CdS based material has been used to develop a tunable metal-insulator-metal (MIM) capacitor. As has been explained the main property of this CdS based material is the increase of its relative permittivity (ε_r) when it is illuminated. Such illumination does also cause an increase in the loss tangent ($tan\delta$) of the material.

From the characterization carried out before, we know that our CdS-polymer mix has a relative permittivity of $\varepsilon_r = 4$ under dark condition increasing to $\varepsilon_r = 4.5$ when illuminated which is 13% change. For the loss tangent, the extracted values were $tan\delta = 0.05$ when dark, increasing to $tan\delta = 0.12$ when the material is illuminated.

MIM capacitors are well known structures consisting of two electrodes or plates and a dielectric material between them. In this case, as we need to shine light onto the dielectric material between the metal plates, one of the electrodes must be optically transparent. Therefore, we use indium tin oxide (ITO), an optically transparent metal, for the bottom plate. Fig. 3.38 gives the cross sectional view of the tunable capacitor as well as its equivalent parallel RC circuit model.

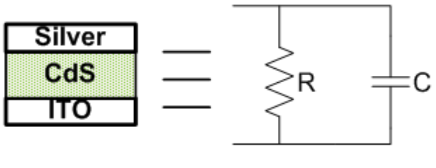

Figure 3.38: Cross section and equivalent model of the MIM CdS-based capacitor.

If we use the common capacitor equation, eq. 3.10, we can see directly that the capacitor value is directly proportional to the relative permittivity of the material.

Therefore, a 13% change on the relative permittivity would provide the same change on the value of the capacitor.

$$C = \frac{\varepsilon \cdot A}{d}. \qquad (3.10)$$

It is demonstrated then that an optically tunable capacitor is possible if we use a photorefractive material.

3.3.2 Photorefractive tunable microwave filter

We present here a proof of concept of an optically tunable band-pass filter based on the variable capacitors just presented. We are going to present first of all a lumped component circuit simulation and we are going to present in the second step the electromagnetic simulation of this filter.

3.3.2.1 Theory

Using the concept of capacitors explained in the previous section, a simple tunable filter concept could be designed. For this proof of concept filter, a design composed of two capacitors connected to ground and an inductor as in Fig. 3.39 is considered. This structure could be used as a loaded line for a phase shifter, but with certain values of the capacitor and the inductor, a bandpass filter can be achieved. For this first schematic an ideal circuit has been simulated without the resistors associated with the capacitor presented in the previous section, just ideal inductor and capacitors. The inclusion of the resistors associated with the component will be carried out later.

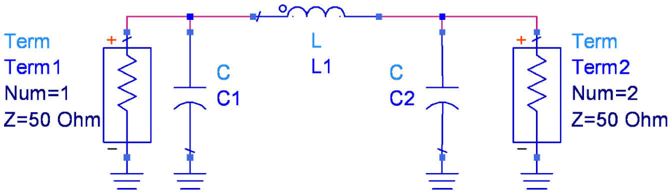

Figure 3.39: Schematic of the proof of concept filter.

If we suppose that there are no constraints in terms of dimensions and that any value of inductor and capacitor can be achieved, a bandpass filter changing its center frequency between $7.5GHz$ and $8GHz$ can be achieved with a change of 13% on the capacitor value. Fig. 3.40 shows the response for an inductor of $L = 0.02nH$ and the capacitors of $C = 40pF$ under dark condition and increasing to $C = 45pF$ when illuminated.

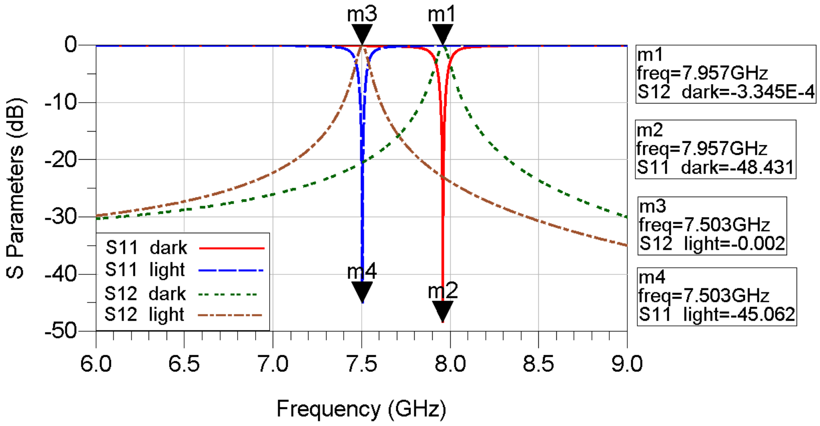

Figure 3.40: Ideal simulation for a lumped component resonator.

Such a filter would be possible if we had no limits in fabrication and no losses. However this will never happen and those limits exist.

Based on eq. 3.10, we can calculate achievable values of the capacitor and from transmission line theory we can extract the value of an inductor that could be fabricated.

Taking this into account, we have simulated a circuit where the inductor is $L = 0.29nH$ and the capacitor value varies a 13% between $C = 2.67pF$ and $C = 3.01pF$. The simulated results are shown in Fig. 3.41.

Comparing the two simulations we observe that a change in the center frequency of around $500MHz$ is achieved varying from $8GHz$ under dark condition to $7.5GHz$ under illumination.

This configuration, normally used for low-pass filter, will then be employed for simplicity of fabrication and for its general adaptability to other filter functions or loaded line phase shifters.

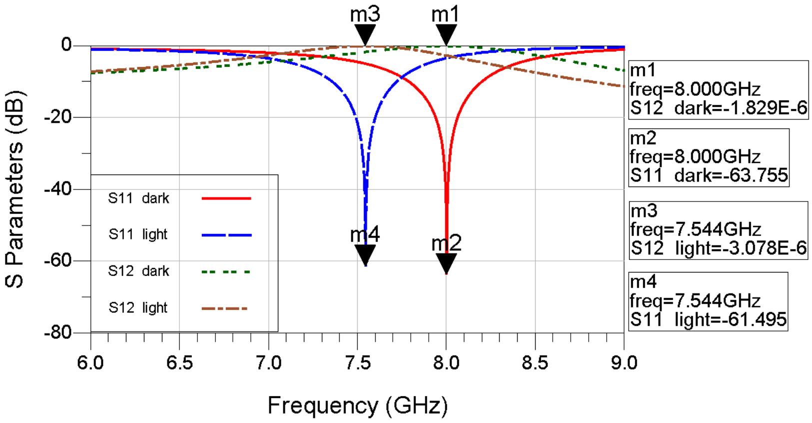

Figure 3.41: Ideal simulation for a lumped component filter with realistic values for L and C.

3.3.2.2 Filter design and EM simulations

The next step is to define the filter in CPW regime with metal-dielectric-metal for the capacitors. As stated before, from the simulated values of the capacitors and the inductor, we can extract the size of the capacitor plates from eq. 3.10 and the width and the gap size of the CPW line from transmission line theory. For the input and the output, 50Ω transmission lines will be used.

The 3D design drawn on the Ansoft HFSS commercial software is shown in Fig. 3.42.

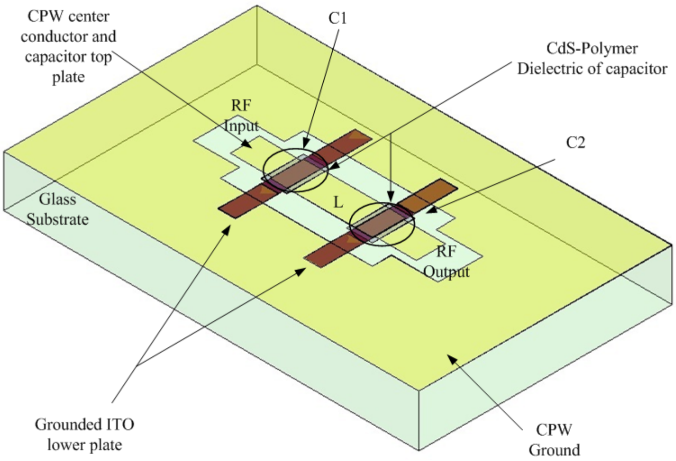

Figure 3.42: 3D structure of the CPW filter.

The connection of the ITO bottom plates to ground is made by straps to the sides of the capacitors as it is shown in Fig. 3.42 and whose detailed view is shown in Fig. 3.43 without the ground plane to facilitate the comprehension of the structure.

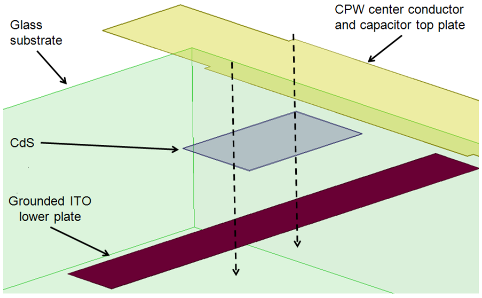

Figure 3.43: Detailed view of the connection between the capacitor and ground.

As a first step, this circuit has been simulated with commercial EM software (Ansoft HFSS). In the simulations, all the metal layers are considered made of silver (conductivity of $\sigma_{silver} = 6.1 \times 10^{+7} S/m$) to show the proof of concept and to verify that the EM simulation matches with the lumped element circuit analysis. For the same reason, the CdS-polymer mix has been considered lossless with a relative permittivity varying between $\varepsilon_r = 4$ when dark increasing to $\varepsilon_r = 4.5$ under illumination. The substrate chosen has been a $600 \mu m$ thick glass substrate whose relative permittivity is $\varepsilon_r = 5$ and loss tangent $tan\delta = 0.005$. The simulation results for both simulated cases under dark and illumination conditions are shown in Fig. 3.44.

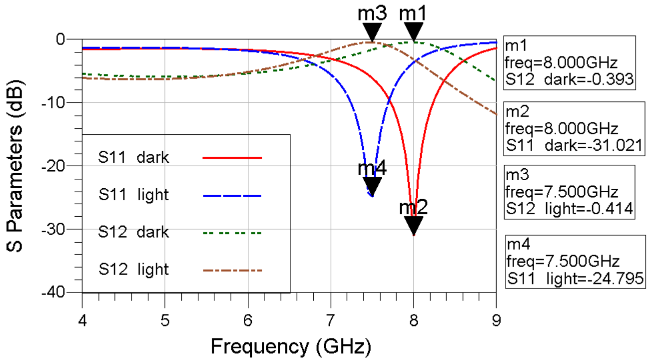

Figure 3.44: Electromagnetic simulation of the bandpass filter without losses.

Comparing the results of the simulations of the lumped component circuit presented in Fig. 3.41 with the electromagnetic simulation results presented in Fig.

3.44, we observe that the filter is resonating at the same frequency of $8GHz$ in dark condition and at $7.5GHz$ under illumination. On the other hand, we observe that the insertion losses have increased. The reason for this is that in lumped element circuit, no losses were taken into account whereas in the first electromagnetic simulation we have included the low losses of the glass substrate as well as the finite, although very high, conductivity of the silver.

In the next simulation, we are going to take into account the losses of the CdS-polymer mix from the extracted values of the previous chapter. The conductivity of the ITO will be defined as $\sigma_{ITO} = 5 \times 10^{+5} S/m$ [15]. However, this conductivity is extracted at low frequencies and it will not be so high at the microwave frequencies we are working at. Fig. 3.45 shows the electromagnetic simulation results for the structure with the all losses included.

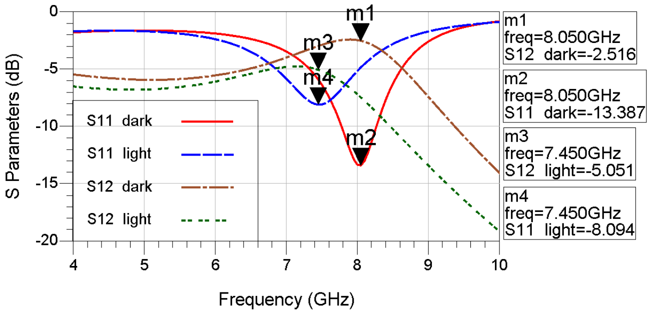

Figure 3.45: Electromagnetic simulation of the bandpass filter with losses.

As it can be seen, the response is quite deteriorated when we include the losses from the CdS-polymer material. We still can observe the filter response but it is quite lossy, especially when the material is illuminated. The shift in frequency is still observed changing the frequency from $8.05GHZ$ to $7.45GHz$. The losses for the OFF state are around $2.5dB$ with a rejection of about $-13dB$ and these performances decrease in the ON state to about $5dB$ of insertion losses and a rejection coefficient of $-8dB$.

More losses would be present with the fabrication as the ITO conductivity will certainly be less than $\sigma_{ITO} = 5 \times 10^{+5} S/m$ at microwave frequencies and the material is not yet optimized. However, and in order to demonstrate the proposed graph, the circuit has been fabricated and the results are presented in section 3.3.3.

3.3.3 Fabrication and measured results

All circuit fabrication was done using standard thin-film process in Carleton University. First of all a layer corresponding to the two bottom electrodes have been developed using a photolithography process. The second step was carried out by Prof. McGarry using screen-printing technique aligning the screen to the underlying pattern (the ITO bottom electrode).The CdS-polymer mix will be the dielectric of the capacitor. Finally, a silver layer was sputtered on top of the circuit with a thickness of $10\mu m$ and then the non needed metal etched off. A close view of the fabricated device is shown in Fig. 3.46.

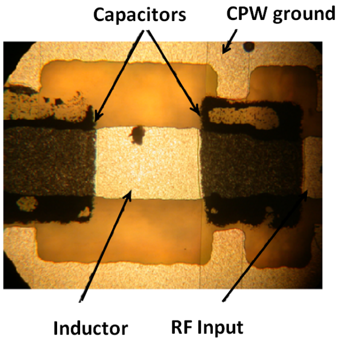

Figure 3.46: Microscope view of the fabricated filter.

In Fig. 3.47 the setup used for the wafer probed measurements is illustrated, showing backside illumination of the circuit. The circuit was illuminated from the backside using a LED array at a wavelength of $450nm$ providing a luminous flux below $800lm$ when applying a forward voltage of $13V$ and a current around $400mA$ at the ports of the array [16]. We have calculated that the optical power provided by the array will be then about $P_{opt} = 1mW$. This optical power is provided by the whole array, but due to the small size of our capacitors, the optical power absorbed by the circuit will be only of about $200nW$ considering that the ITO absorbs no light.

In Fig. 3.48 the measured results of the circuit for both cases, under dark and illuminated conditions. Although an almost negligible difference occurs in the magnitude of the scattering parameters as shown in Fig. 3.48, a more significant change in the phase of the reflection parameter S_{11} can be observed between the

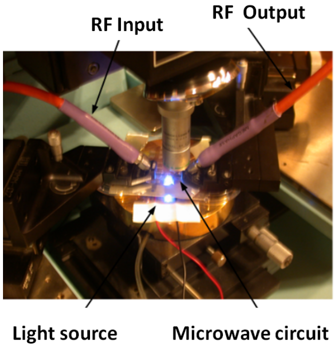

Figure 3.47: Measurement setup for the optically tunable filter with backside illumination.

two states of about 3° at $8GHz$. The measured phase of S_{21} curves for the light and dark states are presented in Fig. 3.49.

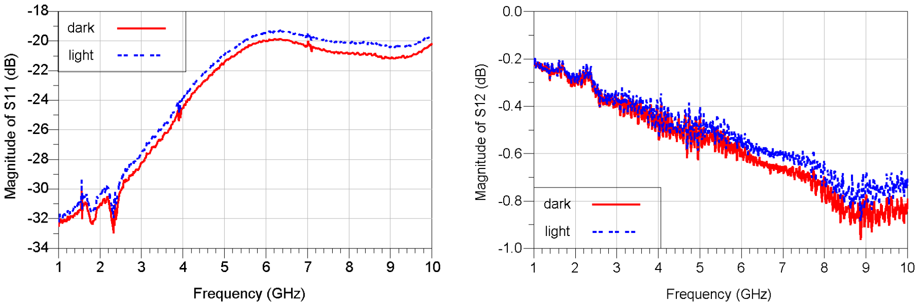

(a) Reflection parameter S_{11}. (b) Transmission parameter S_{12}.

Figure 3.48: Measured magnitude of S parameters for the fabricated device.

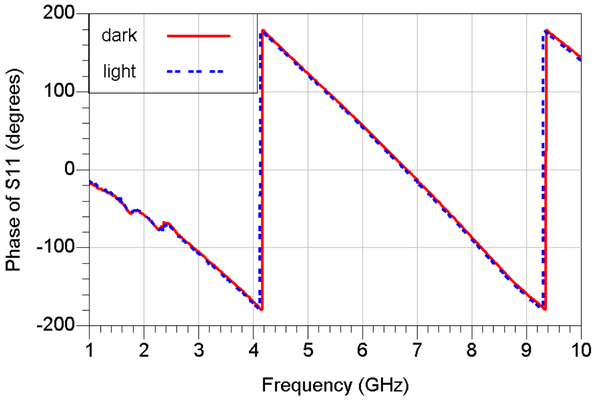

Figure 3.49: Measured phase of S_{11} for the fabricated device.

The expected filter behavior was not seen but this structure was used for its duality with other functions as low-pass filters or phase shifters. There are several reasons for this discrepancy.

First, the losses of the ITO at microwave frequencies were much greater than expected, and so the filter response disappeared with the high resulting resistance and low overall circuit Q. Also, there were some fabrication issues associated with the CdS-polymer mix, such as lack of control with its deposition resulting in an inaccurate size and position of the mix as well as larger thickness of MIM dielectric layer ($\geq 10\mu m$).

Despite the discrepancy between the previously simulated results and the measured results, the fabricated circuit has been modelled to verify the change of the capacitor value with the optical illumination.

In order to understand clearly such behavior, we have divided the fabricated circuit into three parts for the model presented in Fig. 3.50: a series resistor and inductor for the lines between the two capacitors (noted as R_s and L_s); two identical resistors to ground (R_1 and R_2) to model the losses associated with the ITO; and a capacitor-resistor combination for the MIM capacitor itself (R_{1p}, C_1, R_{2p} and C_2).

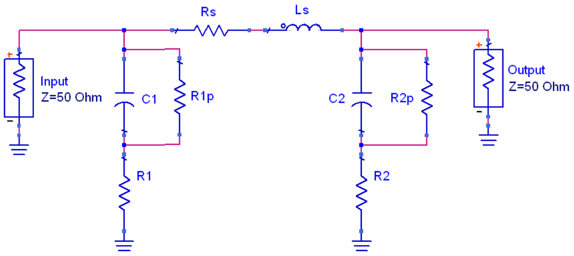

Figure 3.50: Derived equivalent model of the fabricated circuit.

This model is the key for obtaining the capacitance change associated with the light and the extracted values for both measurement cases are shown in table 3.19

State	R_s	L_s	C_1/C_2	R_{1p}/R_{2p}	R_1/R_2
Dark	2.41Ω	$0.53nH$	$0.16pF$	3042Ω	12.5Ω
Light	2.41Ω	$0.53nH$	$0.18pF$	3992Ω	14.5Ω

Table 3.19: Summary of values for the lumped component model.

We see in Fig. 3.51 that the scattering parameter magnitudes for the dark and the illuminated cases are nearly identical. We observe also that the equivalent model (presented in Fig. 3.50) matches the results almost perfectly.

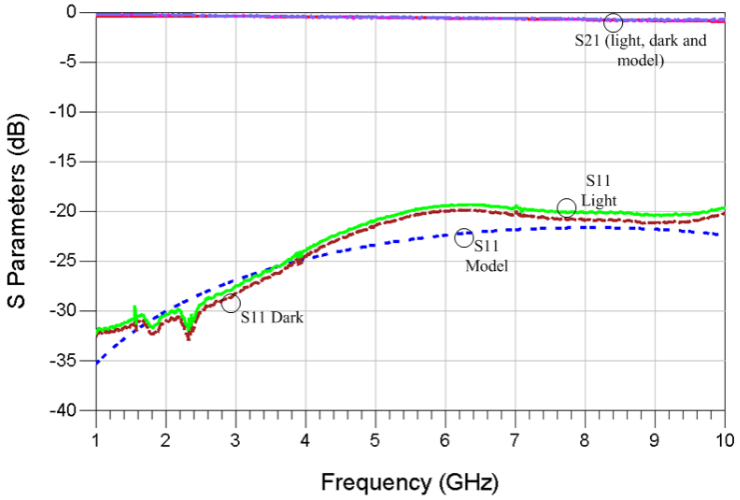

Figure 3.51: Magnitude of S parameters for measured circuit and model simulation.

If we contrast the change in the in the relative permittivity of the photosensitive material with the change in the capacitance value of this novel CdS-polymer capacitor as in table 3.20 we observe as expected a change of 13% in the capacitance value corresponding to the same percentage change in the material's relative permittivity.

Material properties			
ε_r (dark)	$tan\delta$ (dark)	ε_r (light)	$tan\delta$ (light)
4	0.05	4.5	0.12
Capacitor model (Estimated)			
C_{dark} (pF)	R_{dark} (Ω)	C_{light} (pF)	R_{light} (Ω)
0.16	3042	0.18	3992

Table 3.20: Summary of the material properties and the equivalent model of the capacitor.

The only changes in the model due to illumination are the values associated with the capacitor and a slight change in the resistor associated with the ITO.

A comparison for the phase shift between the dark and illuminated states for both the measured results and the simulation results of the model is shown in Fig. 3.52.

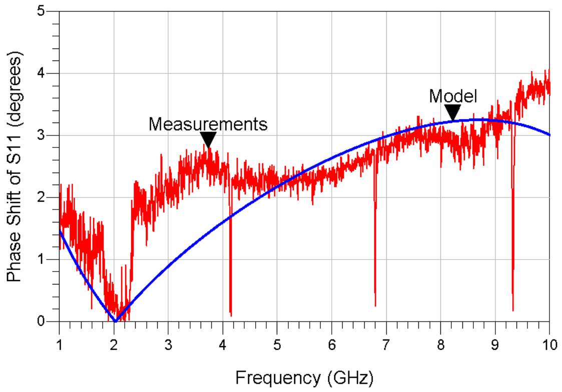

Figure 3.52: Difference in S_{11} phase between light and dark states for the measured fabricated circuit and for the lumped element equivalent model.

Our model closely matches the measured S_{11} phase shift (even small) between the two illumination states, we may conclude then that the tunable capacitor varies by a significative amount under the optical control of the array LED, about 13% as showed in table 3.20.

The main issue with this fabricated device was the ITO as its losses at high frequencies are too high. However, the use of this material may be completely avoided by employing a meshed silver metal lower electrode instead as it will be presented in the next section 3.3.4 to have a working filter instead of the phase shifter we have developed here.

3.3.4 Improvement of the tunable filter

In order to avoid the use of ITO and the losses associated with it, a meshed silver metal lower electrode has been used in an optimized fabrication run. The change on the structure of the filter is just the replacement of the ITO bottom electrode by a meshed silver with 50% of its surface composed of holes in order to allow the light go through. Fig. 3.53 shows a detailed view of the structure focusing on the bottom electrode with the holes. The ground plane has been hidden to make the view more clear.

The electromagnetic simulation has been carried out for both states, light and dark, supposing that the material, even if only the 50% will be directly illuminated,

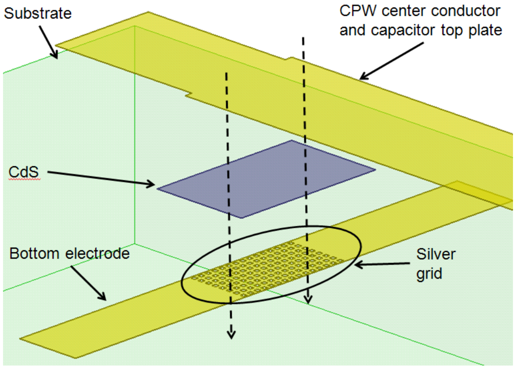

Figure 3.53: Detailed view of the bottom electrode with the argent grid.

will change its state completely. The simulation results in Fig. 3.54 show that the losses related to the fact of having a grid are negligible and that the filter function would appear.

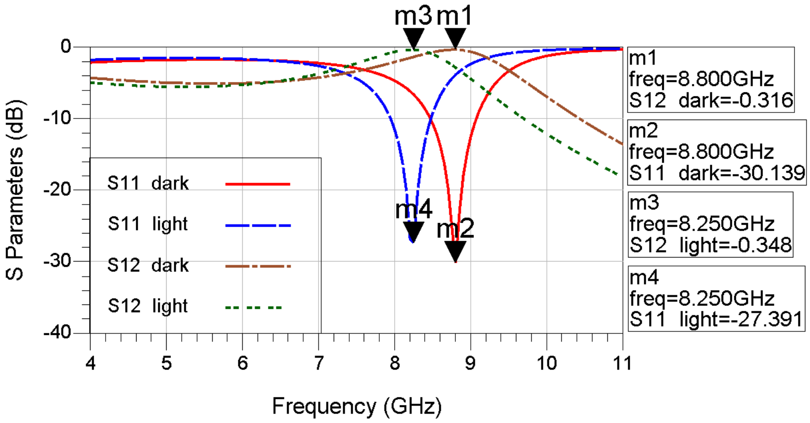

Figure 3.54: EM simulation of the tunable filter with a metal grid as bottom electrode.

We see from the simulations, that in terms of losses, the grid does not introduce any important losses as the grid windows are small enough. The losses are in the same order of magnitude as the losses with a metal surface instead of this grid. However, we have seen an increase on the frequency of work as the filter works now between $8.8GHz$ and $8.25GHz$. Anyways, as we are not pursuing any specific application for this filter, as the frequency shift is still important and as the losses introduced by the grid negligible, this solution seems adequate.

Once the simulation showed that the filter was achievable with low losses even with the metal grid, the filter was fabricated.

The fabrication process was similar to the previous one. In the first place the bottom electrode with a metal grid was deposited using a metal deposition followed by a lift-off process. The fabricated bottom electrode is shown in Fig. 3.55.

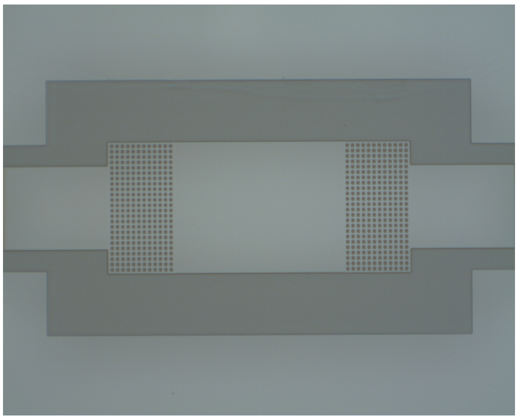

Figure 3.55: Fabricated bottom electrode of the tunable filter.

The process continued with the deposition by Prof. McGarry of the photorefractive material, again using screen-printing. The final step is the deposition of the top layer. The sputtering process used in previous runs showed that shorted circuit were very likely so the process used this time was an evaporation technique made by the NRC-CNRC (National Research Council from Canada).

The fabricated devices were measured using a similar setup as previously with the same LED array configuration to provide the light. The measured results are presented in Fig. 3.56.

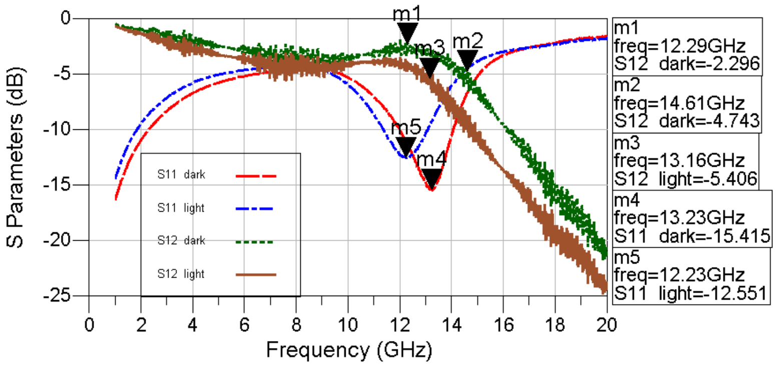

Figure 3.56: Measured results of the tunable filter with a grid.

Again, most likely due to the inaccuracy and lack of control of the thickness of the deposition of the CdS-polymer mix, the measured response do not match the simulated response.

Nevertheless, when it was decided to use this simple structure, the main reason was that this structure could behave as a bandpass filter with some specific values of the inductor and the capacitors but it is also a common structure for low-pass filters and phase shifters.

From the measured results, we observed that the reflection coefficient of this device is not very good. However, the transmission coefficient shows a change of the frequency response of almost $1.5GHz$ as the cut-off frequency of the filter varies from $14.61GHz$ to $13.16GHz$ from the dark state to the illuminate state.

As it has been done for the previous run, we want to verify that the change of the capacitance of the developed capacitor is around 13%. The model developed for this filter is very similar to the previously developed one. The only difference is that for this new device, an inductor and a resistor have been included at the input and the output. The model used is shown in Fig. 3.57.

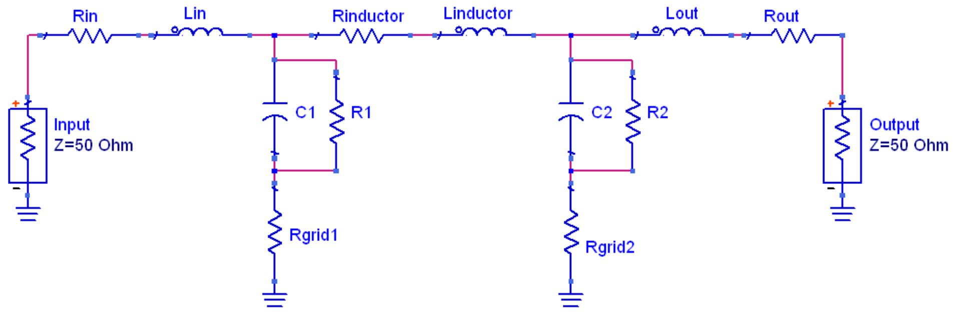

Figure 3.57: Lumped component model for the fabricated low-pass filter.

The lumped component model consists of a resistor and an inductor for the input and the output (R_{in}, L_{in}, R_{out} and L_{out}); an inductor and a resistor too modelling the line between the two capacitors ($R_{inductor}$ and $L_{inductor}$); the capacitors themselves are modelled as a parallel resistor and capacitor (R_1, C_1, R_2 and C_2); and finally the metal grid is modelled by a resistor in series with the modelled capacitors (R_{grid1} and R_{grid1}).

The main difference between the model presented for the previous circuit and the one presented here is that a resistor and an inductor have been added to model the input and the output port. The losses being lower in this circuit due to the replacement of the ITO with a silver grid, the effect of the input and output ports are now more evident and need to be modelled.

The model matches well enough the transmission parameters for both cases as it can be sheen in Fig. 3.58. Unfortunately, the figure shows also that at frequencies below $9GHz$ the reflection parameters do not match so closely.

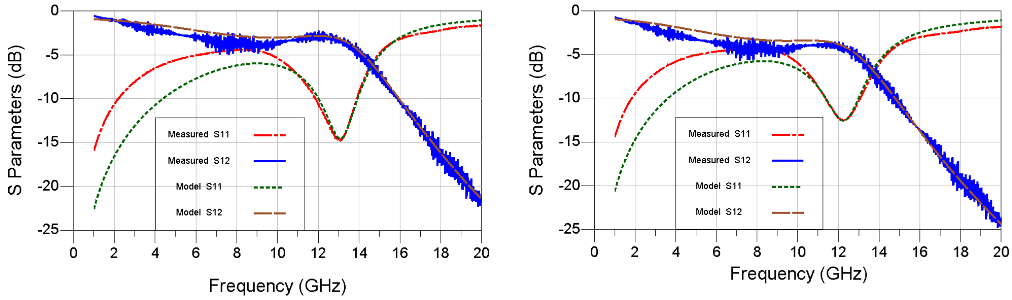

(a) Dark state ($P_{opt} = 0mW$).

(b) Light state ($P_{opt} = 1mW$).

Figure 3.58: Measured and modeled magnitude of S parameters for the fabricated tunable filter device.

The mismatch for the low frequencies is due to the bad quality reflection coefficient measured. Matching a wide band circuit for such a large band $(1 - 20GHz)$ is a really tedious work as more components would be needed. Our goal here being mainly to match the s parameter at the resonance for both states, the obtained results are valid enough. The extracted component values are presented in table 3.21.

State	$R_{in/out}$	$L_{in/out}$	$R_{inductor}$	$L_{inductor}$	$R_{1/2}$	$C_{1/2}$	$R_{grid1/grid2}$
Dark	2.2Ω	$0.49nH$	0.6Ω	$0.58nH$	1000Ω	$0.58pF$	1.3Ω
Light	2.2Ω	$0.49nH$	0.6Ω	$0.58nH$	1000Ω	$0.65pF$	1.9Ω

Table 3.21: Summary of values for the lumped component model of the low-pass filter.

As it can be observed from the table 3.21, the only values that change from the dark to the illumination states are the value associated with the capacitance of the

CdS-polymer capacitor which again increases from $0.58pF$ of about a 13% arriving to $0.65nH$ and the value of the resistor associated with the metal grid. The value of this resistor (R_{grid}) increases due to the contact of the metal with the CdS-polymer matrix becoming more lossy for the lighted state. The two effects cannot be separated and it has been decided to model the lossy effect with the resistor of the metal grid.

3.3.5 Conclusion

In this section an optically tunable capacitor with 13% capacitance change has been developed for the first time. A model of the capacitor has been presented and a possible application has been shown via simulations.

Two fabricated CPW circuits have been measured. Developing a lumped component model for each of the fabricated devices, the functionality of the optically tunable capacitor has been demonstrated. It has been shown that the replacement of the ITO capacitor electrode by a 50% meshed silver electrode reduces the microwave losses very substantially without compromising the range of capacitance variation. This is a very significant result.

Parts of this section have been published at the 2011 European Microwave Conference (see Appendix B).

Although some fabrication issues have come out and that the CdS-polymer material needs to be improved in terms of losses and fabrication tolerances, this hybrid polymer technology shows great promise for future optically tunable microwave circuit design.

On the fabrication side, we intend to improve the deposition of the CdS so the thickness of the material can be completely controlled and then the capacitance value of the capacitors could be defined beforehand. On the material side, a lower volume fill fraction of CdS in the polymer will reduce the losses and also some type of post-processing would be considered in order to maximize the photorefractive effect reducing the losses associated.

3.4 Conclusion

This chapter has focused on direct optical control for tuning passive devices. After explaining the main characteristics of the direct optical control, three different structures have been presented using this effect.

In the first place, a novel LTCC filter has been presented showing great promise if a photoconductive material is used. The structure has been presented as well as a whole study to determine the conductivities of the material needed for the circuit to work properly. The measured results of the first prototypes have been presented showing great promises for future development.

Secondly, a 3D resonator exploiting the photoconductive effect has been presented. Based on the theoretical properties of the previously presented VO_2 material, the study of a 3D resonator showing a low frequency shift with high quality factors or a higher frequency shift with lower quality factors have been presented. The importance of the trade-off between the quality factor and the frequency shift has been explained through simulations and an optimization step presented. Finally, the measured results of this 3D dielectric resonator has been presented confirming the expected behavior and tradeoff, even if frequency shift less than expected from simulations have been measured. Quality factors between 300 and 400 have been observed for the frequency shift from $7MHz$ to $25MHz$ at $11.8GHz$.

Finally, an optically tunable filter has been presented using novel CdS-polymer capacitors. The theoretical study as well as the simulations have been presented showing promising results. However, the measurements did not follow the simulated results due to inaccuracy of the fabrication process but we still were able to show a functional optically configurable phase shifter and a low-pass filter based on these new optically configurable hybrid polymer capacitors.

Through the use of an equivalent lumped circuit model, the 13% permittivity variation of the CdS based polymer (light/dark state) can be modelled by the capacitors having a 13% variation in their capacitance.

All the work presented in this chapter has been carried out with the help of other researchers. We have to thank Prof. C. Champeaux for the deposition of

the VO_2 material on to the sapphire substrate as well as Prof. A. Bessaudou and K. Khoder for the help provided with the use response surface methodology optimization method.

We have to thank also Prof. S. McGarry for the creation of the CdS-polymer material and for its deposition in our samples as well as N. Jess for the previous characterization of the material. Finally we have to thank R. Vandusen for fabricating the photorefractive CdS tunable filter.

Bibliography

[1] S. Vasudevan and A. Shaikh, “Microwave characterization of low temperature cofired ceramic system,” *3rd International Symposium on Advanced Packaging Materials*, pp. 152–157, Mar. 1997. 117

[2] L. Rigaudeau, *Composants 3D en technologie multicouche LTCC. Applications aux fonctions micro-ondes de filtrage et de rayonnement.* PhD thesis, University of Limoges, Oct. 2007. 118, 120, 124

[3] P. Ferrand, D. Baillargeat, S. Verdeyme, J. Puech, M. Lahti, and T. Jaakola, “LTCC reduced-size bandpass filters based on capacitively loaded cavities for Q band application,” *IEEE MTT-S International Microwave Symposium Digest*, pp. 2083–2086, June 2005. 118, 119

[4] M. Lahti, T. Jaakola, and Kondratiev, “Integrated millimeter-wave bandpass filters in LTCC modules,” *VTT Electronics*, 2004. 126

[5] A. Sharma and S. C. Shrivastava, “Analysis of resonant frequency and quality factor of dielectric resonator at different dielectric constant materials,” *International Conference on Recent Advances in Microwave Theory and Applications*, pp. 593–595, Nov. 2008. 134

[6] X. F. Liang and W. D. Blair, “High Q TE_{01} mode DR cavity filters for wireless base stations,” *IEEE MTT-S International Microwave Symposium Digest*, vol. 2, pp. 825–828, 1998. 134

[7] D. Kajfez, *Dielectric resonators.* Tucker Ga.: Noble Pub. Corp., 2nd ed., 1998. ix, 134, 135

[8] G. E. P. Box and K. B. Wilson, “On the experimental attainment of optimum conditions,” *Journal of the Royal Statistical Society. Series B (Methodological)*, vol. 13, pp. 1–45, Jan. 1951. 150

[9] J. P. Muzeau and M. Lemaire, “Reliability analysis with implicit formulations,” in *Probabilistic Methods for Structural Design* (C. G. Soares, ed.), vol. 56, pp. 141–160, Dordrecht: Springer Netherlands, 1997. 151

[10] W. L. Stevens, “Asymptotic regression,” *Biometrics*, vol. 7, p. 247, Sept. 1951. 151

[11] J. Wishart, “Statistical treatment of animal experiments,” *Supplement to the Journal of the Royal Statistical Society*, vol. 6, pp. 1–22, Jan. 1939. 151

[12] A. I. Khuri and M. Conlon, “Simultaneous optimization of multiple responses represented by polynomial regression functions,” *Technometrics*, vol. 23, pp. 363–375, Nov. 1981. 151

[13] N. Delhote, D. Baillargeat, S. Verdeyme, C. Delage, and C. Chaput, “Innovative shielded high Q dielectric resonator made of alumina by Layer-by-Layer stereolithography,” *IEEE Microwave and Wireless Components Letters*, vol. 17, pp. 433–435, June 2007. ix, 158

[14] D. Griffiths, *Introduction to electrodynamics*. Upper Saddle River N.J.: Prentice Hall, 3rd ed., 1999. 160

[15] Delta Technologies, “Unpolished glass ITO on one surface data sheet.” 175

[16] Bridgelux, “Bridgelux ES array series BXRA product data sheet DS11.” 176

Chapter 4

Indirect Optical Control

Contents

In the previous chapter, direct optical control has been explained and demonstrated. The main difference between direct and indirect optical control is the way the photosensitivity is used. In direct optical control, the device to be controlled is illuminated with the optical control signal. The same device performs both optical and microwave functions which often have contradictory design requirements. An alternative scheme is then the indirect optical control where the optical control signal is first converted to a suitable electrical form using a dedicated detector, so the circuit is controlled optically but using an intermediate device such as a photodiode or a phototransistor.

In most of the tunable circuits, the microwave devices require external bias and the control signal is injected directly into the device to adjust its microwave performance. For applications such as reconfigurable and frequency agile antennas, active antenna arrays, beam steering grids, etc., metallic bias wires interfere with the radiation patterns. In these situations, it is desirable that the active devices require no external bias and that the control signal is carried to the devices via optical fibers which, as they are made of low permittivity materials, do not perturb the antenna fields significantly.

Indirect optical control relies on a dedicated photovoltaic detector to convert the optical control signal into an electric bias signal. The electrical output from the photovoltaic detector controls the operating point of the microwave device and, thereby, the microwave characteristics of the device. Since the optical signal performs both bias and control functions, there is no need for external bias circuitry and bias leads.

Another advantage of indirect optical control is that, since the optical detection and microwave functions are separated, the optical and microwave components may be optimized independently of each other. Thus, it is possible to design circuits such that there is no RF penalty for using optical control and, at the same time, make the optical process very efficient so that minimum optical powers are required.

Indirect optical control has been used previously for high frequency applications. Nagra *et al.* developed in [1] a monolithic optically variable capacitor with a maximum capacitance variation at $10GHz$ from $1.1pF$ to $0.47pF$ from a dark condition to a light condition where the optical power was $3.2mW$. This can be seen in Fig. 4.1.

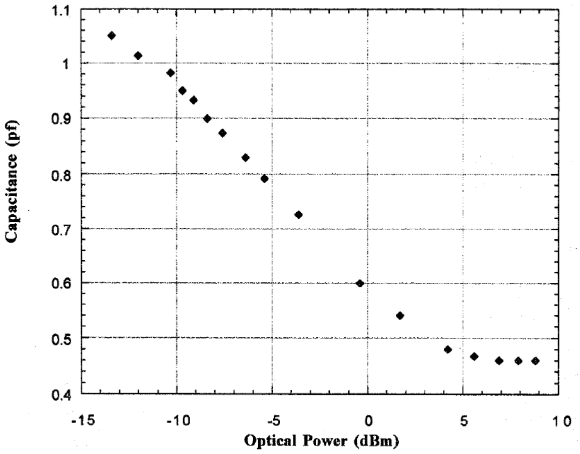

Figure 4.1: Capacitance extracted from S parameters at $10GHz$ [1].

In [2], the authors present the two structures of Fig. 4.2. The optical variable capacitor is comprised of a photovoltaic (PV) array that controls the reverse bias across a varactor diode. A change in the incident optical control leads to a change in the PV array output voltage. This varies the depletion width of the varactor diode and, thereby, its junction capacitance. Hence this arrangement makes it possible to control the capacitance using optical signals.

There are several advantages to this method:

- The optical signal is used for bias, as well as control of the active device, thus eliminating the need for external bias.
- Since the PV array drives a reverse-biased varactor diode, the optical power requirements are small.
- The optical detection and variable capacitance function are provided separately and, hence, it is possible to optimize them independently. The varactor diodes are designed to provide the desired capacitance swing with the lowest possible RF insertion loss while the PV arrays are designed to provide the desired bias swing across the varactors using as low optical power as possible.

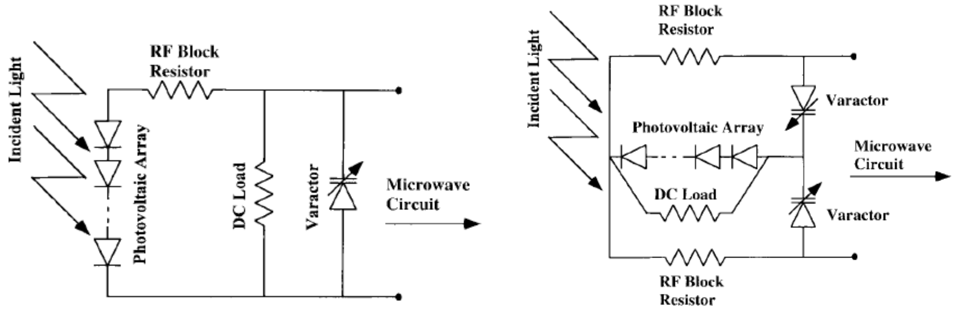

(a) Structure 1.

(b) Structure 2.

Figure 4.2: Circuit schematics for the optically variable capacitor (OVC) [2].

The configuration shown in Fig. 4.2(a) is well suited for applications using several devices in series, since the photovoltage across each optically variable capacitors (OVC) is floating without any common ground. For applications where several OVCs are connected in parallel, it is desirable to have independent bias control over each one and the configuration shown in Fig. 4.2(b) may be used. The advantage of this configuration is that the DC bias voltage does not appear across the two microwave terminals due to back-to-back varactor diode arrangement. Also the configuration in Fig. 4.2(b) has higher RF power handling capability and better linearity than the simpler configuration in Fig. 4.2(a). The improved linearity is due to the fact that the capacitances swing induced by the RF voltage is opposite for the two diodes and cancels each other to the first order.

However, the problem with this approach presented in these papers, is that a state-of-the-art and quite expensive technology is used. The $GaAs/AlGaAs$ material system has been used for the fabrication of the miniature photovoltaic (PV) arrays for several reasons:

- $GaAs$-based PV arrays are sensitive to light with wavelength less than $880nm$, hence, relatively inexpensive semiconductor laser diodes/LED's can be used as illumination sources.
- Varactor diodes fabricated on $GaAs$ have higher cutoff frequencies than corresponding silicon-based devices and can be easily integrated with the $GaAs$ PV arrays.
- Semi-insulating $GaAs$ is a good substrate for microwave transmission lines.
- $GaAs$ technology is widely used in monolithic-microwave integrated-circuit (MMIC) applications.

In [2], the authors have shown the use of these OVC on a tunable notch filter. The equivalent circuit of the designed filter is shown in Fig. 4.3(a).

The circuit was fabricated in the same $GaAs$ wafer as the OVC. The filter consists essentially on a single-shunt resonator with the OVC embedded in the resonator to alter the resonance frequency. Under illumination, the PV-array increases, which, in turn, causes the varactor capacitance to decrease. As a result of lower capacitive loading, the resonance shifts upward, as can be verified from Fig. 4.3(b), which shows the transmission through this structure for different levels of illumination. The rejection in the stopband is greater than $20dB$, and the tuning range is from $4GHz$ when no illumination is applied to $5.9GHz$ under an optical power of $1.5mW$.

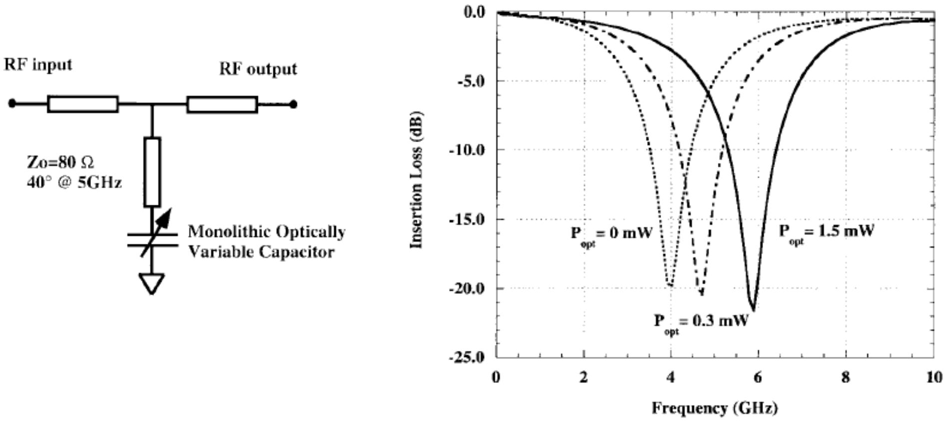

(a) Equivalent circuit.

(b) Measured performance.

Figure 4.3: Optically tunable notch filter incorporating integrated OVC [2].

In [3], an improvement of these optically varactor diodes is emplloyed a phase shifter and a slot antenna.

The phase shifter circuit consists of a high impedance line periodically loaded with varactor diodes. In the small signal or linear regime, the varactor diode loaded transmission line behaves like a synthetic transmission line whose phase velocity can be varied by changing the capacitance of the loading varactor diodes.

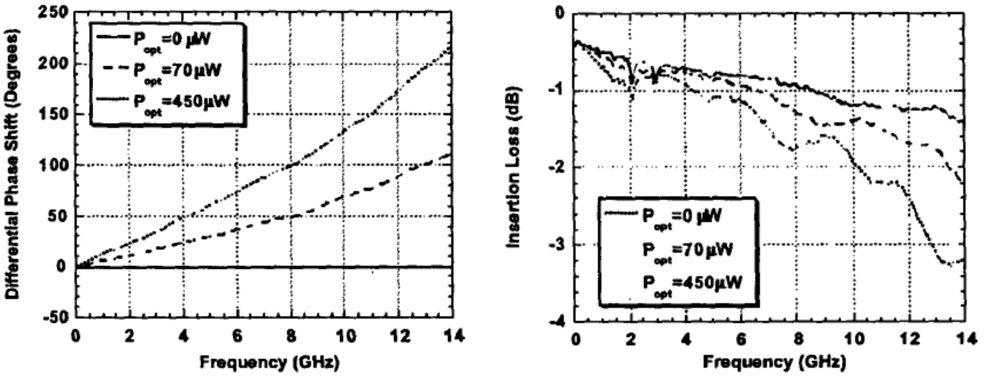

(a) Differential phase shift.

(b) Insertion loss.

Figure 4.4: Measured results of the optically controlled phase shifter [3].

The optically controlled phase shifter circuit generated a maximum phase shift of 175° at $12GHz$ when the optical power was increased from 0 to $450\mu W$. Fig.

4.4 depicts the phase shift and insertion loss for different optical power levels. The maximum insertion loss for this circuit was $2.5dB$ and the return loss was better than $12dB$ over all illumination states.

An optically tunable folded slot antenna incorporating the OVC as the tunable element is shown in Fig. 4.5(a). When optical power is incident on the OVC, the varactor capacitance decreases thus causing the resonance frequency to increase. Fig. 4.5(b) shows that the folded slot antenna resonance frequency can be tuned from $14.5GHz$ to $16GHz$ by using just $450\mu W$ of optical power.

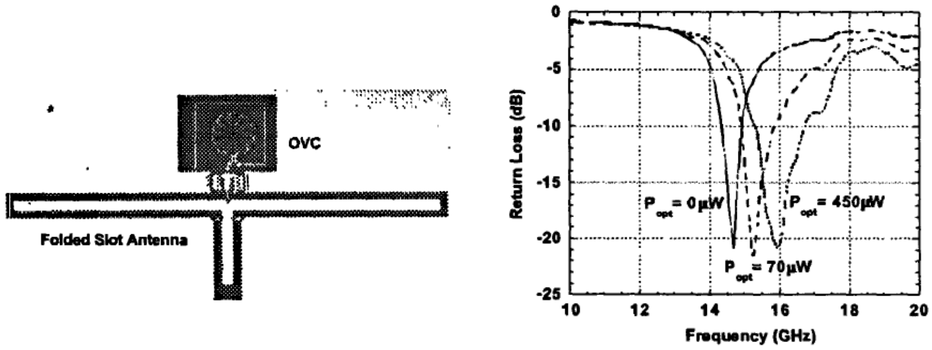

(a) Fabricated device.

(b) Return loss.

Figure 4.5: Optically controlled folded slot antenna [3].

Sun *et al.* present a photovoltaic-FET for optoelectronic RF switching in [4]. They built a hybrid PV-FET with a commercial 12-volt $GaAs$ photovoltaic cell and an InP depletion mode JFET. The circuit schematic used is shown in Fig. 4.6(a).

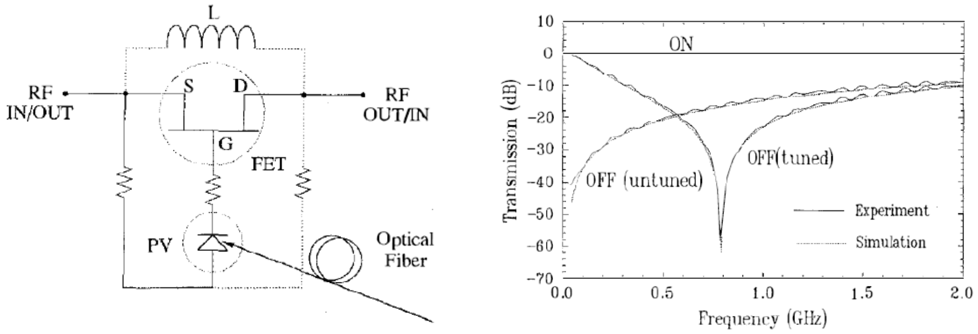

(a) Circuit schematic.

(b) Measured insertion loss and isolation.

Figure 4.6: Photovoltaic-FET for optoelectronic RF switching [4].

Fig. 4.6(b) shows the insertion loss and the isolation of both tuned and untuned PV-FET switches as a function of signal frequency. The insertion loss is $0.33dB$ and $C = 300fF$ the switch capacitance estimated from the untuned isolation of $17dB$ at $790MHz$. The PV-FET was then tuned at $790MHz$ with an inductor of $130nH$ to enhance isolation from the untuned $17dB$ to $57dB$ at the tuned frequency. The tuned switch operated from $580MHz$ to $1070MHz$ with an isolation lower than $-20dB$.

Based on these ideas, in this chapter we are going to explain the design of a zero-bias optically controlled RF switch in standard $0.13\mu m$ CMOS technology as a practical low-cost alternative to the expensive tailor-made technologies used in the reviewed papers for these circuits.

4.1 Zero-bias optically controlled RF switch

As presented in chapter 1, RF circuit reconfigurability and tunability are increasingly important requirements for advanced wireless components that are now expected to cover multiple operating frequency bands, dynamically alter their impedance matching conditions, or provide adaptive antenna characteristics.

The RF switch is one of the most fundamental devices enabling such circuit reconfigurability. However, to date, the available electronic (PIN diode, FET) [5, 6] or MEMS [7] switching devices mostly employ biasing voltages or currents to operate properly, causing a degradation of the circuit's functionality (bandwidth, linearity, efficiency, etc.).

The main motivation of this work is then the need to develop passive, miniature, low-cost switches for adaptive RF circuits without relying on an external DC source.

Optical control of RF switches would be advantageous for agile microwave circuits because high isolation can be maintained between the controlling signals and the microwave circuit itself, due to the fact that the optical waves do not interact with the RF/microwave signal.

Several researchers have attempted to realize optically controlled switches in standard CMOS technology [8] but never for operation at higher frequencies extending into the microwave band. At such frequencies, optoelectronic RF switches have been developed, although these employ much more costly or difficult to access technologies such as InP or $GaAs$ [9]. Recently, major integrated circuit (IC) foundries such as IBM and Intel have been working on the integration of photonics in their fabrication processes in order to realize new types of optoelectronic integrated circuits (OEICs).

In this section we are going to present a new, passive (zero-bias) RF switch using a standard $0.13\mu m$ Si CMOS technology controlled by built-in photodiodes. We are going to explain firstly the technology chosen, followed by a description of the basic device concept as well as its design by way of circuit schematics and chip layouts. Later on, we present both the DC and RF measurements that have been carried out on the fabricated samples. A complete characterization of the chip will be given too. Finally, we will focus on the future prospects of this work and future improvements to the RF switch that may be easily implemented.

4.1.1 Technology

The technology chosen for this work is a commercial silicon RF process, the IBM industry standard CMOS $0.13\mu m$ process more specifically.

The $0.13\mu m$ process refers to the level of semiconductor process technology that was reached in the $2000 - 2001$ time frame by most leading semiconductor companies, like Intel, Texas Instruments, IBM and TSMC.

The origin of the $0.13\mu m$ value is historical, as it reflects a trend of 70% scaling down every $2 - -3$ years. The naming is formally determined by the International Technology Roadmap for Semiconductors (ITRS).

This technology features high density $0.13\mu m$ CMOS logic intended for RF and high speed analog and mixed signal applications, and in this work is provided by IBM Microelectronics.

The IBM CMOS $0.13\mu m$ advanced process technology features $130nm$ lithography. The fine lines and high densities characterizing this state-of-the-art silicon process can support leading-edge microprocessors, communications and computer data processing applications. This process uses low-resistance copper wiring at all metal levels, enabling high wiring density with minimal timing delays. Up to three thick copper wiring metal options provide design flexibility.

This process includes FET structures that support high-frequency RF-compatible models, a broad range of optional passive devices and wiring with a thick last metal ($4\mu m$). A high-quality analog design kit ensures close correlation between simulated and measured performance. This IBM technology is an ideal semiconductor technology for low-cost, high-performance wireless applications such as Bluetooth technologies, local area networks and global positioning systems.

This CMOS process offers [10]:

- Up to 8 metal layers: three thin ($0.29\mu m$,$0.35\mu m$ and $0.32\mu m$), two thick ($0.55\mu m$) and three thick RF-top metals ($0.46\mu m$, $3\mu m$ and $4\mu m$) suitable for high-Q inductors.
- Supply voltage: $V_{DD} = 1.2V$ core and $V_{DD}2.5V$ input/output.
- Substrate resistivity of $1 - 2\Omega \cdot cm$.
- Twin well CMOS technology on non-epi P^{-} substrate.
- Shallow trench isolation.
- Dual gate oxide with physical thickness of $2.2nm$ and $5.2nm$.
- Minimum lithographic image of $0.12nm$ for gate only.
- Low resistance Co salicided N^{+} and P^{+} polysilicon and diffusion areas.
- Planarized passivation and interlevel dielectric with low-K value.
- Wire-bond pads or controlled collapse chip connections
- Optional Electronic Fuse.

Fig. 4.7 shows the cross section of the process (not drawn to scale) to illustrate the different layers of the technology. It should be noted here that this RF CMOS process has no intended provisions for photovoltaic devices (photodiodes) and suffers from significant gate leakage (non zero DC current into the gate) due to the $2.2nm$ ultra-thin gate oxide layer.

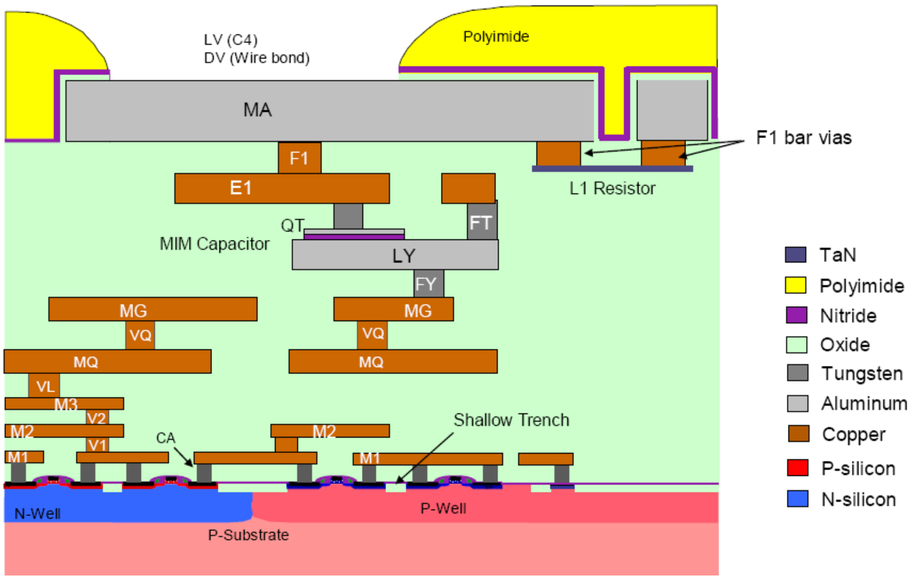

Figure 4.7: Cross section of the IBM CMOS 0.13μm technology [10].

4.1.2 Circuit design and layout

The basic concept of the proposed single-FET RF switch is to provide a low or high impedance path between drain and source by turning the transistor ON or OFF, making V_{gs} greater or smaller than the threshold voltage (V_T) [5, 6] with a dark or illuminated photodiode placed in the gate circuit. Commercially available 0.13μm Si CMOS technology is appropriate for this application, as it provides good quality RF transistors and a simple p-n diode process that could allow the realization of stacked photodiodes (although with no available models to predict photodiode performance).

The devices fabricated on a Si CMOS process are normally very sensitive to optical illumination as silicon is sensitive to light, even broadband low power lights. In order to avoid this sensitivity, the circuits are by default shielded with the top metal layers and with a salicide layer that prevent the light to get to lower layers of the stack. In order to create photodiodes sensitive to visible light sources, we substracted all the metal layers and the salicide layer from the top of the p-n junction of a common diode. In this way, when the chip is illuminated, the light will excite the carriers on the silicon and therefore the p-n junction, creating a voltage at the terminals of the photodiode.

The main technical challenges of this work are the generation of sufficient photo-induced gate voltage using small area diodes, and the achievement in the RF path of low ON-state insertion loss and high OFF-state isolation using no externally applied bias. We believe it is due to these challenges that no previous attempts have been made to create an optically controlled switch in this manner.

The schematic of the designed opto-RF switch is shown in Fig. 4.8.

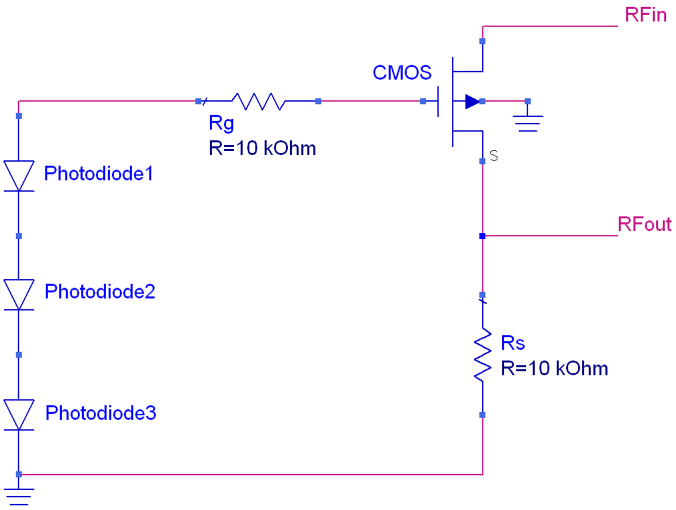

Figure 4.8: Basic circuit schematic of the RF CMOS switch.

As can be seen, this proof of concept circuit is very simple. It consists of only three series photodiodes (potentially generating up to $2.1V$) connected to the gate of a CMOS transistor, which will control the ON/OFF state of the transistor itself. The drain and source of the transistor constitute the RF input and output ports, respectively.

For simulation purposes, the photodiodes have been replaced with a variable DC source, whose value will represent the voltage provided by the three stacked photodiodes. For the RF$_{in}$ and the RF$_{out}$ we have defined two 50Ω ports at which the S parameters will be determined. The schematic used for simulation is shown in Fig. 4.9(b).

The curve at 1 in Fig. 4.9(a) is the conventional diode characteristic correspond-

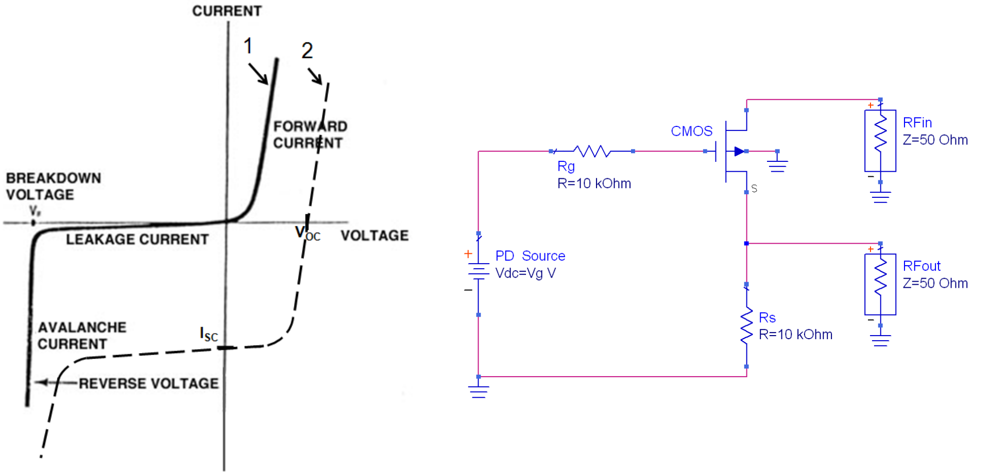

(a) I-V curve of a diode. (b) Simulation schema for the RF CMOS switch.

Figure 4.9: Diode curve and simulation schema for the RF CMOS switch.

ing to operation in the dark state. When light strikes the photodiode, the curve shifts to 2, showing a maximum voltage V_{OC} generated at the terminals (when the photodiode is open-circuited) or a maximum current I_{SC} available from the device (under short-circuit conditions). These extreme conditions are represented by the circuit in Fig. 4.10.

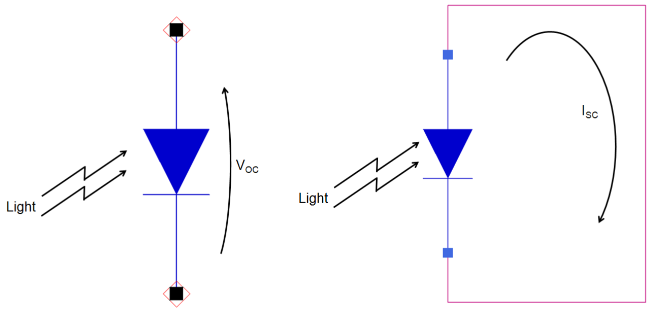

(a) Schematic defining V_{OC}. (b) Schematic defining I_{SC}.

Figure 4.10: Photodiode circuit defining open- and short-circuit operating conditions.

The general photodiode equivalent circuit is given by Fig. 4.11(a) (valid for optically illuminated diode at DC). This gives rise to the $V_{out} - I_{out}$ relationship shown in Fig. 4.11(b). Clearly, if the gate of the CMOS transistor device draws a current due to gate leakage (say $I_G = I_{operating}$) then the photodiode's maximum voltage V_{OC} will drop to a lower value (say $V_{operating}$). In an ideal case where $I_{out} = 0$, we would expect V_{out} to approach $V_{OC} = 0.7V$ for a Si diode; however, realistically, we could expect with leakage the photodiode will produce a substantially lower voltage $V_{operating}$. In the absence of precise knowledge of the p-n diodes photosensitivity and the CMOS gate's leakage current, we estimate $V_{operating} \approx 0.4V$

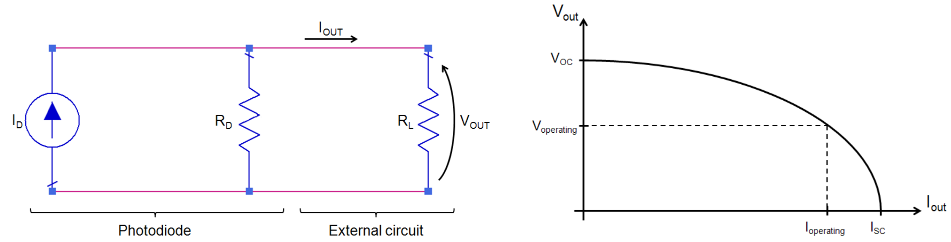

(a) Schematic of a photodiode equivalent circuit.

(b) Output I-V characteristic.

Figure 4.11: Photodiode equivalent circuit and curve.

The transistor gate width has been chosen to be $50\mu m$, provided by 10 fingers of $5\mu m$. This size has been chosen in order to get a switch where the difference between the RF transmission in the ON and OFF states is maximized.

As it has been stated, the photodiodes have been replaced with a DC source in order to determine the number of diodes that would be needed. Table 4.1 shows the simulation results of this circuit using the commercial Cadence CAD software and the IBM $0.13\mu m$ Si CMOS technology design kit. The results correspond to a frequency of $2GHz$.

Voltage on gate	S_{21} **Transmission loss (at** $2GHz$**)**
$0V$	$-40.7dB$
$0.3V$	$-30.9dB$
$0.6V$	$-2.43dB$
$0.9V$	$-1.15dB$
$1.2V$	$-0.878dB$
$1.5V$	$-0.764dB$
$3V$	$-0.654dB$

Table 4.1: Simulated S_{21} transmission results for $V_{DS} = 0V$.

As expected, it can be deduced that the increase of the gate voltage produced by the diodes beyond $V_T = 1.2V$ reduces the resistance in the RF path through the transistor resulting in a reduction of the switch's transmission losses. It is important to note that the simulation accuracy may suffer since the transistor model is being used outside of the range normally employed for the RF simulations where normally $V_{ds} \neq 0$.

The ON state, for which we consider the gate voltage to be above about $V_{GS} = 1V$, exhibits a constant insertion loss up to $10GHz$. At the OFF state, below $V_{GS} = 0.3V$, the response is not so flat but it stays well below $-25dB$ for the complete $0 - 10GHz$ band as can be seen in Fig. 4.12.

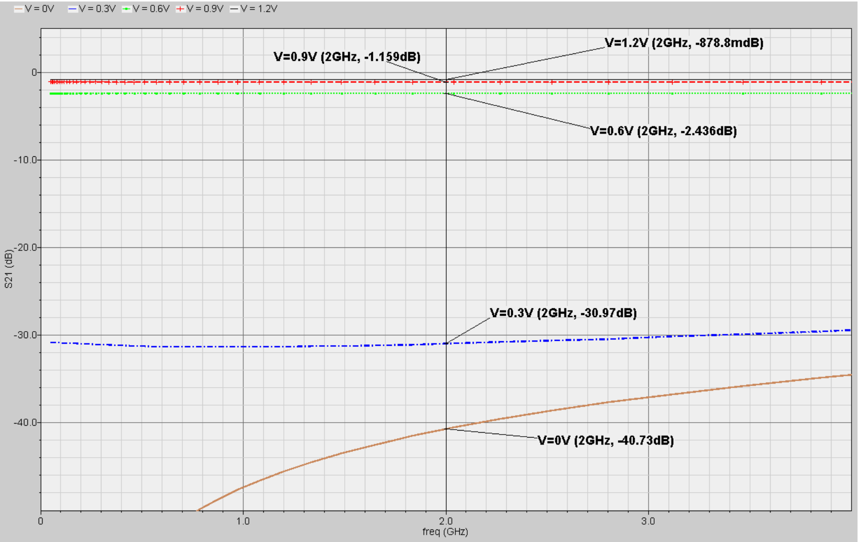

Figure 4.12: Simulation results of the S_{21} parameters of the RF CMOS switch.

These results confirm that three photodiodes should be employed, each one providing at least $0.4V$ in order to obtain sufficient ON state gate voltage, above $1.2V$ and having then transmission losses between the RF ports that are below $1dB$.

Once the design of the circuit was finalized, with the size of the transistor decided, the values of the resistors chosen and the number of stacked photodiodes to place determined, the layout was produced with all the components built-in. Fig. 4.13(b) shows the core layout as created in the Cadence environment.

Note that this is not the complete layout, since the pads and I/O connections

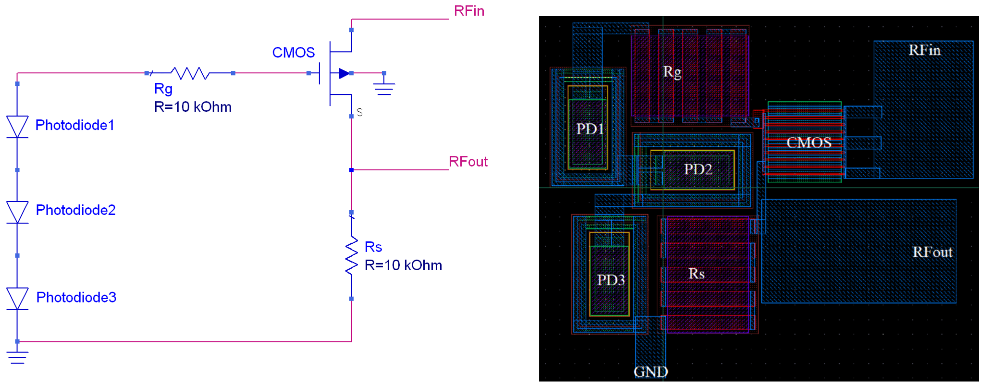

(a) Circuit schematic. (b) Layout.

Figure 4.13: *Si* CMOS switch.

have been omitted to allow important device details to be seen. The diodes measure $5\mu m$ by $8\mu m$ each and the overall chip size incuding I/O pads is $230\mu m$ by $240\mu m$. These dimensions fulfill the small area and low cost objective of this work, while remaining within the strict metal density limits of the "design-rule check" of the IBM process (the metal density rule being easily violated by the large metal openings required for the photodiodes).

4.1.3 Fabrication and measured results

The circuit has been fabricated in IBM's $0.13\mu m$ *Si* CMOS foundry process. Fig. 4.14 shows a photograph of the fabricated chip this containing six separate (nominally identical) switches.

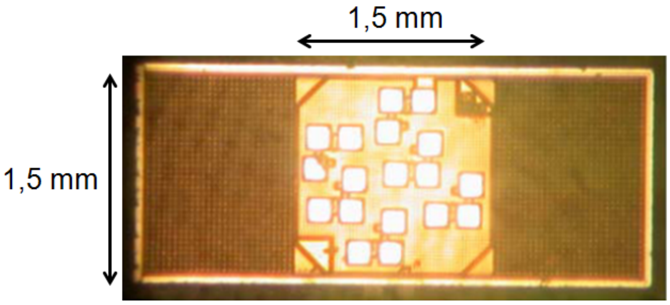

Figure 4.14: Photograph of the fabricated device (6 switches).

4.1.3.1 DC Measurements

The initial characterization of this circuit consisted of measuring its properties at DC to assess its potential in advance of RF measurements. Also, DC measurements are easier to perform and we can access the chip directly with no connector or transition uncertainties in the measurements.

The DC measurements have been carried out using an Agilent 4155 Semiconductor Parameter Analyzer with a voltage source output resistance of $R = 0.3\Omega$ and a voltage measurement input resistance/current source output resistance higher than $10^{13}\Omega$. The light source is a broadband Oriel quartz tungsten lamp (bulb 6333) with maximal emission at a wavelength around $\lambda = 760nm$. The total optical power of this lamp is $0.22W$. The actual power applied to the device can be estimated from the area of the light beam ($5cm^2$) and tha of each photodiode ($40cm^2$). Taking the ratio of these two leads to an optical power of approximately $20nW$ impinging on each photodiode. The DC measured results are shown in Fig. 4.15.

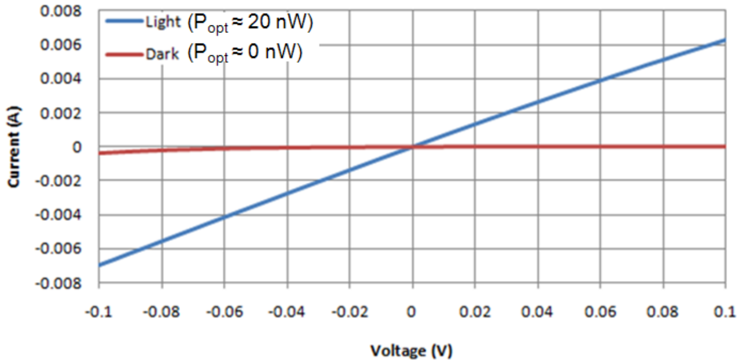

Figure 4.15: DC I-V Measurements of the switch under dark and light conditions.

The I-V measurements points were between the RF_{in} input port and the RF_{out} output port. As can be observed from the curves, when the device is under dark condition, no matter the voltage applied across the ports, the current does not change so the device is in its OFF state. However, when the circuit is illuminated, we see that applying a voltage on the drain and source of the transistor a current flows through it achieving then the ON state of the device.

Following Ohm's law (4.1) we can conclude that for the OFF state the resistance between the two ports is very high as a change in the voltage does not affect the current through the transistor. When we illuminate the device, we observe that the resistance value in the ON state decreases dramatically.

$$R = \frac{V}{I}. \tag{4.1}$$

Table 4.2 shows the resistance value between the ports of both states for this specific circuit.

Light	**Resistance**
Off	3900Ω
On	15Ω

Table 4.2: Simulated S_{21} transmission results for $V_{DS} = 0V$.

These results show that the switch is operational at DC, confirming that the photodiodes are able to turn on the transistor with a moderately powered light source, and that adequate high frequency performance can be expected because of the chosen technology. As cited before, the light source used was an Oriel quartz tungsten lamp (bulb 6333) with a relatively low optical power applied to the RF switch of about $100nW$. However, the circuit shows a change with ambient light (although it does not turn on completely) so we observe that a modest optical power is able to turn the RF switch on completely.

In this first characterization, the switching time has not been measured but we see an instant change when applying the light. As with any Si p-n photodiode, we expect a very fast turn-on time due to the immediate generation of electron-hole paires. The turn-off time will inherently be slower due to the need to discharge the capacitance of the transistor gate to which the diode is connected. A complete analysis of switching speed is beyond the scope of this work.

4.1.3.2 RF Measurements

RF measurements are always more tedious as at high frequencies with any imperfections of the test setup resulting in a change of the response.

For measuring this device at RF frequencies, we have used an Agilent 8722ES Vector Network Analyzer (VNA) and the apparatus shown in Fig. 4.16 to make the transition between the SMA connector of the VNA and the pads of the RF switch. For this first proof-of-concept device the pads were not designed optimally so the use of the probe station was not possible.

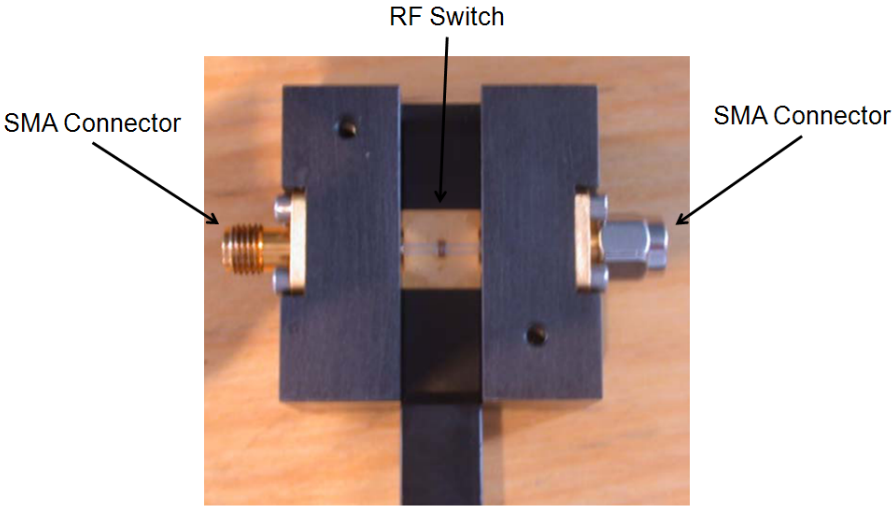

Figure 4.16: Photograph of the RF test fixture.

Although the characterization would need to isolate the effects of the device itself, the VNA calibration could only be done up to the SMA connectors due to the unavailability of calibration substrates for the test fixture employed. Therefore the transition was not taken into account and it has been seen that some resonances appear in the measured results at frequencies above $2.2GHz$.

We therefore present here the results only from $200MHz$ to $2.2GHz$ as the transition is free of resonances on that band. Fig. 4.17 shows the RF measured results for the switch using the same light source as before.

The results confirm the switching operation of the circuit, with more than $20dB$ difference between the ON and the OFF states at $2GHz$, this difference increasing to more than $30dB$ at $1GHz$. However, the insertion losses of $6.8dB$ are too high for the ON state as we expected lower values from simulation. Some of these losses might be due to the transition but we consider that they are mostly associated with the switch itself.

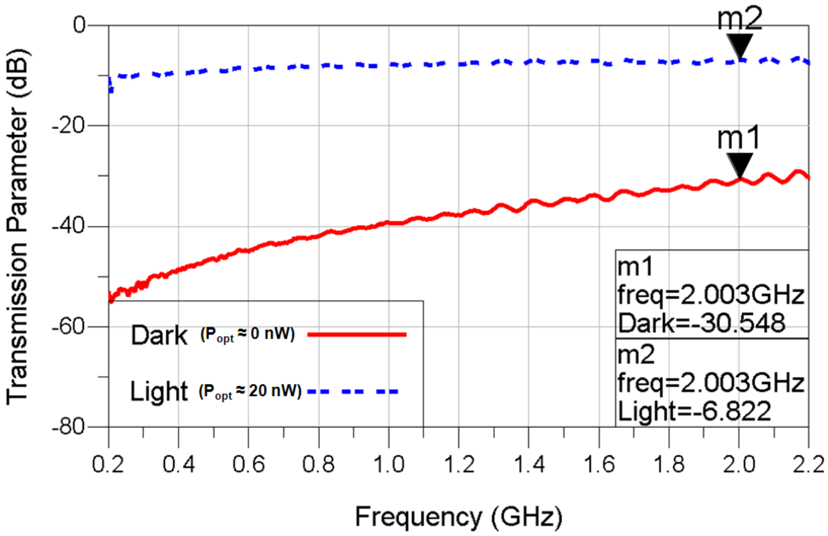

Figure 4.17: RF measurements of the zero-biased switch.

From table 4.1, we can conclude that the three stacked photodiodes are providing a voltage between $0.3V$ and $0.6V$, well below the value we anticipated of $1.2V$. Based in the discussion in 4.1.2, it is obvious that there are some leakage currents having this voltage reduction.

As a solution to this problem, we applied an additional external bias voltage (V_{bias}) through the VNA bias insertion port. The schematic of the circuit together with the schematic of the internal bias circuit of the VNA are shown in Fig. 4.18.

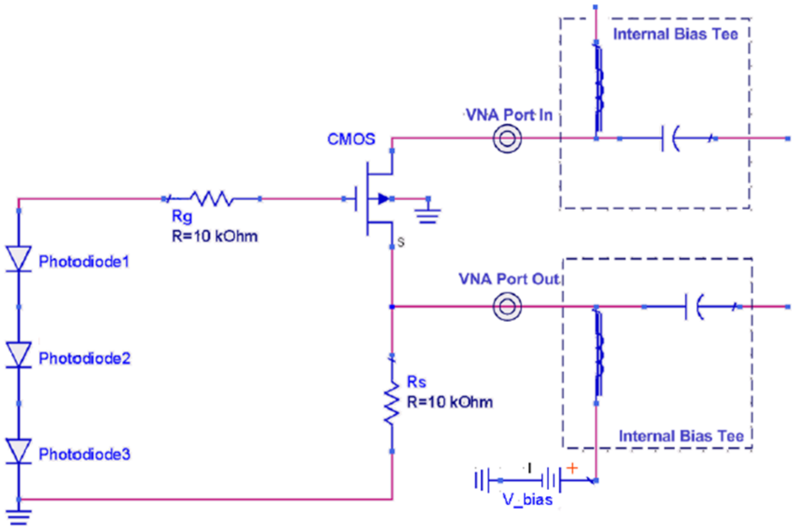

Figure 4.18: Schematic of the circuit with the VNA bias insertion ports.

This way, the gate-source voltage can be effectively increased by applying a negative bias (V_{bias}). Doing so, the resistance of the ON state drops significantly while the high resistance of the OFF state is maintained. Fig. 4.19 shows the measured results when we apply a $V_{bias} = -0.3V$.

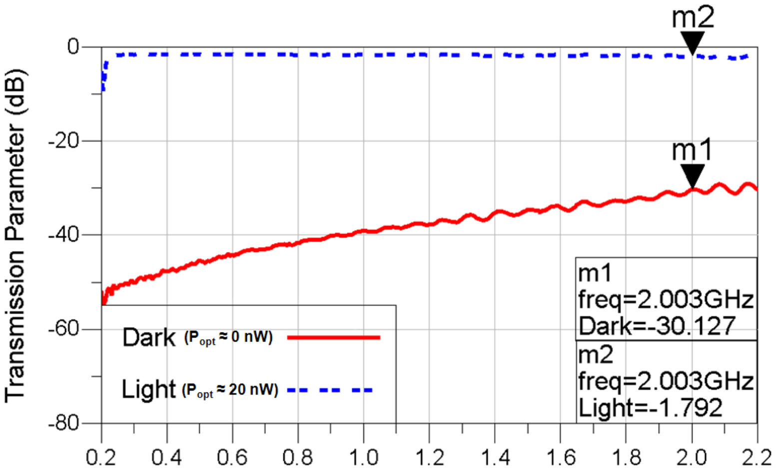

Figure 4.19: RF measurements of the switch with $V_{bias} = -0.3V$.

This modification works very well as it keeps the OFF state isolation extremely high, greater than $30dB$, while reducing by $5dB$ the losses in the ON state. Now a much improved $1.8dB$ insertion loss is achieved at 2GHz.

Effectively, what has been done is to increase the voltage at the gate by $0.3V$ so that the voltage V_G should be somewhere between $0.6V$ and $0.9V$ if the previously obtained results for the zero-biased transistor switch are correct.

Taking the values from table 4.1 for $0.6V$ and $0.9V$ we see that theRF transmission loss values should be between $1.15dB$ and $2.43dB$, which agrees with the measured losses of $1.8dB$.

The requirement for an additional external bias to obtain good RF performance is not desirable. However, in future designs, this can be avoided by using additional photodiodes in the gate circuit to turn the switch completely on.

4.1.4 Future prospects

The newly designed Si CMOS optical-RF switch shows great capabilities so far. However, we have encountered two main problems when measuring the device.

First of all, we have not been able to properly calibrate the VNA for doing these measurements causing a reduction of the bandwidth that could be explored and showing some imperfections in the measured data.

Although broader band measurements were not totally valid due to the resonances that appeared, the results obtained indicated that the device could work up to 7GHz with similar properties.

The second problem encountered was the high losses of the ON state. As already mentioned, one simple solution is to create an additional DC voltage at the gate node to reduce the RF resistance of the ON state. This could be done in one of two ways:by including a forth photodiode of the same size at the gate of the transistor or by increasing the area of the three existing photodiodes (since I_{SC} increases with diode area). In any case the main idea of this work, being a zero DC biasing of an optically controlled switch, would still be achieved.

The size of the transistor employed is fairly small; it is only $50\mu m$ wide. By increasing the width of the transistor, the resistance between the input and the output would decrease, resulting in lower losses on both states. As our OFF state losses are quite high, we could imagine in a future design increasing the transistor width or using multiple transistors [6] to reduce the ON state losses while always keeping a good isolation in the OFF state.

4.1.5 Conclusion

A novel zero-biased optically controlled RF switch in a commonly used $0.13\mu m\ Si$ CMOS technology has been developed for the first time.

Simulation results of the basic circuit have been shown followed by experimental results of the fabricated chip at both DC and RF frequencies. The RF switching performance was found to be acceptable at zero-bias ($S21_{OFF} = -30.55dB$ and $S21_{ON} = -6.82dB$ at $2GHz$), improving significantly with the application of a small DC bias ($S21_{OFF} = -30.13dB$ and $S21_{ON} = -1.79dB$ at $2GHz$). Such bias could be easily produced by the addition of another photodiode, rendering the switch completely passive again with excellent RF properties.

The switching time has not been measured yet but it seems to be an instantaneous response. Switching time measurements would be carried out in the future.

Based on the excellent results obtained, this new RF switch clearly demonstrates the possibility of using commonly available Si IC technology to build optically tunable microwave circuits.

4.2 Conclusion

This chapter has focused on the indirect optical control as a form of achieving tunable microwave circuits. The basis of the indirect optical control is that the optical light will be converted into an electrical signal to achieve the optical tunability studied in this report.

The main advantage of indirect optical control is that the microwave circuit is not optically tunable, but the control system is, so it gives the possibility of optimizing the control system and the microwave circuit separately.

In this chapter we have presented some examples of indirect optical control for tunable microwave circuits. However, all the literature about this used non-standard technologies to achieve good results.

This work focused then on developing an RF switch based in a commonly used technologies. We have presented in this context an optically tunable RF switch fabricated on the standard process from IBM based on $0.13\mu m$ Si CMOS technology.

The developed opto-RF switch showed great promise for achieving optically tunable microwave circuits using standard, low-cost Si IC technologies.

Parts of this section have been published at the IEEE International Topical Meeting on Microwave Photonics in Singapore (see Appendix B).

Bibliography

[1] A. S. Nagra, P. Chavarkar, C. J. Swann, T. Larry, M. L. VanBlaricum, U. K. Mishra, and R. A. York, "Monolithic optically variable capacitors for tunable microwave antennas," *IEEE/Cornell Conference on Advanced Concepts in High Speed Semiconductor Devices and Circuits*, pp. 69–78, 1997. x, 192

[2] A. Nagra, O. Jerphagnon, P. Chavarkar, M. VanBlaricum, and R. A. York, "Indirect optical control of microwave circuits using monolithic optically variable capacitors," *IEEE Transactions on Microwave Theory and Techniques*, vol. 47, pp. 1365–1372, July 1999. x, 192, 193, 194, 195

[3] A. S. Nagra, O. Jerphagnon, P. Chavarkar, M. VanBlaricum, and R. York, "Bias free optical control of microwave circuits and antennas using improved optically variable capacitors," *IEEE MTT-S InternationalMicrowave Symposium Digest*, vol. 2, pp. 687–690, 2000. x, 195, 196

[4] C. K. Sun, R. Nguyen, C. T. Chang, and D. J. Albares, "Photovoltaic-FET for optoelectronic RF/μwave switching," *IEEE Transactions on Microwave Theory and Techniques*, vol. 44, pp. 1747–1750, Oct. 1996. x, 196

[5] F. H. and K. O, "A 0.5-μm CMOS T/R switch for 900-MHz wireless applications," *IEEE Journal of Solid-State Circuits*, vol. 36, pp. 486–492, Mar. 2001. 197, 200

[6] K. Yamamoto, T. Heima, A. Furukawa, M. Ono, Y. Hashizume, H. Komurasaki, S. Maeda, H. Sato, and N. Kato, "A 2.4-GHz-band 1.8-V operation single-chip Si-CMOS T/R-MMIC front-end with a low insertion loss switch," *IEEE Journal of Solid-State Circuits*, vol. 36, pp. 1186–1197, Aug. 2001. 197, 200, 211

[7] D. Bouyge, A. Crunteanu, A. Pothier, P. Martin, P. Blondy, A. Velez, J. Bonache, J. C. Orlianges, and F. Martin, "Reconfigurable 4 pole bandstop

filter based on RF-MEMS-loaded split ring resonators," *IEEE MTT-S International Microwave Symposium Digest*, pp. 1–1, May 2010. 197

[8] F. Utsunomiya and T. Douseki, "Nanowatt-power-level automatic-switch circuit combining CMOS and photodiode," *IEEE Sensors*, pp. 1918–1921, Nov. 2010. 197

[9] Q. Z. Liu and R. I. MacDonald, "Modeling of optoelectronic switch with PIN photodiode and GaAs MESFET transmission gate," *IEEE Transactions on Electron Devices*, vol. 43, pp. 1833–1837, Nov. 1996. 198

[10] IBM Technologies, "CMOS8RF v1.2.0.0 design kit training," 2006. x, 199, 200

Chapter 5

General conclusion and perspectives

An overview of both reconfigurable components and tunability methods has been presented in **Chapter 1**. We have presented a general overview of tunable circuits and frequency control methods and it has been demonstrated that optical tunability offers great advantages to commonly used methods. For example, by developing the use of optical signals for frequency control, the immunity of of the electromagnetic waves can be enhanced and fast switching times can be achieved.

Some test structures to extract properties of photosensitive materials have been presented in **Chapter 2**. The first of this structures consisted on an interdigitated capacitor together with an extraction method to calculate in an easy enough way the relative permittivity and loss tangent of a photosensitive material. The second structure presented consisted of some coplanar lines to define the conductivity at high frequencies under dark and illuminated conditions. These two structures showed great promise to characterize photosensitive materials at microwave frequencies.

However, some future improvements could be done to these structures. In the first place, for the interdigitated capacitor, the connector used for measurements could be avoided and replaced with a GSG probe station. This would permit to isolate the effect of the material placed on top of the fingers of the interdigitated capacitor. Also, using the capacitor at its resonance would permit to maximize the effect of putting a material on top of it making the extraction easier and more accurate in this case. The last improvement of this structure would be more related to the material and would consist on depositing the material more accurately in terms of surface and thickness. This point would allow us to simulate the structure more closely to reality permitting again a more accurate extraction. The structure based *on coplanar lines showed that it could be suitable for giving a first estimation of the conductivity of a material, however materials with greater change in conductivity would be more suitable with this type of structure.*

The second part of **Chapter 2** concentrates on new photosensitive materials studied for our applications, Cadmium Sulfide (CdS)-loaded polymer , Nano-cristallyne Silicon ($nc - Si$)-loaded polymer, Zinc Oxide (ZnO) and Vanadium Dioxide (VO_2). The first of these materials changes by 13% its relative permittivity (from 4 to 4.6 which is considerable) when it is illuminated, however, the losses become more important ($tan\delta$ increasing from 0.05 in dark state to 0.12 when illuminated). This material needs to be improved in terms of the size, concentration and uniformity of the particle insertions to make it optimal for microwave applications. Nano-Crystalline silicon and zinc oxide did not show any change at microwave frequencies when they are placed under an optical source, nevertheless, literature and measurements at DC showed great promise for these two materials. Finally, the vanadium dioxide is not exactly a photosensitive material but a thermosensitive material, thermoconductive more specifically. However, this material could be used as a photoconductive material if the intensity of the light applied is high enough to heat the material. This material changes from a semiconductor state to a metal state according to the literature, but all the measurements have been carried out at low frequency and it is expected to be less sensitive at higher frequencies. The DC conductivity varies from $9.17 \times 10^{+1} S/m$ under dark condition to $4.61 \times 10^{+5} S/m$ under illumination according to the literature. Nonetheless, the change being so great, some applications would be possible with a smaller change in conductivity.

The development of optically functional microwave materials is mainly in its infancy so lots of progress can still be made to improve their properties. For the cadmium sulfide, which has shown the most promising results, studies are being carried out to decrease the dielectric losses while keeping the large relative permittivity change and for improving the deposition and doing it more accurately. For the nano-crystallyne silicon, the idea is to dope the nano-particles in order to maximize the photosensitive effects while for the zinc oxide the main improvement would be related to the light excitation applied, changing it to UV wavelengths. Finally, an *improvement of the deposition of the vanadium dioxide allowing thicker sheets would permit to use this material at higher frequencies with less losses.*

Chapter 3 has presented three different structures using direct optical control. It has been shown that the main interest of optical control is that no conversion of the light signal is needed as the optically tunable part is directly included in the circuit. Three different structures have been presented during the chapter exploiting this method. The first one consisted of a proof of concept of an LTCC photoconductive frequency tunable filter. It has been demonstrated via simulations and basic measurements that an LTCC tunable filter is achievable using a photoconductive material. In this study, we have demonstrated a filter with two states, ON ($6.3GHz$) and OFF ($8.66GHz$), and a filter having both states has been measured. A study to determine the needed conductivity of materials have been carried out ($\sigma < 10^{-3}S/m = \sigma_{max}$ and $\sigma > 10^{+5}S/m = \sigma_{min}$). The results of this study shows great promise for this type of structure. This work was published at URSI 2009 (Spain) and at CCECE 2010 (Canada).

However, as the measurements have been done with a perfect connection and a perfect open, the future prospects of this filter are first of all to use a photoconductive material to achieve real tunability. VO_2 material could be placed in the interconnections to prove the tunable filter, as could the opto-RF switches developed in Chapter 4. The presented filter shows great promise in terms of flexibility, as the addition of more "wings" will make a tunable filter with several states possible. Finally, LTCC technology has shown its capability to work over a wide range of frequencies so the same filter concept could be scaled to work at other bands.

The second structure presented in **Chapter 3** dedicated to direct optical control has been a tunable 3D dielectric resonator. The 3D resonator presented in this section showed, based on theory and simulations, that a perturbation of the electromagnetic field of a resonant mode would lead to a change in both the resonant frequency and the unloaded quality factor of the mode. We have designed three different structures, named basic configuration, configuration 2 and configuration 3, showing those changes. The measured results have shown that the VO_2 material placed in the resonator exhibits a state change from insulator to conductor at high frequencies. The three configurations showed a frequency shift with a degradation of the unloaded quality factor. It is clearly seen then the importance of a tradeoff between the frequency shift and the maximum unloaded quality factor achievable with this structure.

We have estimated by analyzing the measured results that in the OFF state, the VO_2 has no conductivity at high frequencies and that its value increases to about $\sigma = 1 \times 10^{+4}$ in the ON state. An optimization method for the placement of the material has also been presented which would help the designer in placing the photoconductive material at the right location. This method will not provide a final structure but will give the designer a trend to follow.

We are mostly interested in optical control but the material used in this application is vanadium dioxide, which is a thermoconductive material changing its state with temperature. Up until now, the material has been heated using a resistor, so the most important improvement is to change this heating system with a system based on an optical source. The plan is then to route the light directly to the thermoconductive material with a high enough intensity in order to heat the material with infrared light. Another improvement is related to the material itself, an increase of the deposition thickness to some wavelengths would provide better results in terms of unloaded quality factor and frequency shift. We have worked with a VO_2 *thickness of* $250nm$*, an extremely low value compared to the wavelength and the skin depth. However, it would be interesting to work with greater thickness that, based on our simulations and models, would result in higher unloaded quality factors.*

A photorefractive CdS tunable filter has been lastly presented in this chapter. This tunable filter is based on a new CdS-polymer MIM capacitor that changes its capacitance by 13% under illumination (same amount as the CdS-polymer material). By circuit and electromagnetic simulations a frequency tunable bandpass filter ($7.96GHz$ OFF state and $7.5GHz$ ON state) has been shown using the change in capacitance expected for these capacitors. The fabrication process of this filter is not completely developed so the tunable bandpass filter response was not obtained, but rather a phase shifter showing a $3°$ phase shift at $8GHz$ and a low pass filter changing its cutoff frequency from $14.6GHz$ to $13.1GHz$ were obtained instead. The circuits have been modelled with lumped components and the 13% change has been verified through this model. These results represent the largest optically-induced permittivity change ever demonstrated in a polymer material and show the great capabilities of this tunable capacitor. Parts of this work presented at 2011 European Microwave Conference.

There are still improvements to be made to this structure. First of all, a reduction in the dielectric losses of the photorefractive material should be undertaken which would lead to a better frequency response of the filter, decreasing the insertion losses especially. Also related to the material, a more accurate deposition would be desirable, controlling the thickness would permit us to estimate the values of the capacitor that would be fabricated beforehand allowing a more precise design. Finally, more control on the fabrication process would permit to develop higher order filters cascading more of such optically tunable capacitors. The obtained results have been good enough to stimulate more research in this field.

Chapter 4 was devoted to indirect optical control. The main advantage of this method is that the control circuit and the electromagnetic circuit can be optimized separately, but the optical signal then needs to be converted into a bias using a photosensitive device such as photodetector. At the beginning of this chapter, structures from the literature using this indirect optical control have been presented. However, all of these structures used expensive esoteric or tailor made state of the art technologies. In order to provide a practical low cost alternative to these devices, we have decided to develop a zero-bias optically controlled RF switch based on a standard IC technology. The technology chosen for this work has been the well established commercially available $0.13\mu m$ CMOS process from IBM, due to its capability to work at high (RF) frequencies. This IC technology has been presented and the novel circuit design and its layout have been shown in this chapter. The measured results at DC show a change in resistance between the RF ports ranging from 3900Ω in the OFF state to 15Ω when ON. The RF measurements showed insertion losses of $30dB$ in the OFF state of the RF switch and $6.8dB$ in the ON state, at $2GHz$. The ON state losses could however be reduced to only $1.8dB$ by adding a bias at the gate. It has been shown that the required bias is achievable passively with the inclusion of an extra photodiode. This work was presented in the 2011 Microwave Photonics Conference.

This work was a first attempt to exploit standard CMOS technology this way, and especially to use it as a photosensitive RF technology. The results showed great promise and although the insertion losses of the RF switch were relatively high, it has been shown that it would be possible to reduce them easily. In the future, the addition of another photodiode (or an increased area of the existing photodiodes) would be considered in order to increase the optically induced biasing. Also an increase of the switching transistor size could be considered in order to decrease these losses. This increase of the size would result in a worse rejection at its OFF state, but the rejection would still be around $30dB$ *which is sufficient for optical switching. The future of this work is to use this RF switch in high frequency structures such as filters or antennas for example.*

This thesis work has thus focused on optical tunability of RF components and has shown its potential in future applications as an alternative to current tunability methods such as MEMS or ferroelectric materials.

Although the circuits developed have not yet reached the quality of the circuits developed with other reconfigurability methods, we have to keep in mind that this is an early approach to optically-enhanced microwave technology and we have to consider these as initial steps toward optical controllability.

Materials need to be developed further, as do the circuit design techniques, in order to maximize the effects of those materials according to their properties. Nevertheless, we believe that a large part of the circuit tunability at microwave frequencies will eventually be based on optical control, continuing the trend established by a growing body of new microwave photonics concepts.

Appendix A

Other configurations

Configuration 4

Configuration 4 consists on two sheets of $1mm$ height on the top and the bottom of the resonator covering the whole diameter of the resonator as shown in Fig. A.1.

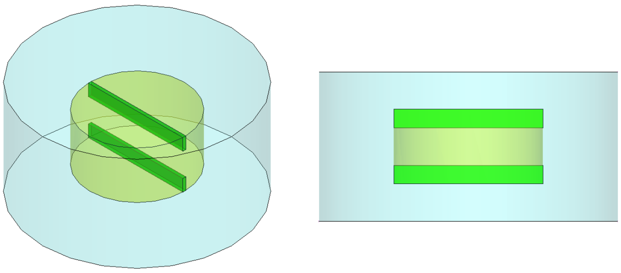

(a) 3D view.

(b) Top view.

Figure A.1: Design of the configuration 4 for the optimization.

The simulation results are presented for the change between $\sigma = 1 \times 10^{+1} S/m$ and $\sigma = 1 \times 10^{+5} S/m$ in table A.1 firstly and for a smaller change between $\sigma = 1 \times 10^{+2} S/m$ and $\sigma = 1 \times 10^{+4} S/m$ in table A.2 later.

Mode	$\sigma = 1 \times 10^{+1} S/m$		$\sigma = 1 \times 10^{+5} S/m$		Δf
	$f_0(GHz)$	Q_0	$f_0(GHz)$	Q_0	(MHz)
TE_{011}	13.384	520	13.522	576	138
TM_{011}	13.683	2881	13.722	475	39
TM_{121}	18.415	874	18.546	657	131
TE_{012}	20.892	443	21.063	1083	171
TM_{111}	21.632	1852	21.654	3417	22

Table A.1: Simulated results for conductivities $\sigma = 1 \times 10^{+1} S/m$ and $\sigma = 1 \times 10^{+5} S/m$ for configuration 4.

Mode	$\sigma = 1 \times 10^{+2} S/m$		$\sigma = 1 \times 10^{+4} S/m$		Δf
	$f_0(GHz)$	Q_0	$f_0(GHz)$	Q_0	(MHz)
TE_{011}	13.410	257	13.499	291	89
TM_{011}	13.684	1794	13.702	576	18
TM_{121}	18.435	420	18.518	366	84
TE_{012}	20.938	264	21.044	492	106
TM_{111}	21.635	1072	21.650	1693	15

Table A.2: Simulated results for conductivities $\sigma = 1 \times 10^{+2} S/m$ and $\sigma = 1 \times 10^{+4} S/m$ for configuration 4.

Configuration 5

Configuration 5 consists on one sheet of $2mm$ width in the middle of the resonator covering the whole height of the resonator as shown in Fig. A.2.

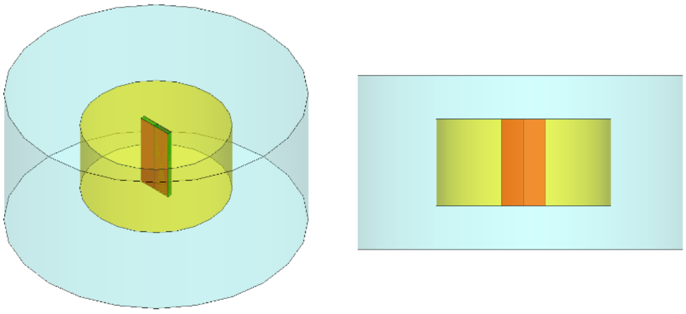

(a) 3D view.

(b) Top view.

Figure A.2: Design of the configuration 5 for the optimization.

The simulation results are presented for the change between $\sigma = 1 \times 10^{+1} S/m$ and $\sigma = 1 \times 10^{+5} S/m$ in table A.3 firstly and for a smaller change between $\sigma = 1 \times 10^{+2} S/m$ and $\sigma = 1 \times 10^{+4} S/m$ in table A.4 later.

Mode	$\sigma = 1 \times 10^{+1} S/m$		$\sigma = 1 \times 10^{+5} S/m$		Δf
	$f_0(GHz)$	Q_0	$f_0(GHz)$	Q_0	(MHz)
TE_{011}	13.387	330	13.292	1637	95
TM_{011}	13.666	5465	13.665	10003	1
TM_{121}	18.393	1675	18.388	13684	5
TE_{012}	20.914	601	20.672	249	242
TM_{111}	21.622	3139	21.629	7989	7

Table A.3: Simulated results for conductivities $\sigma = 1 \times 10^{+1} S/m$ and $\sigma = 1 \times 10^{+5} S/m$ for configuration 5.

Mode	$\sigma = 1 \times 10^{+2} S/m$		$\sigma = 1 \times 10^{+4} S/m$		Δf
	$f_0(GHz)$	Q_0	$f_0(GHz)$	Q_0	(MHz)
TE_{011}	13.378	75	13.285	561	93
TM_{011}	13.666	4190	13.665	9268	1
TM_{121}	18.387	2346	18.388	10884	1
TE_{012}	20.943	210	20.622	60	321
TM_{111}	21.623	2192	21.628	5367	5

Table A.4: Simulated results for conductivities $\sigma = 1 \times 10^{+2} S/m$ and $\sigma = 1 \times 10^{+4} S/m$ for configuration 5.

Configuration 6

Configuration 6 consists of two sheets of $1mm$ width in the borders of the resonator covering the whole height of the resonator as shown in Fig. A.3.

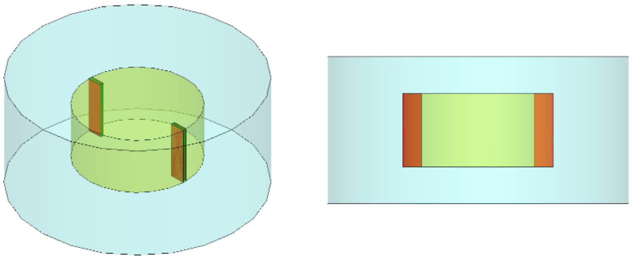

(a) 3D view. (b) Top view.

Figure A.3: Design of the configuration 6 for the optimization.

The simulation results are presented for the change between $\sigma = 1 \times 10^{+1} S/m$ and $\sigma = 1 \times 10^{+5} S/m$ in table A.5 firstly and for a smaller change between $\sigma = 1 \times 10^{+2} S/m$ and $\sigma = 1 \times 10^{+4} S/m$ in table A.6 later.

Mode	$\sigma = 1 \times 10^{+1} S/m$		$\sigma = 1 \times 10^{+5} S/m$		Δf
	$f_0(GHz)$	Q_0	$f_0(GHz)$	Q_0	(MHz)
TE_{011}	13.364	1360	13.363	11789	1
TM_{011}	13.679	3387	13.678	9706	1
TM_{121}	18.395	737	18.380	8809	15
TE_{012}	20.890	2253	20.885	7736	5
TM_{111}	21.644	4583	21.644	9105	0

Table A.5: Simulated results for conductivities $\sigma = 1 \times 10^{+1} S/m$ and $\sigma = 1 \times 10^{+5} S/m$ for configuration 6.

Mode	$\sigma = 1 \times 10^{+2} S/m$		$\sigma = 1 \times 10^{+4} S/m$		Δf
	$f_0(GHz)$	Q_0	$f_0(GHz)$	Q_0	(MHz)
TE_{011}	13.362	3894	13.363	10204	1
TM_{011}	13.678	3466	13.678	8798	0
TM_{121}	18.378	822	18.380	4682	2
TE_{012}	20.884	1849	20.885	6163	2
TM_{111}	21.642	3120	21.643	7573	1

Table A.6: Simulated results for conductivities $\sigma = 1 \times 10^{+2} S/m$ and $\sigma = 1 \times 10^{+4} S/m$ for configuration 6.

Configuration 7

Configuration 7 consists of two sheets of $1mm$ width at a distance of $1.5mm$ from the middle of the resonator covering the whole height of the resonator as shown in Fig. A.4.

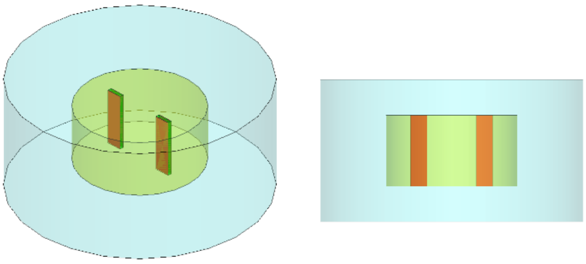
(a) 3D view.
(b) Top view.

Figure A.4: Design of the configuration 7 for the optimization.

The simulation results are presented for the change between $\sigma = 1 \times 10^{+1} S/m$ and $\sigma = 1 \times 10^{+5} S/m$ in table A.7 firstly and for a smaller change between $\sigma = 1 \times 10^{+2} S/m$ and $\sigma = 1 \times 10^{+4} S/m$ in table A.8 later.

Mode	$\sigma = 1 \times 10^{+1} S/m$		$\sigma = 1 \times 10^{+5} S/m$		Δf
	$f_0(GHz)$	Q_0	$f_0(GHz)$	Q_0	(MHz)
TE_{011}	13.354	411	13.344	8754	10
TM_{011}	13.666	3508	13.665	9645	1
TM_{121}	18.414	477	18.375	6246	39
TE_{012}	20.879	732	20.854	4391	25
TM_{111}	21.629	2984	21.629	6511	0

Table A.7: Simulated results for conductivities $\sigma = 1 \times 10^{+1} S/m$ and $\sigma = 1 \times 10^{+5} S/m$ for configuration 7.

Mode	$\sigma = 1 \times 10^{+2} S/m$		$\sigma = 1 \times 10^{+4} S/m$		Δf
	$f_0(GHz)$	Q_0	$f_0(GHz)$	Q_0	(MHz)
TE_{011}	13.341	973	13.344	5996	3
TM_{011}	13.665	3479	13.665	8569	1
TM_{121}	18.375	259	18.374	5907	2
TE_{012}	20.855	284	20.851	2262	4
TM_{111}	21.627	1225	21.627	4345	0

Table A.8: Simulated results for conductivities $\sigma = 1 \times 10^{+2} S/m$ and $\sigma = 1 \times 10^{+4} S/m$ for configuration 7.

Configuration 8

Configuration 8 consists of two sheets of $1mm$ width at the sides of the resonator covering the whole height of the resonator and one sheet of $2mm$ width in the middle of the resonator covering the whole height of the resonator as shown in Fig. A.5.

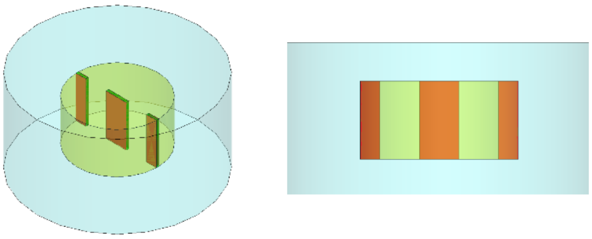

(a) 3D view. (b) Top view.

Figure A.5: Design of the configuration 8 for the optimization.

The simulation results are presented for the change between $\sigma = 1 \times 10^{+1} S/m$ and $\sigma = 1 \times 10^{+5} S/m$ in table A.9 firstly and for a smaller change between $\sigma = 1 \times 10^{+2} S/m$ and $\sigma = 1 \times 10^{+4} S/m$ in table A.10 later.

Mode	$\sigma = 1 \times 10^{+1} S/m$		$\sigma = 1 \times 10^{+5} S/m$		Δf
	$f_0(GHz)$	Q_0	$f_0(GHz)$	Q_0	(MHz)
TE_{011}	13.367	272	13.271	1623	96
TM_{011}	13.658	2619	13.656	9513	2
TM_{121}	18.352	536	18.333	9633	19
TE_{012}	20.894	489	20.646	244	248
TM_{111}	21.614	2229	21.620	6937	6

Table A.9: Simulated results for conductivities $\sigma = 1 \times 10^{+1} S/m$ and $\sigma = 1 \times 10^{+5} S/m$ for configuration 8.

Mode	$\sigma = 1 \times 10^{+2} S/m$		$\sigma = 1 \times 10^{+4} S/m$		Δf
	$f_0(GHz)$	Q_0	$f_0(GHz)$	Q_0	(MHz)
TE_{011}	13.355	74	13.264	560	91
TM_{011}	13.657	3062	13.646	8103	11
TM_{121}	18.329	694	18.332	5643	3
TE_{012}	20.917	190	20.595	59	322
TM_{111}	21.613	1444	21.619	4414	6

Table A.10: Simulated results for conductivities $\sigma = 1 \times 10^{+2} S/m$ and $\sigma = 1 \times 10^{+4} S/m$ for configuration 8.

Configuration 9

Configuration 9 consists of two sheets of $1mm$ width at a distance of $1mm$ from the middle of the resonator covering the whole height of the resonator as shown in Fig. A.6.

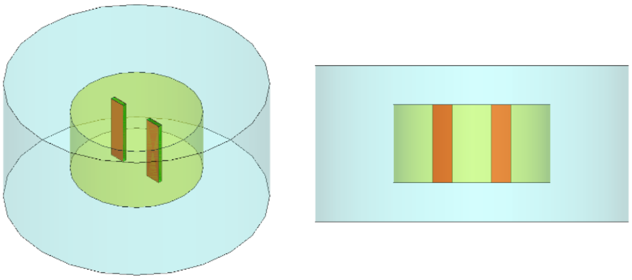

(a) 3D view. (b) Top view.

Figure A.6: Design of the configuration 9 for the optimization.

The simulation results are presented for the change between $\sigma = 1 \times 10^{+1} S/m$ and $\sigma = 1 \times 10^{+5} S/m$ in table A.11 firstly and for a smaller change between $\sigma = 1 \times 10^{+2} S/m$ and $\sigma = 1 \times 10^{+4} S/m$ in table A.12 later.

Mode	$\sigma = 1 \times 10^{+1} S/m$		$\sigma = 1 \times 10^{+5} S/m$		Δf
	$f_0(GHz)$	Q_0	$f_0(GHz)$	Q_0	(MHz)
TE_{011}	13.359	336	13.347	8122	12
TM_{011}	13.666	4134	13.665	9733	1
TM_{121}	18.416	576	18.386	7268	30
TE_{012}	20.887	564	20.854	3703	33
TM_{111}	21.627	2882	21.630	6311	3

Table A.11: Simulated results for conductivities $\sigma = 1 \times 10^{+1} S/m$ and $\sigma = 1 \times 10^{+5} S/m$ for configuration 9.

Mode	$\sigma = 1 \times 10^{+2} S/m$		$\sigma = 1 \times 10^{+4} S/m$		Δf
	$f_0(GHz)$	Q_0	$f_0(GHz)$	Q_0	(MHz)
TE_{011}	13.343	826	13.347	5348	4
TM_{011}	13.666	3766	13.665	8716	1
TM_{121}	18.385	342	18.384	3643	0
TE_{012}	20.854	220	20.849	1829	5
TM_{111}	21.626	1316	21.629	4072	3

Table A.12: Simulated results for conductivities $\sigma = 1 \times 10^{+2} S/m$ and $\sigma = 1 \times 10^{+4} S/m$ for configuration 9.

Configuration 10

Configuration 10 consists of two sheets of $1mm$ width at a distance of $2mm$ from the middle of the resonator covering the whole height of the resonator as shown in Fig. A.7.

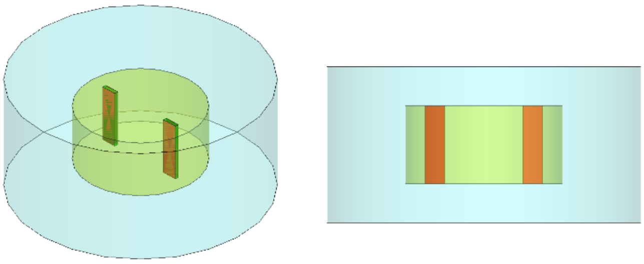

(a) 3D view. (b) Top view.

Figure A.7: Design of the configuration 10 for the optimization.

The simulation results are presented for the change between $\sigma = 1 \times 10^{+1} S/m$ and $\sigma = 1 \times 10^{+5} S/m$ in table A.13 firstly and for a smaller change between $\sigma = 1 \times 10^{+2} S/m$ and $\sigma = 1 \times 10^{+4} S/m$ in table A.14 later.

Mode	$\sigma = 1 \times 10^{+1} S/m$		$\sigma = 1 \times 10^{+5} S/m$		Δf
	$f_0(GHz)$	Q_0	$f_0(GHz)$	Q_0	(MHz)
TE_{011}	13.354	141	13.347	9938	7
TM_{011}	13.671	3101	13.669	9551	2
TM_{121}	18.403	490	18.365	6165	38
TE_{012}	20.877	1062	20.860	5624	17
TM_{111}	21.635	3259	21.632	7106	3

Table A.13: Simulated results for conductivities $\sigma = 1 \times 10^{+1} S/m$ and $\sigma = 1 \times 10^{+5} S/m$ for configuration 10.

Mode	$\sigma = 1 \times 10^{+2} S/m$		$\sigma = 1 \times 10^{+4} S/m$		Δf
	$f_0(GHz)$	Q_0	$f_0(GHz)$	Q_0	(MHz)
TE_{011}	13.344	1263	13.346	6980	2
TM_{011}	13.669	3203	13.669	8378	1
TM_{121}	18.366	258	18.363	2845	2
TE_{012}	20.861	414	20.858	3039	4
TM_{111}	21.632	1271	21.631	9792	1

Table A.14: Simulated results for conductivities $\sigma = 1 \times 10^{+2} S/m$ and $\sigma = 1 \times 10^{+4} S/m$ for configuration 10.

Appendix B

List of publications of José Manuel González

International conference papers:

Zero-bias optically controlled RF switch in $0.13\mu m$ *CMOS technology*

J. M. González, D. Baillargeat, N. Delhote, L. Roy, S. McGarry

IEEE International Topical Meeting on Microwave Photonics, Singapore (Singapore), October 2011.

A new optically controlled CdS-Polymer Capacitor for tunable microwave components

J. M. González, D. Baillargeat, N. Delhote, N. Jess, L. Roy, S. McGarry

European Microwave Conference, Manchester (United Kingdom), October 2011.

National conference papers:

LTCC-based optically tunable microwave filter

J. M. González, D. Baillargeat, L. Roy

23rd Canadian Conference on Electrical and Computer Engineering (CCECE), Calgary (Canada), May 2010.

Concepto de filtros reconfigurables ópticamente en LTCC

J. M. González, D. Baillargeat, L. Roy

XXIV Simposium Unión Científica de Radio (URSI), Santander (Spain), September 2009.

RESUMÉ

Ces travaux de thèse portent sur la conception de composants microondes innovants, reconfigurables par voie optique. L'objectif principal de la thèse est de proposer des solutions alternatives aux méthodes de réconfigurabilité actuelles comme les MEMS ou les diodes par exemple. Dans ces travaux nous nous sommes intéressés à la caractérisation des matériaux photosensibles aux fréquences microondes ainsi qu'aux méthodes de reconfigurabilité optique directe et indirecte.

Pour placer ce travail de thèse dans son contexte, la première partie de ce manuscrit est dédiée à une étude bibliographique des circuits reconfigurables et méthodes associées. Des comparaisons sont proposées pour montrer les avantages qu'un contrôle optique peut présenter.

La deuxième partie porte sur la description de matériaux photosensibles comme le sulfure de Cadmium ou le dioxyde de Vanadium et sur des structures de test utilisées pour les caractériser.

Dans le troisième chapitre de ce manuscrit, des structures agiles en fréquence sont présentées en exploitant un contrôle optique de type direct. Les structures présentées démontrent le concept d'un filtre LTCC reconfigurable en fréquence, d'un résonateur diélectrique 3D agile en se basant sur la photoconductivité ainsi que d'un filtre reconfigurable par variation de permittivité.

La dernière partie de cette thèse est consacrée au contrôle optique indirect et traite le cas d'un interrupteur RF à commande optique basé sur une technologie de fabrication standard Si CMOS.

ABSTRACT

This work focuses on novel optically reconfigurable components for microwave applications, the main objective being to propose alternative solutions to commonly used tuning methods such as MEMS or diodes. In this work, we have investigated photosensitive material characterization at microwave frequencies, and both direct and indirect methods of optical reconfigurability.

To provide context for this thesis, the first part is dedicated to a bibliographic review of reconfigurable circuits and methods, thus giving an overview of the technologies used at present and showing the interest for using optical control.

The second part of this dissertation is about test structures for characterizing photosensitive materials, including a presentation of materials such as Vanadium dioxide or Cadmium sulfide, among others.

In the third chapter of this thesis, frequency tunable structures exploiting direct optical control are studied. The structures presented include a “proof of concept” tunable LTCC filter, a 3D dielectric resonator based on photoconductive materials, and a tunable filter based on the change of a material's relative permittivity.

The last part of this work focuses on indirect optical control showing an opto-RF switch based on a standard Si CMOS fabrication technology.